

**MOLECULAR RECOGNITION: SYNTHESIS AND STUDY OF  
NON-COVALENT INTERACTIONS IN ORGANIC FLEXIMERS**

**A THESIS SUBMITTED IN PARTIAL FULFILLMENT OF THE  
REQUIREMENTS FOR THE DEGREE OF DOCTOR OF  
PHILOSOPHY**

**JAYANTA DOWARAH**

**MZU REGISTRATION NO. : 87 of 2014**

**Ph.D REGISTRATION NO. : MZU/Ph.D/845 of 21.04.2016**



**DEPARTMENT OF CHEMISTRY  
SCHOOL OF PHYSICAL SCIENCES  
FEBRUARY, 2021**

**MOLECULAR RECOGNITION: SYNTHESIS AND STUDY OF NON-  
COVALENT INTERACTIONS IN ORGANIC FLEXIMERS**

**BY**

**JAYANTA DOWARAH**  
**Department of Chemistry**

Under the supervision of  
**Dr. VED PRAKASH SINGH**

Submitted

In partial fulfillment of the requirement of the Degree of Doctor of Philosophy in  
Chemistry of Mizoram University, Aizawl.

MIZORAM UNIVERSITY  
(A central University under the Act of Parliament)  
**Department of Industrial Chemistry**  
School of Physical Sciences

**Dr. Ved Prakash Singh**  
Associate Professor

***CERTIFICATE***

This is to certify that the thesis entitled “*Molecular Recognition: Synthesis and Study of Non-Covalent Interactions in Organic Fleximers*” submitted by **Mr. Jayanta Dowarah**, for the degree of **Doctor of Philosophy** in the Mizoram University, Aizawl, Mizoram, embodies the record of original investigations carried out by him under my supervision. He has been duly registered and the thesis presented is worthy of being considered for the award of the Ph.D. degree. This work has not been submitted for any degree in any other university.

Dated: February 25, 2021

(Dr. VED PRAKASH SINGH)  
Supervisor

**Declaration of the Candidate**

**Mizoram University**

**February, 2021**

I, Jayanta Dowarah, hereby declare that the subject matter of this thesis is the record of work done by me, that the contents of this thesis did not form basis of the award of any previous degree to me or to do the best of my knowledge to anybody else, and that the thesis has not been submitted by me for any research degree in any other University/ Institute.

This is being submitted to the Mizoram University for the degree of Doctor of Philosophy in Chemistry.

(JAYANTA DOWARAH)

Candidate

(Prof. MUTHUKUMARAN R.)

Head

(Dr. VED PRAKASH SINGH)

Supervisor



## ACKNOWLEDGEMENT

At the outset, I would like to thank almighty God for giving me the strength, power and wisdom to accept this research study and complete the research work with sincerity and dedication. By the grace of God, this achievement has been possible.

The journey of my research work begins wherein I found a teacher, a mentor, an inspirational model, a source of strength and a pillar of support in my supervisor, Dr. Ved Prakash Singh, Associate Professor, Department of Industrial Chemistry, Mizoram University for his immense support, motivation, and patience for my Ph.D study and allied research work. His constance guidance has been a key element to me in completing the research work and in drafting the thesis in a better way. His believe in me has been an inspiration during the tenure of research study and his knowledgeable advice has mould me to be a better person in the society.

I extend my valuable and sincere thanks to all the teaching staff **Prof. Diwakar Tiwari, Prof. Muthukumuran R, Dr. N. Mohondas Singh, Dr. Zodinpuia Pachuau, Dr Bimolini Devi** and non-teaching staff, John sir and Brojen sir, Department of Chemistry, Mizoram University for their immeasurable suggestions and support has motivate me during my research work.

The continuous encouragement received from **Prof. Diwakar Tiwari**, Dean, School of Physical sciences, Mizoram University is to be acknowledged.

I express my heartfelt gratitude to Dr. Rajesh Kumar Kharwar, Department of Zoology, Kutir Post Gradaute College, Chakkey, Jaunpur; ISO Cell, Indian

Institute of Chemical Technology, Hyderabad; Prof. Umesh Chand Singh Yadav, Special Centre for Molecular Medicine, Jawaharlal Nehru University, New Delhi; Tezpur University, Assam ( Department of Chemistry); Gauhati University, Assam ( Department of Chemistry) and Guru Nanak Dev University ( Department of Chemistry), Punjab for their support and cooperation in completion of my research work.

I extend my gratitude to Department of Science and Technology (DST), Government of India for granting financial support by “DST-Inspire Fellowship” during the course of this Ph.D work.

I thank my fellow labmates, Mr. Lalhruaizela, Mr. Brilliant N. Marak, Mr. Laldingluaia Khiangte and Mr. Biki Hazarika in ensuring that proper lab experimentation is in process and pulling me up whenever I require motivation and support in the course of the thesis preparation. They also assist me in collection of research data. Their incredible ideas and knowledge has been a great source of contribution in preparation of the thesis. I also acknowledge Mr. Dipanta Gogoi for being a constant support and backbone at any point of time in my life. Again I feel pleasure to acknowledge Dr. Hemangshu Joshi, Mr. Malabya Chetia, Dr. Kalyani Rajkumari, Mr. Bhaskarjit Borah, Miss Shilpi Shikha Gogoi, Mr. Nishanta jyoti Changmai, Mr. Amlanjyoti Gogoi, Mr. Massod Hussain, Mr. Debajit Rabha, Mr. Himangshu Dehingia, Mr. Abhilakh Gogoi, Mr. Lakhyajit Nath, Miss Mali, Miss Siami, Mr. Binnoy Barman, Mr. Gautam raj Bawri, Miss Nayana Borah and Mr. Dibanjyoti Buragohain for their constant support, help and standing by my side at high

and low pace of my life. Their immense contribution in my life shall always be remembered.

Last but not the least; I extend my sincere thanks and gratitude to my parents, sister, brother-in-law, nephew and other family members for supporting and guiding me spiritually and religiously in drafting the thesis and my life in particular. I am thankful to all the well-wishers who have guided and motivated me throughout my research life.

Thank you God for everything.

(JAYANTA DOWARAH)

## **TABLE OF CONTENTS**

Title of the Thesis
Certificate
Declaration of the Candidate
Acknowledgement
Table of Contents
List of Tables
List of Figures
Abbreviations

## **CHAPTER 1**

### **1. INTRODUCTION**

1.1. Background.	1
1.2 Molecular recognition.	2
1.3 The non-covalent interaction involved in molecular recognition.	5
1.4 Survey of literature.	6
1.5 Importance of non-covalent interactions.	12
1.6 Method to study non-covalent interactions.	14
1.7 Scope of study.	16

## CHAPTER 2

### 2. SYNTHESIS AND STUDY OF HETERO-AROMATIC SYSTEM WITH METHYLENE LINKED FLEXIMERS

2.1.	Introduction.	17
2.2.	Present work.	19
2.3.	<b>Scheme 1:</b> Synthesis and study of dihydropyrimidinones derivatives with methylene linkers by the green method.	20
2.4.	Experimental.	21
	2.4.1. General procedure for the synthesis of dihydropyrimidinone (DHPM) derivatives ( <b>1.1-1.5</b> )	21
2.5.	Results and discussions.	23
	2.5.1. Data collection, reduction and refinement.	25
	2.5.2. X-Ray Crystallographic studies and Hirshfeld surface analysis of ( <b>1.1-1.5</b> )	25
2.6.	Cytotoxicity and anti-cancer activity of <b>1.1-1.5</b> .	38
	2.6.1. <i>In-silico</i> analysis of <b>1.1-1.5</b> .	39
	2.6.2. Biological activity of <b>1.1-1.5</b> .	40
2.7.	<b>Scheme 2:</b> Synthesis and study of 2-dihydropyridone and 2-pyridone derivatives with methylene linkers.	48
	2.7.1. General procedure for the synthesis of 4H-pyrans.	49
	2.7.2. General procedure for the synthesis of 3,4-dihydro-2-pyridones	

(2.0-2.6).	49
2.7.3. General procedure for the synthesis of 2-pyridone (2.7-2.12).	51
2.8 Results and discussions.	54
2.8.1. X-Ray crystallographic studies and Hirshfeld surface analysis of 2.1, 2.2, 2.3, 2.4, 2.5, 2.6, 2.7, 2.8 and 2.9.	54
2.9 Cytotoxicity and anti-cancer activity of compounds 2.1-2.6.	91
2.9.1. <i>In-silico</i> analysis of 2.1-2.6.	91
2.9.2. Biological activity of 2.1-2.6.	92
2.10 <b>Scheme 3:</b> Heterocyclic moiety is linked via substituted phenyl ring system through methylene linkers.	98
2.10.1. Experimental.	98
2.10.2. X-Ray crystallographic studies and Hirshfeld surface analysis of 3.2.2 and 3.3.3.	101
2.11 Conclusion.	110

### CHAPTER 3

#### 3. SYNTHESIS AND STRUCTURAL STUDY OF POLY-AROMATIC FLEXIMERS.

3.1. Introduction.	112
3.2. Present work.	114
3.3. <b>Scheme 4:</b> Methylene-linked Aromatic ring with bromide.	116

3.4	<b>Scheme 5:</b> Methylene-linked 2-pyridone derivatives with aromatic System.	119
3.5.	Results and discussions.	125
	3.5.1. X-ray crystallographic studies and Hirshfeld surface analysis of compounds 5.1-5.6	126
3.6	Conclusion.	164

## CHAPTER 4

### 4 SYNTHESIS AND STUDY OF ROSIGLITAZONE BASED BIO-ACTIVE MOLECULES.

4.1	Introduction.	165
4.2	Present work.	172
4.3	Experimental.	173
4.4	Results and discussions.	173
4.5	<b>Scheme 6:</b> Synthesis of benzylidene-TZD-Linker compounds with sesamol lipophilic head ( <b>6.1-6.4</b> ).	174
4.6	<b>Scheme 7:</b> Synthesis of benzylidene-TZD-Linker compounds with 2-cyano pyridone lipophilic head ( <b>7.1-7.8</b> ).	185
4.7	4.7. Antidiabetic activity of synthesized compounds <b>6.1-6.4</b> and <b>7.1-7.8</b>	202
	4.7.1. <i>In-silico</i> analysis of <b>6.1-6.4</b> and <b>7.1-7.8</b>	202
	4.7.2. Biological activity of <b>6.1-6.4</b> and <b>7.1-7.8</b>	207

4.8	Conclusion.	209
-----	-------------	-----

## **CHAPTER 5**

<b>5. SUMMARY AND CONCLUSION</b>	211
----------------------------------	-----

<b>REFERENCES</b>	214
-------------------	-----

### **BIO-DATA**

### **PARTICULARS OF THE CANDIDATE**

#### **List of Publications**

#### **Conferences and Symposium**



## LISTS OF TABLES

<b>Table</b>	<b>Title</b>	<b>Page</b>
1.1	Types and estimated bond energies of non-covalent interactions	6
2.1	Crystal data of compounds <b>1.3</b> , <b>1.4</b> and <b>1.5</b> .	25
2.2	Intermolecular and intramolecular interactions in <b>1.3</b> .	26
2.3	Intermolecular and intramolecular interactions in <b>1.4</b>	30
2.4	Intermolecular and intramolecular interactions in <b>1.5</b> .	34
2.5	Binding energy and the residues involved in the interaction of <b>1.1</b> , <b>1.2</b> , <b>1.3</b> , <b>1.4</b> , and <b>1.5</b> with kinesin Eg5 protein	39
2.6	Crystal data of compounds <b>2.1</b> , <b>2.2</b> and <b>2.3</b>	54
2.7	Intermolecular and intramolecular interactions in <b>2.1</b>	55
2.8	Intermolecular and intramolecular interactions in <b>2.2</b>	60
2.9	Intermolecular and intramolecular interactions in <b>2.3</b>	63
2.10	Crystal data of compounds of <b>2.4</b> , <b>2.5</b> and <b>2.6</b>	67
2.11	Intermolecular and intramolecular interactions in <b>2.4</b>	68
2.12	Intermolecular and intramolecular interactions in <b>2.5</b>	71
2.13	Intermolecular and intramolecular interactions in <b>2.6</b>	75
2.14	Crystal data of compounds <b>2.7</b> , <b>2.8</b> and <b>2.9</b>	79
2.15	Intermolecular and intramolecular interactions in <b>2.7</b>	79
2.16	Intermolecular and intramolecular interactions in <b>2.8</b>	84

<b>Lists of Tables (continued)</b>	<b>Page</b>
2.17 Intermolecular and intramolecular interactions in <b>2.9</b>	87
2.18 Binding energy and the residues involved in the interaction of <b>2.1, 2.2, 2.3, 2.4, 2.5</b> and <b>2.6</b> with kinesin Eg5 protein	92
2.19 Crystal data of compounds <b>3.2.2</b> and <b>3.2.3</b>	103
2.20 Intermolecular and intramolecular interactions in <b>3.2.2</b>	103
2.21 Intermolecular and intramolecular interactions in <b>3.2.3</b>	107
3.1 Crystal data of compounds <b>5.1</b> and <b>5.2</b>	127
3.2 Intermolecular and intramolecular interactions in <b>5.1</b>	128
3.3 Intermolecular and intramolecular interactions in <b>5.2</b>	134
3.4 Crystal data of compounds <b>5.3</b> and <b>5.4</b> .	139
3.5 Intermolecular and intramolecular interactions in <b>5.3</b> .	140
3.6 Intermolecular and intramolecular interactions in <b>5.4</b>	146
3.7 Crystal data of compounds <b>5.5</b> and <b>5.6</b> .	153
3.8 Intermolecular and intramolecular interactions in <b>5.5</b>	154
3.9 Intermolecular and intramolecular interactions in <b>5.6</b> .	160
4.1 Docking score of <b>scheme 6</b> compounds ( <b>6.1-6.4</b> ) with PPAR- $\gamma$ enzyme.	205
4.2 Docking score of <b>scheme 7</b> compounds ( <b>7.1-7.8</b> ) with PPAR- $\gamma$ enzyme.	208
4.3 Effect of different compounds treatment on blood glucose level and body weight	212

## LISTS OF FIGURES

<b>Fig. No.</b>	<b>Title</b>	<b>Page</b>
1.1	Imidazole and pyrimidine linked fleximer.	2
1.2	Formation of a 1:1 complex of sulfonamide and pyridine-N-oxide.	3
1.3	Arene-arene interaction by face to face interaction.	7
1.4	Edge to face aromatic interaction.	8
1.5	Heterocyclic $\pi$ stacking between dUMP and the anticancer drug 1843U89 bound at the active site of thymidylate synthase.	8
1.6	Methane-Benzene Complex shows the C-H/ $\pi$ interaction.	9
1.7	Cation- $\pi$ interaction between benzene and a sodium cation.	10
1.8	Cation/ $\pi$ interactions between a HEPES molecule and Trp143 in the ACh binding site of an ACh-binding protein.	11
1.9	Lone pair/ $\pi$ interactions (green dashed lines) stabilizing the left-handed supramolecular structure of Z-DNA.	11
1.10	A chain of alternating “sulfur and $\pi$ -bonded atoms” as identified in hen egg-white lysozyme.	12
1.11	Base pair stacking in DNA.	13
1.12	Binding mode of the anti-Alzheimer drug E2020 within the active site of acetyl cholinesterase from <i>Torpedo californica</i>	15
2.1	Pyrimidine derivative bases.	18

<b>Lists of Figures (continued)</b>	<b>Page</b>
2.2 Cyanopyridones as anticancer agents.	20
2.3 Design of heterocyclic moieties-linked pyridones and pyrimidinones derivatives	21
2.4 ORTEP diagram of <b>1.3</b>	26
2.5 (a) Packing diagram of <b>1.3</b> , (b) C-H-- $\pi$ interactions in <b>1.3</b> , and (c) C-H--O, N-H--O, and N-H--S interactions in <b>1.3</b>	28
2.6 (a) Hirshfeld surface mapped on $d_{\text{norm}}$ for compound <b>1.3</b> , (b) Two-dimensional fingerprint plot for compound <b>1.3</b>	28
2.7 (a) Non-covalent interactions forming $R_2^2$ (8), (b) CH-- $\pi$ interactions in weak-interactions calculations of <b>1.3</b>	29
2.8 (a) and (b) Curvedness both side view of compound <b>1.3</b> , (c) and (d) Shape index both side view of compound <b>1.3</b> .	30
2.9 ORTEP diagram of <b>1.4</b> .	31
2.10 (a) Packing diagram of <b>1.4</b> , (b) N-H--O, C-H--O & N-H--S interactions in <b>1.4</b>	32
2.11 (a) Hirshfeld surface mapped on $d_{\text{norm}}$ for compound <b>1.4</b> , (b) Two-dimensional fingerprint plot for compound <b>1.4</b>	32
2.12 (a) Non-covalent interactions forming $R_2^2$ (8), (b) C-H-- $\pi$ and C-H--O interactions in weak interactions calculations of <b>1.4</b>	34

<b>Lists of Figures (continued)</b>	<b>Page</b>
2.13 (a) and (b) Curvedness both side view of compound <b>1.4</b> , (c) and (d) Shape index both side view of compound <b>1.4</b> .	34
2.14 ORTEP diagram of <b>1.5</b>	35
2.15 (a) Packing diagram of <b>1.5</b> , (b) $\pi$ -- $\pi$ interactions in <b>1.5</b> , and (c) N-H--O, C-H--O & N-H--S interactions in <b>1.5</b>	36
2.16 (a) Hirshfeld surface mapped on $d_{\text{norm}}$ for compound <b>1.5</b> , (b) Two-dimensional fingerprint plot for compound <b>1.5</b> .	37
2.17 (a) Non-covalent interactions forming $R_2^2$ (8), (b) $\pi$ -- $\pi$ interactions in weak interactions calculations of <b>1.5</b> .	38
2.18 (a) and (b) Curvedness both side view of compound <b>1.5</b> , (c) and (d) Shape index both side view of compound <b>1.5</b>	39
2.19 (a) and (b) Binding mode of compounds <b>1.2</b> and <b>1.5</b> in the active site cavity of Eg5 protein and 2D represent their interactions.	41
2.20 A549 lung adenocarcinoma cells were treated with (A) different concentrations (10 $\mu$ M, 25 $\mu$ M, 50 $\mu$ M, 100 $\mu$ M, 200 $\mu$ M, 300 $\mu$ M) of different compounds ( <b>1.1</b> , <b>1.2</b> , <b>1.3</b> , <b>1.4</b> and <b>1.5</b> ) and cell viability was analysed by MTT assay. (B) Cells were treated with different concentrations of selected <b>1.2</b> , <b>1.4</b> , and <b>1.5</b> for 24 h, 48 h, and 72 h, and cell viability was examined by MTT assay.	44

<b>Lists of Figures (continued)</b>	<b>Page</b>
2.21 Trypan blue assay was performed to check the effect of <b>1.2</b> , <b>1.4</b> , and <b>1.5</b> at 50, 100, and 200 $\mu\text{M}$ doses. Graphs represent percent cell death and the total number of cells for (A) 24 h and (B) 48 h.	46
2.22 A549 adenocarcinoma cells were treated with 200 $\mu\text{M}$ <b>1.2</b> and <b>1.5</b> compounds for 24 and 48 h and stained with acridine orange and ethidium bromide.	47
2.23 A549 adenocarcinoma cells were treated with 200 $\mu\text{M}$ <b>1.2</b> and <b>1.5</b> compounds for 24 and 48 h and stained with Hoechst stain, Cell death was assessed using a fluorescence microscope, and images were taken at 200X magnification.	48
2.24 ORTEP diagram of <b>2.1</b> .	55
2.25 (a) Packing diagram of <b>2.1</b> , (b) C-H--O, and C-H--N interactions in <b>2.1</b> , (c) C-H-- $\pi$ interactions in <b>2.1</b> .	58
2.26 (a) Hirshfeld surface of compound <b>2.1</b> , (b) Two-dimensional fingerprint plot for compound <b>2.1</b> .	58
2.27 (a) Non-covalent interactions forming $R_2^1(8)$ , (b) N-H--O, CH-- $\pi$ interactions in <b>2.1</b> .	59
2.28 (a) and (b) Curvedness both side view of compound <b>2.1</b> , (c) and (d) Shape index both side view of compound <b>2.1</b> .	59

<b>Lists of Figures (continued)</b>	<b>Page</b>
2.29 ORTEP diagram of <b>2.2</b>	60
2.30 (a) Packing diagram, (b), (c) and (d) represents the C-H-- $\pi$ , C-H--O, and N-H--O interaction in <b>2.2</b> .	61
2.31 (a) Hirshfeld surface of compound <b>2.2</b> , (b) Two-dimensional fingerprint plot for compound <b>2.2</b> .	62
2.32 (a) Weak hydrogen bonds interactions of <b>2.2</b> , (b) CH-- $\pi$ interactions in weak interactions calculations of <b>2.2</b> .	62
2.33 (a) and (b) Curvedness both side view of compound <b>2.2</b> , (c) and (d) Shape index both side view of compound <b>2.2</b> .	63
2.34 ORTEP diagram of <b>2.3</b> .	63
2.35 (a) Packing diagram of <b>2.3</b> , (b) C-H--O, N-H--O, C-H--N interactions in <b>2.3</b> and (c) C-H-- $\pi$ interactions in <b>2.3</b> .	65
2.36 (a) Hirshfeld surface of compound <b>2.3</b> , (b) Two-dimensional fingerprint plot for compound <b>2.3</b> .	65
2.37 (a) C-H--O and C-H--H interactions, and (b) C-H-- $\pi$ interactions in weak interactions calculations of <b>2.3</b> .	66
2.38 (a) and (b) Curvedness both side view of compound <b>2.3</b> , (c) and (d) Shape index both side view of compound <b>2.3</b> .	67
2.39 ORTEP diagram of <b>2.4</b> .	67

<b>Lists of Figures (continued)</b>	<b>Page</b>
2.40 (a) Packing diagram of <b>2.4</b> , (b) C-H-- $\pi$ interactions in <b>2.4</b> and (c) C-H--O, and N-H--O interactions in <b>2.4</b> .	69
2.41 (a) Hirshfeld surface of compound <b>2.4</b> , (b) Two-dimensional fingerprint plot for compound <b>2.4</b> .	70
2.42 (a) Non-covalent interactions forming $R_2^2(8)$ , (b) CH--O interactions in weak interactions calculations of <b>2.4</b> .	70
2.43 (a) and (b) Curvedness both side view of compound <b>2.4</b> , (c) and (d) Shape index both side view of compound <b>2.4</b> .	71
2.44 ORTEP diagram of <b>2.5</b> .	71
2.45 (a) Packing diagram of <b>2.5</b> , (b) Cl-- $\pi$ , C-H-- $\pi$ , C-H--O, and C-H--N interactions in <b>2.5</b> .	73
2.46 (a) Hirshfeld surface of compound <b>2.5</b> , (b) Two-dimensional fingerprint plot for compound <b>2.5</b> .	73
2.47 (a) Non-covalent interactions forming $R_2^2(8)$ , (b) C-H-- $\pi$ interactions in <b>2.5</b> .	74
2.48 (a) and (b) Curvedness both side view of compound <b>2.5</b> , (c) and (d) Shape index both side view of compound <b>2.5</b> .	74
2.49 ORTEP diagram of <b>2.6</b> .	75
2.50 (a), (b), (c), and (d) C-H-- $\pi$ , C-H--O, and N-H--O in interactions in <b>2.6</b> .	76



<b>Lists of Figures (continued)</b>	<b>Page</b>
2.51 (a) Hirshfeld surface of compound <b>2.6</b> , (b) Two-dimensional fingerprint plot for compound <b>2.6</b> .	77
2.52 (a), and (b) C-H--O interactions in <b>2.6</b> .	77
2.53 (a) and (b) Curvedness both side view of compound <b>2.6</b> , (c) and (d) Shape index both side view of compound <b>2.6</b> .	78
2.54 ORTEP diagram of <b>2.7</b> .	78
2.55 (a) Packing diagram of <b>2.7</b> , (b) C-H-- $\pi$ interactions in <b>2.7</b> , and (c) C-H--O, N-H...O, and N-H--S interactions in <b>2.7</b> .	81
2.56 (a) Hirshfeld surface of compound <b>2.7</b> , (b) Two-dimensional fingerprint plot for compound <b>2.7</b> .	82
2.57 (a) C-H--O and N-H--O interactions, and (b) C-H-- $\pi$ interactions in weak interactions calculations of <b>2.7</b> .	83
2.58 (a) and (b) Curvedness both side view of compound <b>2.7</b> , (c) and (d) Shape index both side view of compound <b>2.7</b> .	83
2.59 ORTEP diagram of <b>2.8</b> .	84
2.60 (a) Packing diagram of <b>2.8</b> , (b), (c) and (d) represents the C-H--O, N-H--O and C-H-- $\pi$ interaction in <b>2.8</b> .	85
2.61 (a) Hirshfeld surface of compound <b>2.8</b> , (b) Two-dimensional fingerprint plot for compound <b>2.8</b> .	86

<b>Lists of Figures (continued)</b>	<b>Page</b>
2.62 (a) and (b) Weak interactions calculations of <b>2.8</b> .	86
2.63 (a) and (b) Curvedness both side view of compound <b>2.8</b> , (c) and (d) Shape index both side view of compound <b>2.8</b> .	87
2.64 ORTEP diagram of <b>2.9</b> .	87
2.65 (a) Packing diagram of <b>2.9</b> , (b) C-H--O, N-H--O, C-H--H interactions in <b>2.9</b> , and (c) C-H-- $\pi$ interactions in <b>2.9</b> .	89
2.66 (a) Hirshfeld surface of compound <b>2.9</b> , (b) Two-dimensional fingerprint plot for compound <b>2.9</b> .	90
2.67 (a) C-H--O and N-H--O interactions in weak interactions calculations of <b>2.9</b> and (b) C-H-- $\pi$ interactions in weak interactions calculations of <b>2.9</b> .	91
2.68 (a) and (b) Curvedness both side view of compound <b>2.9</b> , (c) and (d) Shape index both side view of compound <b>2.9</b> .	91
2.69 (a) and (b) Binding mode of compounds <b>2.1</b> and <b>2.3</b> in the active site cavity of Eg5 protein and 2D represent their interactions.	93
2.70 A549 lung adenocarcinoma cells were treated with (A) different concentrations (10 $\mu$ M, 25 $\mu$ M, 50 $\mu$ M, 100 $\mu$ M, 200 $\mu$ M, 300 $\mu$ M) of different compounds ( <b>2.1</b> , <b>2.2</b> , <b>2.3</b> , <b>2.4</b> , <b>2.5</b> and <b>2.6</b> ) and cell viability was analysed by MTT assay. (B) Cells were treated with different concentrations of selected <b>2.1</b> and <b>2.2</b> for 24 h and 48 h,	

<b>Lists of Figures (continued)</b>	<b>Page</b>
and cell viability was examined by MTT assay.	95
2.71 Trypan blue assay was performed to check the effect of <b>2.1</b> and <b>2.2</b> at 25, 50, and 100 $\mu$ M doses on A549 cells. Graphs represent the percent cell death and the total number of cells for (A) 24 h and (B) 48 h.	96
2.72 A549 adenocarcinoma cells were treated with 100 $\mu$ M <b>2.1</b> and <b>2.2</b> compounds for 24 and 48 h and stained with acridine orange and ethidium bromide.	97
2.73 A549 adenocarcinoma cells were treated with 100 $\mu$ M <b>2.1</b> and <b>2.2</b> compounds for 24 and 48 h and stained with Hoechst stain, and cell death was assessed by fluorescence microscope, and images were taken at 200X magnification with 100 $\mu$ M, <b>2.1</b> , and <b>2.2</b> compounds.	98
2.74 ORTEP diagram of <b>3.2.2</b> .	102
2.75 Packing diagram of a unit cell of compound <b>3.2.2</b> along the b axis.	104
2.76 (a) $\pi$ -- $\pi$ interactions and (b) C-H... $\pi$ interactions in compound <b>3.2.2</b> .	104
2.77 (a) Hirshfeld surface of compound <b>3.2.2</b> , (b) Two-dimensional fingerprint plot for compound <b>3.2.2</b> .	105
2.78 (a) $\pi$ -- $\pi$ interaction and (b) C-H-- $\pi$ and C-H--N interactions in compound <b>3.2.2</b> in Hirshfeld surface analysis.	106
2.79 (a) and (b) Curvedness both side view of compound <b>3.2.2</b> ,	

<b>Lists of Figures (continued)</b>	<b>Page</b>
(c) and (d) Shape index both side view of compound <b>3.2.2.</b>	107
2.80 ORTEP diagram of <b>3.2.3.</b>	107
2.81 (a) Packing diagram of <b>3.2.3</b> , (b) C-H--O, and C-H--N interactions in <b>3.2.3.</b>	108
2.82 (a) C-H-- $\pi$ interactions intermolecular and (b) $\pi$ -- $\pi$ interactions in <b>3.2.3.</b>	109
2.83 (a) Hirshfeld surface of compound <b>3.2.3</b> , (b) Two-dimensional fingerprint plot for compound <b>3.2.3.</b>	110
2.84 (a) $\pi$ -- $\pi$ interactions and (b) C-H--O interactions in compound <b>3.2.3.</b>	110
2.85 (a) and (b) Curvedness both side view of compound <b>3.2.3</b> , (c) and (d) Shape index both side view of compound <b>3.2.3.</b>	110
3.1 2-Pyridone compounds which possess physiological activity.	114
3.2 Flexible dipyrindone.	115
3.3 Design of heterocyclic moieties-linked dihydropyridone derivatives.	116
3.4 ORTEP diagram of compound <b>5.1.</b>	127
3.5 Packing diagram of molecule <b>5.1.</b>	129
3.6 (a), (b) and (c) diagram showing non-covalent interactions in molecule <b>5.1.</b>	129
3.7 (a) and (b) C-H-- $\pi$ and C-O-- $\pi$ interactions in molecule <b>5.1.</b>	130

<b>Lists of Figures (continued)</b>	<b>Page</b>
3.8 (a) Hirshfeld surface mapped on $d_{\text{norm}}$ for compound <b>5.1</b> , (b) Two-dimensional fingerprint plot for compound <b>5.1</b> .	131
3.9 (a) C-H-- $\pi$ interaction, (b) $\pi$ -- $\pi$ interaction and (c) lone pair-- $\pi$ interactions forming in Hirshfeld analysis of compound <b>5.1</b> .	132
3.10 (a) and (b) Curvedness both side view of compound <b>5.1</b> , (c) and (d) Shape index both side view of compound <b>5.1</b> .	133
3.11 ORTEP diagram of compound <b>5.2</b> .	133
3.12 Packing diagram of molecule <b>5.2</b> .	135
3.13 (a) and (b) diagram showing C-H-- $\pi$ and C-N-- $\pi$ , C-H--N, C-H--O interactions in molecule <b>5.2</b> .	136
3.14 (a) Hirshfeld surface mapped on $d_{\text{norm}}$ for compound <b>5.2</b> , (b) Two-dimensional fingerprint plot for compound <b>5.2</b> .	136
3.15 (a) and (b) C-H-- $\pi$ interaction, (c) lone pair-- $\pi$ interactions, and N--C interaction forming in Hirshfeld analysis of compound <b>5.2</b> .	137-138
3.16 (a) and (b) Curvedness both side view of compound <b>5.2</b> , (c) and (d) Shape index both side view of compound <b>5.2</b> .	138
3.17 ORTEP diagram of compound <b>5.3</b> .	139
3.18 Packing diagram of molecule <b>5.3</b> .	141
3.19 (a) C-H--O, C-H--N, N--C interactions in molecule <b>5.3</b> ,	

<b>Lists of Figures (continued)</b>	<b>Page</b>
(b) C-H-- $\pi$ interactions of compound <b>5.3</b> .	141
3.20 (a) lone pair-- $\pi$ interactions of <b>5.3</b> and (b) $\pi$ -- $\pi$ interactions of <b>5.3</b> .	142
3.21 (a) Hirshfeld surface mapped on $d_{\text{norm}}$ for compound <b>5.3</b> ,	
(b) Two-dimensional fingerprint plot for compound <b>5.3</b> .	143
3.22 (a) $\pi$ -- $\pi$ interactions of <b>5.3</b> , (b) C-H--N and C-H--O interactions of compound <b>5.3</b> , and (c) lone pair-- $\pi$ forming in Hirshfeld analysis of compound <b>5.3</b> .	144-145
3.23 (a) and (b) Curvedness both side view of compound <b>5.3</b> ,	
(c) and (d) Shape index both side view of compound <b>5.3</b> .	145
3.24 ORTEP diagram of compound <b>5.4</b> .	146
3.25 Packing diagram of molecule <b>5.4</b> .	147
3.26 (a), (b) and (b) C-H-- $\pi$ , C-H--O, and C-H--N interactions of <b>5.4</b> , and (d) Lone pair-- $\pi$ interaction of <b>5.4</b> .	149
3.27 (a) Hirshfeld surface mapped on $d_{\text{norm}}$ for compound <b>5.4</b> ,	
(b) Two-dimensional fingerprint plot for compound <b>5.4</b> .	150
3.28 (a) C-H--O interaction and (b) C-H-- $\pi$ and C-H--C (b) lone pair-- $\pi$ interactions forming in Hirshfeld analysis of compound <b>5.4</b> .	152
3.29 (a) and (b) Curvedness both side view of compound <b>5.4</b> ,	
(c) and (d) Shape index both side view of compound <b>5.4</b> .	152

<b>Lists of Figures (continued)</b>	<b>Page</b>
3.30 ORTEP diagram of compound <b>5.5</b> .	153
3.31 Packing diagram of molecule <b>5.5</b> .	155
3.32 (a) C-H--O and C-H-- $\pi$ interactions, (b) C-H--O, C-H-- $\pi$ , lone pair-- $\pi$ and $\pi$ -- $\pi$ , and (c) C-H-- $\pi$ , lone pair-- $\pi$ and $\pi$ -- $\pi$ interactions in molecule <b>5.5</b> .	156
3.33 (a) Hirshfeld surface mapped on $d_{\text{norm}}$ for compound <b>5.5</b> , (b) Two-dimensional fingerprint plot for compound <b>5.5</b> .	157
3.34 (a) C-H--O interaction, (b) C-H-- $\pi$ interactions (c) $\pi$ -- $\pi$ interaction forming in Hirshfeld analysis of compound <b>5.5</b> .	159
3.35 (a) and (b) Curvedness both side view of compound <b>5.5</b> , (c) and (d) Shape index both side view of compound <b>5.5</b> .	159
3.36 ORTEP diagram of compound <b>5.6</b> .	160
3.37 Packing diagram of molecule <b>5.6</b> .	161
3.38 (a) C-H--O and C-H--N interactions, (b) C-H-- $\pi$ interactions, and (c) C-H-- $\pi$ , lone pair-- $\pi$ and $\pi$ -- $\pi$ interactions in molecule <b>5.6</b> .	162
3.39 (a) Hirshfeld surface mapped on $d_{\text{norm}}$ for compound <b>5.6</b> , (b) Two-dimensional fingerprint plot for compound <b>5.6</b> .	163
3.40 (a) C-H--N interaction and (b) CH-- $\pi$ and $\pi$ -- $\pi$ interactions forming in Hirshfeld analysis of compound <b>5.6</b> .	164

<b>Lists of Figures (continued)</b>	<b>Page</b>
3.41 (a) and (b) Curvedness both side view of compound <b>5.6</b> , (c) and (d) Shape index both side view of compound <b>5.6</b> .	165
4.1 Thiazolidinedione derivatives <b>4.0.1</b> and <b>4.0.2</b> as potent PTP1B inhibitors.	170
4.2 5-arylidene-2,4-thiazolidinedione derivative <b>4.0.3</b> as potent aldose reductase inhibitor.	171
4.3 Pyrazole based thiazolidinedione derivative <b>4.0.4</b> as potent PPAR- $\gamma$ Agonis.	171
4.4 Mechanism action of TZD.	172
4.5 Currently available, approved TZD class of drugs: troglitazone, pioglitazone, rosiglitazone, and ciglitazone.	173
4.6 Key interactions between Rosiglitazone and the PPAR- $\gamma$ receptor.	174
4.7 Designing the compounds on the structural basis of rosiglitazone.	175
4.8 $^1\text{H}$ NMR of 5-(4-(2-(benzo[d][1,3]dioxol-5-yloxy)ethoxy)benzylidene)thiazolidine-2,4-dione ( <b>6.1</b> ).	183
4.9 $^1\text{H}$ NMR of 5-(4-(3-(benzo[d][1,3]dioxol-5-yloxy)propoxy)benzylidene)thiazolidine-2,4-dione ( <b>6.2</b> ).	184
4.10 $^1\text{H}$ NMR of 5-(3-(3-(benzo[d][1,3]dioxol-5-yloxy)propoxy)benzylidene)thiazolidine-2,4-dione ( <b>6.3</b> ).	185



<b>Lists of Figures (continued)</b>	<b>Page</b>
4.11 <sup>1</sup> H NMR of 5-(2-(3-(benzo[d][1,3]dioxol-5-yloxy)propoxy)benzylidene)thiazolidine-2,4-dione ( <b>6.4</b> ).	186
4.12 <sup>1</sup> H NMR of 2-(2-(4-((2,4-dioxothiazolidin-5-ylidene)methyl)phenoxy)ethoxy)-4,6-dimethyl-nicotinonitrile ( <b>7.1</b> ).	195
4.13 <sup>1</sup> H NMR of 2-(3-(4-((2,4-dioxothiazolidin-5-ylidene)methyl)phenoxy)propoxy)-4,6-dimethyl-nicotinonitrile ( <b>7.2</b> ).	196
4.14 <sup>1</sup> H NMR of 2-(3-(3-((2,4-dioxothiazolidin-5-ylidene)methyl)phenoxy)propoxy)-4,6-dimethyl-nicotinonitrile ( <b>7.3</b> ).	197
4.15 <sup>1</sup> H NMR of 2-(3-(2-((2,4-dioxothiazolidin-5-ylidene)methyl)phenoxy)propoxy)-4,6-dimethyl-nicotinonitrile ( <b>7.4</b> ).	198
4.16 <sup>1</sup> H NMR of 2-(2-(2-((2,4-dioxothiazolidin-5-ylidene)methyl)phenoxy)ethoxy)-4,6-dimethyl-nicotinonitrile ( <b>7.5</b> ).	199
4.17 <sup>1</sup> H NMR of 1-(2-(4-((2,4-dioxothiazolidin-5-ylidene)methyl)phenoxy)ethyl)-4,6-dimethyl-2-oxo-1,2-dihydropyridine-3-carbonitrile ( <b>7.6</b> ).	202
4.18 <sup>1</sup> H NMR of 1-(3-(4-((2,4-dioxothiazolidin-5-ylidene)methyl)phenoxy)propyl)-4,6-dimethyl-2-oxo-1,2-dihydropyridine-3-carbonitrile ( <b>7.7</b> ).	203
4.19 <sup>1</sup> H NMR of 1-(3-(2-((2,4-dioxothiazolidin-5-ylidene)methyl)phenoxy)propyl)-4,6-dimethyl-2-oxo-1,2-dihydropyridine-3-carbonitrile ( <b>7.8</b> ).	204

<b>Lists of Figures (continued)</b>	<b>Page</b>
xy)propyl)-4,6-dimethyl-2-oxo-1,2-dihydropyridine-3-carbonitrile ( <b>7.8</b> ).	204
4.20 Binding mode of compound <b>6.1</b> in the active site cavity of PPAR- $\gamma$ enzyme.	206
4.21 Binding mode of compound <b>6.2</b> in the active site cavity of PPAR- $\gamma$ enzyme.	206
4.22 Binding mode of compound <b>6.3</b> in the active site cavity of PPAR- $\gamma$ enzyme.	207
4.23 Binding mode of compound <b>6.4</b> in the active site cavity of PPAR- $\gamma$ enzyme.	207
4.24 Compounds <b>6.1, 6.2, 6.3 &amp; 6.4</b> with rosiglitazone (blue) overlapped at the active site of PPAR- $\gamma$ enzyme.	207
4.25 Binding mode of compound <b>7.2</b> in the active site cavity of PPAR- $\gamma$ enzyme.	209
4.26 Binding mode of compound <b>7.3</b> in the active site cavity of PPAR- $\gamma$ enzyme.	209
4.27 Binding mode of compound <b>7.6</b> in the active site cavity of PPAR- $\gamma$ enzyme.	209
4.28 Overlapped diagram of compound <b>7.2</b> (grey), <b>7.3</b> (pink), <b>7.6</b> (bright orange) and <b>rosiglitazone</b> (blue) at the active site activity of PPAR- $\gamma$ enzyme.	210

## ABBREVIATIONS

1843U89	(2 <i>S</i> )-2-[6-[(3-methyl-1-oxo-2 <i>H</i> -benzo[ <i>f</i> ]quinazolin-9-yl)methylamino]-3-oxo-1 <i>H</i> -isoindol-2-yl]pentanedioate
A–A	Acceptor-Acceptor
ANOVA	Annalysis of Variance
ATCC	American Type Culture Collection
Ach	Acetylcholine protein
BSSE	Basis set superposition energy
CP	Counterpoise
C57BL/6J	Common inbred strain of laboratory mouse
CMC	Carboxymethyl cellulose
D–A	Donor-Acceptor
D–D	Donor-Donor
DHPM	Dihydropyrimidinone
DDQ	2,3-Dichloro-5,6-dicyano-1,4-benzoquinone
DNA	Deoxyribonucleic acid
dUMP	Deoxyuridine monophosphate
DMSO	Dimethyl sulfoxide
DHP	Dihydro-2-pyridone
DMF	Dimethylformamide
E2020	(( <i>R,S</i> )-1-benzyl-4-[(5,6-dimethoxy-1-indanon)-2-yl]methyl)pi peridine
EDTA	Ethylenediamine tetraacetic acid
EtOAc	Ethyl acetate
FBS	Fetal Bovine Serum
FTNMR	Fourier Transform Nuclear Magnetic Resonance
IDF	International Diabetes Federation
iNOS	Inducible nitric oxide synthase
MTT	[3-(4,5-dimethylthiazol-2-yl)-2,5-diphenyltetrazolium bromide]

MS	Mass spectrometry
NMR	Nuclear Magnetic Resonance
NR1C3	Nuclear receptor subfamily 1, group C, member 3
NF-kB	Nuclear factor kappa light chain enhancer of activated B cells
ORTEP	Oak Ridge Thermal Ellipsoid Plot
PPAR	Peroxisome proliferator-activated receptor
PDB	Protein Data Bank
PSA	Penicillin-streptomycin-amphotericin B
PBS	Phosphate-buffered saline
PTP1B	Potent protein tyrosine phosphatase 1B enzyme
RSCB	Research Collaboratory for Structural Bioinformatics
RNA	Ribonucleic acid
RPMI	Roswell Park Memorial Institute Medium
RXR	Retinoid-X receptor
SCXRD	Single-crystal X-ray diffraction
SAR	Structure activity relationship
SEM	Standard Error of Mean
TZD	Thiazolidinedione
TLC	Thin-layer chromatography
TMS	Tetramethylsilane
THPM	2-thiotetrahydropyrimidine
T2DM	Type 2 diabetes mellitus

# **CHAPTER-1**

---

## **INTRODUCTION**

---

# **CHAPTER-2**

---

**SYNTHESIS AND STUDY OF HETERO-  
AROMATIC SYSTEM WITH  
METHYLENE LINKED FLEXIMERS**

---

# **CHAPTER-3**

---

## **SYNTHESIS AND STRUCTURAL STUDY OF POLY-AROMATIC FLEXIMERS**

---

# **CHAPTER-4**

---

## **SYNTHESIS AND STUDY OF ROSIGLITAZONE BASED BIO-ACTIVE MOLECULES**

---



# **CHAPTER-5**

---

## **SUMMARY AND CONCLUSION**

---

## **1. INTRODUCTION**

---

### **1.1. Background**

Seley et al. introduced the term "fleximers" in 2001, where they split the nucleosides, i.e., purine base, into two linked heterocycles, imidazole and pyrimidine (Figure 1.1) (Chudinov, 2020; Seley et al., 2001). At first, these fleximers were used as model compounds to study the binding sites of enzymes and characterize the interactions between proteins and nucleic acids. Later these also showed remarkable antiviral and antitumor activity (Seley-Radtke, 2018), from which the concept of fleximer as biological importance has started. The category of fleximers can also be extended to some other nucleosides, the heterocyclic base of which contains two or more linked rings. In recent times many research has already been done on this. Due to the flexible nature, fleximers fit nicely into the proteins' cavity, and they tend to form polymorphs. Also, in some cases, rigid analogues show biological activity. However, they could not fit well or occupied the enzyme's active site cavity due to the analogues' rigid nature. But, the analogues with flexibility in nature can easily fit into the active sites' cavity. Therefore, the synthesis and study of new organic fleximers is an emerging topic for a synthetic organic chemist.

Our present work deals with the synthesis of heterocyclic fleximers, poly-aromatic fleximers, and rosiglitazone-based fleximers and the study of non-covalent interactions by X-ray crystallographic technique and Hirshfeld surface analysis. We have used the molecular docking simulation technique to study the drug-receptor interactions of these fleximers. We have also studied the biological activity of some of these fleximers.

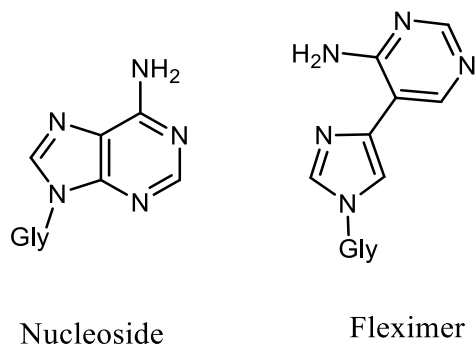


**Figure 1.1:** Imidazole and pyrimidine linked fleximer

## 1.2. Molecular recognition

Molecular recognition mainly relies on non-covalent interactions. It referred to the specific interactions between two or more molecules through non-covalent bonding such as hydrogen bonding, metal coordination, hydrophobic forces, Van der Waals forces,  $\pi\cdots\pi$  stacking interactions, electrostatic and/or electromagnetic interactions (Jeffery, 1997). Molecular recognition includes essential life self-replication elements, information processing, and metabolism-occurring mainly by specific interactions between biological molecules. Certain supramolecular synthons have been introduced to understand molecular recognition processes, which indicate the possibility for 1:1 complex formation due to some weak interaction (Gautam R. Desiraju, 1995). Supramolecular synthons are further categorized into two or more terminologies; 'homo synthons' and 'hetero synthons.' In 'homo synthons,' complexation occurs between the same functional systems, whereas 'hetero synthons' recognition processes happen between two different types of functional moiety (Walsh et al., 2003).

Molecular recognition can be subdivided into 'static molecular recognition' and 'dynamic molecular recognition (Shinkai et al., 2001). Static molecular recognition occurs when the interaction between a key and a keyhole, which is a 1:1 type complexation reaction between a host molecule and a guest molecule to form a host-guest complex. In static molecular recognition, there are specific recognition sites available in host molecules for guest molecules. An example of static molecular

recognition is aryl sulfonyl compounds, sulfa drugs, which can form a 1:1 complex (Figure 1.2) with pyridine-N-oxide via a strong hydrogen bonding (Goud et al., 2011). However, in dynamic molecular recognition, the first guest's binding to the first binding site affects a second guest's association constant with a second binding site.

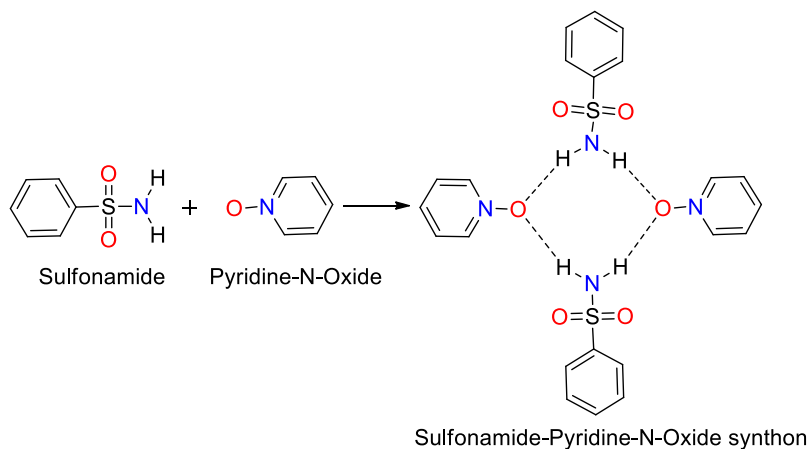


**Figure 1.2:** Formation of a 1:1 complex of sulfonamide and pyridine-N-oxide

### 1.2.1. Origin of molecular recognition

In molecular recognition processes, intermolecular forces play a vital role (Buckingham, Fowler, and Hutson, 1988). In terms of intermolecular distance, there are two types of Intermolecular forces. One is a long-range power of  $R$  ( $E \sim R^{-n}$ , where  $R$  is the intermolecular distance), and the other one is the short-range one, such as exchange-repulsion and charge-transfer interactions. The energies of short-range interactions decrease exponentially with the distance ( $E \sim e^{-aR}$ ) (Stone, 1996).

The electrostatic and dispersion interactions are responsible for the attraction and directionality of aromatic molecules' intermolecular interactions (Tsuzuki et al., 1999). The dispersion interaction is the primary source of the attraction in the CH/ $\pi$  interaction. The aromatic molecules have extensive dispersion interactions with a hydrocarbon molecule since they have large polarizabilities (Tsuzuki, Uchimaru, and Tanabe, 1994). Benzene has a quadrupole moment due to the symmetry of charge distribution. The attractive electrostatic interaction between the positive charge on the hydrogen atom of

the C-H bond and the negative charge on the center of benzene stabilizes the monodentate structure. The C-H bond points toward the benzene ring. Even in typical C-H... $\pi$  interactions of benzene clusters, the very weak electrostatic interaction plays a vital role in determining the C-H bond's orientation (Tsuzuki et al., 2000).

### **1.2.2. Electrostatics involved in recognition processes**

Understanding how two molecules recognize each other is one of the fundamental issues in chemistry and biochemistry. Molecular recognition is also a central topic in applied biochemistry because it determines whether a compound possesses useful clinical properties.

Interactions between electron-rich (donor) and electron-poor (acceptor) aromatic systems have been extensively studied over the past 60 years. Now the time has come to study the effect of electron-withdrawing groups on  $\pi$  systems. The face-to-face stacked geometry is always favored by Van der Waals interactions and solvatophobic effects but is generally disfavored by  $\pi$ ... $\pi$  repulsion. However, the presence of good electron-withdrawing groups has a significant influence on the electrostatic interaction. When both groups are good donating groups, the apparent results are obtained: like polarizations repel and unlike polarizations exhibit attraction. For neutral atoms in this geometry, the dominant interaction is n-electron repulsion, so an electron-withdrawing group stabilizes the interaction by decreasing this repulsion.

Conversely, an electron-donating group would destabilize the interaction further. According to electrostatic models of aromatic interactions, A-A and D-A stacks are more favorable than D-D stacks (Griffiths & Stoddart, 2008; Ono et al., 2008; Yamauchi et al., 2008; Yoshizawa et al., 2007, 2009). While discussing the charge transfer or electrostatic behavior of aromatic systems, one cannot forget to mention the 1,8-disubstituted naphthalene ring system (Cozzi et al., 1992, 1993). This model was used to study the effect of a substituent on aromatic interactions, as the rings were in a face-to-face orientation.

The consequence of this asymmetry is the prediction that the interaction between two  $\pi$ -deficient rings can be more favorable than that between  $\pi$ -deficient and  $\pi$ -rich rings. Interactions should be favorable in appropriate orientations, and for example, quinones crystallize in a face-to-face geometry.

Molecular recognition plays a vital role in biological systems and is observed between receptor-ligand like antigen-antibody, DNA-protein, sugar-lectin, RNA-ribosome, etc. Molecular recognition is also a central topic in applied biochemistry because it determines whether a compound possesses useful clinical properties or not. Here some of the compounds have been proposed to synthesize based on the rosiglitazone-based antidiabetic drug. Rosiglitazone-based analogues will be studied in the following synthesized fleximers to understand non-covalent interactions and molecular recognition.

### **1.3. The non-covalent interaction involved in molecular recognition**

J. D. Van der Waals first recognized Non-covalent interactions in the later part of the 19th century. Unlike covalent interactions, non-covalent interactions do not lead to a classical molecule formation, but it leads to molecular clusters' formation. These are the weak forces that facilitate the break and make processes in biochemical processes. The contribution of several non-covalent bonds ensures a flexible but stable system in both biological and non-biological systems. Non-covalent interactions, also called weak interactions, are responsible for molecular recognition, and both these terms are interrelated. The main non-covalent interactions responsible for molecular recognition are hydrogen bonding, ion-pairing, and  $\pi\cdots\pi$  interactions (Table 1.1). Hydrogen bonding is a strong interaction and plays an important role in naturally occurring non-covalent interactions. Complexes that possess hydrogen bonding have high stability constant.  $\Pi\cdots\pi$  interactions are comparatively weak electrostatic interactions and occur between aromatic rings in polar solvents. The driving forces of ion-pairing interactions (ion-ion, dipole-ion, and dipole-dipole) are coulombic interactions.

**1.3.1. Table 1.1:** Types and estimated bond energies of non-covalent interactions

Bond type	Bond energy [kJ/mol]	Relative strength
<b>Hydrogen bonding</b>	4-120	Weak/medium
Classical	40-120	
Non Classical	4-40	
Hydrophobic effects	1-3	weak
Ion-ion ( $1/r$ )	50-200	strong
Dipole-ion ( $1/r^2$ )	50-200	weak
Dipole-dipole ( $1/r^3$ )	10-50	Weak/medium
$\pi$ ... $\pi$ stacking	0-50	Weak/medium
Dispersion (London) ( $1/r^6$ ) (attractive Vander Waals)	2 <5	weak
Cation- $\pi$	5-80	medium

#### 1.4. Survey of literature

Much work is going on to understand the non-covalent interactions in synthetic as well as natural systems. Non-bonding intermolecular interactions are of fundamental importance for understanding molecular recognition phenomena, biological processes (von Feilitzsch, 2006), and physical and chemical properties of new materials (G. R Desiraju, 1989; Editor, 2001; Hunter & Sanders, 1990; Müller-Dethlefs & Hobza, 2000; Pollino & Weck, 2005; Steiner, 2002; Sudha et al., 2005; Swierczynski et al., 2005)

##### 1.4.1. Aromatic Interactions

Attractive interactions between aromatic  $\pi$  systems are among the principal non-covalent forces governing supramolecular organization and recognition processes. These aromatic interactions are ubiquitous in diverse areas of science and molecular Engineering. They are key interactions influencing the tertiary structure of proteins, the vertical base stacking in DNA, and the intercalation of different drugs into DNA. These interactions are of utmost importance in drug chemistry as most of the drugs are aromatic, and about 20% of amino acids are aromatic (Ashish Kumar Tewari & Dubey, 2008).

Aromatic interactions have been utilized in materials, asymmetric catalysis, rotaxanes and have been implicated in the formation of amyloid fibrils (Klärner & Schrader, 2013; Meyer et al., 2003).

#### 1.4.2. Aromatic $\pi$ ... $\pi$ stacking Interaction

Aromatic  $\pi$ ... $\pi$  stacking interaction is a non-covalent interaction between organic compounds containing aromatic moieties. These interactions are caused by intermolecular overlapping of p-orbitals in  $\pi$ -conjugated systems, so they become more robust as the number of  $\pi$ -electrons increases. It acts powerfully on flat polycyclic aromatic hydrocarbons such as anthracene, triphenylene, and coronene because of the many delocalized  $\pi$ -electrons. This interaction, which is a bit stronger than other Van der Waal's interactions, plays an important role in supramolecular chemistry. The benzene dimer has three geometries that have been modeled, parallel-displaced, T-shaped edge-to-face, and eclipsed face-to-face (Figures 1.3) at high levels of theory and found to be attractive with a preference for the parallel displaced and T-shaped geometries. Edge-to-face packing appears to have been first noted by Cox et al. (1958) in single crystals of benzene (Cox et al., 1958). Pioneering work by Burley and Petsko (Burley & Petsko, 1986; Salonen et al., 2011) established the importance of edge-to-face interactions between aromatic rings in determining the tertiary and quaternary crystalline structure of peptides and proteins.

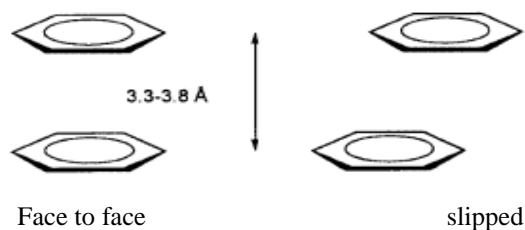


**Figure 1.3:** Arene-arene interaction by face to face interaction

X-ray crystallographic and NMR evidence indicates that relatively weak intramolecular edge-to-face (Jennings et al., 2001) (Figure 1.4 (a), (b) and (c)) interactions between aromatic rings can affect or determine the conformation of organic molecules in the solid-state and solution (Muraki, 2002; Ringer et al., 2006).



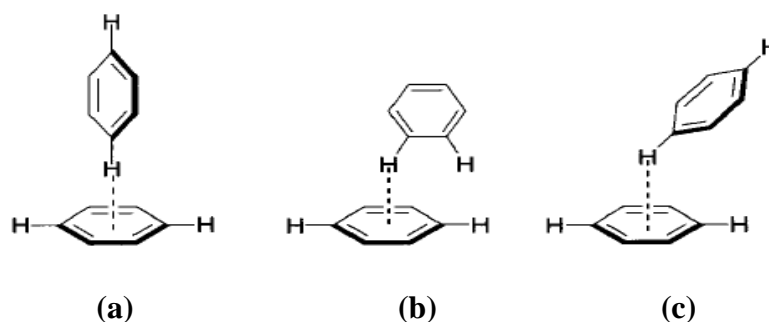


**Figure 1.4:** Edge to face aromatic interaction

Aromatic  $\pi$ - $\pi$  stacking interactions are abundant between heterocyclic  $\pi$  systems. An excellent example of heterocyclic  $\pi$  stacking is provided by the ternary complex of the anticancer drug 1843U89 and dUMP formed at the active site of thymidylate synthase (Figure 1.5). Moreover, supramolecular architectures, such as helices, have been constructed through stacking interactions (Ringer et al., 2006).

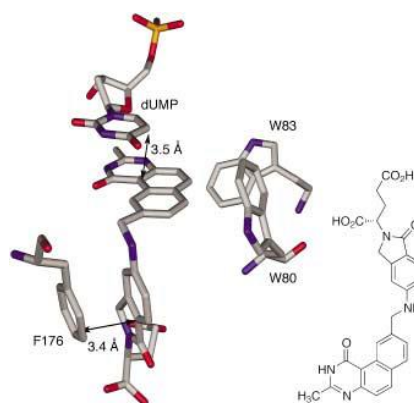


**Figure 1.5:** Heterocyclic  $\pi$  stacking between dUMP and the anticancer drug 1843U89 bound at the active site of thymidylate synthase

### 1.4.3. C-H... $\pi$ Interaction

The interactions between arenes, alkenes, or alkynes with hydrocarbons are C-H... $\pi$  interaction plays an essential tool in chemistry and biology (Aliev et al., 2014). Non-covalent interactions are essential in many chemistry and biochemistry fields, as it determines the structures and properties of liquids, molecular crystals, and biological

molecules. The weak attraction between the C-H bond and the  $\pi$  system is called CH... $\pi$  interaction.

The classic hydrogen bond is one of the most important, and it occurs between an aliphatic C-H group and an aromatic  $\pi$  system (Aliev et al., 2014; Tsuzuki & Fujii, 2008). This type of non-covalent interaction has been shown to contribute to crystal packing, stereoselectivity, protein stability, and conformation of the system. The C-H... $\pi$  bond also plays a vital role in molecular recognition for numerous ligand-binding proteins, carbohydrate-binding proteins that affect binding affinity and conformation (Mazik, 2012; Muraki, 2002). The interaction has already been used in drug design for a significant increase in a tyrosine phosphatase inhibitor (Pace, Kim, and Gao, 2012; Nishio *et al.*, 2014).

For participation in a C-H... $\pi$  interaction, the hydrogen atom does not need to be positioned directly above the  $\pi$ -plane; it may be slightly offset outside the ring. Earlier reports confirm that heterocyclic compounds are engaged in favorable interactions with one another and with aromatic hydrocarbon units (Ashish K. Tewari & Dubey, 2009).

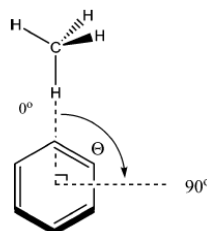


**Figure 1.6:** Methane-Benzene Complex shows the C-H/ $\pi$  interaction

Tsuzuki and co-workers found that for the methane-benzene complex (Figure 1.6), the preferred configuration has the methane directly above the center of the benzene with one hydrogen pointed at the center of the ring and three directed away.

#### 1.4.4. Cation... $\pi$ interaction

Cation- $\pi$  interaction is a non-covalent molecular interaction between the face of an electron-rich  $\pi$  system (e.g., benzene, ethylene) with an adjacent cation (e.g.,  $\text{Li}^+$ ,

$\text{Na}^+$ ) (Figure 1.7). This unusual interaction of non-covalent bonding between a monopole (cation) and a quadrupole ( $\pi$  system).

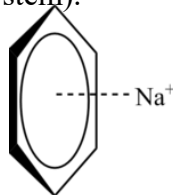


**Figure 1.7:** Cation... $\pi$  interaction between benzene and a sodium cation

Nature's building blocks consist of aromatic moieties; for example, amino acids' side chain of tryptophan and tyrosine or the DNA base can bind to cationic species. Therefore, cation- $\pi$  interactions can play an essential role in stabilizing the three-dimensional structure of a protein (Wu & McMahon, 2008).

Another example of the cation- $\pi$  interaction is observed in the nicotinic acetylcholine receptor. Its endogenous ligand, acetylcholine (a positively charged molecule), binds via a cation- $\pi$  interaction to the quaternary ammonium. The cation- $\pi$  interaction between a protonated buffer molecule (N-2 hydroxyethylpiperazine-N'-2-ethanesulfonic acid) and Trp in the acetylcholine (ACh) binding site protein (Figure 1.8) shows the importance of weak interactions in the function of biomolecules.

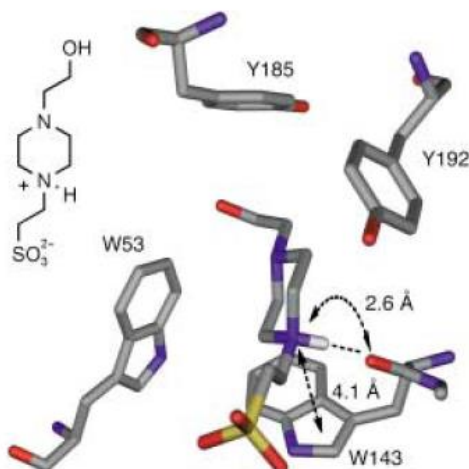


**Figure 1.8:** Cation... $\pi$  interactions between a HEPES molecule and Trp143 in the ACh binding site of an ACh-binding protein

### 1.4.5. Lone pair... $\pi$ interaction

In the last of the twentieth century, Egli and co-workers reported an exceptional case of lone-pair  $\pi$  interactions observed in a bio-macromolecule in Z-DNA (Avasthi et al., 1998). It was demonstrated that the stability of the left-handed Z-DNA duplex (A-DNA and B-DNA are right-handed double-stranded helices), despite poor base-pair stacking, is attributable to an unusual bonding interaction between the lone pair of an oxygen atom belonging to a cytidine 20-deoxyribose unit and the guanidinium moiety of guanosine (Figure 1.9) (Mooibroek et al., 2008).

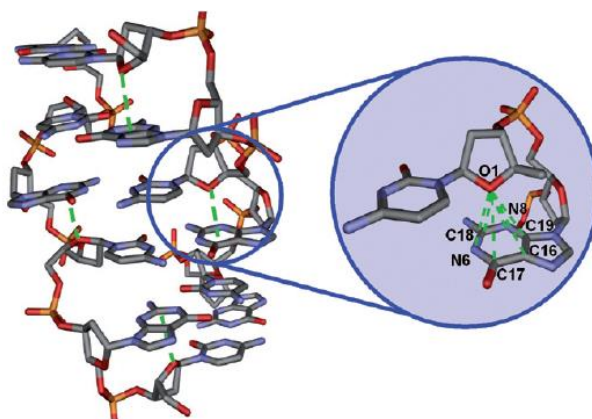


**Figure 1.9:** Lone pair... $\pi$  interactions (green dashed lines) stabilizing the left-handed supramolecular structure of Z-DNA

Lone pair- $\pi$  interactions appear to be of great importance for stabilizing biological macromolecules and binding inhibitors in the binding pocket of biochemical receptors. Sankararamakrishnan et al. have studied the protein database for carbonyl (lone pair)- $\pi$  interactions (Jain et al., 2007). It can be observed in smaller molecular host-guest systems (Wan et al., 2008). Several computational studies have demonstrated that such interactions between a lone donor and an aromatic acceptor can be energetically favorable.

### 1.4.6. Sulphur... $\pi$ Interaction

Interaction between sulfur-containing amino acid side chains (Met, Cys) and aromatic side chains (Tyr, Trp, Phe) was first recognized in globular protein crystal structures (Morgan et al., 2009). Morgan and the group identified eight proteins that

contained one or more chains of alternating sulfur and  $\pi$ -bonded atoms. One good example is the lysozyme from hen egg (Figure 1.10) (Diamond, 1974).

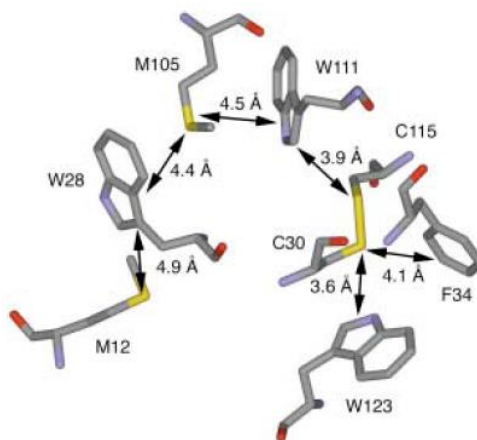


**Figure 1.10:** A chain of alternating “sulfur and  $\pi$ -bonded atoms” as identified in hen egg-white lysozyme

## 1.5. Importance of non-covalent interactions

Non-covalent interactions play an essential role in chemistry as well as in medicinal chemistry. It helps in drug design, stabilization of DNA structure, protein folding, crystal engineering, material science, etc. (Johnson et al., 2019; Kazantsev et al., 2018). Especially, arene-arene interactions are significant because about 20% are aromatic, so the role of aromatic interactions become prominent in drug-receptor interactions.

### 1.5.1. Arene-arene ( $\pi\cdots\pi$ ) interactions in biological system

Arene-arene interactions are believed to provide stability to duplex DNA (E. T. Kool, 2001; Šponer et al., 2008) and they have also been proposed to contribute to the unique properties of thermophilic proteins (Kannan & Vishveshwara, 2000). Arene-arene interactions may also play a role in the aggregation of amyloid  $\beta$  in Alzheimer's disease (Gazit, 2002).

### 1.5.2. Stabilization of DNA structure

In DNA molecule, the aromatic rings are lying nearly perpendicular to the DNA strand's length (Figure 1.11). These rings' faces are arranged parallel to each other with a

distance of 3.4 Å, allowing the two adjacent bases to participate in  $\pi\cdots\pi$  interaction. Therefore, the sum of all  $\pi\cdots\pi$  interactions within the double-stranded DNA molecules becomes significant stabilization energy of double-stranded DNA (P. Hobza et al., 1990; Hunter, 1993; null Kool et al., 2000).

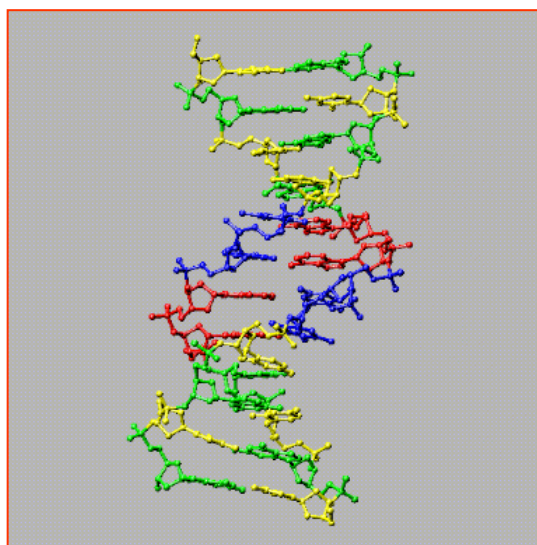


**Figure 1.11:** Base pair stacking in DNA

### 1.5.3. Protein folding

Protein folding is a process by which a polypeptide folds into its characteristic and functional 3D-structure to form a random coil.  $\pi\cdots\pi$  interaction plays a crucial role in protein folding. The X-ray structures of a 12-membered peptide with polypeptide sequence KFFEAAKKFFE revealed that the polypeptides formed an anti-parallel  $\beta$ -sheets cross- $\beta$  arrangement. The anti-parallel  $\beta$ -sheets were zipped together utilizing  $\pi\cdots\pi$  interactions between adjacent phenylalanine rings and salt-bridges between charge pairs, thus controlling and stabilizing the structure (Makin et al., 2005).

### 1.5.4. Arene-arene ( $\pi\cdots\pi$ ) interactions in structure based drug design

Generally, a drug binds to its receptor through non-covalent interactions. Especially,  $\pi\cdots\pi$  interactions and hydrogen bonding interactions are very important, which involves binding the drug with the receptor. Understanding the  $\pi\cdots\pi$  interactions and hydrogen bonding interactions in drug-receptor interaction helps structure-based drug design. The X-ray crystallographic analysis of the complex of E2020 with the

enzyme acetylcholinesterase revealed  $\pi\cdots\pi$ , O-H $\cdots\pi$  and cation $\cdots\pi$  interactions as major forces that stabilize the association (Figure 1.12) (Pavel Hobza & Šponer, 1999; Kryger et al., 1998).

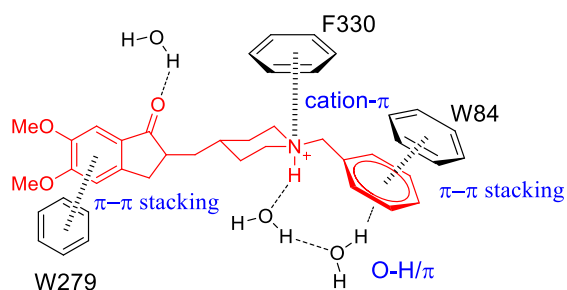


**Figure 1.12:** Binding mode of the anti-Alzheimer drug E2020 within the active site of acetyl cholinesterase from *Torpedo californica*

## 1.6. Method to study non-covalent interactions

Stacking interaction is a very weak interaction, so it is challenging to study with many tools. Here, we have used X-ray crystallography and Hirshfeld surface analysis tools to study non-covalent interactions. We have done molecular docking simulations in the biological system to study the ligand's interactions with the individual protein molecule.

### 1.6.1. X-Ray Crystallography

This method of determining the arrangement of atoms within a crystal, in which a beam of X-rays strikes a crystal and diffracts into many specific directions. From the diffracted beams' angles and intensities, a crystallographer can produce a three-dimensional picture of electrons' density within the crystal. The atoms' mean positions in the crystal can be determined from this electron density, their chemical bonds, their disorder, and various other information.

Crystal symmetry was first investigated experimentally by Nicolas Steno (1669), who showed that the angles between the faces are the same in every exemplar of a particular type of crystal (Steno et al., 1669). René Just Haüy (1784) discovered that every

face of a crystal could be described by simple stacking patterns of blocks of the same shape and size. Hence, William Hallowes Miller, in 1839, was able to give each face a unique label of three small integers, the Miller indices, which are still used today for identifying crystal faces. Haüy's study led to the correct idea that crystals are a regular three-dimensional array (a Bravais lattice) of atoms and molecules; a single unit cell is repeated indefinitely along with three principal directions that are not necessarily perpendicular. In the 19th century, a complete catalog of the possible symmetries of a crystal was worked out by Johann Hessel (Hessel, 1830), Auguste Bravais (Bravais, 1850), Arthur Schönflies and William Barlow (Barlow, 1883). From the available data and physical reasoning, Barlow proposed several crystal structures in the 1880s that were validated later by X-ray crystallography; (Barlow, 1883) however, the available data were too scarce in the 1880s to accept his models as conclusive.

X-ray crystallography has led to a better understanding of chemical bonds and non-covalent interactions. The initial studies revealed the typical radii of atoms. They confirmed many theoretical models of chemical bonding, such as the tetrahedral bonding of carbon in the diamond structure (Diamond, 1974), the octahedral bonding of metals observed in ammonium hexachloroplatinate (IV) (Bragg, 1921), and the resonance observed in aromatic molecules (Bragg, 1921).

X-ray crystallography is now used routinely by scientists to determine how a pharmaceutical drug interacts with its protein target and what changes might improve it (Scapin, 2006). However, intrinsic membrane proteins remain challenging to crystallize because they require detergents or other means to solubilize them in isolation, and such detergents often interfere with crystallization. Such membrane proteins are a large component of the genome and include many significant physiological importance proteins, such as ion channels and receptors (Lundstrom, 2006).

### **1.6.2. Hirshfeld surface analysis**

Hirshfeld surface analysis (McKinnon et al., 2004) is a useful tool that assists in the visual study of the intermolecular interactions in crystal structures by using 3D



molecular surface contours 2D fingerprint plots of intermolecular interactions. An analysis of intermolecular interactions for all compounds carried out using PLATON (Spek, 2009). The differing vdW radii determine the distance between the points on the surface to a nucleus (atom) inside (di) and outside (de) the mean surface. The Hirshfeld surface, fingerprint plots, and interaction energies of compounds have been calculated using CrystalExplorer17 (Mackenzie et al., 2017). The C-H bond lengths converted to normalized values based on neutron diffraction results. The interaction energies of compounds have been calculated using the CE-B3LYP/6-31G(*d,p*) functional/basis set combination and corrected for basis set superposition energy (BSSE) using the counterpoise (CP) method (Boys & Bernardi, 1970). The interaction energy is as

$$E_{\text{tot}} = k_{\text{ele}}E'_{\text{ele}} + k_{\text{pol}}E'_{\text{pol}} + k_{\text{dis}}E'_{\text{dis}} + k_{\text{rep}}E'_{\text{rep}}$$

where the *k* values are scale factors ( $k_{\text{ele}} = 1.057$ ;  $k_{\text{pol}} = 0.740$ ;  $k_{\text{dis}} = 0.871$ ;  $k_{\text{rep}} = 0.618$ ),  $E'_{\text{ele}}$  represents the electrostatic component,  $E'_{\text{pol}}$  the polarization energy,  $E'_{\text{dis}}$  the dispersion energy, and  $E'_{\text{rep}}$  the exchange-repulsion energy (Mackenzie et al., 2017; Turner et al., 2014). A contact sphere of 3.8 Å was used to determine primary intermolecular contacts for interaction energy calculations.

### 1.7. Scope of study

The proposed work is to synthesize new organic fleximers to study molecular recognition property within the system (intra-molecular) and in biological systems. In this proposed work, the biological activity will be performed and compared for both monomer and its methylene linked fleximers. These experimental results will be compared with *in silico* analysis. Our work will provide a new platform in drug discovery and crystal engineering as well as material science.

## 2 SYNTHESIS AND STUDY OF HETERO-AROMATIC SYSTEM WITH METHYLENE LINKED FLEXIMERS

---

### 2.1. Introduction

The heterocyclic skeleton containing nitrogen and sulphur atom is essential in many pharmaceuticals and physiologically active natural products. Molecules containing heterocyclic substructures continue to be attractive targets for synthesis since they often exhibit diverse and vital biological properties. Accordingly, novel strategies for the stereo-selective synthesis of heteropolycyclic ring systems continue to receive considerable attention in the field of synthetic organic chemistry. It has been reported that organic fleximers have great demands in the medicinal and biological field due to their flexible nature. Moreover, organic fleximers found attention in crystal engineering and also in material science. Therefore, fleximers of the hetero-aromatic system like dihydropyrimidinones (DHPMs) and 2-pyridone with methylene linker could be an interesting topic for researchers. This is because both these dihydropyrimidinones (DHPMs) and 2-pyridone possess a wide range of bioactivities.

Dihydropyrimidinones (DHPMs) are also well known for their wide range of bioactivities and their applications in the field of drug discovery. Three out of the five significant bases in Nucleic acids are pyrimidine derivatives, which comprises Cytosine, found in DNA and RNA, Uracil in RNA, and Thymine in DNA (Figure 2.1). Therefore, the synthesis and study of dihydropyrimidinones (DHPMs) system with methylene-linked fleximers makes it an exciting topic for synthetic organic chemistry.

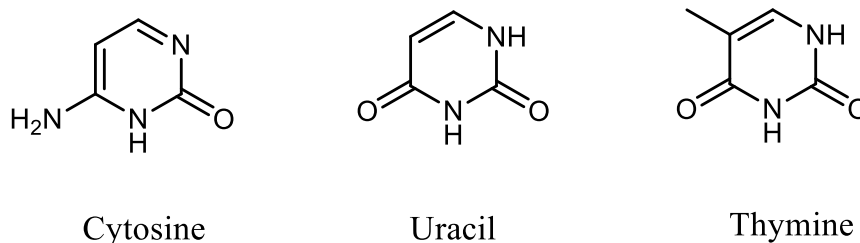


**Figure: 2.1** Pyrimidine derivative bases

Dihydropyrimidinone (DHPM) class of compounds are structural analogs of monastrol, became important to medicinal chemistry because monastrol is a very important bio-molecule with many biological activities (Mayer, 1999). Dihydropyrimidinone (DHPM) class of compounds also possesses interesting fascinating and multifaceted biological activities, such as antiviral (Hurst & Hull, 1961), antitumor (Klein et al., 2007), and antibacterial (Ramesh & Bhalgat, 2011) as well as calcium channel modulating activity (Rovnyak et al., 1992). Monastrol is the protagonist of the DHPMs class. Several studies have revealed that its inhibitory action on human kinesin Eg5 leads to mitotic arrest and, consequently, to apoptosis (Kapoor et al., 2000). At first, this was the main action described for this class of compounds. However, some studies have shown other possible targets for these molecules, such as centrin (Duan et al., 2015), calcium channels (Abassi et al., 2009), and topoisomerase I (Zhu et al., 2011). Thus, the synthesis of dihydropyrimidinone (DHPM) via eco-friendly and green method is of recent interest by the researchers.

2-pyridones are a particular class of compounds with unique pharmacophores that exhibit several biological activities such as analgesic (Öztürk et al., 2001), antimalarial (A. Abadi et al., 1999), antitumoral (Cocco, 2003), anti-HIV (Storck et al., 2005), and anti-inflammatory (Dowarah et al., 2020). Cyanopyridines are important intermediates for synthesizing many important biological analogs like nicotinamide, nicotinic acid, and isonicotinic acid. 3-cyano-2-pyridone are very significant frameworks in the past few decades. These are the structural basis of the alkaloid ricinine, the first known cyano group-containing alkaloid. Milrinone is also a 3-cyano-2-pyridone derivative used for the treatment of congestive heart failure (Fleming et al., 2010; Mirkovic et al., 2013). Some derivative of 3-cyano-2-pyridone has shown anticancer activity (Aqui & Vonderheide, 2008; Cheney et al., 2007; Shimizu et al., 2002). 3-cyano-4,6-diaryl-2-pyridone derivatives I and IV (Figure 2.2) possess anticancer activity due to their ability to act as survivin inhibitors (A. H. Abadi et al., 2010).

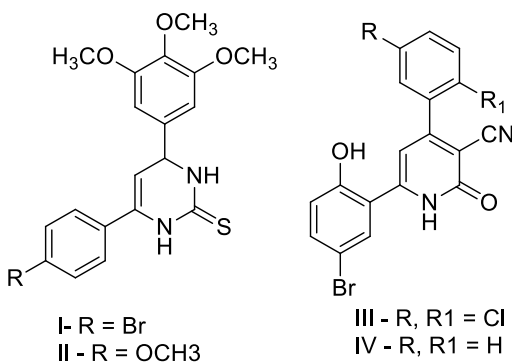


**Figure 2.2:** Cyanopyridones as anticancer agents

## 2.2. Present work

The present chapter deals with the synthesis and studies of weak interactions, incredibly aromatic  $\pi\cdots\pi$  interactions, C-H $\cdots\pi$  and lone pair $\cdots\pi$  interactions. Based on the above literature, our first afford to understand non-covalent interactions, which was done by synthesizing hetero-aromatic systems with methylene-linked fleximers. Moreover, the effect of substituents with the different electronic environments on conformations of some selected synthesized molecules. Here, we have designed our compounds based on monastrol and surviving inhibitor (Figure 2.3).

This chapter has reported the synthesis and study of 2-pyridones, 2-dihydropyridones, and dihydropyrimidinones derivatives with **methylene linkers in Scheme 1, Scheme 2, and Scheme 3**. Also, Hirshfeld surface analyses were performed to analyze molecular packing and surface interactions. *In silico* analysis, it is used to locate small molecules binding affinity in the target protein's active site. In other words, molecular docking investigated the ligand's most stable conformation in the protein's binding package and scored. Therefore, the molecular docking analyses investigated between synthesized compounds and the target protein.

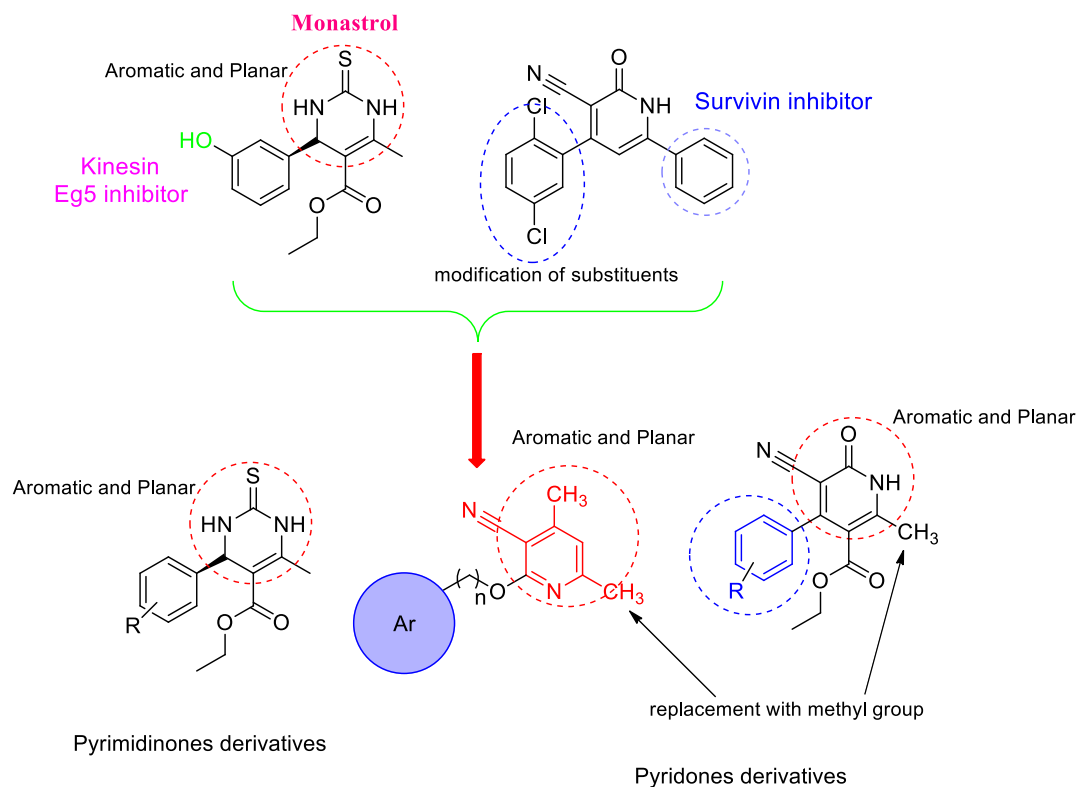


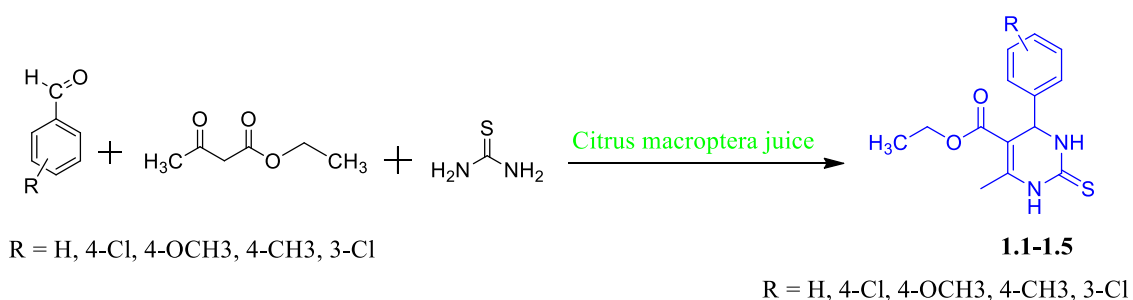
**Figure 2.3:** Design of heterocyclic moieties-linked pyridones and pyrimidinones derivatives.

### 2.3. Scheme 1: Synthesis and study of dihydropyrimidinones derivatives with methylene linkers by the green method

Our main objective is to perform a green synthesis of the Dihydropyrimidinone (DHPM) series containing electron-rich and electron-deficient phenyl rings by *Citrus macroptera* juice and then study the non-covalent interactions of these compounds by X-ray crystallographic study. The required *Citrus macroptera* juices were extracted directly from the naturally obtained *Citrus macroptera* fruit, and it was used straightaway for the reaction without adding any foreign chemicals or additives. Now, we are reporting a green procedure for DHPM synthesis via Biginelli reaction with electron-rich and electron-deficient aromatic aldehydes in *Citrus macroptera* juice medium at room temperature.

## 2.4. Experimental

$^1\text{H}$  NMR (300 MHz) and  $^{13}\text{C}$  (75 MHz) NMR spectra were recorded on **JEOL AL300 FTNMR** spectrometer using TMS as an internal reference, and chemical shift values are expressed in  $\delta$ , ppm units. Melting points of all the compounds were recorded on the electrically heated instrument and are uncorrected. All the reactions were monitored by thin-layer chromatography (TLC) on pre-coated aluminum sheets of Merck using an appropriate solvent system, and chromatograms were visualized under UV light. The compound was purified from column chromatography (silica gel size 60-120 mesh) and flash chromatography (silica gel size 230-400 mesh).



### Scheme 1

#### 2.4.1. General procedure for the synthesis of dihydropyrimidinone (DHPM) derivatives (1.1-1.5)

The equimolar quantities of ethyl acetoacetate (20 mmole, 2.6 g), thiourea (2 mmole, 1.2 g), an aromatic aldehyde (20 mmole, 2.4 mL) were stirred together in 4 mL of *Citrus macroptera juice* at room temperature continuously for 12 h. Upon completion of reaction after 12 h, the solid product was precipitated out of the reaction medium. Upon filtration of the reaction mixture, the crude solid product was collected, and the crude product was recrystallized from hot ethanol to get the pure compounds (**1.1-1.5**) as pale yellow solid.

**2.4.1.1. Ethyl-6-methyl-4-phenyl-2-thioxo-1,2,3,4-tetrahydropyrimidine-5-carboxylate (1.1)**

**Yield:** 5.6 g (83%), m.p. 205-207°C.

**<sup>1</sup>H NMR(300 MHz, CDCl<sub>3</sub>): (δ) :** 1.11-1.15 (3H, t, CH<sub>3</sub>, *J* = 7.2); 2.11-2.16 (3H, s, CH<sub>3</sub>); 4.15-4.18 (2H, q, CH<sub>2</sub>, *J* = 7.2); 5.29-5.37 (1H, s, CH); 7.22-7.35 (5H, s, Ar-H); 9.21-9.24 (1H, s, NH); 9.87-9.91(1H, s, NH). **<sup>13</sup>C NMR (75MHz, DMSO): (δ):** 14.2, 18.3, 58.6, 61.7, 104.2, 126.3, 126.9, 128.5, 143.3, 160.3, 167.2, 174.1. **MS (m/z):** 277.09(M+1). **Element analysis: (i). Calculated:** C=60.85%; H=5.84%; N=10.14%; **(ii). Found:** C=60.64%; H=5.46%; N=10.33%.

**2.4.1.2. Ethyl-4-(4-chlorophenyl)-6-methyl-2-thioxo-1,2,3,4-tetrahydropyrimidine-5-carboxylate (1.2)**

**Yield:** 4.4 g (87%), m.p. 202-204°C.

**<sup>1</sup>H NMR (300 MHz, CDCl<sub>3</sub>): (δ) :** 1.12-1.16 (3H, t, CH<sub>3</sub>, *J* = 7.2); 2.31-2.39 (3H, s, CH<sub>3</sub>); 4.1-4.13 (2H, q, CH<sub>2</sub>, *J* = 7.2); 5.28-5.33 (1H, s, CH); 7.21-7.32 (4H, s, Ar-H); 9.27-9.34 (1H, s, NH); 9.88-9.95 (1H, s, NH). **<sup>13</sup>C NMR (75MHz, DMSO): (δ):** 14.2, 18.3, 58.6, 61.7, 104.2, 126.9, 128.5, 132.3, 143.3, 160.3, 167.2, 174.1. **MS (m/z):** 311.05(M+1). **Element analysis: (i). Calculated:** C=54.10%; H=4.86%; N=9.01%; **(ii). Found:** C=54.21%; H=4.53%; N=9.12%.

**2.4.1.3. Ethyl-4-(4-methoxyphenyl)-6-methyl-2-thioxo-1,2,3,4-tetrahydropyrimidine-5-carboxylate (1.3)**

**Yield:** 4.1 g (79%), m.p. 210-214°C.

**<sup>1</sup>H NMR(300 MHz, CDCl<sub>3</sub>): (δ) :** 1.11-1.23 (3H, t, CH<sub>3</sub>, *J* = 7.2); 2.32-2.39 (3H, s, CH<sub>3</sub>); 3.74-3.79 (3H, s, OCH<sub>3</sub>); 4.11-4.13 (2H, q, CH<sub>2</sub>, *J* = 8.4); 5.31-5.35 (1H, s, CH); 6.78-6.86 (2H, d, Ar-H, *J* = 8.4); 7.16-7.23 (2H, d, Ar-H, *J* = 8.4); 7.8-7.84 (1H, s, NH); 8.43-8.51 (1H, s, NH). **<sup>13</sup>C NMR (75MHz, DMSO): (δ):** 14.2, 18.3, 55.8, 58.3, 61.7, 104.2, 114.1, 125.7, 135.6, 158.6, 160.3, 167.2, 174.1. **MS (m/z):** 307.10(M+1). **Element analysis: (i). Calculated:** C=58.80%; H=5.92%; N=9.14%; **(ii). Found:** C=58.60%; H=5.84%; N=9.06%.

#### 2.4.1.4. Ethyl-6-methyl-2-thioxo-4-(p-tolyl)-1,2,3,4-tetrahydropyrimidine-5-carboxylate (1.4)

**Yield:** 5.3 g (85%), m.p. 209-2011°C.

**<sup>1</sup>H NMR (300 MHz, CDCl<sub>3</sub>): (δ) :** 1.12-1.23 (3H, t, CH<sub>3</sub>, *J* = 7.2); 2.26-2.32 (3H, s, CH<sub>3</sub>); 2.33-2.38 (3H, s, CH<sub>3</sub>); 4.1-4.13 (2H, q, CH<sub>2</sub>, *J* = 7.2); 5.28-5.33 (1H, s, CH); 7.08-7.12 (2H, d, Ar-H, *J* = 8.2); 7.14-7.23 (2H, d, Ar-H, *J* = 8.1); 8.81-8.86(1H, s, NH); 9.48-9.52 (1H, s, NH). **<sup>13</sup>C NMR (75MHz, DMSO): (δ):** 14.2, 18.3, 21.3, 58.3, 61.7, 104.2, 126.8, 128.8, 136.4, 140.3, 160.3, 167.2, 174.1. **MS (m/z):** 291.11(M+1). **Element analysis: (i). Calculated:** C=62.04%; H=6.25%; N=9.65%; **(ii). Found:** C=62.21%; H=6.11%; N=9.38%.

#### 2.4.1.5. Ethyl-4-(3-chlorophenyl)-6-methyl-2-thioxo-1,2,3,4-tetrahydropyrimidine-5-carboxylate (1.5)

**Yield:** 4.5 g (92%), m.p. 212-215°C.

**<sup>1</sup>H NMR (300 MHz, CDCl<sub>3</sub>): (δ):** 1.13-1.21 (3H, t, CH<sub>3</sub>, *J* = 7.2); 2.24-2.37 (3H, s, CH<sub>3</sub>); 4.1-4.13 (2H, q, CH<sub>2</sub>, *J* = 7.2); 5.27-5.31 (1H, s, CH); 7.18-7.31 (4H, m, Ar-H); 9.37-9.44 (1H, s, NH); 9.98-10.03 (1H, s, NH). **<sup>13</sup>C NMR (75MHz, DMSO): (δ):** 14.2, 18.3, 57.8, 61.7, 104.2, 125.0, 126.7, 126.8, 129.9, 134.1, 144.7, 160.3, 167.2, 174.1. **MS (m/z):** 311.05(M+1). **Element analysis: (i). Calculated:** C=54.10%; H=4.86%; N=9.01%; **(ii). Found:** C=54.04%; H=4.45%; N=9.21%.

## 2.5. Results and discussions

A series of Dihydropyrimidinone (DHPM) derivatives were synthesized using thiourea, ethyl acetoacetate with electron-rich and electron-deficient aromatic aldehydes, an eco-friendly and green catalyzed reaction in **Scheme 1**. *Citrus macroptera* juices were used as bio-catalyst for the first time to synthesize Dihydropyrimidinone (DHPM) derivatives, which showed better yield and shorter time duration. This procedure is also an eco-friendly one, which did not require an organic solvent for the reaction. Out of five compounds, three compounds formed single crystals suitable for single-crystal X-ray diffraction analysis.



### 2.5.1. Data collection, reduction and refinement

**SHELXL-97** in the program suite **WinGX** (version 1.80.05) has been used to solve and refine the crystal structure. The molecular graphics were developed by using **ORTEP-3** software. For 3D structure visualization and packing diagrams, **Mercury 3.3** software has been used throughout the experiment. **PARST-95** and **PLATON** were used for geometrical calculations. Hydrogen bonds were represented by broken light green lines in the packing diagram. Carbon atoms were represented by grey color, hydrogen atoms white, oxygen atoms red, nitrogen atoms light blue, Sulphur atoms yellow, chlorine atoms blue, etc. in the packing diagram. The Hirshfeld surface and the associated 2D fingerprint plots for the compounds were calculated using **Crystal Explorer 3.0**.

### 2.5.2. X-Ray Crystallographic studies and Hirshfeld surface analysis of 1.1-1.5

The idea that crystals could be used as a diffraction grating for X-rays arose in 1912 in a conversation between Paul Peter Ewald and Max von Laue in Munich's English Garden. Ewald had proposed a resonator model of crystals for his thesis. However, this model could not be validated using visible light since the wavelength was much larger than the resonators' spacing. Von Laue realized that electromagnetic radiation of a shorter wavelength was needed to observe such small spacings and suggested that X-rays might have a wavelength comparable to the unit-cell spacing in crystals. Hirshfeld surface analysis is done to analyze the various intermolecular interactions in both the structure. This study gives the clue of driving force in the self-assembly of molecules in crystal lattices.

### 2.5.2.1. X-ray crystal structure of 1.3

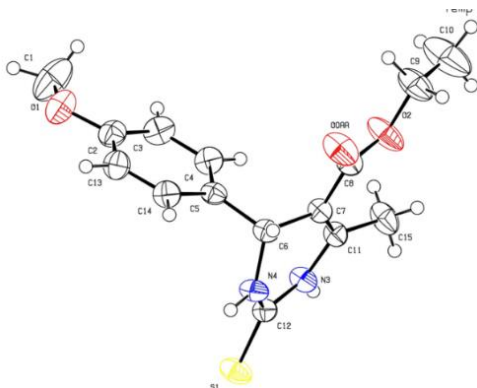


**Figure 2.4:** ORTEP diagram of **1.3**

### 2.5.2.2. Table 2.1: Crystal data of compounds **1.3**, **1.4** and **1.5**

Compound	1.3	1.4	1.5
Identification code	1936021	1936022	1936023
Empirical formula	C <sub>15</sub> H <sub>18</sub> N <sub>2</sub> O <sub>3</sub> S	C <sub>15</sub> H <sub>18</sub> N <sub>2</sub> O <sub>2</sub> S	C <sub>14</sub> H <sub>15</sub> N <sub>2</sub> O <sub>2</sub> S
Formula weight	306.39	290.39	310.81
Temperature(K)	296(2)	296 (2)	296 (2)
Crystal system	Monoclinic	Triclinic	Triclinic
Space group	<i>C2/c</i>	<i>P-1</i>	<i>P-1</i>
a(Å)	18.2332 (17)	7.3603 (10)	7.3066 (6)
b(Å)	7.3341 (6)	9.4648 (12)	10.4657 (8)
c(Å)	25.197 (2)	12.2076 (16)	10.6788 (9)
α(°)	90	74.216 (4)	107.568 (3)
β(°)	101.888 (4)	88.729 (4)	90.538 (3)
γ(°)	90	69.819 (4)	107.829 (2)
Volume(Å <sup>3</sup> )	3297.2 (5)	765.70 (18)	736.37 (10)
Z	8	2	2
ρ (g/cm <sup>3</sup> )	1.2343	1.2594	1.4016
μ(mm <sup>-1</sup> )	0.207	0.214	0.403
F(000)	1297.5879	308.3750	324.6689
Crystal size(mm <sup>3</sup> )	0.24 x 0.22 x 0.22	0.22 x 0.20 x 0.18	0.26 x 0.25 x 0.20
Radiation	MoKα (λ = 0.71073)	MoKα (λ = 0.71073)	MoKα (λ = 0.71073)
2θ range for data collection(°)	2.28 to 28.37	2.96 to 27.15	3.38 to 27.16
Reflections collected	39480	18180	14725
Independent reflections	4117	3387	3263
Data/restraints/parameters	4117/0/201	3387/0/192	3263/0/191
Goodness-of-fit on F <sup>2</sup>	1.0714	1.0675	1.0760
Final R indexes [I>=2σ (I)]	R1 = 0.0636, wR2 = 0.1885	R1 = 0.0423, wR2 = 0.1218	R1 = 0.0384, wR2 = 0.1104
Final R indexes [all data]	R1 = 0.0764, wR2 = 0.2033	R1 = 0.0487, wR2 = 0.1298	R1 = 0.0429, wR2 = 0.1156
Largest diff. peak/hole / e Å <sup>-3</sup>	0.57/-0.43	0.34/-0.38	0.28/-0.43

### 2.5.2.3. Table 2.2. Intermolecular and intramolecular interactions in **1.3**

D-H...A	D-H (Å)	H...A (Å)	D...A (Å)	D-H...A (°)
C1-H1c...Oaa	0.959	2.770	3.534	137.19
C3-H3a...O1	0.930	2.918	3.468	119.22
C4-H4a...O1	0.930	2.953	3.497	118.79
C15-H15c...O0aa	0.960	2.716	3.439	132.54
N3-H3...O0aa	0.804	2.184	2.983	172.54
C10-H10a...S1	0.961	3.251	4.001	137.89
C9-H9a...S1	0.970	3.144	4.111	176.98
C1-H1a... $\pi$ (C2,C3,C4,C5,C13,C14)	0.980	3.627	3.684	
C1-H1c... $\pi$ (C2,C3,C4,C5,C13,C14)	0.961	2.925	3.684	
<b>Intramolecular</b>				
C3-H3a...O1	0.930	2.644	2.443	
C13-H13a...O1	0.930	2.492	2.341	
C9-H9a...O0aa	0.970	2.588	2.675	
C9-H9b...O0aa	0.970	2.736	2.675	
C15-H15c...N3-H3	0.960	2.125	2.394	

#### Crystal analysis of **1.3**

The compound **1.3** chiral compound containing one asymmetric carbon was analysed by single-crystal X-ray diffraction (Figure 2.4 and Table 2.1). The chiral compound crystallized in the orthorhombic space group  $C2/c$  in the crystal lattice unit cell (Table 2.1). The unit cell contains eight molecules in the crystals.

The overall structure of **1.3** exhibits a stacked arrangement of molecules that exhibit a combination of parallel-displaced C-H... $\pi$ , C-H...O, N-H...O, and N-H...S interactions (Table 2.2). **D** is the donor and **A** is the acceptor in non-covalent interactions in table 2.2. Both rings are arranged in the ABBA pattern in the crystal packing. The acute angle (dihedral angle) between the non-aromatic ring plane and the phenyl ring is  $87.68^\circ$ . The hydrogen-bonding network for compound **1.3** and crystal packing is in Figure 2.5. In addition to intermolecular C-H...O interactions compound, **1.3** are also having intra-molecular C-H...O interactions. The stacking distance for C-H... $\pi$  are 2.669, 2.925, 3.376 Å. (Table 2.2). In extensive hydrogen-bonding network terminal thioamide & ester oxygen are involved in weak interaction, and non-traditional hydrogen bond results in the  $R_2^1$  (6),  $R_2^2$  (8) &  $R_4^4$  (20) graph-set notation in which N-H...O, C-H...O & N-H...S interactions (Figure 2.5) are involved. The N-H...O and N-H...S bond distances for hydrogen bonding are 2.184, 2.463 Å, and angles on hydrogen

atoms are  $169.84^\circ$ ,  $172.54^\circ$  while another C-H...O bond distance and angle on hydrogen atom are  $2.716 \text{ \AA}$  and  $132.63^\circ$ , respectively (Table 2.2).

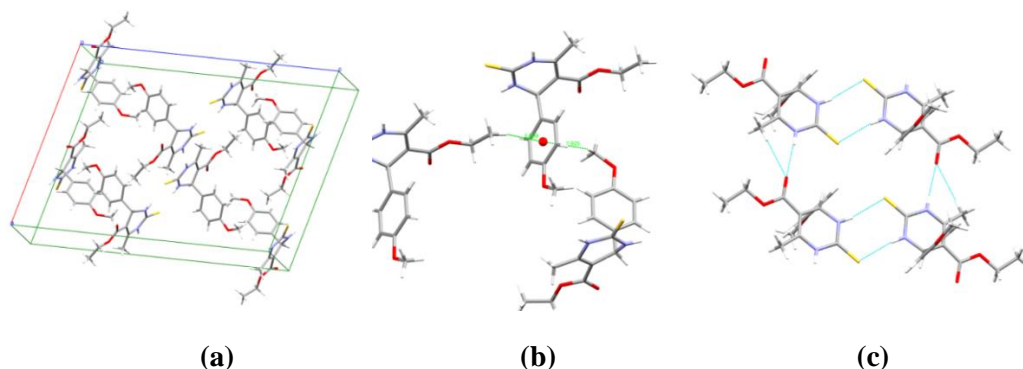


**Figure 2.5:** (a) Packing diagram of **1.3**, (b) C-H... $\pi$  interactions in **1.3**, and (c) C-H...O, N-H...O, and N-H...S interactions in **1.3**

#### 2.5.2.4. Hirshfeld surface analysis of **1.3**

The Hirshfeld surface mapped on  $d_{\text{norm}}$  of compound **1.3** is displayed in Figure 2.6 (a). The red color represents the more dominant non-covalent C-H...O interactions involved in the crystal structure (Figure 2.6 (a)).

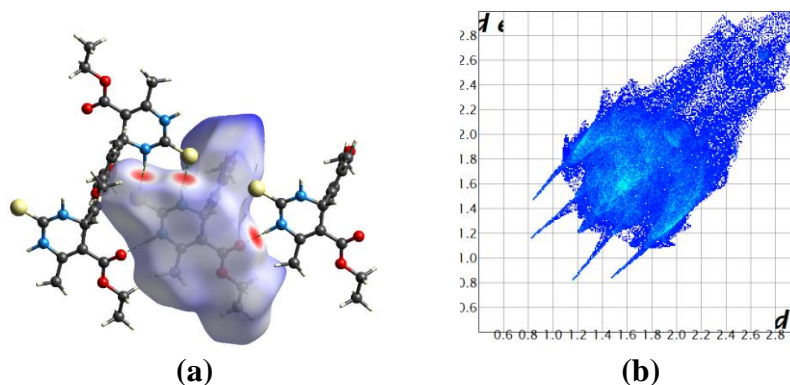


**Figure 2.6:** (a) Hirshfeld surface mapped on  $d_{\text{norm}}$  for compound **1.3**, (b) Two-dimensional fingerprint plot for compound **1.3**

The 2D fingerprint plots represent the summary of weak intermolecular interactions in the crystal structure and provide information about the percentage contribution of a 3D Hirshfeld surface. The 2D fingerprint plot of compound **1.3** is shown in Figure 2.6 (b). The fingerprint analysis of compound **1.3** shows the percentage

contribution of intermolecular interactions are H-H for around 52.2 %, O-H for 12.4 %, C-H for 15.2%, S-H for 15.1%, N-H for 1.8%, C-C for 1.1%, O-O for 0.3%, N-C for 0.3%, C-O for 0.9%, and O-N for 0.7 % of the close contacts in the Hirshfeld surfaces. The yellowish-red bin on the fingerprint plots is absent in compound **1.3**, which means the absence of weak  $\pi\cdots\pi$  stacking in the crystal structure (Figure 2.6 (b)). The spoke-like pattern in the fingerprint plots of **1.3** represents the C-H...O interactions in the crystal lattice in the region of  $d_i + d_e = 2.00\text{-}2.9\text{\AA}$  (Figure 2.6 (b)). The second spoke-like pattern in the fingerprint plots of **1.3** represents the C-H...S interactions in the crystal lattice in the region of  $d_i + d_e = 2.30\text{-}3.4\text{\AA}$  (Figure 2.6 (b)). The C-H... $\pi$  interactions in **1.3** can be seen as a pair of unique blue-colored wings in the region of  $d_i + d_e = 3.2\text{-}3.6\text{\AA}$  (Figure 2.6 (b)). The C-H...N pair of contacts is also reflected as two characteristic wings occupied in the  $d_i + d_e = 3.2\text{-}3.4\text{\AA}$  in **1.3**.

The Hirshfeld weak interactions calculation also supports the presence of weak non-covalent intermolecular interactions as in crystal packing, where C-H... $\pi$  interactions, C-H...N, and C-H...O interactions of compound **1.3** in the crystal packing structure is in figure 2.7. In an extensive hydrogen-bonding network of calculated interactions of compound **1.3**, terminal carbonyl oxygen, thio-pyrimidine nitrogen, and thio-pyrimidine sulfur are involved in weak interaction and were forming 8 membered  $R_2^2(8)$  ring in which N-H...S interactions is involved (Figure 2.7 (a)). The CH... $\pi$  weak interaction calculations of **1.3** are shown in Figure 2.7 (b).

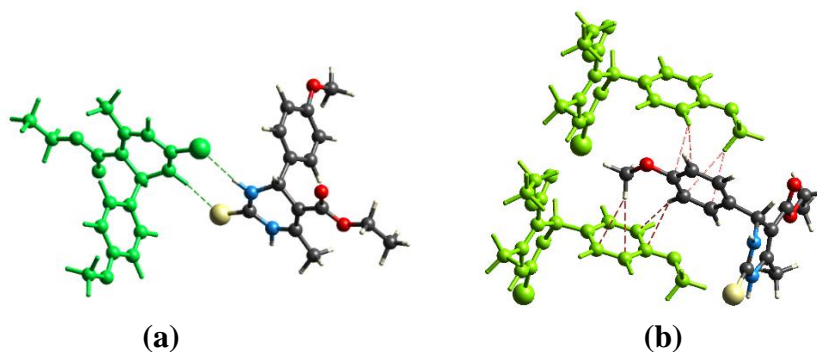


**Figure 2.7:** (a) Non-covalent interactions forming  $R_2^2(8)$ , (b) CH... $\pi$  interactions in weak-interactions calculations of **1.3**

The curvedness plots and the Shape index plots of 3D Hirshfeld also reveal the various weak intermolecular interactions in compounds **1.3**. The 3D Hirshfeld surface on Curvedness plots for compound **1.3** is shown in Figure 2.8 (a) and (b). In the Curvedness plots, very weak intermolecular interactions are seen inside the contours by yellow spots. The absence of green-colored flat regions in the curvedness plot shows the absence of  $\pi\cdots\pi$  stacking interaction in the crystal packing. The red-yellow colored spots in curvedness plots show strong hydrogen-bonding interactions in the crystal structure of **1.3**.

The shape index of compound **1.3** indicated the nature of interactions (i.e., donor and acceptor property) (Figure 2.8 (c) and (d)). The red and blue areas of the shape index indicated the acceptor and the donor property, respectively. In the Shape index plots of compound **1.3**, the yellowish-red colored concave regions on the Hirshfeld surface represent weak intermolecular interactions in the crystal packing. The absence of red and blue colored triangles on the surface of rings of the molecule indicated that there is no  $\pi\cdots\pi$  stacking interaction in the crystal packing.

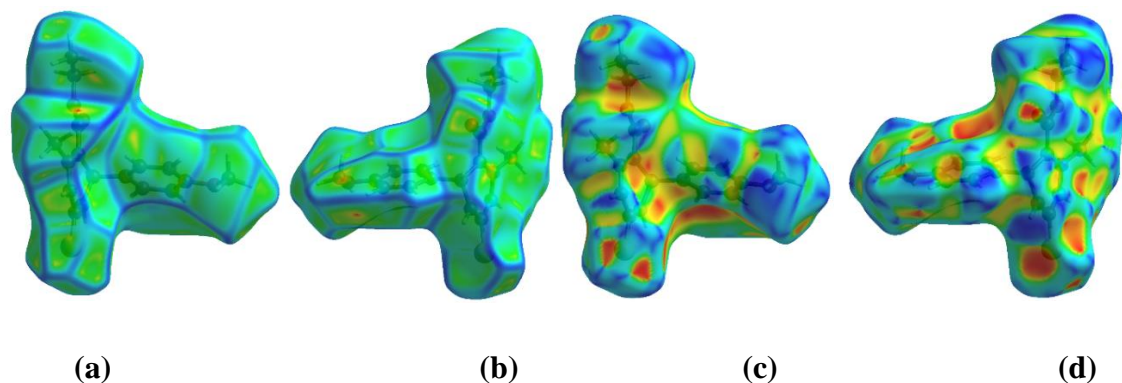


**Figure 2.8:** (a) and (b) Curvedness both side view of compound **1.3**, (c) and (d) Shape index both side view of compound **1.3**.

### 2.5.2.5. X-ray crystal structure of 1.4

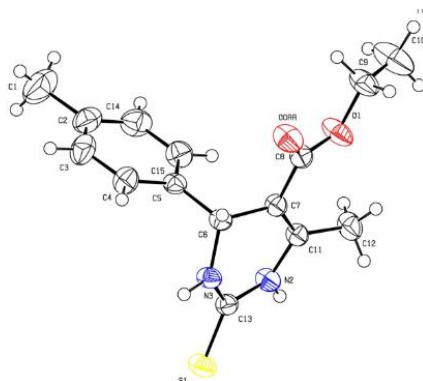


**Figure 2.9:** ORTEP diagram of **1.4**

### 2.5.2.6. Table 2.3. Intermolecular and intramolecular interactions in **1.4**

<b>D-H...A</b>	<b>D-H (Å)</b>	<b>H...A (Å)</b>	<b>D...A (Å)</b>	<b>D-H...A (°)</b>
C12-H12c....Oaa	0.960	2.713	3.403	129.33
C4-H4....S1	0.930	3.063	3.731	130.12
C6-H6....S1	0.980	3.268	4.146	150.03
N3-H3....S1	0.889	2.450	3.322	166.91
N2-H2....O0aa	0.810	2.257	3.058	170.02
<b>Intramolecular</b>				
C15-H15.... $\pi$ (C6,C7,C11,C,13,N2,N3)	0.931	2.846	3.067	
C12-H12a....O1	0.960	2.914	2.800	
C12-H12b....O1	0.960	2.317	2.800	110.40
C6-H6....O0aa	0.980	2.474	2.812	
C9-H9a....O0aa	0.970	2.546	2.686	

### Crystal analysis of **1.4**

The compound **1.4** chiral compound containing one asymmetric carbon was analysed by single-crystal X-ray diffraction (Figure 2.9 and Table 2.1). The chiral compound crystallized in the triclinic space group *P-1* in the crystal lattice unit cell (Table 2.1). The unit cell contains two molecules in the crystals.

The overall structure of **1.4** exhibits a combination of C-H...O, N-H...O, and N-H...S interactions (Table 2.3). Phenyl rings are arranged in the hairbone pattern in the crystal packing. The acute angle (dihedral angle) between the non-aromatic ring plane and the phenyl ring is 80.95°. The hydrogen-bonding network for compound **1.4** and crystal packing is in Figure 2.10. In addition to intermolecular C-H...O interactions

compound, **1.4** are also having intra-molecular C-H...O interactions. In an extensive hydrogen-bonding network terminal, thioamide & ester oxygen are involved in weak interaction, and non-traditional hydrogen bond results in the  $R_2^1$  (6),  $R_2^2$  (8) &  $R_4^4$  (20) graph-set notation in which N-H...O, C-H...O & N-H...S interactions are involved. The N-H...O and N-H...S bond distances for hydrogen bonding are 2.257, 2.450 Å, and angles on hydrogen atoms are 170.02°, 166.91° while another C-H...O bond distance and angle on hydrogen atom are 2.713 Å and 129.33°, respectively (Table 2.3 and Figure 2.10).

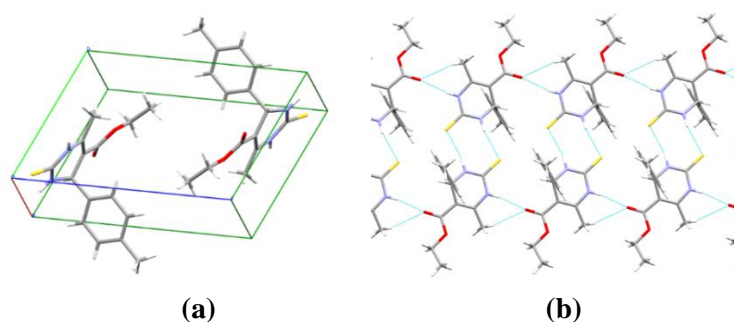


**Figure 2.10:** (a) Packing diagram of **1.4**, (b) N-H...O, C-H...O & N-H...S interactions in **1.4**

#### 2.5.2.7. Hirshfeld surface analysis of **1.4**

The Hirshfeld surface and fingerprint plots for compound **1.4** are shown in Figures 2.11 (a) and (b), respectively. The red color in the Hirshfeld surface represents the more dominant non-covalent C-H...O interactions involved in the crystal structure of **1.4** (Figure 2.11 (a)).

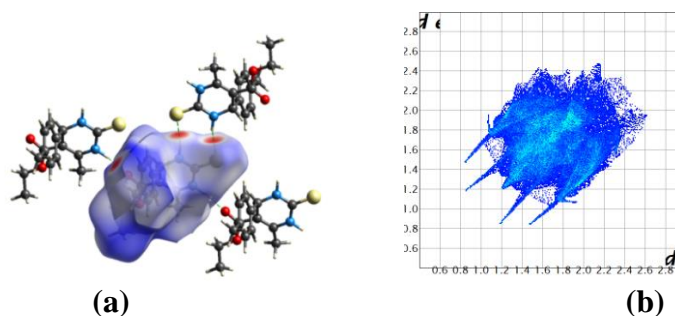


**Figure 2.11:** (a) Hirshfeld surface mapped on  $d_{\text{norm}}$  for compound **1.4**, (b) Two-dimensional fingerprint plot for compound **1.4**



The yellowish-red bin on the fingerprint plots is absent in **1.4**, which means weak  $\pi\cdots\pi$  stacking in the crystal structure (Figure 2.11 (b)). The spoke-like pattern in the fingerprint plots of **1.4** represents the C-H...O interactions in the crystal lattice in the region of  $d_i + d_e = 2.00\text{-}2.9\text{ \AA}$  (Figure 2.11 (b)). The second spoke-like pattern in the fingerprint plots of **1.4** represents the C-H...S interactions in the crystal lattice in the region of  $d_i + d_e = 2.30\text{-}3.4\text{ \AA}$  (Figure 2.11 (b)). The C-H... $\pi$  interactions in **1.4** can be seen as a pair of unique blue-colored wings in the region of  $d_i + d_e = 3.2\text{-}3.6\text{ \AA}$  (Figure 2.11 (b)). The C-H...N pair of contacts is also reflected as two characteristic wings occupied in the  $d_i + d_e = 3.2\text{-}3.4\text{ \AA}$  in **1.4**.

Hirshfeld's surface view exactly explained the pattern of molecule conformation that exists in the solid-state. Electronic distribution within the compound also explained non-covalent interactions (Figure 2.11 (b)). The fingerprint analysis of compound **1.4** shows the percentage contribution of intermolecular interactions. Those are H-H 57.6 %, C-O 1.25%, S-H 15.5%, O-H 6.9%, C-H 14.2%, N-H 1.6%, and C-C 1.6%, and other interactions are less than 1.0% (Figure 2.11 (b)).

The Hirshfeld weak interactions calculation also supports the presence of weak non-covalent intermolecular interactions as in crystal packing, where C-H... $\pi$  interactions, C-H...N, and C-H...O interactions of compound **1.4** in the crystal packing structure is in Figure 2.12. In an extensive hydrogen-bonding network of calculated interactions of compound **1.4**, terminal carbonyl oxygen, thio-pyrimidine nitrogen, and thio-pyrimidine sulfur are involved in weak interaction and were forming 8 membered  $R_2^2(8)$  (Figure 2.12 (a)) ring in which N-H...S is involved. The CH... $\pi$  weak interactions calculations of **1.4** are shown in Figure 2.12 (b).

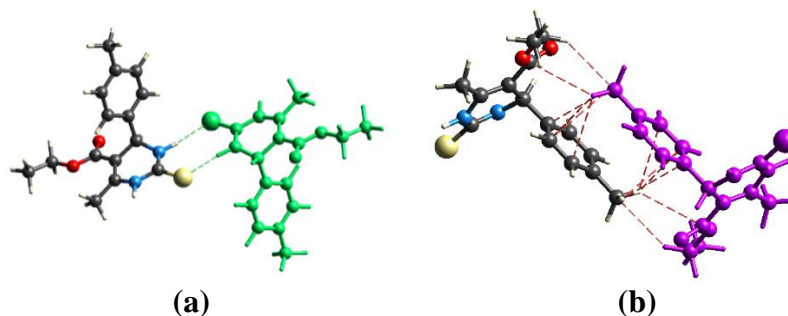


**Figure 2.12:** (a) Non-covalent interactions forming  $R_2^2(8)$ , (b) C-H... $\pi$  and C-H...O interactions in weak interactions calculations of **1.4**

The curvedness plots and the Shape index plots of 3D Hirshfeld also reveal the various weak intermolecular interactions in compound **1.4**. Yellow spots represent the crystal structure's weak interactions, shown in Figure 2.13 (a) and (b). The absence of green-colored flat regions in the curvedness plots indicated the absence of  $\pi$ ... $\pi$  stacking in the crystal structure of compound **1.4**. The red-yellow colored spots in curvedness plots show strong hydrogen-bonding interactions in the crystal structure.

Red and blue areas represent the acceptor and the donor property, respectively, in the shape index of compound **1.4** (Figure 2.13 (c) and (d)). Yellowish-red colored concave regions indicate the presence of weak intermolecular interactions in the Shape index plots. The absence of red and blue colored triangles on the surface of rings of the molecule in the Shape index plots also indicated the absence of weak  $\pi$ ... $\pi$  stacking in the crystal structure (Figure 2.13 (c) and (d)). Hirshfeld surface analysis gives evidence about weak intermolecular interactions, and all these weak interactions stabilize and strengthen the crystal packing structure of compound **1.4**.

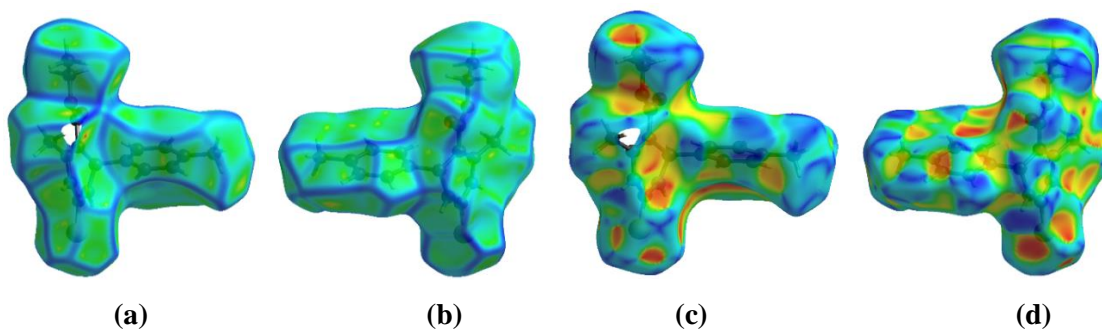


**Figure 2.13:** (a) and (b) Curvedness both side view of compound **1.4**, (c) and (d) Shape index both side view of compound **1.4**.

### 2.5.2.8. X-ray crystal structure of 1.5

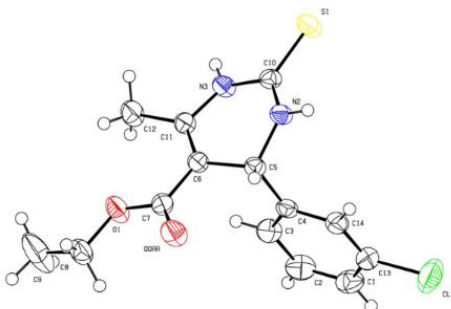


Figure 2.14: ORTEP diagram of 1.5

### 2.5.2.9. Table 2.4. Intermolecular and intramolecular interactions in 1.5

D-H—A	D-H (Å)	H...A (Å)	D....A (Å)	D-H...A (°)
C1-H1....O0aa	0.980	2.747	3.684	159.68
C12-H12a.....O0aa	0.960	3.456	3.390	119.22
C12-H12c.....O0aa	0.960	2.705	3.390	118.79
N3-H3....O0aa	0.805	2.186	2.981	189.86
C8-H8a....Cl2	0.970	2.952	3.767	142.39
N2-H2....S1	0.829	2.584	3.401	188.89
C5-H5....S1	0.980	3.213	4.126	155.57
C8-H8b....S1	0.970	3.098	4.024	160.25
C9-H9a....S1	0.960	3.385	4.211	145.54
C14-H14....S1	0.980	3.060	3.888	149.30
C12-H12a.....Cl2	0.960	2.989	3.758	138.64
C12-H12b.....Cl2	0.960	3.759	3.758	82.59
C9-H9c... $\pi$ (C1,C2,C3,C4,C13,C14)	0.959	3.180	4.128	
(C1,C2,C3,C4,C13,C14) $\pi$ ... $\pi$ (C1,C2,C3,C4,C13,C14)		3.665		
<b>Intramolecular</b>				
C5-H5a...O0aa	0.980	2.449	2.786	
C8-H8a...O0aa	0.970	2.578	2.670	
C8-H8b...O0aa	0.970	2.732	2.670	
C12-H12a....O1	0.960	2.881	2.786	
C12-H12b....O1	0.960	2.309	2.786	

### Crystal analysis of 1.5

The compound **1.5** chiral compound containing one asymmetric carbon was analysed by single-crystal X-ray diffraction (Figure 2.14 and Table 2.1). The summary of crystallographic information is listed in Table 2.1. The chiral compound crystallized

in the triclinic space group  $P-1$  in the crystal lattice unit cell. The unit cell contains two molecules in the crystals.

The overall structure of **1.5** exhibits a combination of parallel-displaced C-H... $\pi$ , C-H...O, N-H...O, and N-H...S interactions (Table 2.4). Both rings are arranged in the AABB pattern in the crystal packing. The acute angle (dihedral angle) between the non-aromatic ring plane and the phenyl ring is  $80.18^\circ$ . The hydrogen-bonding network for compound **1.5** and crystal packing is in Figure 2.15. In addition to intermolecular C-H...O interactions compound, **1.5** are also having intra-molecular C-H...O interactions. The stacking distance for C-H... $\pi$  are 3.665, 3.180, 3.912 Å. (Table 2.4). In an extensive hydrogen-bonding network terminal, thioamide & ester oxygen are involved in weak interaction, and non-traditional hydrogen bond results in the  $R_2^1$  (6),  $R_2^2$  (8) &  $R_4^4$  (20) graph-set notation in which N-H...O, C-H...O & N-H...S interactions are involved. The N-H...O and N-H...S bond distances for hydrogen bonding are 2.1876, 2.584 Å, and angles on hydrogen atoms are  $138.86^\circ$ ,  $168.69^\circ$  while another C-H...O bond distance and angle on hydrogen atom are 2.705 Å and  $169.86^\circ$ , respectively (Table 2.4 and Figure 2.15).

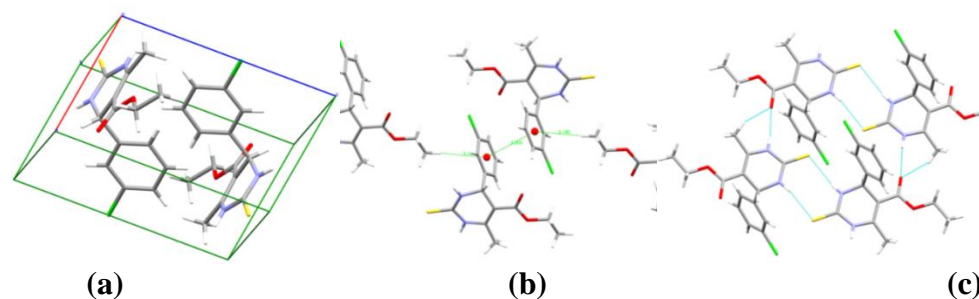


**Figure 2.15:** (a) Packing diagram of **1.5**, (b)  $\pi$ ... $\pi$  interactions in **1.5**, and (c) N-H...O, C-H...O & N-H...S interactions in **1.5**

#### 2.5.2.10. Hirshfeld surface analysis of **1.5**

The Hirshfeld surface mapped on  $d_{\text{norm}}$  of compound **1.5** is displayed in Figure 2.16 (a). The red color represents the more dominant non-covalent C-H...O interactions involved in the crystal structure (Figure 2.16 (a)).

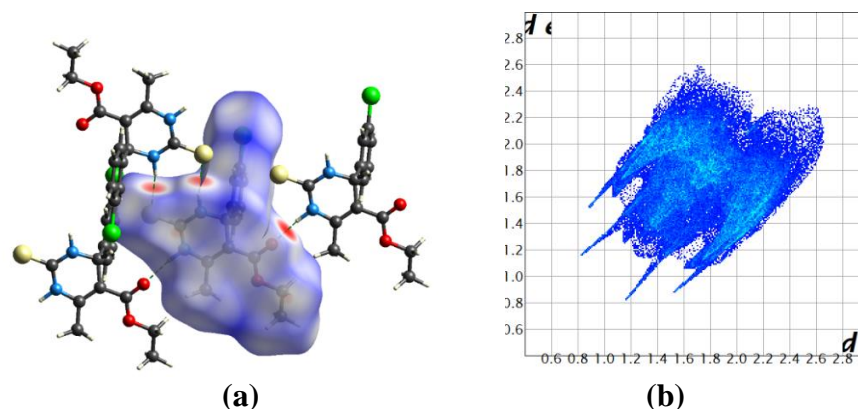


**Figure 2.16:** (a) Hirshfeld surface mapped on  $d_{\text{norm}}$  for compound **1.5**, (b) Two-dimensional fingerprint plot for compound **1.5**

The 2D fingerprint plots represent the summary of weak intermolecular interactions in the crystal structure and provide information about the percentage contribution of a 3D Hirshfeld surface. The 2D fingerprint plot of compound **1.5** is shown in Figure 2.16(b). The fingerprint analysis of compound **1.5** shows the percentage contribution of intermolecular interactions are H-H for around 37.9 %, O-H for 7.7 %, C-H for 12.9%, S-H for 16.7%, N-H for 2.9%, C-C for 3.9%, Cl-C for 0.1%, Cl-H for 16.7%, Cl-O for 0.7%, S-H for 0.7%, S-S for 0.7%, C-O for 0.7% and O-N for 0.2 % of the close contacts in the Hirshfeld surfaces. The spoke-like pattern in the fingerprint plots of **1.5** represents the C-H...O interactions in the crystal lattice in the region of  $d_i + d_e = 2.00\text{-}2.9\text{\AA}$  (Figure 2.16(b)). The second spoke-like pattern in the fingerprint plots of **1.5** represents the C-H...S interactions in the crystal lattice in the region of  $d_i + d_e = 2.00\text{-}2.9\text{\AA}$  (Figure 2.16(b)). The C-H... $\pi$  interactions in **1.5** can be seen as a pair of unique blue-colored wings in the region of  $d_i + d_e = 3.2\text{-}3.6\text{\AA}$  (Figure 2.16(b)). The C-H...N pair of contacts is also reflected as two characteristic wings occupied in the  $d_i + d_e = 3.2\text{-}3.4\text{\AA}$  in **1.5**.

In an extensive hydrogen-bonding network of calculated interactions of compound **1.5**, terminal carbonyl oxygen, thio-pyrimidine nitrogen, and thio-pyrimidine sulfur are involved in weak interaction and were forming 8 membered  $R_2^2(8)$  ring in which N-H...S interactions (Figure 2.17 (a)) is involved. The  $\pi$ ... $\pi$  stacking interaction found in **1.5** is shown in Figure 2.17 (b).

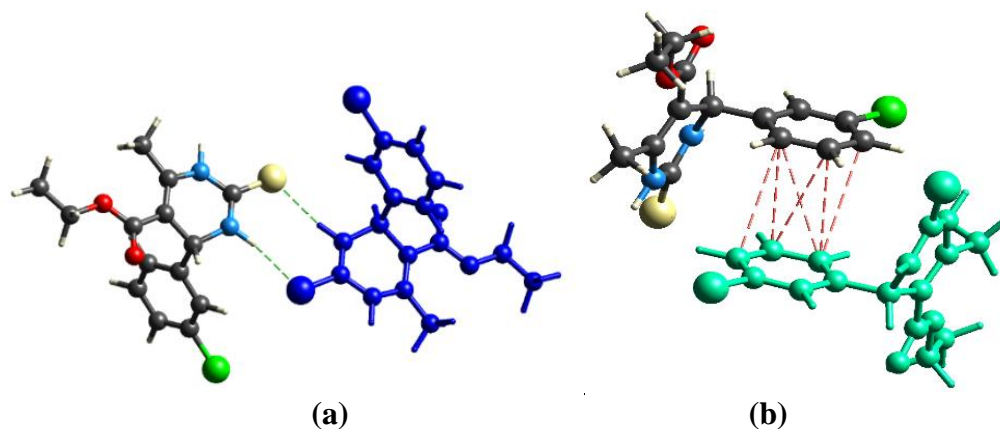


**Figure 2.17:** (a) Non-covalent interactions forming  $R_2^2(8)$ , (b)  $\pi\cdots\pi$  interactions in weak interactions calculations of **1.5**

The 3D Hirshfeld surface on Curvedness plots for compound **1.5** is shown in Figure 2.18. In the Curvedness plots, Very weak intermolecular interactions are seen inside the contours by yellow spots. The green-colored flat regions provided the information of the presence of  $\pi\cdots\pi$  stacking interaction in the crystal packing in Figure 2.18 (a) and (b). The shape index of compound **1.5** indicated the nature of interactions (i.e., donor and acceptor property) (Figure 2.18 (b) and (b)). The red and blue areas of the shape index indicated the acceptor and the donor property, respectively. In the Shape index plots of compound **1.5**, the red and blue colored triangles on the surface of rings of the molecule also provided the information of the presence of  $\pi\cdots\pi$  stacking interaction in the crystal packing (Figure 2.18 (c) and (d)). The yellowish-red colored concave region on the Hirshfeld surface of compound **1.5** represents the weak intermolecular interactions in the crystal packing. Therefore, the Hirshfeld surface analysis also proved the presence of  $\pi\cdots\pi$  stacking and other different weak non-covalent interactions in the crystal packing, which stabilizes the crystal packing structure of compound **1.5**.

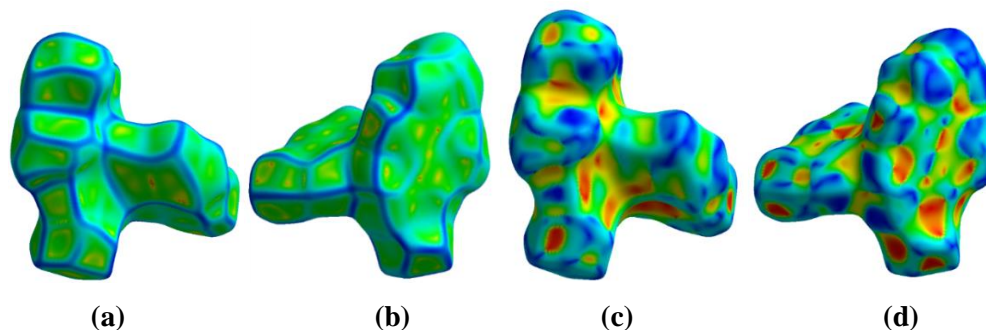


**Figure 2.18:** (a) and (b) Curvedness both side view of compound **1.5**, (c) and (d) Shape index both side view of compound **1.5**

## 2.6. Cytotoxicity and anti-cancer activity of 1.1-1.5

### 2.6.1. *In-silico* analysis of 1.1-1.5

Molecular docking investigation carried out using the autodock Vina (Trott & Olson, 2009). The crystal structures of mitotic kinesin Eg5 were retrieved from the RSCB protein data bank (PDB id: 3UIH). The protein preparation was done in a chimera (Pettersen et al., 2004) by removing co-crystallized ligands, cofactors, and embedded water molecules. It was further processed by adding polar hydrogens and assigning partial charges. The grid parameters for the Eg5 protein were determined based on the native ligand monastrol. The grid is centered on monastrol, making sure all the residues of the binding cavity are encompassed (centered at  $x= 18.06$ ,  $y= 24.56$ ,  $z = 49.31$ ;  $18.46\text{\AA} \times 21.52 \text{\AA} \times 21.82 \text{\AA}$ ). The exhaustiveness parameter for analyzing the binding affinity was set to 9 modes, and the synthesized compounds (**1.1**, **1.2**, **1.3**, **1.4**, and **1.5**) are subjected to molecular docking with the monomer proteins. The re-docking of compounds (**1.1**, **1.2**, **1.3**, **1.4**, and **1.5**) confirmed docking parameters validation. Further, validation of parameters for Eg5 was done by re-docking of the crystal structure of monastrol, which was extracted from Eg5 protein, and then superimposing it with the native monastrol in Eg5 protein. The analysis of docking results was carried out using the pymol and Discovery studio visualizer.

### 2.6.1.1. *In-silico* analysis of 1.1, 1.2, 1.3, 1.4, and 1.5

### 2.6.1.2. Table 2.5. Binding energy and the residues involved in the interaction of 1.1, 1.2, 1.3, 1.4, and 1.5 with kinesin Eg5 protein

Compounds	Docking score	Residues involved in H-bond	Residues involved in other interactions ( $\pi$ -anion, $\pi$ - $\sigma$ , $\pi$ - $\pi$ , $\pi$ -alkyl, and alkyl)
1.1	-7.8	Glu116	Ala 133, Pro 137
1.2	<b>-7.9</b>	Glu116	Leu214, Arg221, Ile136, Phe239, Leu160
1.3	-7.1	Glu116	Glu116, Ala218, Leu214, Arg119
1.4	-7.7	Glu116	Glu116, Leu214, Ile136, Phe239
1.5	<b>-7.9</b>	Glu116, Trp127 (halogen bond)	Ala 133, Leu214, Arg221, Pro137, Tyr211
1 (Monastrol)	-7.8	Glu116, Glu118	Ala218, Leu214, Arg119, Ala133, Pro137

The common trend in the binding interactions of compounds **1.2**, **1.5**, and **1 (monastrol)** in the cavity of Eg5 is that the ester group protrudes outside the cavity. *In-silico* analysis revealed that compounds **1.2** and **1.5** showed better binding energy (-7.9 and -7.9, respectively) than the standard drug **monastrol** (-7.8) (Table 2.5). The chlorobenzene ring of compounds **1.2** and **1.5** is directed towards the hydrophobic region of the active site of Eg5 (Figure 2.19 (a) and (b)). The chlorobenzene ring of **1.2** and **1.5** are situated so that  $\pi$ -anion interactions with the negatively charged residue Glu116 will be favorable. Compound **1.5** also showed one halogen bond with the residue Trp127, which indicated that compounds **1.5** fits well in to the cavity of Eg5. Further, the residues Ala 133, Leu214, Arg221, Pro137 and Tyr211 facilitates the hydrophobic  $\pi$ -alkyl and alkyl interactions with compound **1.5** (Figure 2.19 (b)) (Table 2.5).



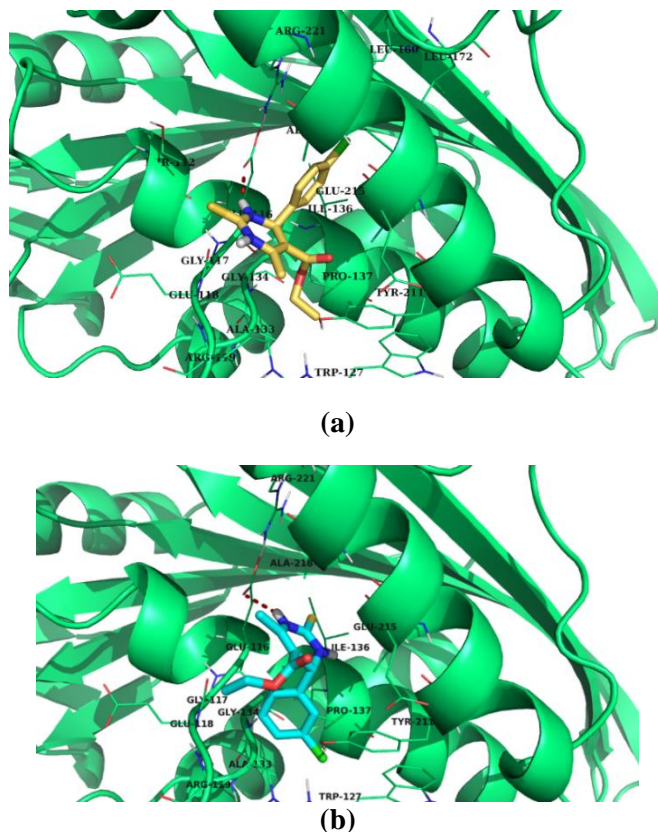


**Figure 2.19:** (a) and (b) Binding mode of compounds **1.2** and **1.5** in the active site cavity of **Eg5** protein, respectively.

### 2.6.2. Biological activity of 1.1-1.5

RPMI-1640 cell culture medium was purchased from Hyclone (GE healthcare life sciences, Marlborough, USA), penicillin-streptomycin-amphotericin B (PSA) cocktail, 0.25% Trypsin EDTA, and Fetal Bovine Serum (FBS) were bought from Gibco, Thermo-fisher Scientific (Waltham, MA, USA), [3-(4,5-dimethylthiazol-2-yl)-2,5-diphenyltetrazolium bromide] (MTT) was purchased from Sisco Research Laboratories Pvt. Ltd. (Maharashtra, India) were purchased. Dimethyl sulfoxide (DMSO), acridine orange, trypan blue, ethidium bromide, and Hoechst 33342 were acquired from Sigma-Aldrich (St. Louis, MO, USA).

### **2.6.2.1 Cell culture**

Human adenocarcinoma A549 cells were acquired from American Type Culture Collection (ATCC). Cells were cultured in RPMI-1640 medium complemented with 1% PSA and 10% FBS at 37<sup>0</sup>C in a humidified 5% CO<sub>2</sub> incubator. The medium was changed every alternate day, and cells were trypsinized after achieving the confluency.

### **2.6.2.2. MTT assay**

MTT assay was performed to determine the effect of compounds **1.1**, **1.2**, **1.3**, **1.4** and **1.5** on cytotoxicity or viability of A549 cells. Approximately 8,000 cells/well were seeded in a 96-well plate and incubated for 24 h in humidified 5% CO<sub>2</sub> incubator at 37<sup>0</sup>C. After attachment, cells were treated with different **1.1**, **1.2**, **1.3**, **1.4** and **1.5**. Media was removed from individual wells after 24 and 48 h treatment time points, and 50 µl of MTT solution (5 mg/mL) was added to each well. The plate was incubated in the dark for 4 h at 37<sup>0</sup>C in a humidified 5% CO<sub>2</sub> incubator. 150 µl of DMSO was added after 4 h of incubation to dissolve formazan crystals, and absorbance was taken at 570 nm in a multimode plate reader (Synergy H1 Hybrid Reader, Biotek; Winooski, VT, USA).

### **2.6.2.3. Trypan blue assay**

Trypan blue is an azo dye that stains dead cells with the compromised membrane in blue colour, and it does not stain live cells with the intact membrane, thus appears with clear cytoplasm. Around 30,000 cells were seeded in a 12-well plate and treated with **1.2**, **1.4**, and **1.5** for 24 and 48 h. After specific treatment time points, cells were trypsinized and centrifuged at 1200 rpm for 5 min. The cell pellet was suspended in 200 µl 1X PBS after removing the supernatant, and 0.5% trypan blue dye was added. Cells were counted under a phase-contrast microscope (Zeiss, Germany).

#### **2.6.2.4. Acridine orange-ethidium bromide staining**

Acridine orange- ethidium bromide staining was used to observe apoptosis and necrosis in A549 cells. 60,000 cells were seeded in a 12-well plate followed by treatment with selected compounds **1.2** and **1.5** (200  $\mu$ M) for 24 and 48 h time points. After individual time points, cells were trypsinized and centrifuged at 1200 rpm for 5 min. The cell pellet was suspended in 50  $\mu$ l of 1X PBS after removing the supernatant. 10  $\mu$ l of cell suspension was mixed with 1  $\mu$ l acridine orange (1 $\mu$ g/mL) and 1  $\mu$ l ethidium bromide (1  $\mu$ g/mL) on a slide and mounted with the coverslip. The slide was observed under a fluorescence microscope (Olympus, Japan), and images were taken at 200X magnification.

#### **2.6.2.5. Hoechst 33342 staining**

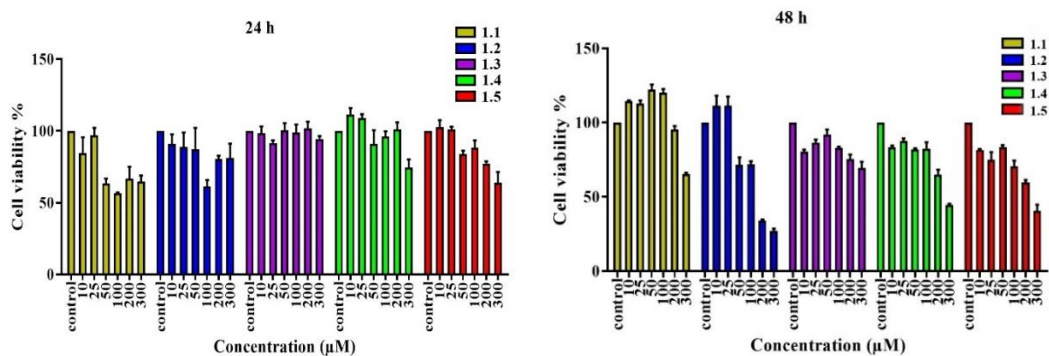
Hoechst 33342 is a nucleic acid staining dye that is used to observe morphological changes in apoptotic cells. Hoechst 33342 assay was performed in a 12-well plate in which tissue cultured coverslips were placed. 60,000 cells/well was seeded and incubated at 37<sup>0</sup>C in a humidified CO<sub>2</sub> incubator. Cells were treated with **1.2** and **1.5** compounds at 200  $\mu$ M concentration after they were attached and appeared in morphology. After the individual treatment point, the media was removed from the plate, and cells were washed with 1X PBS. 1 mL hoechst 33342 stain (1 $\mu$ g/mL in 1X PBS) was added to the wells and incubated in the dark for 15-20 mins at 37<sup>0</sup>C. Hoechst 33342 was removed, and cells were washed thrice by chilled 1X PBS. Coverslips were removed from the wells and placed on the slide upside down. Cells were observed under a fluorescent microscope (Olympus, Japan) at 200X magnification, and images were taken.

### **2.6.3. Result and Discussion**

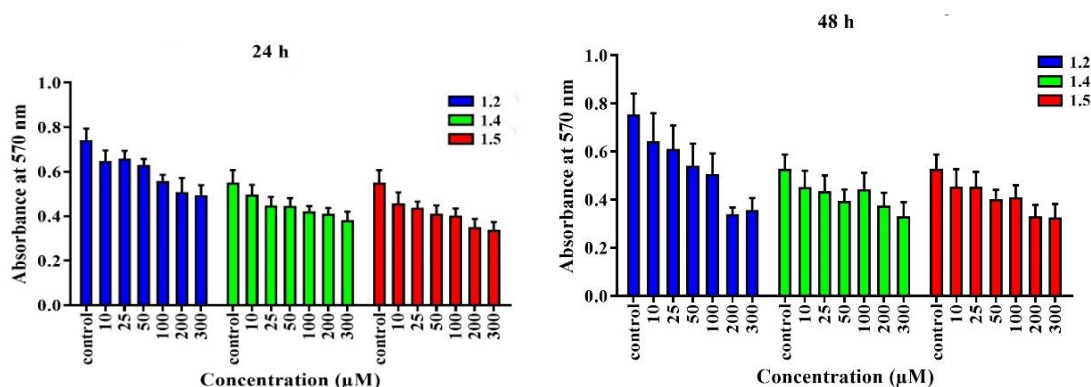
#### **2.6.3.1. Compounds 1.1, 1.2, 1.3, 1.4 and 1.5 variants decreased lung adenocarcinoma A549 cells viability**

A549 adenocarcinoma cells were treated at different concentrations (10-300  $\mu\text{M}$ ) of compound variants (**1.1**, **1.2**, **1.3**, **1.4** and **1.5**) to screen the highly effective variant. **1.1** treatment (10-300  $\mu\text{M}$ ) decreased cell viability to 3-43.47 % at 24 h and 4.6-34.8 % at 48 h (Figure 2.20A). **1.3** treatment (10-300  $\mu\text{M}$ ) decreased cell viability to 0-8.34 % at 24 h and 8-30.7 % at 48 h (Figure 2.20A). **1.2**, **1.4**, and **1.5** (10-300  $\mu\text{M}$ ) treatment decreased cell viability to 13-33.3%, 10-30.7% and 17-38.7 % respectively after 24 h. After 48 h treatment (10-300  $\mu\text{M}$ ), **1.2**, **1.4**, and **1.5** decreased cell viability to 14-55 %, 17-38.7 % and 14-38.3 % respectively. After 72 h time point, **1.2**, **1.4**, and **1.5** decreased cell viability to 3-72.5 %, 15.1-46.2 % and 14-58 % respectively (Figure 2.20B). Among this series of variant **1.2**, **1.4**, and **1.5** decreases the cell viability significantly.

(A)



(B)



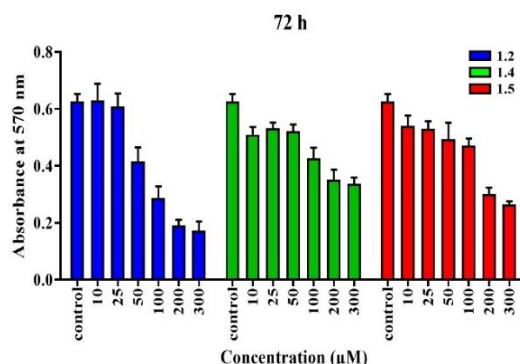
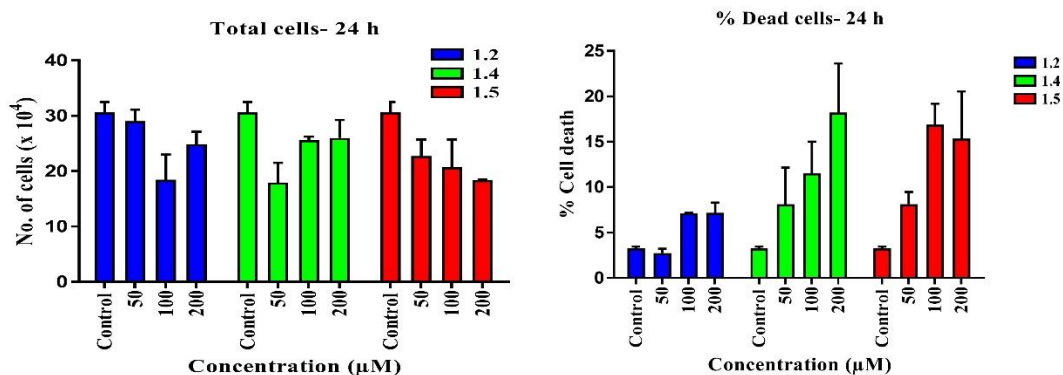


**Figure 2.20:** A549 lung adenocarcinoma cells were treated with (A) different concentrations (10 μM, 25 μM, 50 μM, 100 μM, 200 μM, 300 μM) of different compounds (**1.1, 1.2, 1.3, 1.4 and 1.5**) and cell viability was analysed by MTT assay. (B) Cells were treated with different concentrations of selected **1.2, 1.4, and 1.5** for 24 h, 48 h, and 72 h, and cell viability was examined by MTT assay.

### 2.6.3.2. Compounds **1.1, 1.2, 1.3, 1.4 and 1.5** variants increased cell death in lung adenocarcinoma cells A549

Trypan blue assay was performed to check cell growth inhibition and cell death. Lung adenocarcinoma A549 cells were treated with **1.2, 1.4, and 1.5** at defined doses (50 μM, 100 μM, and 200 μM) for 24 h and 48 h. In **1.2** treated groups 7.18 %, **1.4** treated groups 18.22 %, and in **1.5** treated groups, 16.88 % cell death was observed at 24 h (Figure 2.21 A) in the 200 μM treatment group. At 48 h time point, 14.92 %, 11.07%, and 10.27 % cell death was observed in **1.2, 1.4, and 1.5** treated groups, respectively (Figure 2.21B). The number of total cells decreased as the concentration of variants was increased compared to control groups at 24 h (Figure 2.21A). We chose **1.2, and 1.5** compounds for further study as the percentage of cell death was higher in these groups after treatment. At 200 μM concentration, **1.2** treatment caused the highest cell death at 48 h, and **1.2 and 1.5** treatment decreased total cell number to less than 50 % at 48 h (Figure 2.21 B). These results suggest that treatment with **1.2, 1.4, and 1.5** compounds induced cell death in A549 cells.

(A)



(B)

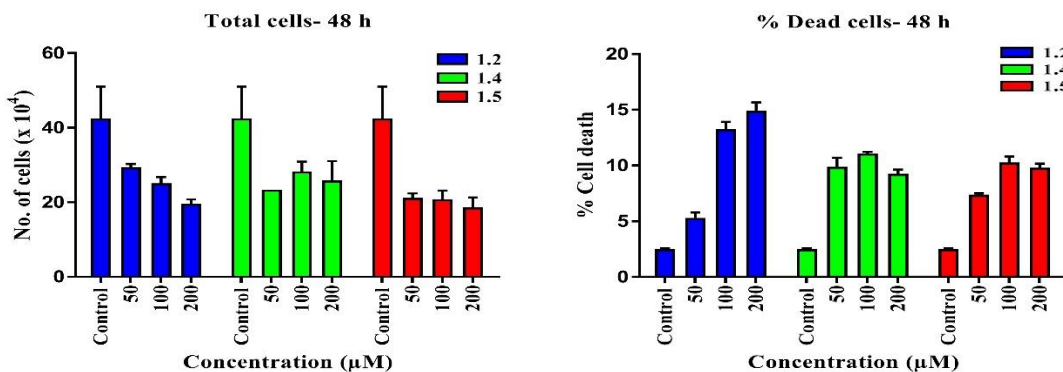


**Figure 2.21** Trypan blue assay was performed to check the effect of **1.2**, **1.4**, and **1.5** at 50, 100, and 200 μM doses. Graphs represent percent cell death and the total number of cells for (A) 24 h and (B) 48 h.

### 2.6.3.3. Compounds 1.2 and 1.5 induced apoptotic cell death in A549 adenocarcinoma cells

**1.2** and **1.5** were selected for induced apoptotic cell death in A549 adenocarcinoma cells because the percentage of cell death is higher with these two analogues. Acridine orange–ethidium bromide staining was performed to distinguish between live cells, apoptotic cells, and necrotic cells. Live cells were stained by acridine orange in green color, and dead cells with compromised membranes were stained by ethidium bromide in red color. Control cells did not show any characteristics of cell

death at any time point. Treatment of **1.2** and **1.5** compounds at 200  $\mu\text{M}$  for 24 and 48 h showed typical apoptotic characteristics. Membrane blebbing, apoptotic body formation and nuclear fragmentation were observed 24 and 48 h of treatment. **1.5** treatment for 48 h caused necrosis in cells that appeared red (**Figure 2.22**). These results suggest that **1.2** and **1.5** compound treatment induced cell death in A549 cells.

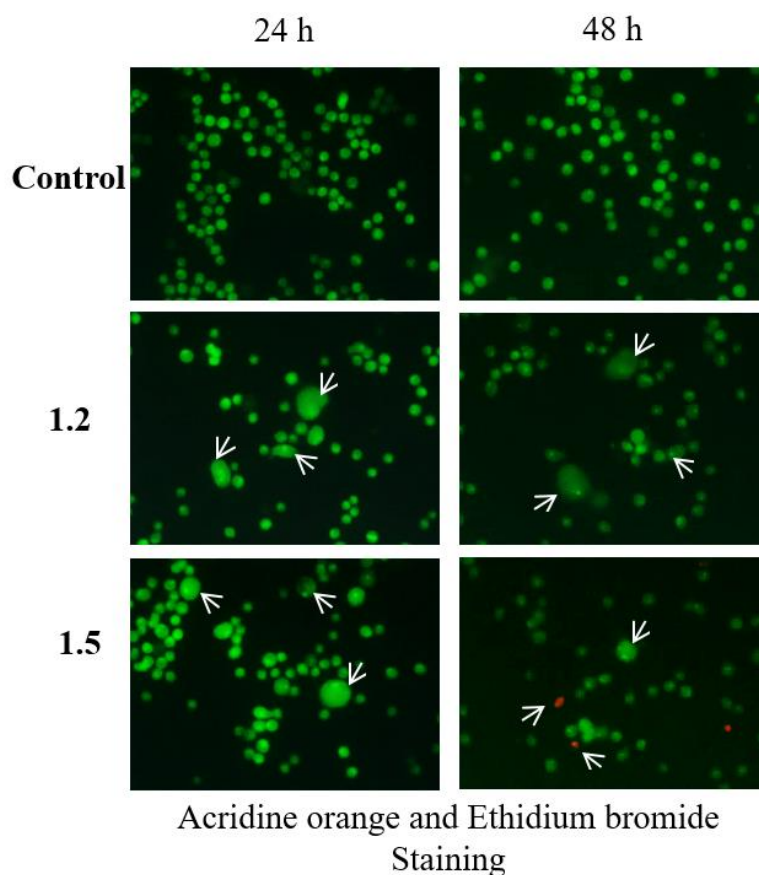


**Figure 2.22:** A549 adenocarcinoma cells were treated with 200  $\mu\text{M}$  **1.2** and **1.5** compounds for 24 and 48 h and stained with acridine orange and ethidium bromide

#### **2.6.3.4. Compounds 1.2 and 1.5 induced nuclear fragmentation A549 adenocarcinoma cells**

Hoechst assay was performed to analyze the effect of **1.2** and **1.5** compounds on apoptosis of A549 cells. Control cells did not show any characteristics associated with

cell death. In contrast, in **1.2** and **1.5** (200  $\mu$ M) treated groups, DNA fragmentation, nuclear condensation, and apoptotic body formation was observed along with bright blue fluorescence after 24 and 48 h of treatment (**Figure 2.23**). These results suggest that **1.2** and **1.5** treatment induced apoptosis in A549 cells.

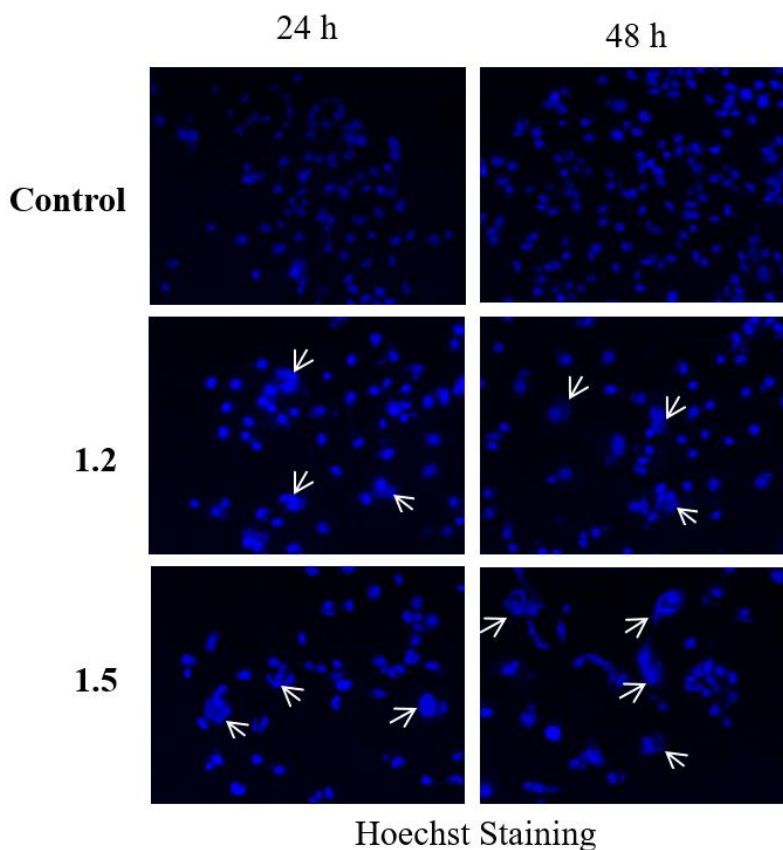


**Figure 2.23:** A549 adenocarcinoma cells were treated with 200  $\mu$ M **1.2** and **1.5** compounds for 24 and 48 h and stained with Hoechst stain. Cell death was assessed using a fluorescence microscope, and images were taken at 200X magnification.

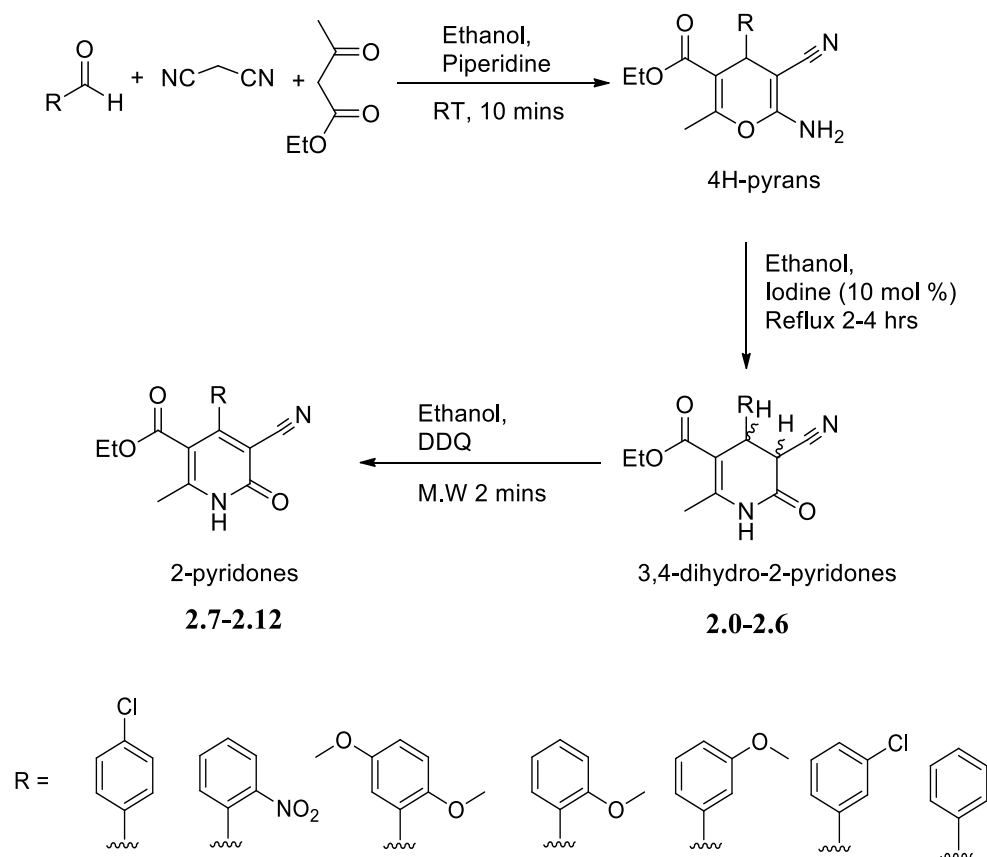
Among the 2-thiotetrahydropyrimidine (THPM) series of compounds, intracellular oxidation can be induced in the redox cycle to resulting in both cytotoxicity and genotoxicity in cancer cells. These may induce an imbalance in cellular antioxidant/oxidant status and causes DNA damage. This phenomenon can further trigger molecular events, which might eventually cause alterations in the tumor cell



cycle and initiate apoptosis. These can also reduce migration ability and could inhibit tumor growth and reduce the size of migration ability of A549 cells. These findings suggest that **1.2** and **1.5** might be anticancer drug candidates. Its analogues are promising agents for treating different types of cancers, particularly for cancer of the lung.

## 2.7. Scheme 2: Synthesis and study of 2-dihydropyridone and 2-pyridone derivatives with methylene linkers

In **Scheme 2**, we have synthesized and studied the non-covalent interaction of 2-pyridones based derivatives. Here, we have synthesized 2-pyridones and 3, 4-dihydropyridones derivatives using methylene linkers attached with a methyl group to develop flexible models to understand nature's interactions by these models.



**Scheme 2**

### 2.7.1 General procedure for the synthesis of 4H-pyrans

To a 100 mL RB was taken ethanol (40 mL) and was added aldehyde (10 mmol) and malononitrile (10 mmol) and stirred. The mixture ethyl acetoacetate (10 mmol) was added, followed by piperidine (0.2 mL, 2 mmol). The mixture was then stirred at room temperature in an open atmosphere for 10 mins. The precipitated solid was filtered and washed with methanol.

### 2.7.2. General procedure for the synthesis of 3,4-dihydro-2-pyridones (2.0-2.6)

To a 2-neck 150 mL RB the synthesized 4H-pyrans (6.7 mmol) were dissolved in ethanol (50 mL) at 80°C. Iodine (10 mol %) was added to the reaction vessel and refluxed for 2-4 hours monitored by TLC (EtOAc/hexane 3:7). After the reaction is completed, the mixture was concentrated under reduced pressure and then treated with sodium thiosulphate solution (5 mol %) to remove unreacted iodine. The organic layer was back-extracted with ethyl acetate (twice), usual workup and purification over silica gel column using Hexane: EtOAc (7:3) afforded 3,4-dihydro-2-pyridones (2.0-2.6).

#### 2.7.2.1. Ethyl 4-(4-chlorophenyl)-5-cyano-2-methyl-6-oxo-1,4,5,6-tetrahydropyridine -3-carboxylate (2.0)

**Yield:** 1.88 g (88%), m.p. 202-205°C.

**<sup>1</sup>H NMR** (300 MHz, CDCl<sub>3</sub>): δ 1.18 – 1.23 (3H, t, CH<sub>3</sub>, *J* = 7.2 Hz); 2.44 (3H, s, CH<sub>3</sub>); 4.08 – 4.17 (3H, m, CH<sub>3</sub>); 4.46 – 4.49 (1H, d, CH, *J* = 6.9 Hz); 7.18 – 7.20 (2H, d, Ar-H, *J* = 8.4 Hz); 7.30- 7.33 (2H, d, Ar-H, *J* = 8.4 Hz); 8.42 (1H, s, NH,); **<sup>13</sup>C NMR: δC (ppm):** 14.2, 18.1, 27.9, 38.8, 61.7, 104.3, 116.8, 128.7, 129.1, 131.5, 138.7, 148.9, 167.2, 171.8; **MS (m/z):** 319.75(M+1). **Element analysis: (i). Calculated:** C=60.29%; H=4.74%; N=8.79%; **(ii). Found:** C=60.54%; H=4.36%; N=8.62%

#### 2.7.2.2. Ethyl-5-cyano-2-methyl-4-(2-nitrophenyl)-6-oxo-1,4,5,6-tetrahydropyridine-3-carboxylate (2.1)

**Yield:** 1.71 g (81%), m.p. 182-185°C.

**<sup>1</sup>H NMR**(300 MHz, CDCl<sub>3</sub>): δ 1.19 – 1.23 (3H, t, CH<sub>3</sub>, *J* = 7.2 Hz); 2.41 (3H, s, CH<sub>3</sub>); 3.79 (3H, s, CH<sub>3</sub>); 4.08 – 4.18 (3H, m, CH<sub>3</sub>); 4.45 – 4.48 (1H, d, CH, *J* = 6.9 Hz); 6.79 – 6.86 (3H, m, Ar-H); 7.23 – 7.28 (1H, t, Ar-H, *J* = 7.8 Hz); 8.30 (1H, s, NH). **<sup>13</sup>C NMR:**

**$\delta$ C (ppm):** 14.2, 18.1, 23.3, 37.8, 61.7, 104.3, 116.8, 124.8, 126.8, 128.3, 128.6, 134.0, 148.0, 148.9, 167.2, 171.8. **MS (m/z):** 333.40(M+1). **Element analysis: (i). Calculated:** C=78.88%; H=6.06%; N=8.43%; **(ii). Found:** C=78.47%; H=6.14%; N=8.62%

**2.7.2.3. Ethyl-5-cyano-4-(2,5-dimethoxyphenyl)-2-methyl-6-oxo-1,4,5,6-tetrahydropyridine-3-carboxylate (2.2)**

**Yield:** 1.6 g (79%), m.p. 192-194°C.

**$^1$ H NMR**(300 MHz, CDCl<sub>3</sub>):  $\delta$  1.18 – 1.23 (3H, t, CH<sub>3</sub>CH<sub>2</sub>-,  $J$  = 7.2 Hz); 2.44 (3H, s, CH<sub>3</sub>-); 4.08 – 4.17 (3H, m, CH<sub>3</sub>CH<sub>2</sub>-, CH,); 4.46 – 4.49 (1H, d, CH-,  $J$  = 6.9 Hz); 7.18 – 7.20 (2H, d, Ar-H,  $J$  = 8.4 Hz); 7.30- 7.33 (2H, d, Ar-H,  $J$  = 8.4 Hz); 8.42 (1H,s, -NH,).

**$^{13}$ C NMR:  $\delta$ C (ppm):** 14.2, 18.1, 22.3, 39.1, 55.8, 56.1, 61.7, 104.3, 112.0, 112.5, 115.6, 116.8, 127.2, 148.1, 148.9, 152.8, 167.2, 171.8. **MS (m/z):** 345.36(M+1).

**Element analysis: (i). Calculated:** C=62.78%; H=5.85%; N= 8.13% **(ii). Found:** C=62.45%; H=5.77%; N=8.28%.

**2.7.2.4. Ethyl-5-cyano-4-(2-methoxyphenyl)-2-methyl-6-oxo-1,4,5,6-tetrahydropyridine-3-carboxylate (2.3)**

**Yield:** 1.70 g (80%), m.p. 179-182°C.

**$^1$ H NMR**(300 MHz, CDCl<sub>3</sub>):  $\delta$  1.18 – 1.23 (3H, t, CH<sub>3</sub>CH<sub>2</sub>-,  $J$  = 7.2 Hz); 2.44 (3H, s, CH<sub>3</sub>-); 4.08 – 4.17 (3H, m, CH<sub>3</sub>CH<sub>2</sub>-,  $J$  = 7.2); 4.46 – 4.49 (1H, d, CH-,  $J$  = 6.9 Hz); 7.18 – 7.20 (2H, d, Ar-H,  $J$  = 8.4 Hz); 7.30- 7.33 (2H, d, Ar-H,  $J$  = 8.4 Hz); 8.42 (1H,s, -NH,).

**$^{13}$ C NMR:  $\delta$ C (ppm):** 14.2, 18.1, 22.0, 39.1, 56.1, 61.7, 104.3, 112.2, 116.8, 120.9, 126.2, 126.9, 128.7, 148.9, 155.8, 167.2, 171.8. **MS (m/z):** 315.36(M+1).

**Element analysis: (i). Calculated:** C=64.96%; H=5.77%; N=8.91%; **(ii). Found:** C=64.59%; H=5.46%; N=8.67%.

**2.7.2.5. Ethyl-5-cyano-4-(3-methoxyphenyl)-2-methyl-6-oxo-1,4,5,6-tetrahydropyridine-3-carboxylate (2.4)**

**Yield:** 1.67 g (78%), m.p. 188-190°C.

**$^1$ H NMR**(300 MHz, CDCl<sub>3</sub>):  $\delta$  1.19 – 1.23 (3H, t, CH<sub>3</sub>,  $J$  = 7.2 Hz); 2.41 (3H, s, CH<sub>3</sub>); 3.79 (3H, s, CH<sub>3</sub>); 4.08 – 4.18 (3H, m, CH<sub>2</sub>, CH); 4.45 – 4.48 (1H, d, CH,  $J$  = 6.9 Hz); 6.79 – 6.86 (3H, m, Ar-H); 7.23 – 7.28 (1H, t, Ar-H,  $J$  = 7.8 Hz); 8.30 (1H, s, NH).  **$^{13}$ C**

**NMR:  $\delta$ C (ppm):** 14.2, 18.1, 28.2, 38.8, 55.8, 61.7, 104.3, 111.5, 111.8, 116.8, 120.0, 129.6, 141.6, 148.9, 160.5, 167.2, 171.8. **MS (m/z):** 315.34(M+1). **Element analysis:** (i). **Calculated:** C=64.96%; H=5.77%; N=8.91%; (ii). **Found:** C=64.54%; H=5.86%; N=8.46%.

#### **2.7.2.6. Ethyl-4-(3-chlorophenyl)-5-cyano-2-methyl-6-oxo-1,4,5,6-tetrahydropyridine-3-carboxylate (2.5)**

**Yield:** 1.75 g (82%), m.p. 192-195°C.

**$^1$ H NMR**(300 MHz, CDCl<sub>3</sub>):  $\delta$  1.19 – 1.23 (3H, t, CH<sub>3</sub>,  $J$  = 7.2 Hz); 2.43 (3H, s, CH<sub>3</sub>); 4.10 – 4.19 (3H, m, CH<sub>2</sub>, CH); 4.45 – 4.47 (1H, d, CH,  $J$  = 7.2 Hz); 7.16 – 7.70 (2H, m, Ar-H); 7.25 – 7.30 (2H, m, Ar-H); 8.58 (1H, s, NH).  **$^{13}$ C NMR:  $\delta$ C (ppm):** 14.2, 18.1, 27.4, 38.8, 61.7, 104.3, 116.8, 125.8, 126.0, 127.5, 130.0, 134.2, 142.0, 148.9, 167.2, 171.8. **MS (m/z):** 319.75(M+1). **Element analysis:** (i). **Calculated:** C=60.29%; H=4.74%; N=8.79% (ii). **Found:** C=60.57%; H=4.39%; N=8.65%.

#### **2.7.2.7. Ethyl-5-cyano-2-methyl-6-oxo-4-phenyl-1,4,5,6-tetrahydropyridine-3-carboxylate (2.6)**

**Yield:** 1.6 g (77%), m.p. 191-193°C.

**$^1$ H NMR**(300 MHz, CDCl<sub>3</sub>):  $\delta$  1.18 – 1.23 (3H, t, CH<sub>3</sub>CH<sub>2</sub>-,  $J$  = 7.2 Hz); 2.44 (3H, s, CH<sub>3</sub>-); 4.08 – 4.17 (3H, m, CH<sub>3</sub>CH<sub>2</sub>-,  $J$  = 7.2); 4.46 – 4.49 (1H, d, CH-,  $J$  = 6.9 Hz); 7.18 – 7.20 (2H, d, Ar-H,  $J$  = 8.4 Hz); 7.30- 7.33 (2H, d, Ar-H,  $J$  = 8.4 Hz); 8.42 (1H, s, -NH,).  **$^{13}$ C NMR:  $\delta$ C (ppm):** 14.2, 18.1, 27.9, 38.8, 61.7, 104.3, 116.8, 125.9, 127.7, 128.6, 140.6, 148.9, 167.2, 171.8. **MS (m/z):** 285.31(M+1). **Element analysis:** (i). **Calculated:** C=67.59%; H=5.67%; N=9.85% (ii). **Found:** C=67.77%; H=5.54%; N=9.63%.

### **2.7.3. General procedure for the synthesis of 2-pyridone (2.7-2.12)**

To a solution of 3,4-dihydro-2-pyridone (3.52 mmol) (**2.0-2.6**) in ethanol (15 mL), DDQ (3.52 mmol) was added and was irradiated in the microwave oven for 2 minutes. The reaction was monitored by TLC (EtOAc/hexane 5:5). After the reaction is completed, ethanol (10 mL) is added to the reaction vessel, which allows to form pure

crystals of 2-pyridone (**2.7-2.12**) (which is further collected). The remaining solvents that contain 2-pyridone were collected and purified over silica gel by column chromatography Hexane: EtOAc (50:50).

#### **2.7.3.1. Ethyl-5-cyano-2-methyl-4-(2-nitrophenyl)-6-oxo-1,6-dihydropyridine-3-carboxylate (2.7)**

**Yield:** .083 g (85%), m.p. 210-212°C.

**<sup>1</sup>H NMR**(300 MHz, CDCl<sub>3</sub>): δ 0.85 – 0.89 (3H, t, CH<sub>3</sub>, *J* = 7.2 Hz); 2.75 (3H, s, CH<sub>3</sub>); 3.90 – 3.97 (2H, q, CH<sub>2</sub>, *J* = 7.2 Hz); 7.30 – 7.33 (1H, d, Ar-H, *J* = 7.5 Hz); 7.68 – 7.72 (1H,d, Ar-H, *J* = 7.5 Hz); 7.77 – 7.82 (1H,d, Ar-H, *J* = 7.2 Hz); 8.33 – 8.36 (1H, d, Ar-H, *J* = 8.1 Hz); 13.65 (1H, s, NH). **<sup>13</sup>C NMR: δC (ppm):** 14.2, 19.6, 61.8, 109.0, 115.3, 115.8, 123.8, 127.3, 128.8, 130.0, 134.7, 145.0, 151.4, 161.5, 165.0, 169.4. **MS (m/z):** 328.09(M+1). **Element analysis: (i). Calculated:** C=58.72%; H=4.00%; N=12.84% **(ii). Found:** C=58.56%; H=4.16%; N=12.77%.

#### **2.7.3.2. Ethyl-5-cyano-4-(2-methoxyphenyl)-2-methyl-6-oxo-1,6-dihydropyridine-3-carboxylate (2.8)**

**Yield:** 0.82 g (83%), m.p. 208-210°C.

**<sup>1</sup>H NMR**(300 MHz, CDCl<sub>3</sub>): δ 1.18 – 1.23 (3H, t, CH<sub>3</sub>CH<sub>2</sub>-, *J* = 7.2 Hz); 2.44 (3H, s, CH<sub>3</sub>-); 4.08 – 4.17 (3H, m, CH<sub>3</sub>CH<sub>2</sub>-, CH-); 4.46 – 4.49 (1H, d, CH-, *J* = 6.9 Hz); 7.18 – 7.20 (2H, d, Ar-H, *J* = 8.4 Hz); 7.30- 7.33 (2H, d, Ar-H, *J* = 8.4 Hz); 8.42 (1H,s, -NH-). **<sup>13</sup>C NMR: δC (ppm):** 14.2, 19.6, 56.2, 61.8, 109.0, 111.4, 115.3, 115.8, 119.9, 120.9, 128.9, 129.7, 151.4, 157.6, 161.5, 165.0, 169.4. **MS (m/z):** 313.32(M+1). **Element analysis: (i). Calculated:** C=65.38%; H=5.16%; N=8.97% **(ii). Found:** C=63.59%; H=5.31%; N=8.74%.

#### **2.7.3.3. Ethyl-5-cyano-2-methyl-6-oxo-4-phenyl-1,6-dihydropyridine-3-carboxylate (2.9)**

**Yield:** 0.85 g (87%), m.p. 204-206°C.

**<sup>1</sup>H NMR** (300 MHz, CDCl<sub>3</sub>): δ 0.78 – 0.83 (3H, t, CH<sub>3</sub>, *J* = 7.2 Hz); 2.63 (3H, s, CH<sub>3</sub>); 3.88 – 3.95 (2H, q, CH<sub>2</sub>, *J* = 7.2 Hz); 7.35 – 7.39 (2H, m, Ar-H); 7.47 – 7.49 (3H, t, Ar-H, *J* = 3 Hz); 13.69 (1H, s, NH). **<sup>13</sup>C NMR: δC (ppm):** 14.2, 19.6, 61.8, 109.0, 115.3,

115.8, 127.9, 128.6, 128.9, 132.5, 151.4, 161.5, 165.0, 169.4. **MS (m/z):** 283.29(M+1). **Element analysis: (i). Calculated:** C=68.07%; H=5.00%; N=9.92%; **(ii). Found:** C=68.36%; H=5.11%; N=9.68%.

**2.7.3.4. Ethyl 4-(4-chlorophenyl)-5-cyano-2-methyl-6-oxo-1,6-dihydropyridine-3-carboxylate (2.10)**

**Yield:** 0.75 g (79%), m.p. 214-216°C.

**<sup>1</sup>H NMR** (300 MHz, CDCl<sub>3</sub>): δ 0.88 – 0.93 (3H, t, CH<sub>3</sub>, *J* = 7.2 Hz); 2.63 (3H, s, CH<sub>3</sub>); 3.93 - 4.0 (2H, q, CH<sub>2</sub>, *J* = 7.2 Hz); 7.30 – 7.32 (2H, d, Ar-H, *J* = 8.4 Hz); 7.46 – 7.49 (2H, d, Ar-H, *J* = 8.4 Hz); 13.63 (1H, s, -NH); **<sup>13</sup>C NMR: δC (ppm):** 14.2, 19.6, 61.8, 109.0, 115.3, 115.8, 128.7, 130.0, 130.6, 133.5, 151.4, 161.5, 165.0, 169.4; **MS (m/z):** 317.74(M+1). **Element analysis: (i). Calculated:** C=60.67%; H=4.14%; N=8.84%; **(ii). Found:** C=60.33%; H=4.65%; N=8.76%

**2.7.3.5. Ethyl-5-cyano-4-(3-methoxyphenyl)-2-methyl-6-oxo-1,6-dihydropyridine-3-carboxylate (2.11)**

**Yield:** 0.79 g (81%), m.p. 207-209°C.

**<sup>1</sup>H NMR** (300 MHz, CDCl<sub>3</sub>): δ 0.84 – 0.89 (3H, t, CH<sub>3</sub>, *J* = 7.2 Hz); 2.62 (3H, s, CH<sub>3</sub>); 3.83 (3H, s, CH<sub>3</sub>); 3.92 – 3.99 (2H, q, CH<sub>2</sub>, *J* = 7.2 Hz); 6.89 – 7.03 (2H, m, Ar-H); 7.27 (1H, s, Ar-H); 7.36 – 7.41 (1H, t, Ar-H, *J* = 8.1 Hz); 13.67 (1H, s, NH); **<sup>13</sup>C NMR: δC (ppm):** 14.2, 19.6, 55.8, 61.8, 109.0, 110.5, 113.5, 115.3, 115.8, 121.2, 129.6, 133.5, 151.4, 160.5, 161.5, 165.0, 169.4; **MS (m/z):** 313.32(M+1). **Element analysis: (i). Calculated:** C=65.38%; H=5.16%; N=8.97%; **(ii). Found:** C=65.12%; H=5.66%; N=8.74%

**2.7.3.6. Ethyl-4-(3-chlorophenyl)-5-cyano-2-methyl-6-oxo-1,6-dihydropyridine-3-carboxylate (2.12)**

**Yield:** 0.81 g (84%), m.p. 223-225°C.

**<sup>1</sup>H NMR** (300 MHz, CDCl<sub>3</sub>): δ 0.87 – 0.92 (3H, t, CH<sub>3</sub>, *J* = 7.2 Hz); 2.64 (3H, s, CH<sub>3</sub>); 3.94 – 4.01 (2H, q, CH<sub>2</sub>, *J* = 7.2 Hz); 7.26 (1H, m, Ar-H); 7.33 (1H, s, Ar-H), 7.41 – 7.7.49 (2H, m, Ar-H) ; 13.61 (1H, s, NH); **<sup>13</sup>C NMR : δC (ppm):** 14.2, 19.6, 61.8, 109.0, 115.3, 115.8, 126.4, 127.0, 128.0, 130.0, 133.9, 134.2, 151.4, 161.5, 165.0, 169.4;

**MS (m/z):** 317.74(M+1). **Element analysis: (i). Calculated:** C=60.67%; H=4.14%; N=8.84%; **(ii). Found:** C=60.55%; H=4.43%; N=8.71%

## 2.8. Results and discussions

In Scheme 2, we have synthesized two series of compounds, those are **dihydro-2-pyridones** derivatives (**2.0-2.6**) and **2-pyridone** derivatives (**2.7-2.12**). From **dihydro-2-pyridones** derivatives, six compounds (**2.1, 2.2, 2.3, 2.4, 2.5 and 2.6**) gave suitable single crystal and from **2-pyridones** derivatives, three compounds (**2.7, 2.8 and 2.9**) gave suitable single crystal, which were studied by single crystal X-ray diffraction (SCXRD) and Hirshfeld surface analysis.

### 2.8.1. X-Ray Crystallographic studies and Hirshfeld surface analysis of 2.1, 2.2, 2.3, 2.4, 2.5, 2.6, 2.7, 2.8 and 2.9

#### 2.8.1.1 X-Ray Crystal Structure of 2.1

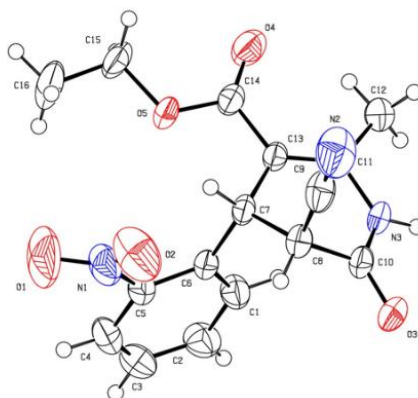


**Figure 2.24:** ORTEP diagram of **2.1**

#### 2.8.1.2 Table 2.6. Crystal data of compounds **2.1, 2.2** and **2.3**

Compound	<b>2.1</b>	<b>2.2</b>	<b>2.3</b>
Identification code	2062965	1937280	2062946
Empirical formula	C <sub>16</sub> H <sub>15</sub> N <sub>3</sub> O <sub>5</sub>	C <sub>18</sub> H <sub>20</sub> N <sub>2</sub> O <sub>5</sub>	C <sub>17</sub> H <sub>18</sub> N <sub>2</sub> O <sub>4</sub>
Formula weight	329.31	344.36	314.33
Temperature(K)	296.15	296.15	296.15
Crystal system	triclinic	triclinic	monoclinic
Space group	<i>P</i> -1	<i>P</i> -1	<i>P</i> 2 <sub>1</sub> / <i>n</i>

a(Å)	7.792(3)	9.3469(8)	8.527(3)
b(Å)	10.348(3)	10.2075(8)	10.259(4)
c(Å)	10.852(4)	10.5446(9)	18.960(8)
$\alpha$ (°)	68.319(3)	61.650(2)	90
$\beta$ (°)	89.451(4)	87.825(2)	102.295(5)
$\gamma$ (°)	85.748(4)	83.189(2)	90
Volume(Å <sup>3</sup> )	810.7(5)	878.94(13)	1620.5(11)
Z	2	2	4
$\rho$ (g/cm <sup>3</sup> )	1.349	1.301	1.288
$\mu$ (mm <sup>-1</sup> )	0.102	0.096	0.093
F(000)	344.0	364.0	664
Crystal size(mm <sup>3</sup> )	0.24 × 0.19 × 0.17	0.19 × 0.16 × 0.14	0.24 × 0.18 × 0.13
Radiation	MoK $\alpha$ ( $\lambda$ = 0.71073)	MoK $\alpha$ ( $\lambda$ = 0.71073)	MoK $\alpha$ ( $\lambda$ = 0.71073)
2 $\theta$ range for data collection(°)	4.248 to 57.68	4.39 to 58.388	2.886 to 28.458
Reflections collected	25054	42795	27676
Independent reflections	4168	4745	4000
Data/restraints/parameters	4168/0/223	4745/0/230	4000/1/214
Goodness-of-fit on F <sup>2</sup>	1.027	1.048	1.062
Final R indexes [ $I \geq 2\sigma(I)$ ]	R1 = 0.0524, wR2 = 0.1380	R1 = 0.0582, wR2 = 0.1731	R1 = 0.0496, wR2 = 0.1421
Final R indexes [all data]	R1 = 0.0729, wR2 = 0.1555	R1 = 0.0663, wR2 = 0.1826	R1 = 0.0692, wR2 = 0.1546
Largest diff. peak/hole / e Å <sup>-3</sup>	0.30/-0.31	0.76/-0.34	0.29/-0.33

**2.8.1.3 Table 2.7.** Intermolecular and intramolecular interactions in **2.1**

D-H...A	D-H (Å)	H...A (Å)	D...A (Å)	D-H...A (°)
C16-H16C...O1	0.961	2.702	3.380	128.08
C4-H4...O3	0.930	2.672	3.423	137.96
N3-H3A...O3	0.860	2.101	2.946	167.32
C12-H12C... $\pi$ (C1-C6)	0.960	3.341		
$\pi$ (C1-C6)... $\pi$ (C1-C6)		4.161		
<b>Intramolecular</b>				
C-H7...O2	0.980	2.276	2.859	117.15
C12-H12C...O4	0.960	2.208	2.919	129.95

### Crystal analysis of 2.1

The compound **2.1** chiral compound containing two asymmetric carbons was analysed by single-crystal X-ray diffraction (Figure 2.24). The summary of crystallographic information is listed in Table 2.6. The chiral compound crystallized in the triclinic space group *P-1* in the crystal lattice unit cell. The unit cell contains a pair of molecules in the crystals.



The overall structure of **2.1** exhibits a stacked arrangement of molecules that exhibit a combination of parallel-displaced  $\pi\cdots\pi$ , C-H $\cdots\pi$ , C-H $\cdots$ O, and C-H $\cdots$ N interactions (Table 2.7). Both rings are arranged in the AB pattern in the orthogonal pattern in crystal packing. The acute angle (dihedral angle) between the pyridone ring plane and the phenyl ring is 89.52°. The hydrogen-bonding network for compound **2.1** and crystal packing is in Figure 2.25. In compound **2.1**, pyridone and ester group oxygen and nitrogen are involved in weak interactions. In addition to intermolecular C-H $\cdots$ O interactions compound, **2.1** are also having intra-molecular C-H $\cdots$ O interactions. Apart from these interactions, bifurcated (three centers) hydrogen bonding at the oxygen atom is also observed, i.e., two C-H $\cdots$ O. This bifurcated hydrogen bonding assists the linear chain formation as well as interlayer connectivity. In an extensive hydrogen-bonding network, terminal carbonyl, oxygen & pyridone oxygen are involved in weak interaction, and non-traditional hydrogen bonds result in the R<sub>2</sub><sup>2</sup> (8), R<sub>6</sub><sup>4</sup> (16) & R<sub>2</sub><sup>2</sup> (20) graph-set notation. The C-H $\cdots$ O bond distances for bifurcated hydrogen bonding are 2.672 & 2.101 Å, and angles on hydrogen atoms are 137.96°, 167.32° while another C-H $\cdots$ O bond distance and angle on hydrogen atom are 2.702 Å and 128.08°, respectively (Table 2.7).

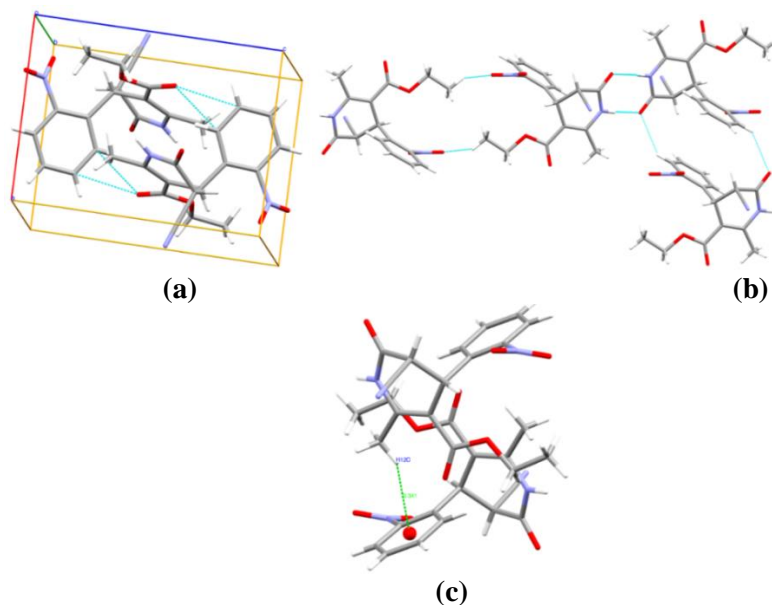


**Figure 2.25:** (a) Packing diagram of **2.1**, (b) C-H $\cdots$ O, and C-H $\cdots$ N interactions in **2.1**, (c) C-H $\cdots\pi$  interactions in **2.1**

#### 2.8.1.4. Hirshfeld surface analysis of **2.1**

The Hirshfeld surface mapped on  $d_{\text{norm}}$  of compound **2.1** is displayed in Figure 2.26 (a). The red color represents the more dominant non-covalent C-H...O interactions involved in the crystal structure (Figure 2.26 (a)).

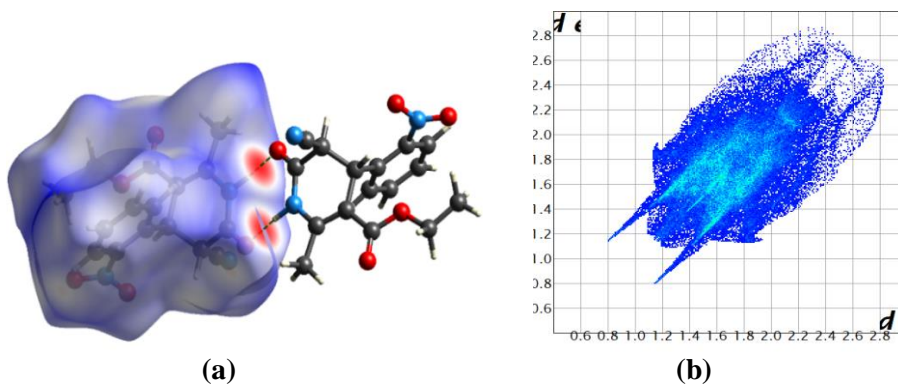


**Figure 2.26:** (a) Hirshfeld surface of compound **2.1**, (b) Two-dimensional fingerprint plot for compound **2.1**

The yellowish-red bin on the fingerprint plots is absent in **2.1**, which means the absence of weak  $\pi\cdots\pi$  stacking in the crystal structure (Figure 2.26 (b)). The spoke-like pattern in the fingerprint plots of **2.1** represents the C-H...O interactions in the crystal lattice in the region of  $d_i + d_e = 2.00\text{-}2.9\text{\AA}$  (Figure 2.26 (b)). The C-H... $\pi$  interactions in **2.1** can be seen as a pair of unique blue-colored wings in the region of  $d_i + d_e = 3.0\text{-}3.6\text{\AA}$  (Figure 2.26 (b)). The C-H...N pair of contacts is also reflected as two characteristic wings occupied in the  $d_i + d_e = 3.2\text{-}3.4\text{\AA}$  in **2.1**.

The fingerprint analysis of compound **2.1** shows the percentage contribution of intermolecular interactions and those H-H 35.8 %, C-C 2.0%, C-N 1.8 %, O-H 30.7 %, C-H 10.6%, N-H 11.2%, N-N 1.9%, C-O 2.2%, O-O 1.7%, and N-O 2.1%, (Figure 2.26 (b)). The weak interaction of **2.1** is shown in Figure 2.27 (a) and (b).

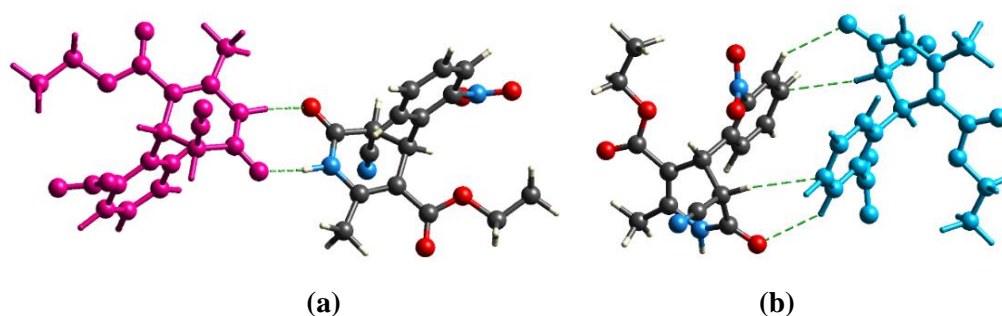


**Figure 2.27:** (a) Non-covalent interactions forming  $R_2^2(8)$ , (b) N-H...O, CH... $\pi$  interactions in **2.1**

The absence of green colored flat regions in the curvedness plot provided the information of absence of  $\pi$ ... $\pi$  stacking interaction in the crystal packing in Figure 2.28 (a) and (b). In the Shape index plots of compound **2.1**, the red and blue colored triangles on the surface of rings of the molecule are also missing, which means the absence of  $\pi$ ... $\pi$  stacking interaction in the crystal packing (Figure 2.28 (c) and (d)). The yellowish-red colored concave regions on the Hirshfeld surface of compound **2.1** represents the weak intermolecular interactions in the crystal packing (Figure 2.28 (c) and (d)).

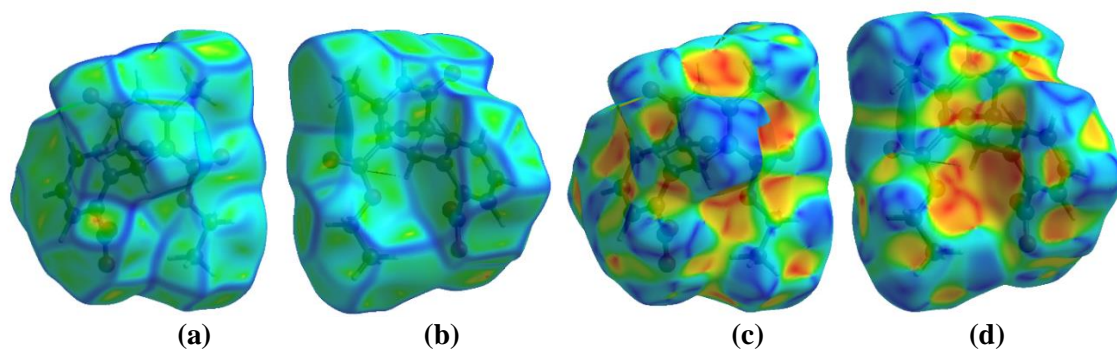


**Figure 2.28:** (a) and (b) Curvedness both side view of compound **2.1**, (c) and (d) Shape index both side view of compound **2.1**.

### 2.8.1.5. X-ray crystal structure of 2.2

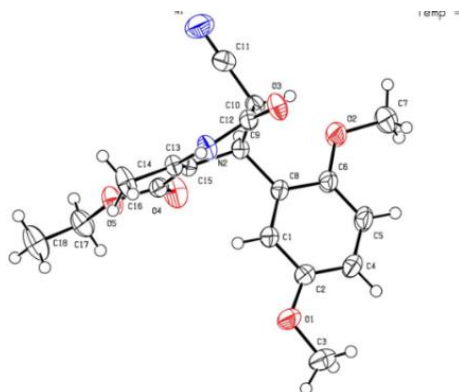


Figure 2.29: ORTEP diagram of 2.2

### 2.8.1.6 Table 2.8: Intermolecular and intramolecular interactions in 2.2

D-H...A	D-H (Å)	H...A (Å)	D...A (Å)	D-H...A (°)
C1-H1C...O2	0.960	2.619	3.561	166.97
C13-H13C...O2	0.962	2.678	3.557	152.11
C14-H14...O0AA	0.954	2.540	3.338	141.29
C11-H11...N5	0.930	2.706	3.470	139.97
N4-H4...O1AA	0.991	1.883	2.860	168.30
C10-H10... $\pi$ (C6-C12)	0.930	3.510		
C13-H13A... $\pi$ (C6-C12)	0.962	3.306		
N5... $\pi$ (C6-C12)		3.763		
<b>Intramolecular</b>				
C17-H17B...O0aa	0.961	2.138	2.845	129.24

### Crystal analysis of 2.2

The compound **2.2** containing two asymmetric carbons was analysed by single-crystal X-ray diffraction (Figure 2.29). The summary of crystallographic information is listed in Table 2.6. The chiral compound crystallized in the triclinic space group *P*-1 in the crystal lattice unit cell. The unit cell contains a pair of molecules in the crystals.

The overall structure of **2.2** exhibits a stacked arrangement of molecules that exhibit a combination of parallel-displaced  $\pi$ ... $\pi$ , C-H... $\pi$ , C-H...O, and N-H...O

interactions (Table 2.8). Both rings are arranged in the AB pattern in the orthogonal design in crystal packing. The acute angle (dihedral angle) between the pyridone ring plane and the phenyl ring is  $87.61^\circ$ . The hydrogen-bonding network for compound **2.2** and crystal packing is in Figure 2.30. In addition to intermolecular C-H...O interactions compound, **2.2** are also having intra-molecular C-H...O interactions. The distance for C-H... $\pi$  interaction is  $3.034 \text{ \AA}$  (Table 2.8). Apart from these interactions, trifurcated (four centers) hydrogen bonding at the oxygen atom is also observed, i.e., two C-H...O. This trifurcated hydrogen bonding assists the linear chain formation as well as interlayer connectivity. In an extensive hydrogen-bonding network, terminal carbonyl, oxygen & pyridone oxygen are involved in weak interaction, and non-traditional hydrogen bond results in the  $R_2^2(8)$ ,  $R_3^2(10)$ ,  $R_2^2(18)$  &  $R_2^2(22)$  graph-set notation in which C-H...O interactions are involved. The H...O bond distances for trifurcated hydrogen bonding are  $2.028$ ,  $2.590$  &  $2.699 \text{ \AA}$ , and angles on hydrogen atoms are  $172.86^\circ$ ,  $163.89^\circ$ ,  $139.93^\circ$  while another C-H...O bond distance and angle on hydrogen atom are  $2.627$ ,  $2.641 \text{ \AA}$ , and  $161.75^\circ$ ,  $153.86^\circ$  respectively (Table 2.8) (Figure 2.30).

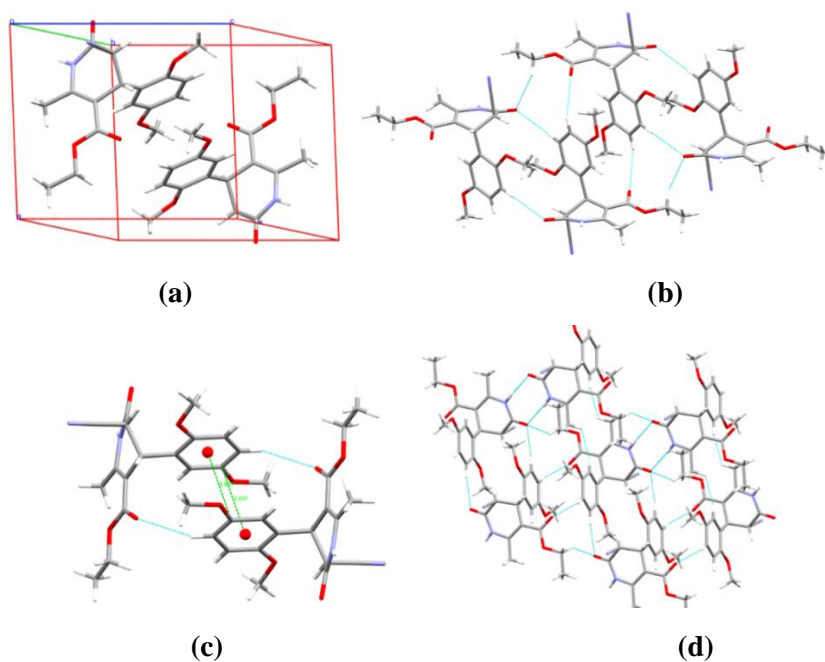


**Figure 2.30:** (a) Packing diagram, (b), (c) and (d) represents the C-H... $\pi$ , C-H...O, and N-H...O interaction in **2.2**

### 2.8.1.7. Hirshfeld surface analysis of 2.2

The Hirshfeld surface mapped on  $d_{\text{norm}}$  of compound **2.2** is displayed in Figure 2.31 (a). The red color represents the more dominant non-covalent C-H...O interactions involved in the crystal structure (Figure 2.31 (a)).

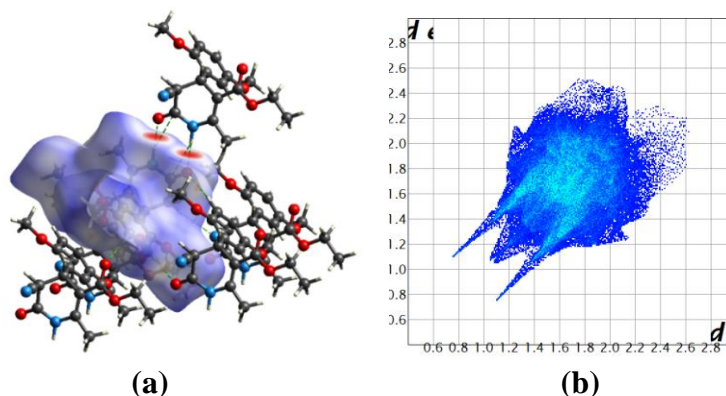


**Figure 2.31:** (a) Hirshfeld surface of compound **2.2**, (b) Two-dimensional fingerprint plot for compound **2.2**

The fingerprint analysis of compound **2.2** shows the percentage contribution of intermolecular interactions and those H-H 46.4 %, C-C 1.7%, O-H 25.0%, C-H 11.7%, N-H 13.3%, and other interactions are less than 1.0% (Figure 2.31 (b)). The calculated weak interactions of the **2.2** compound are shown in Figures 2.32.

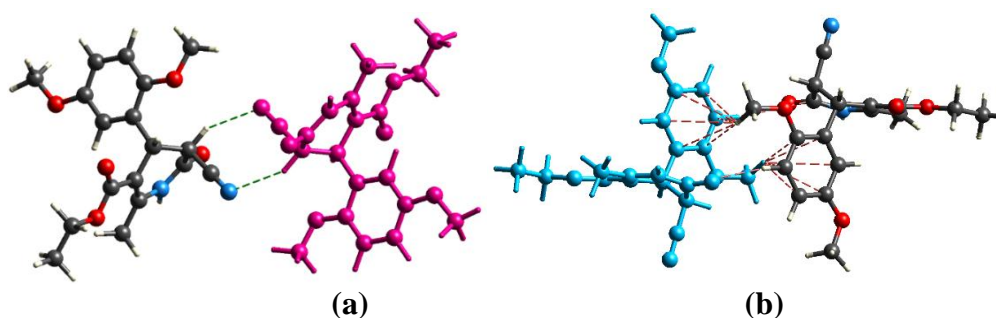


**Figure 2.32:** (a) Weak hydrogen bonds interactions of **2.2**, (b) CH... $\pi$  interactions in weak interactions calculations of **2.2**

The absence of green colored flat regions in the curvedness plot provided the information of absence of  $\pi$ ... $\pi$  stacking interaction in the crystal packing in Figure 2.33 (a) and (b). In the Shape index plots of compound **2.2**, the red and blue colored triangles



on the surface of rings of the molecule are also missing, which means the absence of  $\pi\cdots\pi$  stacking interaction in the crystal packing (Figure 2.33 (c) and (d)). The yellowish-red colored concave regions on the Hirshfeld surface of compound **2.2** represent weak intermolecular interactions in the crystal packing.

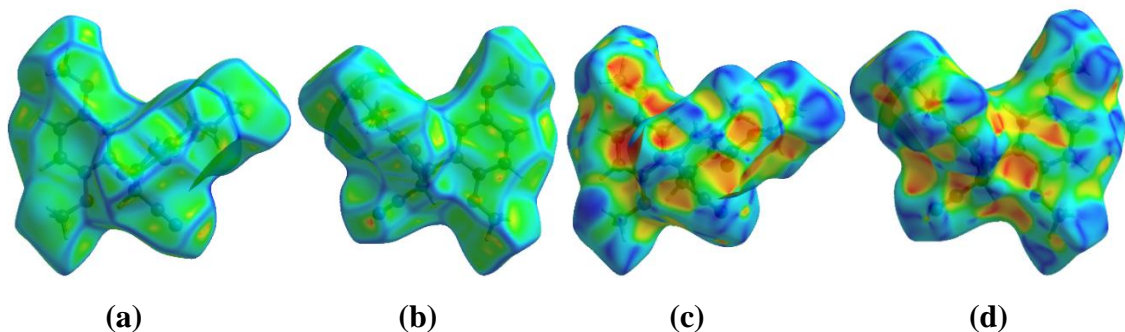


**Figure 2.33:** (a) and (b) Curvedness both side view of compound **2.2**, (c) and (d) Shape index both side view of compound **2.2**.

#### 2.8.1.8. X-Ray Crystal Structure of **2.3**

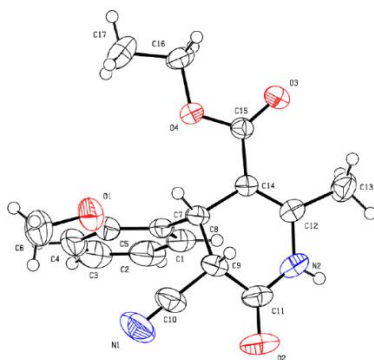


**Figure 2.34:** ORTEP diagram of **2.3**

#### 2.8.1.9. Table 2.9. Intermolecular and intramolecular interactions in **2.3**

D-H...A	D-H (Å)	H...A (Å)	D...A (Å)	D-H...A (°)
C17-H17B...O2	0.960	2.670	3.320	125.45
C13-H13C...O2	0.960	2.604	3.440	145.78
C9-H9...O3	0.980	2.380	3.231	144.85
C1-H1...N1	0.930	2.765	3.471	133.38
C4-H4...O2	0.930	3.286	3.626	104.05
N2-H2A...N1	0.787	3.296	3.587	105.45
C19-H19B...C8	1.044	2.870	3.901	169.56

C16-H16A...O2	0.960	3.073	3.982	139.82
C8-H8...O3	0.980	3.012	3.381	103.71
C13-H13B...O4	0.960	3.012	3.719	103.71
C13-H13A... $\pi$ (C3,C4,C5,C7,C1,C2)	0.960	3.250	4.145	
N2-H2A... $\pi$ (C3,C4,C5,C7,C1,C2)	0.787	2.986	3.762	
<b>Intramolecular</b>				
C8-H8...O4	0.980	2.335	2.652	
C8-H8...O1	0.980	2.318	2.744	
C6-H6A...N1	0.960	3.236	3.643	

### Crystal analysis of **2.3**

The compound **2.3** chiral compound containing two asymmetric carbons was analysed by single-crystal X-ray diffraction (Figure 2.34). Compound **2.3** was crystallized in hexane: ethyl acetate (90:10) solution at room temperature by a slow evaporation method. The perspective view of compound **2.3** ORTEP diagram at a 50% probability along (010) and packing diagram of compound **2.3** views is shown in Figure 2.34 and 2.35 (a), respectively. The summary of crystallographic information is listed in Table 2.6. The chiral compound crystallized in the monoclinic space group P 1 2<sub>1</sub>/n 1 in the crystal lattice unit cell. The unit cell contains a pair of molecules in the crystals.

The overall structure of **2.3** exhibits a stacked arrangement of molecules that exhibit a combination of parallel-displaced  $\pi\cdots\pi$ , C-H... $\pi$ , C-H...O, and C-H...N interactions (Table 2.9). In **2.3**, C-H...O and C-H...N interactions play a vital role in forming the self-assembly of the molecule. Intramolecular C-H...O interactions are also supporting the folded pattern of the crystal packing of 2.335 Å & 2.318 Å in the system (Figure 2.35). In addition to C-H...O interactions in the extended structure of compound **2.3** are also having intermolecular C-H... $\pi$  interactions in the crystal packing between C13-H13A and  $\pi$ -electrons of the ring of an adjacent molecule with the distance of 3.250 Å (Table 2.9) (Figure 2.35).



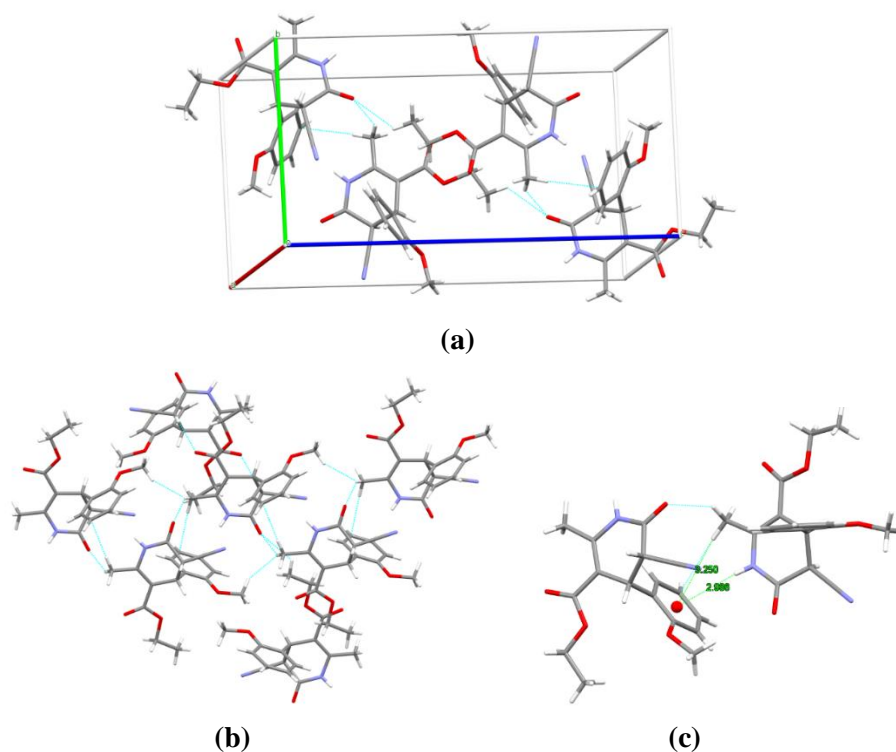


**Figure 2.35:** (a) Packing diagram of **2.3**, (b) C-H...O, N-H...O, C-H...N interactions in **2.3** and (c) C-H... $\pi$  interactions in **2.3**

#### 2.8.1.10. Hirshfeld surface analysis of **2.3**

The Hirshfeld surface mapped on  $d_{\text{norm}}$  of compound **2.3** is displayed in Figure 2.36 (a). The red color represents the more dominant non-covalent C-H...O interactions involved in the crystal structure (Figure 2.36 (a)).

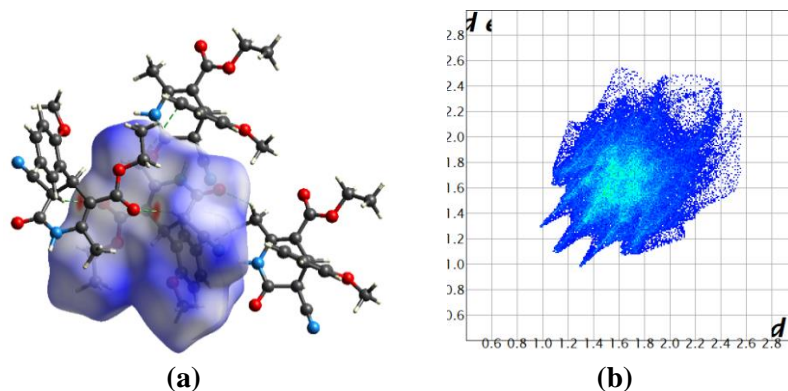


**Figure 2.36:** (a) Hirshfeld surface of compound **2.3**, (b) Two-dimensional fingerprint plot for compound **2.3**

The fingerprint analysis of compound **2.3** shows the percentage contribution of intermolecular interactions and that C-H 15.4 %, H-H 48.8%, N-H 13.9%, O-H 20.6%, and other interactions are less than 1.0% (Figure 2.36 (b)). The yellowish-red bin on the fingerprint plots is absent in compound **2.3**, which means the absence of  $\pi\cdots\pi$  stacking in the crystal structure (Figure 2.36 (b)). The spoke-like pattern in the fingerprint plots of **2.3** represents the C-H...O interactions in the crystal lattice in the region of  $d_i + d_e = 2.30\text{--}2.9\text{\AA}$  (Figure 2.36 (b)). The C-H... $\pi$  interactions in **2.3** can be seen as a pair of unique blue-colored wings in the region of  $d_i + d_e = 2.8\text{--}3.6\text{\AA}$  (Figure 2.36 (b)). The C-H...N pair of contacts is also reflected as two characteristic wings occupied in the  $d_i + d_e = 3.2\text{--}3.4\text{\AA}$  in **2.3**.

The Hirshfeld weak interactions calculation also supports the presence of weak non-covalent intermolecular interactions as in crystal packing, where C-H... $\pi$  interactions, interactions, C-H...N, and C-H...O interactions of compound **2.3** in the crystal packing structure is in Figure 2.37.

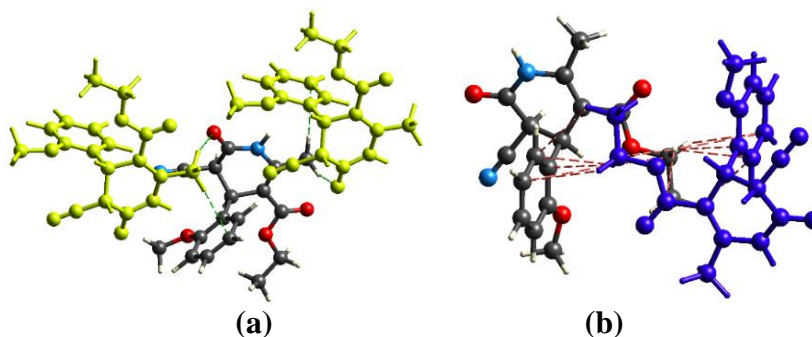


**Figure 2.37:** (a) C-H...O and C-H...H interactions, and (b) C-H... $\pi$  interactions in weak interactions calculations of **2.3**

The absence of green colored flat regions in the curvedness plot provided the information of absence of  $\pi\cdots\pi$  stacking interaction in the crystal packing in Figure 2.38 (a) and (b). In the Shape index plots of compound **2.3**, the red and blue colored triangles on the surface of rings of the molecule are also missing, which means the absence of  $\pi\cdots\pi$  stacking interaction in the crystal packing (Figure 2.38 (c) and (d)). The yellowish-

red colored concave regions on the Hirshfeld surface of compound **2.3** represents the weak intermolecular interactions in the crystal packing.

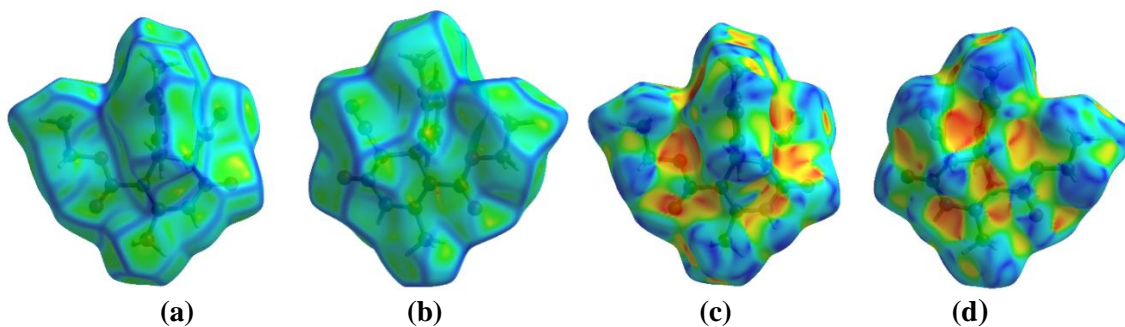


**Figure 2.38:** (a) and (b) Curvedness both side view of compound **2.3**, (c) and (d) Shape index both side view of compound **2.3**.

#### 2.8.1.11. X-Ray Crystal Structure of **2.4**

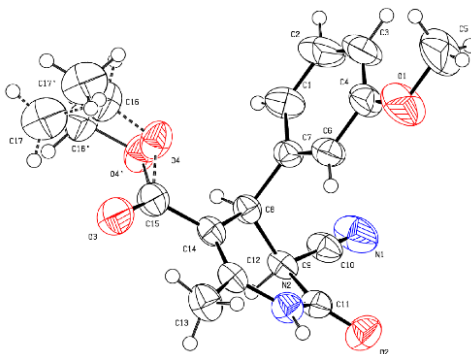


**Figure 2.39:** ORTEP diagram of **2.4**

#### 2.8.1.12. Table 2.10. Crystal data of compounds of **2.4**, **2.5** and **2.6**

Compound	<b>2.4</b>	<b>2.5</b>	<b>2.6</b>
Identification code	1937283	2062964	2062955
Empirical formula	C <sub>17</sub> H <sub>18</sub> N <sub>2</sub> O <sub>4</sub>	C <sub>16</sub> H <sub>15</sub> ClN <sub>2</sub> O <sub>3</sub>	C <sub>16</sub> H <sub>14</sub> N <sub>2</sub> O <sub>3</sub>
Formula weight	314.33	318.76	282.29
Temperature(K)	296.15	296.15	296.15
Crystal system	monoclinic	monoclinic	monoclinic
Space group	<i>P2<sub>1</sub>/c</i>	<i>P2<sub>1</sub>/c</i>	<i>P2<sub>1</sub>/c</i>
a(Å)	13.3858(17)	30.565(3)	13.4922(18)
b(Å)	13.1141(16)	12.3858(8)	7.4528(11)
c(Å)	9.3148(11)	9.1055(6)	14.2574(19)
α(°)	90	90	90
β(°)	93.101(4)	107.079(8)	95.621(8)
γ(°)	90	90	90
Volume(Å <sup>3</sup> )	1632.8(3)	3295.1(4)	1426.8(3)

Z	4	2	4
$\rho$ (g/cm <sup>3</sup> )	1.279	1.2850	1.314
$\mu$ (mm <sup>-1</sup> )	0.092	2.172	0.092
F(000)	664.0	1335.0023	592.0
Crystal size(mm <sup>3</sup> )	0.23 × 0.18 × 0.14	0.32 × 0.13 × 0.9	0.21 × 0.17 × 0.14
Radiation	MoK $\alpha$ ( $\lambda$ = 0.71073)	MoK $\alpha$ ( $\lambda$ = 0.71073)	MoK $\alpha$ ( $\lambda$ = 0.71073)
2 $\theta$ range for data collection(°)	4.352 to 58.46	3.02 to 55.16	3.034 to 57.752
Reflections collected	21030	14949	28190
Independent reflections	4409	2067	3682
Data/restraints/parameters	4409/2/228	2067/0/259	3682/0/192
Goodness-of-fit on F <sup>2</sup>	0.949	1.0422	1.025
Final R indexes [ $I \geq 2\sigma(I)$ ]	R1 = 0.0666, wR2 = 0.1920	R1 = 0.0501, wR2 = 0.1361	R1 = 0.0491, wR2 = 0.1153
Final R indexes [all data]	R1 = 0.0897, wR2 = 0.2190	R1 = 0.0653, wR2 = 0.1515	R1 = 0.0863, wR2 = 0.1377
Largest diff. peak/hole / e $\text{\AA}$	0.53/-0.37	0.46/-0.41	0.37/-0.24

### 2.8.1.13. Table 2.11. Intermolecular and intramolecular interactions in 2.4

D-H...A	D-H ( $\text{\AA}$ )	H...A ( $\text{\AA}$ )	D...A ( $\text{\AA}$ )	D-H...A ( $^\circ$ )
C9-H9...O3	0.980	2.427	3.267	143.44
C13-H13C...O3	0.960	2.580	3.458	152.08
N2-H2...O2	0.834	2.166	2.995	172.93
C5-H5B... $\pi$ (C1-C4, C6, C7)	0.960	3.020		
C13-H13C... $\pi$ (C1-C4, C6, C7)	0.960	3.455		
C2-H2A... $\pi$ (C1-C4, C6, C7)	0.960	3.810		
<b>Intramolecular</b>				
C13-H13B...O3	0.960	2.148	2.847	128.54

### Crystal analysis of 2.4

The compound **2.4** containing two asymmetric centres was analysed by single-crystal X-ray diffraction (Figure 2.39). The summary of crystallographic information is listed in Table 2.10. The chiral compound crystallized in the triclinic space group  $P2_1/c$  in the crystal lattice unit cell. The unit cell contains four molecules in the crystal lattice.

The overall structure of **2.4** exhibits a stacked arrangement of molecules that exhibit a combination of parallel-displaced C-H... $\pi$ , C-H...O, and N-H...O interactions (Table 2.11). The acute angle (dihedral angle) between the pyridone ring plane and the phenyl ring is 88.93°. Both rings are arranged in the AABB pattern in crystal packing. The hydrogen-bonding network for compound **2.4** and crystal packing is in Figure 2.40.

In addition to intermolecular C-H...O interactions compound, **2.4** are also having intramolecular C-H...O interactions. The stacking distance for C-H... $\pi$  are 3.020, 3.455, 3.810 Å (Table 2.11). Apart from these interactions, bifurcated (three centers) hydrogen bonding at the oxygen atom is also observed, i.e., two C-H...O. This bifurcated hydrogen bonding assists the linear chain formation as well as interlayer connectivity. In an extensive hydrogen-bonding network, terminal carbonyl, oxygen & pyridone oxygen are involved in weak interaction, and non-traditional hydrogen bond results in the  $R_2^2(8)$ ,  $R_2^2(12)$ , &  $R_4^2(16)$  graph-set notation in which C-H...O & N-H...O interactions are involved. The H...O bond distances for bifurcated hydrogen bonding are 2.427 & 2.580 Å, and angles on hydrogen atoms are 143.44°, 152.08° while another N-H...O bond distance and angle on hydrogen atom are 2.166 Å and 172.93°, respectively (Table 2.11) and (Figure 2.40).

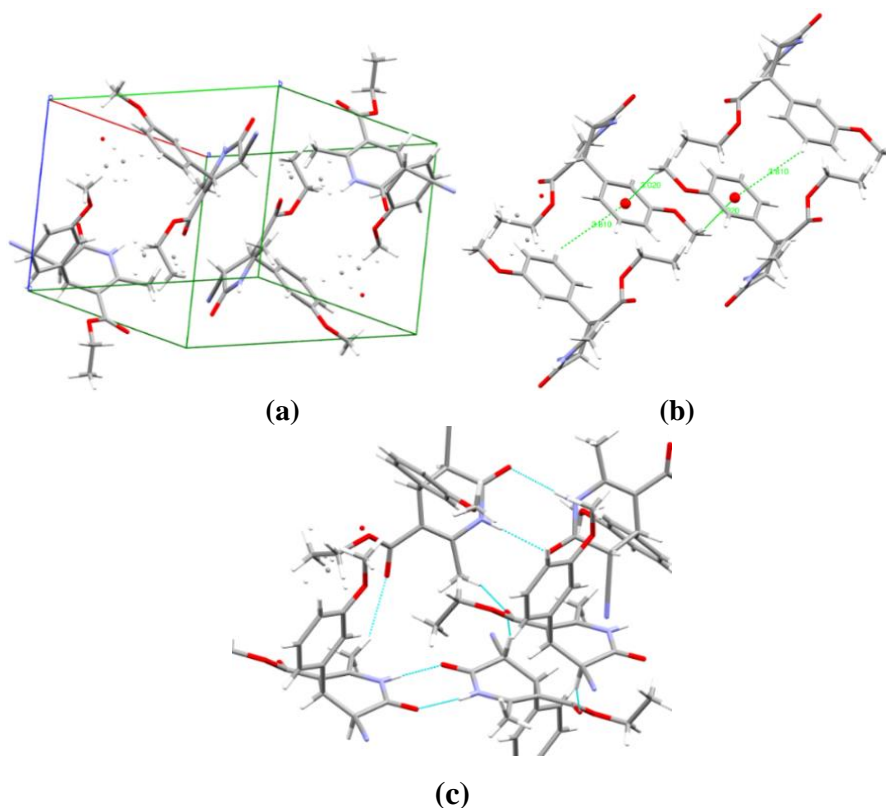


**Figure 2.40:** (a) Packing diagram of **2.4**, (b) C-H... $\pi$  interactions in **2.4** and (c) C-H...O, and N-H...O interactions in **2.4**

#### 2.8.1.14. Hirshfeld surface analysis of 2.4

The Hirshfeld surface mapped on  $d_{\text{norm}}$  of compound **2.4** is displayed in Figure 2.41 (a). The red color represents the more dominant non-covalent C-H...O interactions involved in the crystal structure (Figure 2.41 (a)).

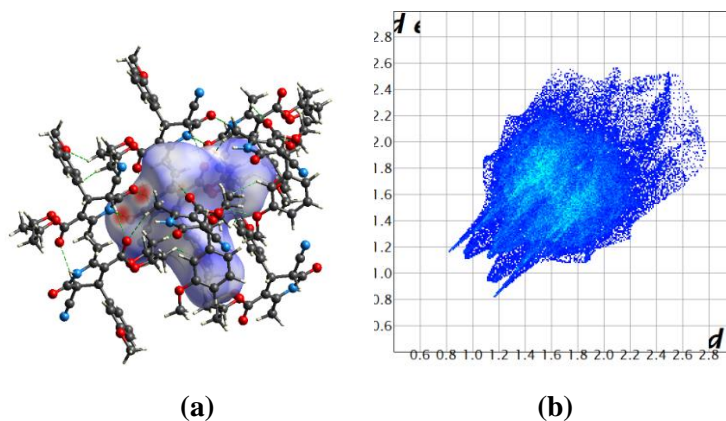


**Figure 2.41:** (a) Hirshfeld surface of compound **2.4**, (b) Two-dimensional fingerprint plot for compound **2.4**

The fingerprint analysis of compound **2.4** shows the percentage contribution of intermolecular interactions and those H-H 46.3 %, O-H 23.3%, C-H 13.4%, N-H 14.7%, and other interactions are less than 1.0% (Figure 2.41 (b)). The calculated weak interactions of the **2.4** compound are shown in 2.42.

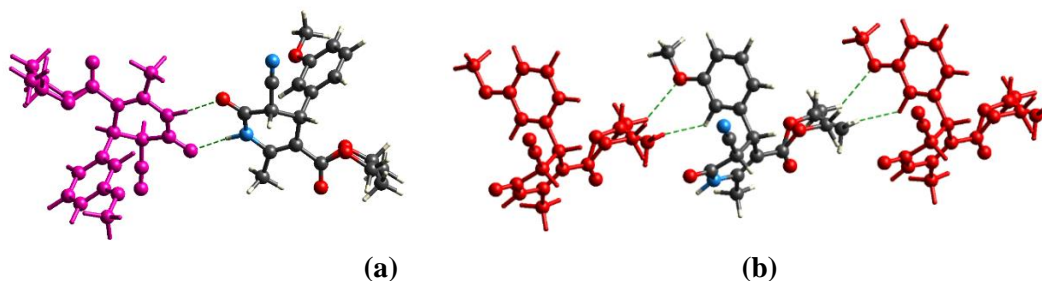


**Figure 2.42:** (a) Non-covalent interactions forming  $R_2^2(8)$ , (b) CH...O interactions in weak interactions calculations of **2.4**

The absence of green colored flat regions in the curvedness plot provided the information of absence of  $\pi$ ... $\pi$  stacking interaction in the crystal packing in Figure 2.43 (a) and (b). In the Shape index plots of compound **2.4**, the red and blue colored triangles on the surface of rings of the molecule are also missing, which means the absence of

$\pi$ ... $\pi$  stacking interaction in the crystal packing (Figure 2.43 (c) and (d)). The yellowish-red colored concave regions on the Hirshfeld surface of compound **2.4** represent weak intermolecular interactions in the crystal packing.

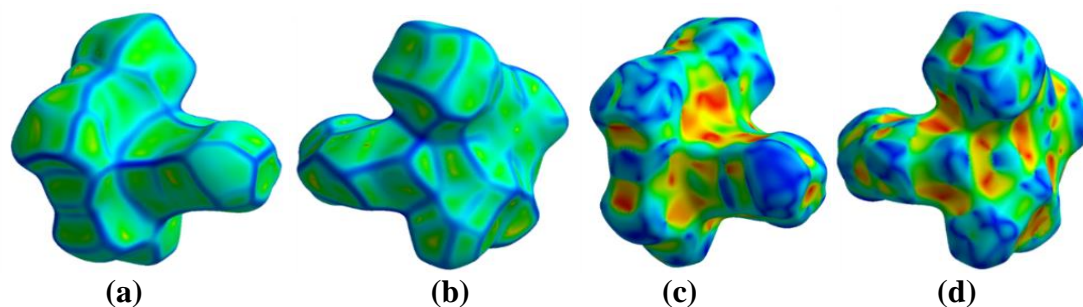


**Figure 2.43:** (a) and (b) Curvedness both side view of compound **2.4**, (c) and (d) Shape index both side view of compound **2.4**.

#### 2.8.1.15. X-ray crystal structure of **2.5**

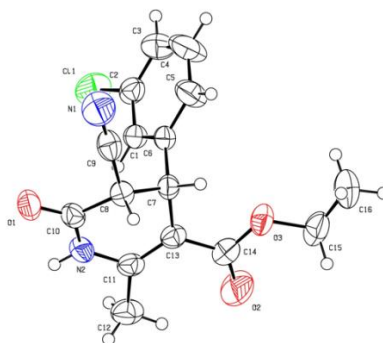


**Figure 2.44:** ORTEP diagram of **2.5**

#### 2.8.1.16. Table 2.12. Intermolecular and intramolecular interactions in **2.5**

D-H...A	D-H (Å)	H...A (Å)	D...A (Å)	D-H...A (°)
C12-H12C...O2	0.960	2.429	3.353	161.32
N2-H2...O1	0.846	2.086	2.920	168.39
C15-H15B...O1	0.970	2.718	3.488	136.75
C7-H7...N1	0.979	2.730	3.677	162.55
C16-H16A... $\pi$ (C1- C6)	0.970	3.054		
C11... $\pi$ (C1-C6)		3.545		
<b>Intramolecular</b>				
C15-H15B...O2	0.970	2.635	2.760	81.85
C12-H12B...O2	0.960	2.142	2.873	131.84

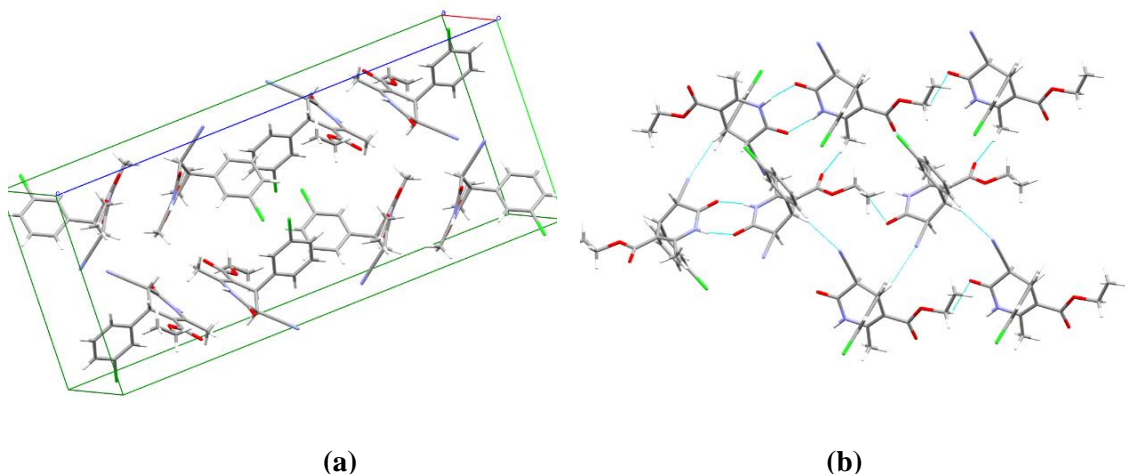


### Crystal analysis of **2.5**

The compound **2.5** chiral compound containing two asymmetric carbons was analysed by single-crystal X-ray diffraction (Figure 2.44). The summary of crystallographic information is listed in Table 2.10. The chiral compound crystallized in the orthorhombic space group  $P2_1/c$  in the crystal lattice unit cell. The unit cell contains eight molecules in the crystals.

The overall structure of **2.5** exhibits a stacked arrangement of molecules that exhibit a combination of parallel-displaced lone pair... $\pi$ , C-H... $\pi$ , C-H...O, and C-H...N interactions (Table 2.12). Both rings are arranged in the ABAB pattern in the orthogonal pattern in crystal packing. The acute angle (dihedral angle) between the pyridone ring plane and the phenyl ring is  $89.13^\circ$ . The hydrogen-bonding network for compound **2.5** and crystal packing is in Figure 2.45. In compound **2.5**, pyridone and ester group oxygen and nitrogen are involved in weak interactions. In addition to intermolecular C-H...O interactions compound, **2.5** are also having intra-molecular C-H...O interactions. The stacking distance for lone pair of Cl... $\pi$  is  $3.545 \text{ \AA}$  (Table 2.12), while for C-H... $\pi$  is  $3.054 \text{ \AA}$ . (Table 2.12). Apart from these interactions, bifurcated (three centers) hydrogen bonding at the oxygen atom is also observed, i.e., two C-H...O. This bifurcated hydrogen bonding assists the linear chain formation as well as interlayer connectivity. In an extensive hydrogen-bonding network, terminal carbonyl, oxygen & pyridone oxygen are involved in weak interaction, and non-traditional hydrogen bond results in the  $R_2^2(8)$  &  $R_3^3(17)$  graph-set notation in which C-H...O & N-H...O interactions are involved. The H...O bond distances for bifurcated hydrogen bonding are  $2.086$  &  $2.718 \text{ \AA}$ , and angles on hydrogen atoms are  $168.39^\circ$ ,  $136.75^\circ$  while another C-H...O and C-H...N bond distance and angle on hydrogen atoms are  $2.429$ ,  $2.730 \text{ \AA}$ , and  $161.32^\circ$ ,  $162.55^\circ$  respectively (Table 2.12) (Figure 2.45).

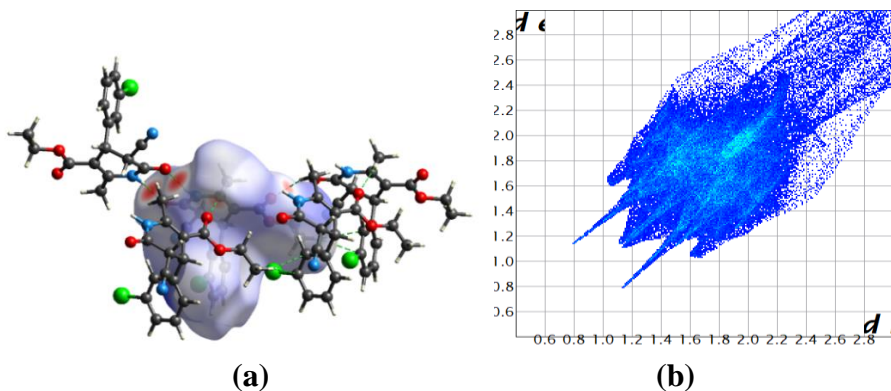




**Figure 2.45:** (a) Packing diagram of **2.5**, (b) Cl... $\pi$ , C-H... $\pi$ , C-H...O, and C-H...N interactions in **2.5**

#### 2.8.1.17. Hirshfeld surface analysis of **2.5**

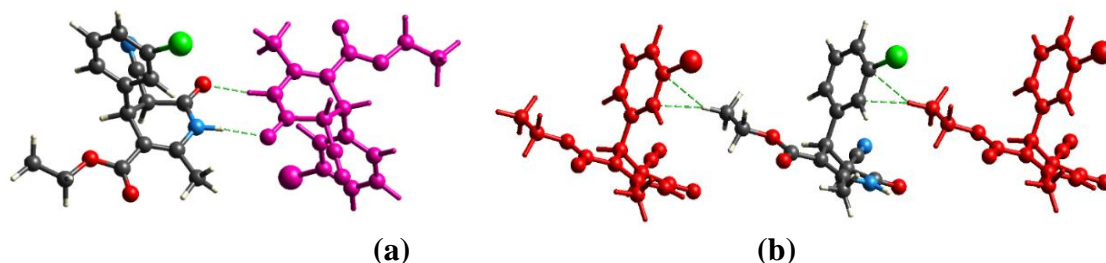
The Hirshfeld surface mapped on the  $d_{\text{norm}}$  of compound **2.5** is displayed in Figure 2.46 (a). The red color represents the more dominant non-covalent C-H...O interactions involved in the crystal structure (Figure 2.46 (a)).



**Figure 2.46:** (a) Hirshfeld surface of compound **2.5**, (b) Two-dimensional fingerprint plot for compound **2.5**

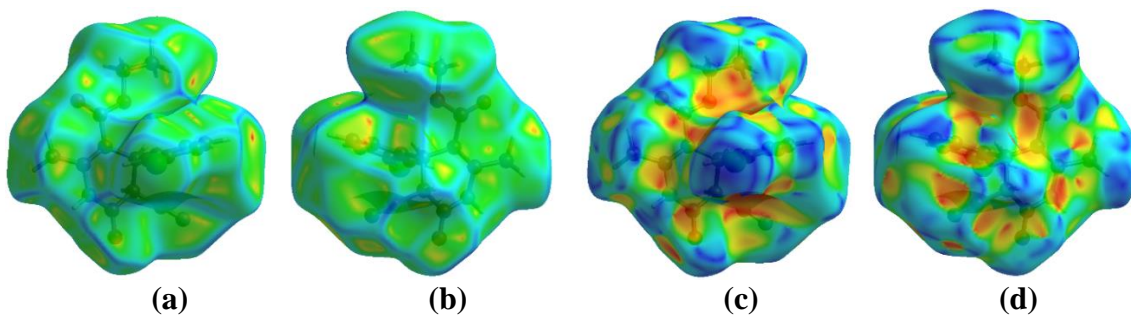
The fingerprint analysis of compound **2.5** shows the percentage contribution of intermolecular interactions and those H-H 36.5 %, Cl-C 5.5%, Cl-H 9.5%, Cl-O 1.0%, O-H 18.1%, C-H 11.4%, N-H 15.8%, and other interactions are less than 1.0% (Figure 2.46 (b)). The Hirshfeld calculated weak non-covalent interactions of **2.5** are shown in

Figure 2.47. Hirshfeld surface analysis also proved that compound **2.5** possesses lone pair... $\pi$  interactions. The C-H... $\pi$  interaction of compound **2.5** in weak interaction calculation is shown in Figure 2.47 (b).



**Figure 2.47:** (a) Non-covalent interactions forming  $R_2^2(8)$ , (b) C-H... $\pi$  interactions in **2.5**

The absence of green colored flat regions in the curvedness plot provided the information of absence of  $\pi$ ... $\pi$  stacking interaction in the crystal packing in Figure 2.48 (a) and (b). In the Shape index plots of compound **2.5**, the red and blue colored triangles on the surface of rings of the molecule are also missing, which means the absence of  $\pi$ ... $\pi$  stacking interaction in the crystal packing (Figure 2.48 (c) and (d)). The yellowish-red colored concave regions on the Hirshfeld surface of compound **2.5** represent weak intermolecular interactions in the crystal packing.



**Figure 2.48:** (a) and (b) Curvedness both side view of compound **2.5**, (c) and (d) Shape index both side view of compound **2.5**

### 2.8.1.18. X-ray crystal structure of 2.6

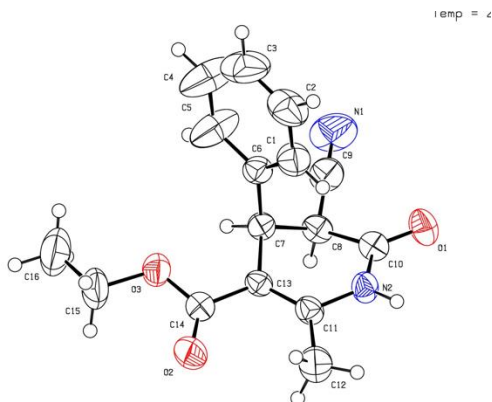


**Figure 2.49:** ORTEP diagram of **2.6**

### 2.8.1.19 Table 2.13. Intermolecular and intramolecular interactions in 2.6

D-H...A	D-H (Å)	H...A (Å)	D...A (Å)	D-H...A (°)
C12-H12B...O1	0.960	2.546	3.427	152.70
N2-H2...O1	0.858	2.102	2.954	172.19
C4-H4...O2	0.930	2.659	3.567	165.41
C8-H8...O2	0.980	2.385	3.143	133.65
C1-H1...N1	0.930	2.665	3.491	148.27
C17-H17A...O3	0.970	2.699	3.497	139.93
C4-H4...O4	0.930	2.641	3.500	153.86
C3-H3... $\pi$ (C1-C6)		3.071		
C16-H16A... $\pi$ (C1-C6)		3.189		
<b>Intramolecular</b>				
C14-H14C...O5	0.970	2.474	2.669	90.72
C12-H12C...O2	0.960	2.611	2.828	92.99
C12-H12C...O2	0.960	2.429	3.353	161.32

### Crystal analysis of 2.6

The compound **2.6** also containing two asymmetric carbons was analysed by single-crystal X-ray diffraction (Figure 2.49). The summary of crystallographic information is listed in Table 2.10. The chiral compound crystallized in the triclinic space group  $P2_1/c$  in the crystal lattice unit cell. The unit cell contains eighteen molecules in the crystal lattice.

The overall structure of **2.6** exhibits a stacked arrangement of molecules that exhibit a combination of parallel-displaced C-H... $\pi$ , C-H...O, and N-H...O interactions

(Table 2.13). The acute angle (dihedral angle) between the pyridone ring plane and the phenyl ring is  $88.93^\circ$ . The hydrogen-bonding network for compound **2.6** and crystal packing is in Figure 2.50. In addition to intermolecular C-H...O interactions compound, **2.6** are also having intra-molecular C-H...O interactions. The stacking distance for C-H... $\pi$  are 3.073, 3.189 Å (Table 2.13). Apart from these interactions, two bifurcated (three centers) hydrogen bonding at the oxygen atom is also observed, i.e., two C-H...O in each. This bifurcated hydrogen bonding assists the linear chain formation as well as interlayer connectivity. In an extensive hydrogen-bonding network, terminal carbonyl, oxygen & pyridone oxygen are involved in weak interaction, and non-traditional hydrogen bond results in the  $R_2^1(6)$ ,  $R_2^2(13)$ , &  $R_4^4(20)$  graph-set notation in which C-H...O & N-H...O interactions are involved. The H...O bond distances for bifurcated hydrogen bonding are 2.546, 2.102, 2.659 & 2.385 Å, and angles on hydrogen atoms are  $152.70^\circ$ ,  $172.19^\circ$ ,  $165.41^\circ$ ,  $133.65^\circ$  while another C-H...O bond distance and angle on hydrogen atom are 2.669 Å and  $139.93^\circ$  respectively (Table 2.13).

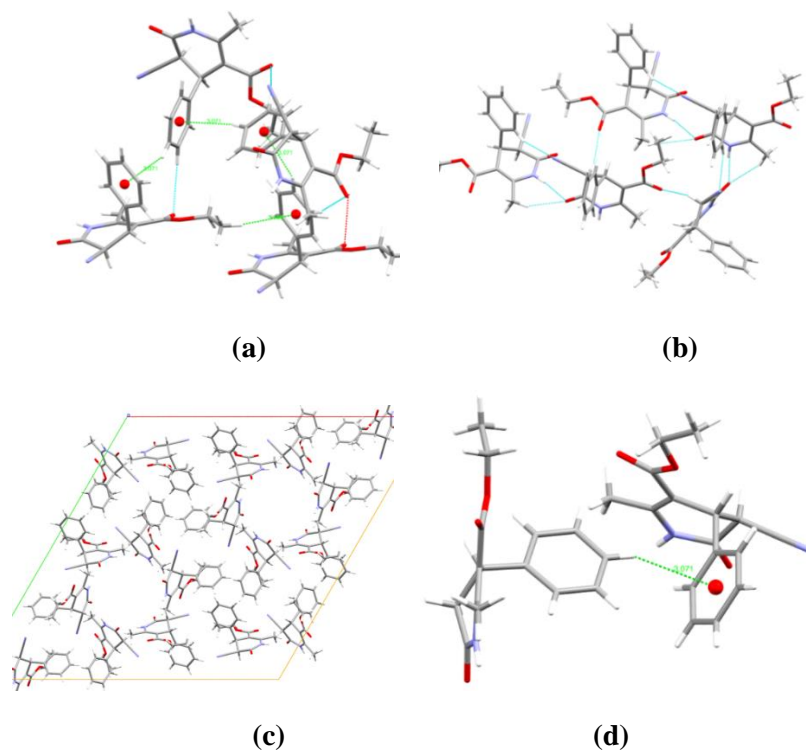


**Figure 2.50:** (a), (b), (c), and (d) C-H... $\pi$ , C-H...O, and N-H...O in interactions in **2.6**.

### 2.8.1.20. Hirshfeld surface analysis of 2.6

The Hirshfeld surface mapped on  $d_{\text{norm}}$  of compound **2.6** is displayed in Figure 2.51 (a). The red color represents the more dominant non-covalent C-H...O interactions involved in the crystal structure (Figure 2.51 (a)).

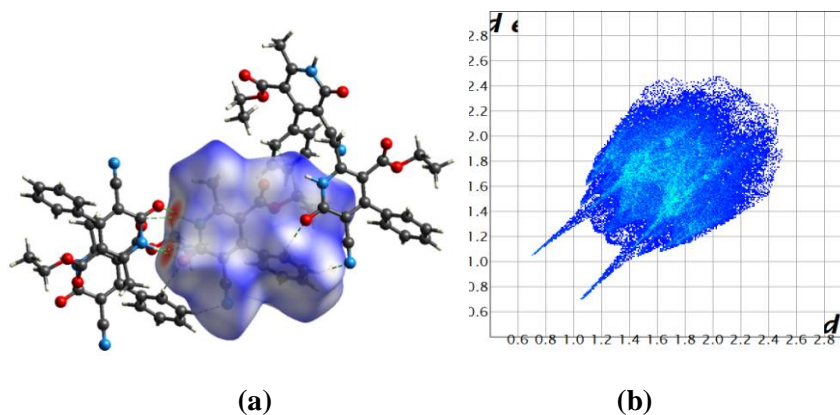


**Figure 2.51:** (a) Hirshfeld surface of compound **2.6**, (b) Two-dimensional fingerprint plot for compound **2.6**

The fingerprint analysis of compound **2.6** shows the percentage contribution of intermolecular interactions and those H-H 39.4%, C-N 2.3%, O-N 1.3%, O-O 1.0%, O-H 19.9%, C-H 18.5%, N-H 16.2%, and other interactions are less than 1.0% (Figure 2.51 (b)). All the Hirshfeld calculated weak non-covalent interactions of **2.6** are shown in Figure 2.52.

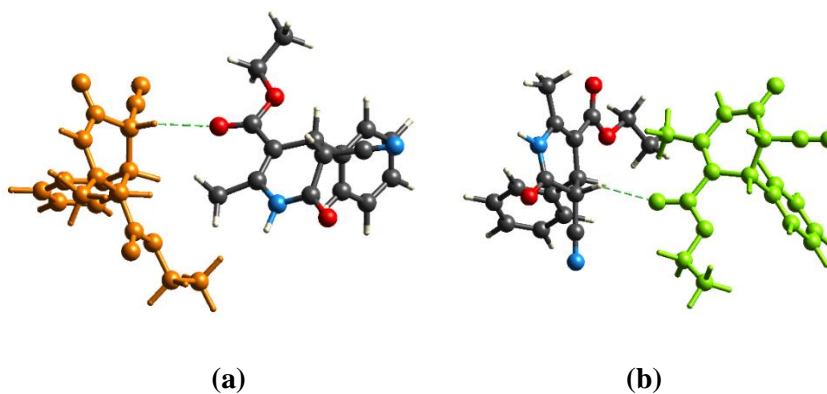


**Figure 2.52:** (a), and (b) C-H...O interactions in **2.6**

The absence of green colored flat regions in the curvedness plot provided the information of absence of  $\pi$ ... $\pi$  stacking interaction in the crystal packing in Figure 2.53

(a) and (b). In the Shape index plots of compound **2.6**, the red and blue colored triangles on the surface of rings of the molecule are also missing, which means the absence of  $\pi\cdots\pi$  stacking interaction in the crystal packing (Figure 2.53 (c) and (d)). The yellowish-red colored concave regions on the Hirshfeld surface of compound **2.6** represent weak intermolecular interactions in the crystal packing.

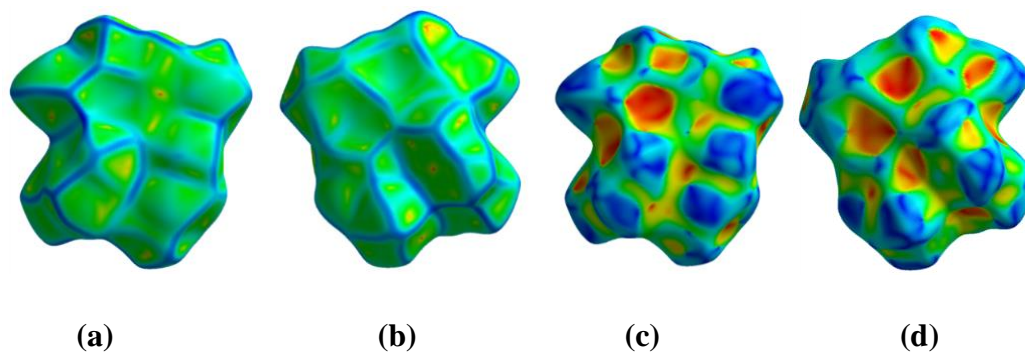


**Figure 2.53:** (a) and (b) Curvedness both side view of compound **2.6**, (c) and (d) Shape index both side view of compound **2.6**

#### 2.8.1.21. X-Ray Crystal Structure of **2.7**

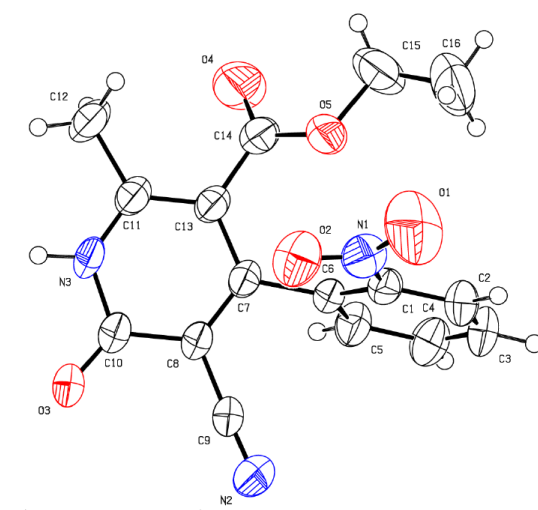


**Figure 2.54:** ORTEP diagram of **2.7**

**2.1.22. Table 2.14.** Crystal data of compounds **2.7**, **2.8** and **2.9**

Compound	2.7	2.8	2.9
Identification code	2062943	1937282	2062944
Empirical formula	C <sub>16</sub> H <sub>13</sub> N <sub>3</sub> O <sub>5</sub>	C <sub>17</sub> H <sub>16</sub> N <sub>2</sub> O <sub>4</sub>	C <sub>16</sub> H <sub>14</sub> N <sub>2</sub> O <sub>3</sub>
Formula weight	327.29	312.32	282.30
Temperature(K)	296.15	296.15	296.15
Crystal system	triclinic	triclinic	monoclinic
Space group	<i>P</i> -1	<i>P</i> -1	<i>P</i> 2 <sub>1</sub> / <i>c</i>
a(Å)	7.779(3)	7.6290(8)	13.4922(18)
b(Å)	7.878(3)	7.8979(8)	7.4528(11)
c(Å)	13.281(5)	13.2634(13)	14.2574(19)
α(°)	97.131(5)	96.566(3)	90
β(°)	90.174(5)	96.381(3)	95.621(8)
γ(°)	102.735(6)	97.410(3)	90
Volume(Å <sup>3</sup> )	787.4(5)	780.83(14)	1426.8(3)
Z	2	2	4
ρ (g/cm <sup>3</sup> )	1.380	1.328	1.3141
μ(mm <sup>-1</sup> )	0.105	0.096	0.092
F(000)	340.0	328.0	592.3089
Crystal size(mm <sup>3</sup> )	0.21 × 0.19 × 0.16	0.21 × 0.17 × 0.15	0.18 × 0.10 × 0.19
Radiation	MoKα (λ = 0.71073)	MoKα (λ = 0.71073)	MoKα (λ = 0.71073)
2θ range for data collection(°)	2.91 to 27.37	5.742 to 58.416	1.52 to 28.88
Reflections collected	13368	17292	28190
Independent reflections	3554	4189	3682
Data/restraints/parameters	3554/0/223	4189/0/211	3682/0/246
Goodness-of-fit on F <sup>2</sup>	0.994	1.058	1.0734
Final R indexes [I>=2σ (I)]	R1 = 0.0561, wR2 = 0.1604	R1 = 0.0482, wR2 = 0.1389	R1 = 0.0478, wR2 = 0.1093
Final R indexes [all data]	R1 = 0.0880, wR2 = 0.1808	R1 = 0.0580, wR2 = 0.1486	R1 = 0.0849, wR2 = 0.1336
Largest diff. peak/hole / e Å <sup>-3</sup>	0.45/-0.32	0.28/-0.26	0.28/-0.26

**2.8.1.23. Table 2.15.** Intermolecular and intramolecular interactions in **2.7**

D-H...A	D-H (Å)	H...A (Å)	D...A (Å)	D-H...A (°)
N3-H3...O3	0.883	1.917	2.790	169.75
N3-H3...OC10	0.883	2.772	3.390	161.69
C5-H5...O1	0.930	2.597	3.250	127.72
C12-H12B...O2	0.960	2.696	3.276	119.39
C15-H15B...O4	0.970	2.605	3.431	143.20
C3-H3A...H16B	0.960	2.338	3.035	128.99
C15-H15B...N3	0.970	3.691	4.478	140.05
C12-H12C...O5	0.960	3.160	3.661	114.26
C15-H15A...O3	0.970	3.247	4.084	145.47
C12-H12A...O4	0.960	3.773	4.048	99.78
C12-H12A...πCg(C10,C8,C7,C13,C11,N3)	0.960	2.899	3.821	
<b>Intramolecular</b>				
C16-H16B...O1	0.960	3.580	3.589	

C16-H16C...O1	0.960	2.839	3.589	
C12-H12C...N3	0.960	2.428	2.404	
C12-H12B...O4	0.960	2.661	2.874	
C16-H16B... $\pi$ Cg(C1-C6)	0.960	3.460	4.121	
O5... $\pi$ Cg(C1-C6)		3.448		

### Crystal analysis of **2.7**

The compound **2.7** chiral compound containing two asymmetric carbons was analysed by single-crystal X-ray diffraction (Figure 2.54). Compound **2.7** was crystallized in hexane: ethyl acetate (90:10) solution at room temperature by a slow evaporation method. The perspective view of compound **2.7** ORTEP diagram at a 50% probability along (010) and packing diagram of compound **2.7** views is shown in Figure 2.54 and 2.55 (a), respectively. The summary of crystallographic information is listed in Table 2.14. The chiral compound crystallized in the triclinic space group *P-1* in the crystal lattice unit cell. The unit cell contains a pair of molecules in the crystals.

The overall structure of **2.7** exhibits a stacked arrangement of molecules that exhibit a combination of parallel-displaced  $\pi\cdots\pi$ , C-H... $\pi$ , C-H...O, and C-H...N interactions (Table 2.15). Both rings are arranged in the AB pattern in the orthogonal pattern in crystal packing. The acute angle (dihedral angle) between the pyridone ring plane and the phenyl ring is 89.52°. The hydrogen-bonding network for compound **2.7** and crystal packing is in Figure 2.55. In compound **2.7**, pyridone and ester group oxygen and nitrogen are involved in weak interactions. In addition to the intermolecular C-H...O interactions compound, **2.7** are also having intra-molecular C-H...O interactions. Apart from these interactions, **2.7** also has intramolecular C-H...O and C-H...N interactions. Also, C-H... $\pi$  intermolecular interaction plays a vital role in strengthening the system **2.7** by the distance of 2.899 Å (Figure 2.55). Moreover, compound **2.7** also has one intramolecular C-H... $\pi$  interaction with the distance of 3.460 Å (Table 2.15).



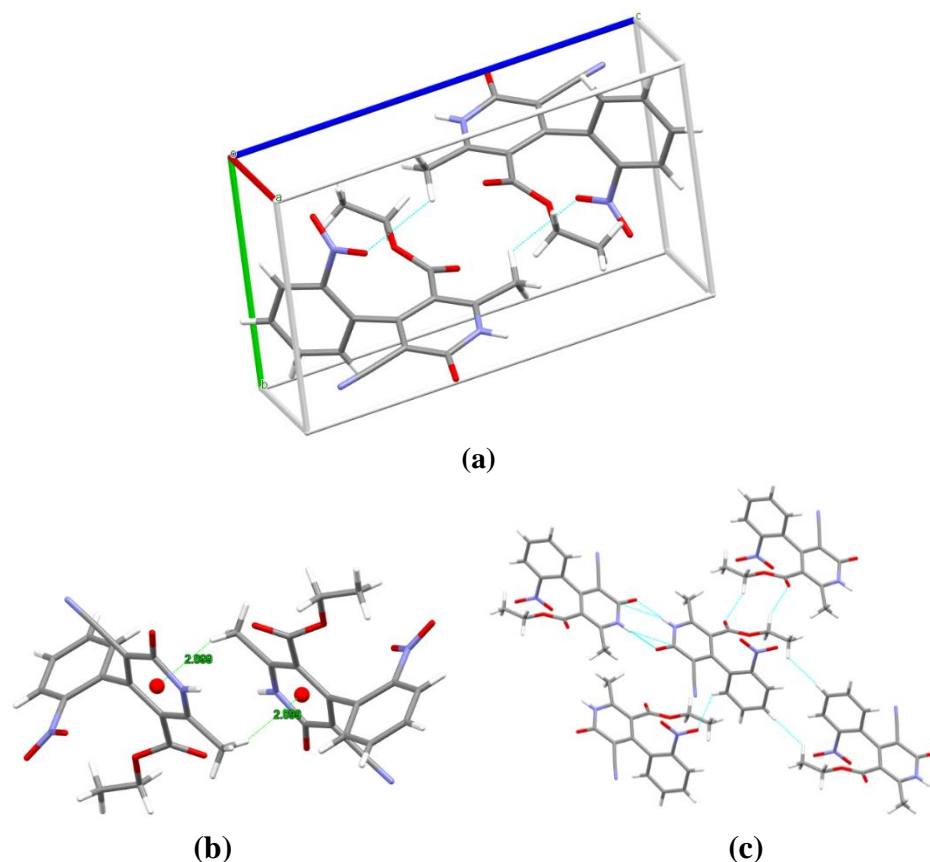


**Figure 2.55:** (a) Packing diagram of **2.7**, (b) C-H... $\pi$  interactions in **2.7**, and (c) C-H...O, N-H...O, and N-H...S interactions in **2.7**

#### 2.8.1.24. Hirshfeld surface analysis of **2.7**

The Hirshfeld surface mapped on  $d_{\text{norm}}$  of compound **2.7** is displayed in Figure 2.56 (a). The red color represents the more dominant non-covalent C-H...O interactions involved in the crystal structure (Figure 2.56 (a)).

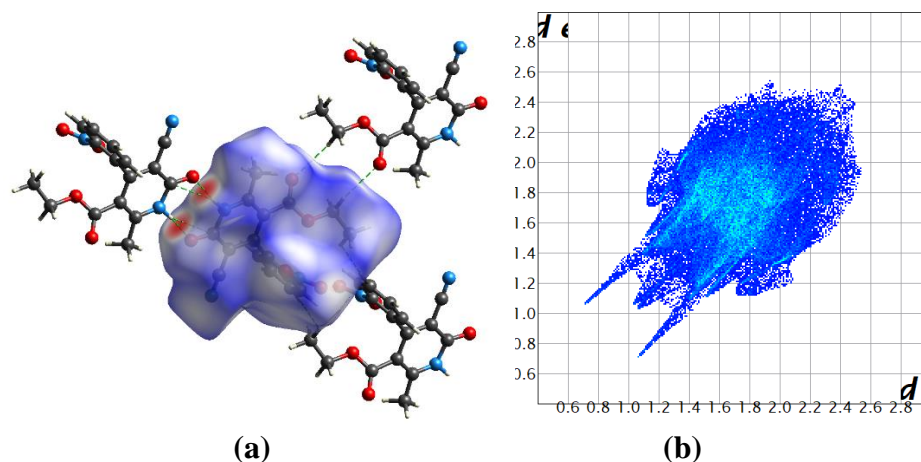


**Figure 2.56:** (a) Hirshfeld surface of compound **2.7**, (b) Two-dimensional fingerprint plot for compound **2.7**

The fingerprint analysis of compound **2.7** shows the percentage contribution of intermolecular interactions and those O...N 1.1%, O...C 2.9%, O...H 36.1%, N...C 1.8%, N...H 17.4%, C...H 14.0%, H...H 25.4%, and other interactions are less than 1.0% (Figure 2.56 (b)). A wing in the fingerprint plot indicates the major contribution of C-H... $\pi$  interactions in the crystal lattice, which are prominent between  $d_i + d_e = 3.0\text{--}3.8$  Å. There is a sharp peak in the fingerprint plots for C-H...O interactions, which are prominent in between  $d_i + d_e = 1.9\text{--}3.4$  Å in the 2D plot of compound **2.7**. There is another sharp peak in the fingerprint plots for C-N...H interactions, which are prominent in between  $d_i + d_e = 2.6\text{--}3.4$  Å in the 2D plot of compound **2.7** (Figure 2.56 (b)).

The Hirshfeld weak interactions calculation also supports the presence of weak non-covalent intermolecular interactions as in crystal packing, where C-H... $\pi$  interactions, C-H...N, and C-H...O interactions of compound **2.7** in the crystal packing structure is in Figure 2.57 (a) and (b).

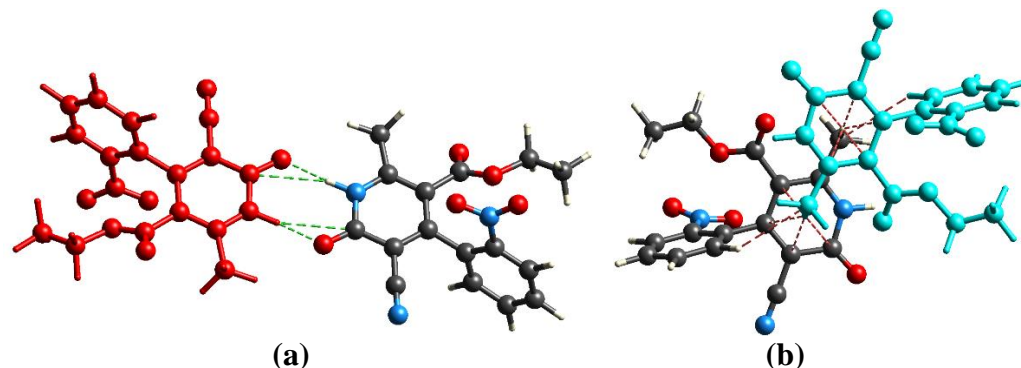


**Figure 2.57:** (a) C-H...O and N-H...O interactions, and (b) C-H... $\pi$  interactions in weak interactions calculations of **2.7**

Decomposed fingerprints of compound **2.7** are showing their characteristic distribution of colored bins for various interactions. The shape index of compound **2.7** indicated the nature of interactions (i.e., donor and acceptor property) (Figure 2.58 (c) and (d)). The red and blue areas of the shape index indicated the acceptor and the donor property, respectively. The surface morphology of the shape index of compound **2.7** showed that the molecules were involved in an unsymmetrical way with neighboring molecules. Curvedness plots showed the presence of flat surface patches above the hetero-aromatic rings, and this is the evidence of planar stacking between the molecules (Figure 2.58 (a) and (b)). Red hollows over both aromatic rings were observed due to these rings' involvement in the C-H... $\pi$  interactions.

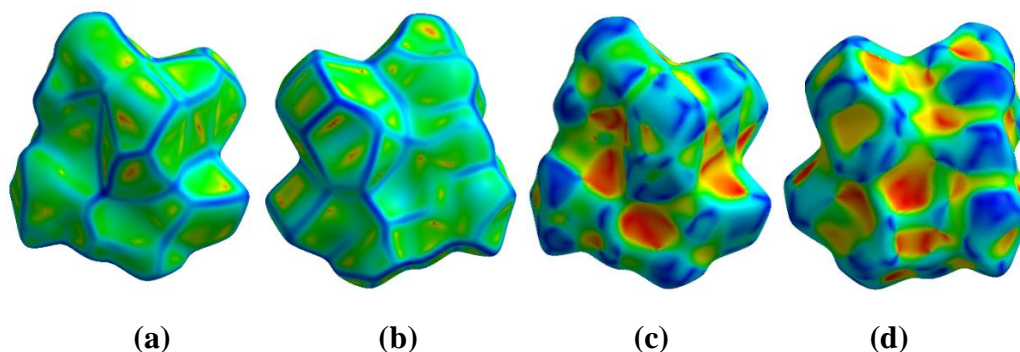


**Figure 2.58:** (a) and (b) Curvedness both side view of compound **2.7**, (c) and (d) Shape index both side view of compound **2.7**.

### 2.8.1.25. X-Ray Crystal Structure of 2.8

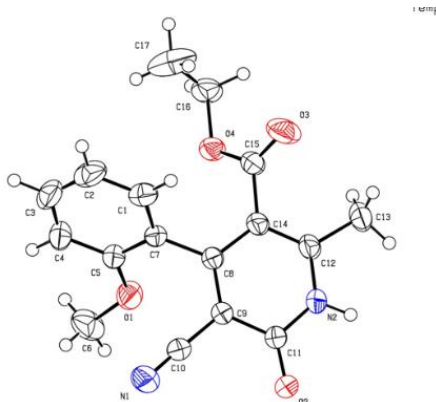


Figure 2.59: ORTEP diagram of 2.8

### 2.8.1.26. Table 2.16. Intermolecular and intramolecular interactions in 2.8

D-H...A	D-H (Å)	H...A (Å)	D...A (Å)	D-H...A (°)
C9-H9...O3	0.980	2.380	3.231	144.85
C17-H17B...O2	0.960	2.670	3.320	125.45
C13-H13C...O2	0.960	2.604	3.440	145.78
C16-H16A... $\pi$ (C1-C5, C7)	0.960	3.411		
C16-H16B... $\pi$ (C1-C5, C7)	0.960	3.973		
C13-H13A... $\pi$ (C1-C5, C7)	0.960	3.250		
C13-H13A... $\pi$ (N2,C8, C9, C11, C12, C14)	0.960	3.522		
C17-H17A... $\pi$ (N2,C8, C9, C11, C12, C14)	0.960	3.304		
N2-H2A... $\pi$ (C1-C5, C7)		2.986		
<b>Intramolecular</b>				
C8-H8...O1	0.980	2.318	3.357	105.26
C13-H13B...O3	0.960	2.510	2.861	101.54
O4... $\pi$ (C1-C5, C7)		4.055		

### Crystal analysis of 2.8

The compound 2.8 containing one asymmetric nitrogen was analysed by single-crystal X-ray diffraction (Figure 2.59). The summary of crystallographic information is listed in Table 2.14. The chiral compound crystallized in the triclinic space group *P*-1 in the crystal lattice unit cell. The unit cell contains a pair of molecules in the crystals.

The overall structure of 2.8 exhibits a stacked arrangement of molecules that exhibit a combination of parallel-displaced C-H... $\pi$ , C-H...O, and N-H... $\pi$  interactions

(Table 2.16). The acute angle (dihedral angle) between the pyridone ring plane and the phenyl ring is  $60.82^\circ$ . The hydrogen-bonding network for compound **2.8** and crystal packing is in Figure 2.60. In addition to the intermolecular C-H...O interactions compound, **2.8** are also having intra-molecular C-H...O interactions. The stacking distance for C-H... $\pi$  are 3.411, 3.973, 3.250 Å, while N-H... $\pi$  is 2.986 Å. (Table 2.16). Apart from these interactions, bifurcated (three centers) hydrogen bonding at the oxygen atom is also observed, i.e., two C-H...O. This bifurcated hydrogen bonding assists the linear chain formation as well as interlayer connectivity. In an extensive hydrogen-bonding network, terminal carbonyl, oxygen & pyridone oxygen are involved in weak interaction and non-traditional hydrogen bond results in the R21(6), R22(8), & R42(18) graph-set notation in which C-H...O & N-H...O interactions are involved. The H...O bond distances for bifurcated hydrogen bonding are 2.670 & 2.604 Å, and angles on hydrogen atoms are  $125.45^\circ$ ,  $145.78^\circ$  while another C-H...O bond distance and angle on hydrogen atom are 2.380 Å and  $144.85^\circ$ , respectively (Table 2.16).

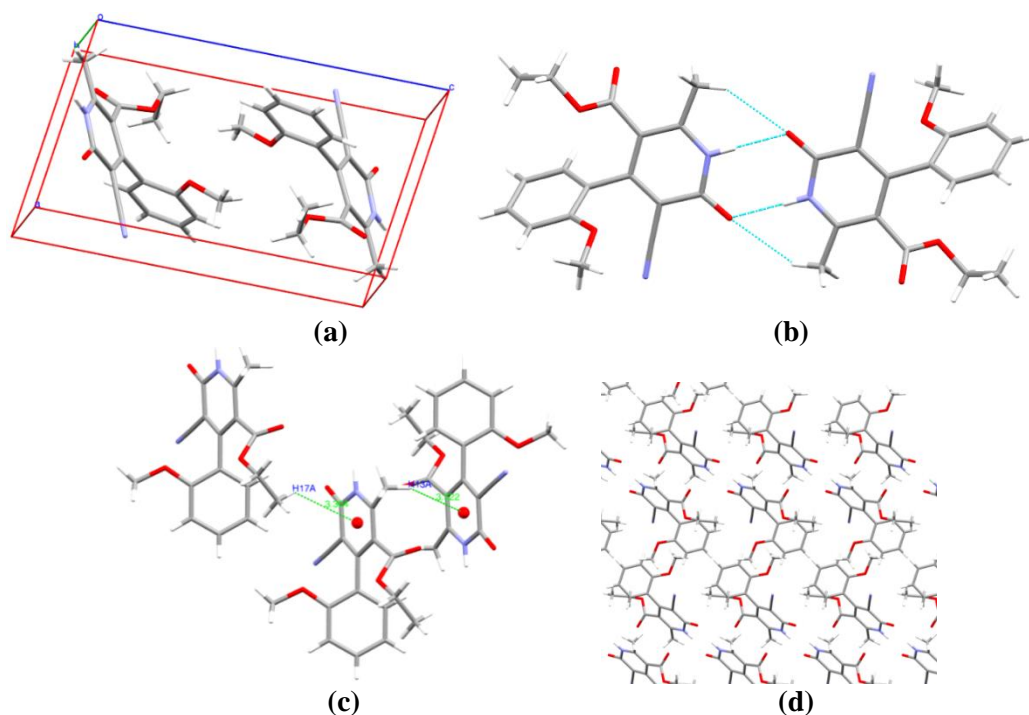


**Figure 2.60:** (a) Packing diagram of **2.8**, (b), (c) and (d) represents the C-H...O, N-H...O and C-H... $\pi$  interaction in **2.8**

### 2.8.1.27. Hirshfeld surface analysis of 2.8

The Hirshfeld surface mapped on  $d_{\text{norm}}$  of compound **2.8** is displayed in Figure 2.61 (a). The red color represents the more dominant non-covalent C-H...O interactions involved in the crystal structure (Figure 2.61 (a)).

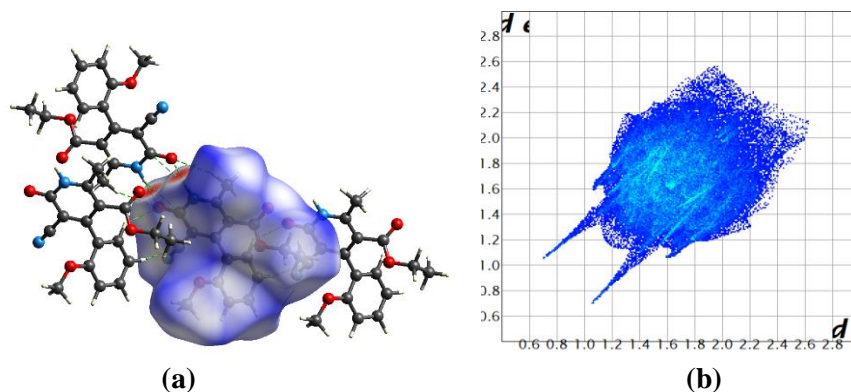


**Figure 2.61:** (a) Hirshfeld surface of compound **2.8**, (b) Two-dimensional fingerprint plot for compound **2.8**

The fingerprint analysis of compound **2.8** shows the percentage contribution of intermolecular interactions and that H-H 41.1 %, N-H 13.3%, O-C 1.4%, O-H 21.4%, O-N 2.9%, O-O 1.0%, C-H 17.7%, and other interactions are less than 1.0% (Figure 2.61 (b)). The calculated weak interactions of the **2.8** compound are shown in Figures 2.62 (a) and (b).

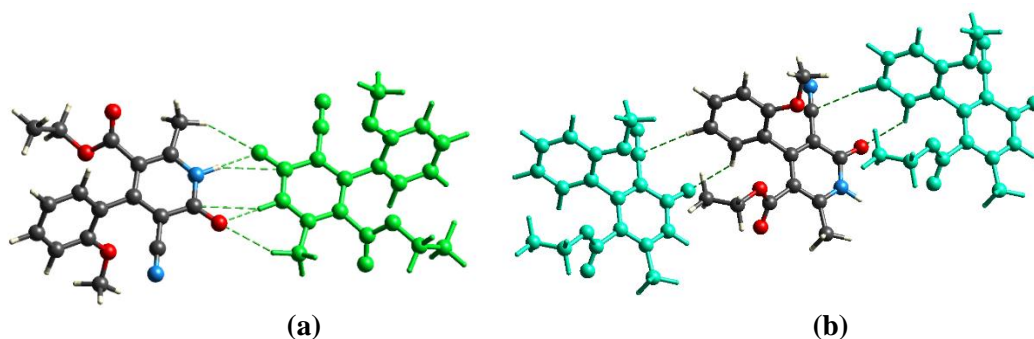


**Figure 2.62:** (a) and (b) Weak interactions calculations of **2.8**.

The absence of green-colored flat regions in the curvedness plot provided the information of the absence of  $\pi$ ... $\pi$  stacking interaction in the crystal packing in Figures 2.63 (a) and (b). In the Shape index plots of compound **2.8**, the red and blue colored



triangles on the surface of rings of the molecule are also missing, which means the absence of  $\pi\cdots\pi$  stacking interaction in the crystal packing (Figure 2.63 (c) and (d)). The yellowish-red colored concave regions on the Hirshfeld surface of compound **2.8** represent weak intermolecular interactions in the crystal packing.

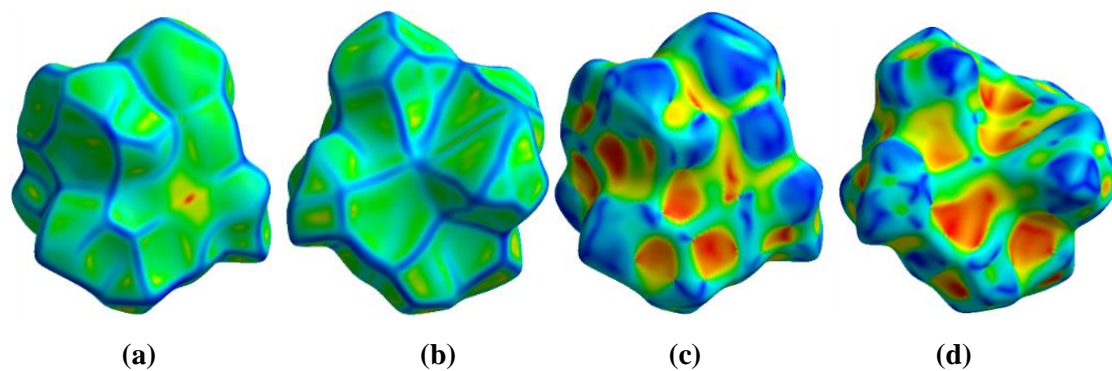


**Figure 2.63:** (a) and (b) Curvedness both side view of compound **2.8**, (c) and (d) Shape index both side view of compound **2.8**.

#### 2.8.1.28. X-Ray Crystal Structure of **2.9**

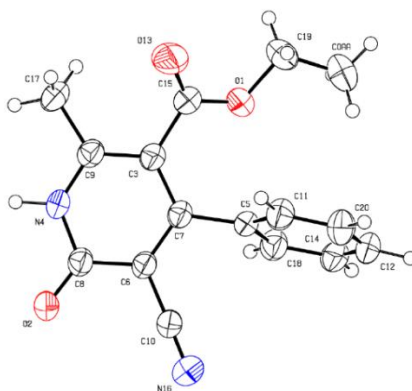


**Figure 2.64:** ORTEP diagram of **2.9**

#### 2.8.1.29. Table 2.17. Intermolecular and intramolecular interactions in **2.9**

D-H...A	D-H (Å)	H...A (Å)	D...A (Å)	D-H...A (°)
C20-H20...N16	0.978	2.632	3.560	158.62
C11-H11...O2	1.000	2.622	3.517	149.11
N4-H4...O2	0.957	1.821	2.774	173.50
N4-H4...C8	0.957	2.724	3.626	157.46

C20-H20...N16	0.978	2.632	3.560	158.62
C19-H19B...C8	1.044	2.870	3.901	169.56
C17-H17c...O2	0.983	2.757	3.514	134.23
C17-H17b...O2	0.978	2.830	3.706	149.57
C17-H17b...N16	0.978	3.113	3.698	119.80
C0aa-H0ac...N16	0.957	3.124	3.770	126.21
C19a-H19a... $\pi$ (C5, C18, C14, C12, C20, C11)	0.949	3.296	4.054	
C0aa-H0ab... $\pi$ (C5,C18,C14,C12,C20,C11)	1.071	3.560	4.194	
C17-H17c... $\pi$ (C9,C3,C7,C6,C8,N4)	0.960	3.063	3.877	
<b>Intramolecular</b>				
C11-H11...O1	1.000	3.259	3.100	
C17-H17b...O13	0.978	2.618	2.895	
C19-H19a...O13	0.949	2.696	2.651	
C0aa-H0aa... $\pi$ (C5, C18, C14, C12, C20, C11)	0.982	2.978	3.767	
O1... $\pi$ (C5, C18, C14, C12, C20, C11)		3.372		

### Crystal analysis of **2.9**

The compound **2.9** chiral compound containing two asymmetric carbon was analysed by single-crystal X-ray diffraction (Figure 2.64). Compound **2.9** was crystallized in hexane: ethyl acetate (90:10) solution at room temperature by a slow evaporation method. The perspective view of compound **2.9** ORTEP diagram at a 50% probability along (010) and packing diagram of compound **2.9** views is shown in Figure 2.40 and 2.41 (a), respectively. The summary of crystallographic information is listed in Table 2.14. The chiral compound crystallized in the monoclinic space group  $P2_1/c$  in the crystal lattice unit cell. The unit cell contains a pair of molecules in the crystals.

The overall structure of **2.9** exhibits a stacked arrangement of molecules that exhibit a combination of parallel-displaced  $\pi\cdots\pi$ , C-H... $\pi$ , C-H...O, and C-H...N interactions (Table 2.17). Both rings are arranged in the AB pattern in the orthogonal pattern in crystal packing. The angle between the two planes of the pyridone ring and phenyl ring is  $65.96^\circ$ . The packing of the crystal is stabilized by alternate  $\pi\cdots\pi$ , O... $\pi$  and C-H... $\pi$  interactions. There are three C-H... $\pi$  intermolecular interactions in **2.9**, strengthening the system with the distance of 3.296, 3.560 & 3.063 Å, respectively (Figure 2.65). In compound **2.9**, pyridone and ester group oxygen and nitrogen are involved in weak interactions. In addition to the intermolecular C-H...O interactions



compound, **2.9** are also having intra-molecular C-H...O interactions. Apart from these interactions, **2.9** also have intramolecular C-H...O and C-H...N interactions.

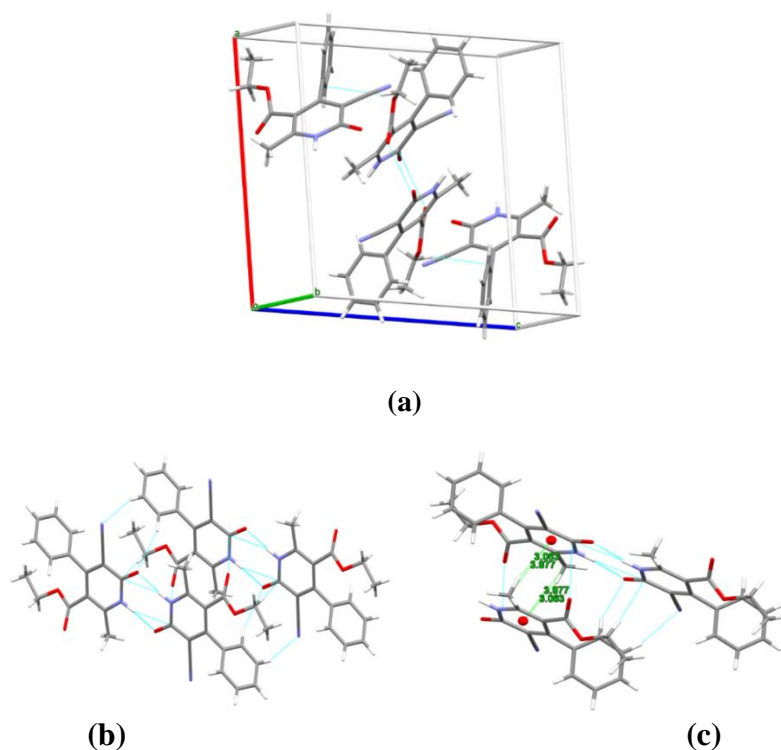


**Figure 2.65:** (a) Packing diagram of **2.9**, (b) C-H...O, N-H...O, C-H...H interactions in **2.9**, and (c) C-H... $\pi$  interactions in **2.9**

#### 2.8.1.30. Hirshfeld surface analysis of **2.9**

The Hirshfeld surface mapped on  $d_{\text{norm}}$  of compound **2.9** is displayed in Figure 2.66 (a). The red color represents the more dominant non-covalent C-H...O interactions involved in the crystal structure (Figure 2.66 (a)).

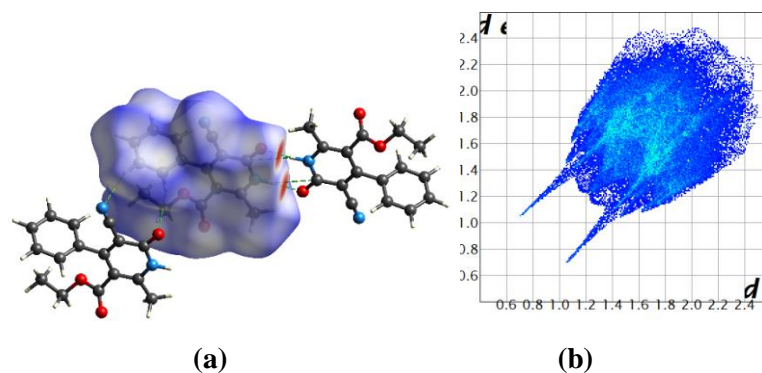


**Figure 2.66:** (a) Hirshfeld surface of compound **2.9**, (b) Two-dimensional fingerprint plot for compound **2.9**

The fingerprint analysis of compound **2.9** shows the percentage contribution of intermolecular interactions and those O-O 1.0%, O-N 1.3%, O-H 19.9%, N-C 2.3%, C-H 18.5%, N-H 16.2%, H-H 39.4%, and other interactions are less than 1.0% (Figure 2.66 (b)). The yellowish-red bin on the fingerprint plots is absent in compound **2.9**, which means the absence of  $\pi\cdots\pi$  stacking in the crystal structure (Figure 2.66 (b)). The spoke-like pattern in the fingerprint plots of **2.9** represents the C-H...O interactions in the crystal lattice in the region of  $d_i + d_e = 2.00\text{-}2.9\text{\AA}$  (Figure 2.66 (b)). The C-H... $\pi$  interactions in **2.9** can be seen as a pair of unique blue-colored wings in the region of  $d_i + d_e = 3.2\text{-}3.6\text{\AA}$  (Figure 2.66 (b)). The C-H...N pair of contacts is also reflected as two characteristic wings occupied in the  $d_i + d_e = 3.2\text{-}3.4\text{\AA}$  in **2.9**.

The Hirshfeld weak interactions calculation also supports the presence of weak non-covalent intermolecular interactions as in crystal packing, where C-H... $\pi$  interactions, C-H...N, and C-H...O interactions of compound **2.9** in the crystal packing structure is in Figure 2.67 (a) and (b).

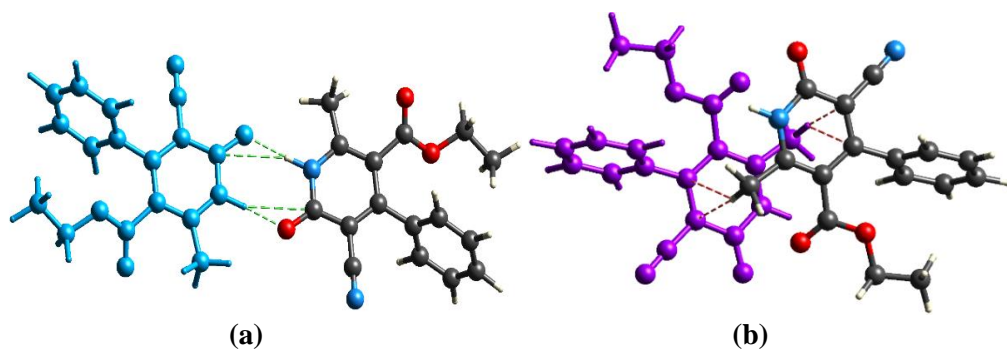


**Figure 2.67:** (a) C-H...O and N-H...O interactions in weak interactions calculations of **2.9** and (b) C-H... $\pi$  interactions in weak interactions calculations of **2.9**

The absence of green-colored flat regions in the curvedness plot provided the information of the absence of  $\pi$ ... $\pi$  stacking interaction in the crystal packing in Figures 2.68 (a) and (b). In the Shape index plots of compound **2.9**, the red and blue colored triangles on the surface of rings of the molecule are also missing, which means the absence of  $\pi$ ... $\pi$  stacking interaction in the crystal packing (Figure 2.68 (c) and (d)). The yellowish-red colored concave regions on the Hirshfeld surface of compound **2.9** represent weak intermolecular interactions in the crystal packing.

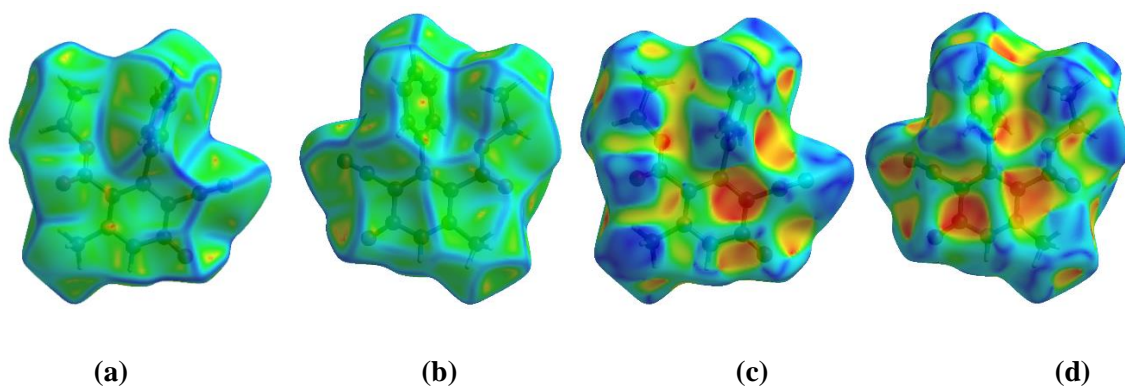


**Figure 2.68:** (a) and (b) Curvedness both side view of compound **2.9**, (c) and (d) Shape index both side view of compound **2.9**.

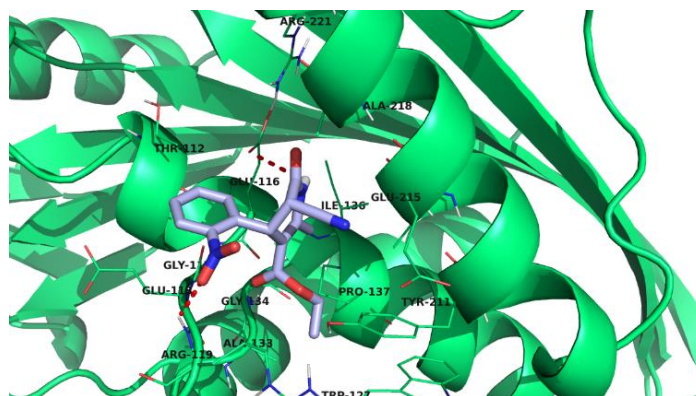
## 2.9. Cytotoxicity and anti-cancer activity of compounds 2.1-2.6

### 2.9.1. *In-silico* analysis of 2.1-2.6

*In-silico* analysis was carried out for compounds **2.1**, **2.2**, **2.3**, **2.4**, **2.5**, and **2.6** to study the interactions and binding energies of these compounds with kinesin Eg5 protein (PDB id: 3UIH). Here also we have used monastrol as a standard drug and grid parameter  $x= 18.06$ ,  $y= 24.56$ ,  $z = 49.31$ ;  $18.46 \text{ \AA} \times 21.52 \text{ \AA} \times 21.82 \text{ \AA}$ , which are similar with our previous synthesized compounds **1.1**, **1.2**, **1.3**, **1.4** and **1.5**. The analysis of docking results was carried out using the pymol and Discovery studio visualizer.

**2.9.1.1. Table 2.18.** Binding energy and the residues involved in the interaction of **2.1**, **2.2**, **2.3**, **2.4**, **2.5** and **2.6** with kinesin Eg5 protein

Compounds	Docking score	Residues involved in H-bond	Residues involved in other interactions ( $\pi$ -anion, $\pi$ - $\sigma$ , $\pi$ - $\pi$ , $\pi$ -alkyl, and alkyl)
<b>2.1</b>	<b>-8.0</b>	Glu116, Arg119	Glu116, Glu118, Leu214
<b>2.2</b>	<b>-7.9</b>	Arg119	Glu116, Glu118, Leu214
<b>2.3</b>	-7.1	Arg119	Glu116, Ala218, Leu214, Arg119
<b>2.4</b>	-7.7	Glu116	Glu116, Leu214, Ile136, Phe239
<b>2.5</b>	-7.9	Glu117	Glu116, Leu214, Pro137, Ile136
<b>2.6</b>		...	Glu116, Ala218, Pro137, Ala133
<b>1 (Monastrol)</b>	-7.8	Glu116, Glu118	Ala218, Leu214, Arg119, Ala133, Pro137



(a)

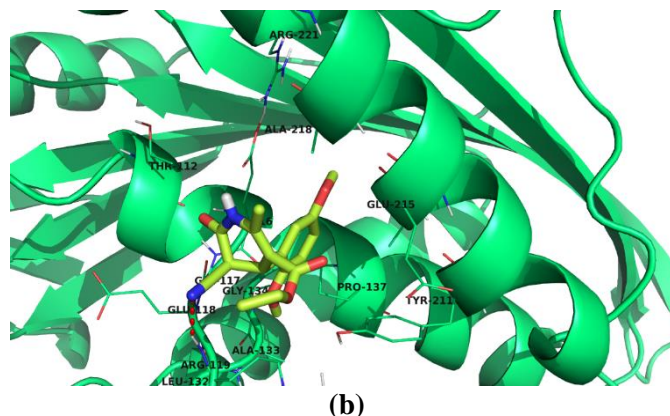


**Figure 2.69:** (a) and (b) Binding mode of compounds **2.1** and **2.3** in the active site cavity of Eg5 protein, respectively.

In-silico analysis revealed that compounds **2.1** and **2.2** exhibited the highest binding energy with Eg5 protein than other compounds, which is also greater than standard drug monastrol (Table 2.18). Compound **2.1** formed two hydrogen bond interactions with Glu116 and Arg 119 residues of Eg5 protein, which stabilized the compound in the protein's active site cavity. Compound **2.1** also formed other hydrophobic interactions such as  $\pi$ -anion,  $\pi$ - $\sigma$ ,  $\pi$ - $\pi$ ,  $\pi$ -alkyl, and alkyl with the residues Glu116, Glu118, Leu214 (Table 2.18) (Figure 2.69). Compound **2.2** formed only one hydrogen bond interaction with residue Arg119 but showed better binding energy than standard monastrol (Figure 2.69). Therefore, from *in silico* analysis, we can say that compound **2.1** and **2.2** could be better Eg5 inhibitor than standard monastrol.

### 2.9.2. Biological activity of 2.1-2.6

Cytotoxicity and anticancer activity of compounds **2.1**, **2.2**, **2.3**, **2.4**, **2.5**, and **2.6** were done in similar methods as in the previous series of compounds (**1.1-1.5**). All materials and cell culture were done as previously done in **Scheme 1**.

#### 2.9.2.1. MTT assay

MTT assay of all variants (**2.1**, **2.2**, **2.3**, **2.4**, **2.5**, and **2.6**) was performed in the same protocol as in Scheme 1 to determine the effect of different variants on cytotoxicity or viability A549 cells.

#### **2.9.2.2. Trypan blue assay**

Trypan blue assay was performed to analyze the cell death induced by various compounds. The experimental method was the same as in **Scheme 1**.

#### **2.9.2.3. Acridine orange-ethidium bromide staining**

Acridine orange-ethidium bromide staining of **2.1** and **2.2** for 24 h and 48 h time points were performed to analyze the type of cell death in A549 cells. The experimental method was the same as in **Scheme 1**.

#### **2.9.2.4. Hoechst 33342 staining**

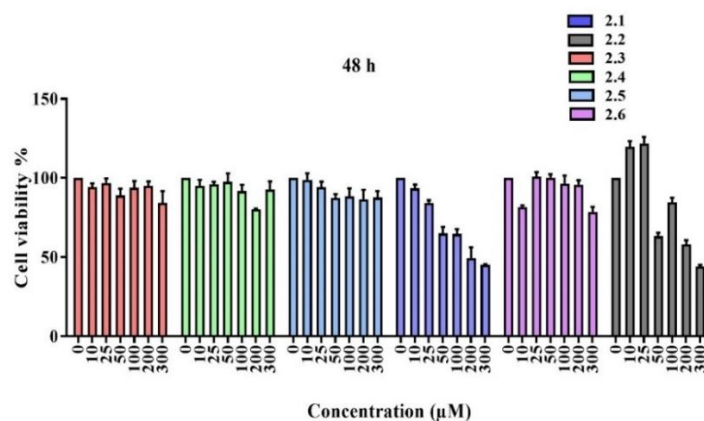
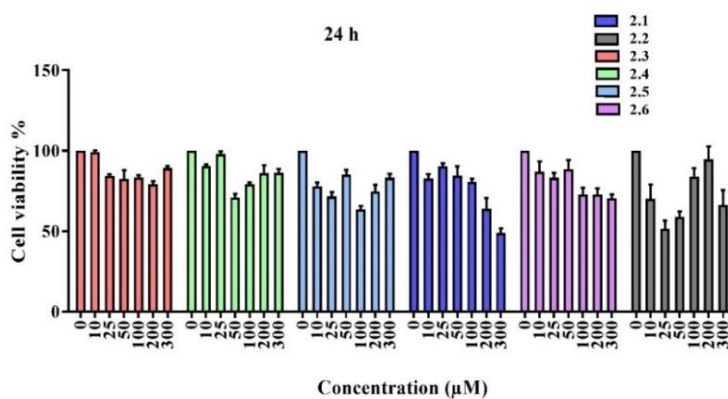
Morphological changes in the apoptotic cells were analysed via Hoechst 33342 assay. Treatment of variants **2.1** and **2.2** (100  $\mu$ M) and analysis was done with the same procedure as in **Scheme 1**.

### **2.9.3. Result and Discussion**

#### **2.9.3.1. Compounds 2.1, 2.2, 2.3, 2.4, 2.5, and 2.6 variants decreased viability of A549 lung adenocarcinoma cells**

To determine the anticancer activity of compound variants **2.1**, **2.2**, **2.3**, **2.4**, **2.5**, and **2.6** against A549 cells, cells were treated with different concentrations of these compounds. The effect on cell viability was analysed via performing an MTT assay. Cell viability reduced to 0-20.78% by **2.3**, 2.02-29.1 % by **2.4**, 14.84-36.44 % by **2.5** and 13.04-29.5 % by **2.6** at 10-300  $\mu$ M concentrations after 24 h (Figure 2.70 (A)). Whereas after 48 h treatment (10-300  $\mu$ M), cell viability was reduced 3.4-15.7 % by **2.3**, 2.45-19.74 % by **2.4**, 1.24-13.5% by **2.5** and 0-21.46 % by **2.6** (Figure 2.70 (A)). **2.1** and **2.2** showed promising results and were used in further experiments. Treatment (10-300  $\mu$ M) of **2.1** decreased cell viability by 9.2-38.45 % at 24 h and 11.41-46.84 % at 48 h (Figure 2.70 (B)). Whereas, **2.2** treatment (10-300  $\mu$ M) decreased cell viability by 22.2-33.83 % at 24 h and 0-38 % at 48 h (Figure 2.70 (B)) with respect to control.

(A)



(B)

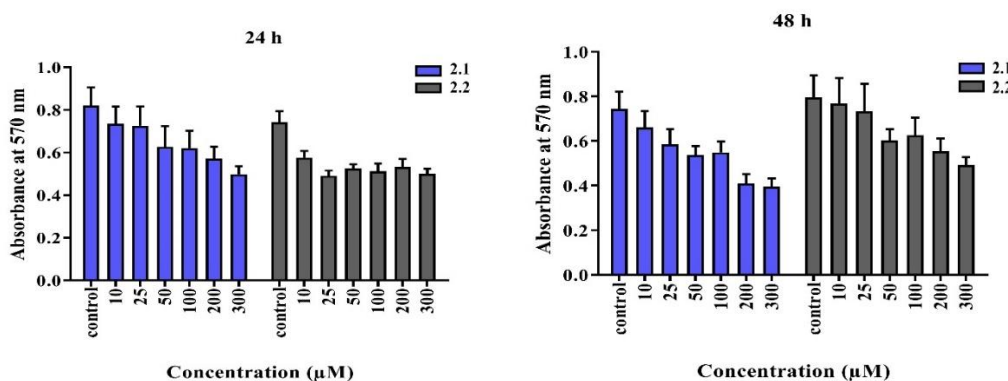


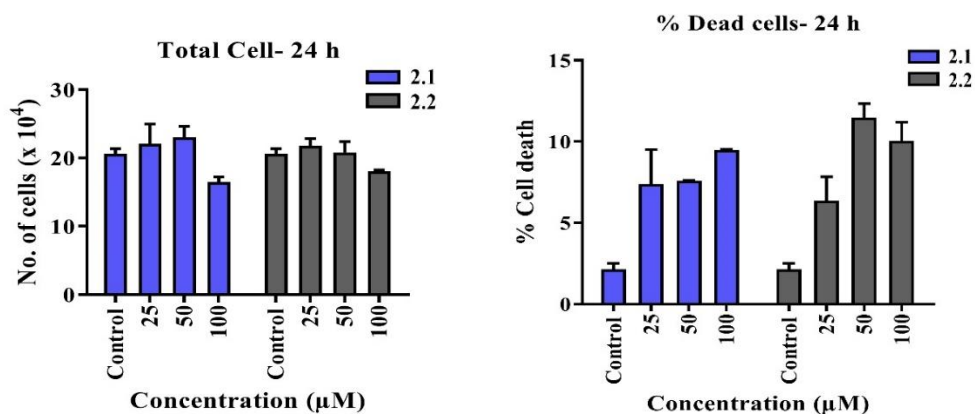
**Figure 2.70:** A549 lung adenocarcinoma cells were treated with (A) different concentrations (10  $\mu\text{M}$ , 25  $\mu\text{M}$ , 50  $\mu\text{M}$ , 100  $\mu\text{M}$ , 200  $\mu\text{M}$ , 300  $\mu\text{M}$ ) of different compounds (**2.1**, **2.2**, **2.3**, **2.4**, **2.5** and **2.6**) and cell viability was analysed by MTT assay. (B) Cells were treated with different concentrations of selected **2.1** and **2.2** for 24 h and 48 h, and cell viability was examined by MTT assay.



### 2.9.3.2. Compounds 2.1 and 2.2 increased cell death in A549 cells

Trypan blue assay was performed to determine the effect of **2.1** and **2.2** on cell death. A549 cells were treated with defined doses (25  $\mu\text{M}$ , 50  $\mu\text{M}$ , and 100  $\mu\text{M}$ ) of **2.1** and **2.2** for 24 h and 48 h. In the **2.1** treated group (100  $\mu\text{M}$ ), 9.47%, and in the **2.2** treated group (50  $\mu\text{M}$ ), 11.47% cell death was observed at 24 h (Figure 2.71 (A)). At 48 h time point, 12.13% and 10.93% cell death was observed in **2.1** treated group (50  $\mu\text{M}$ ) and **2.2** treated groups (100  $\mu\text{M}$ ), respectively (Figure 2.71 (B)). In the treated group, the numbers of total cells were decreased as the concentration of variants was increased in comparison to control at 24 h and 48 h (Figure 2.71 (A) & 2.71 (B)).

(A)



(B)

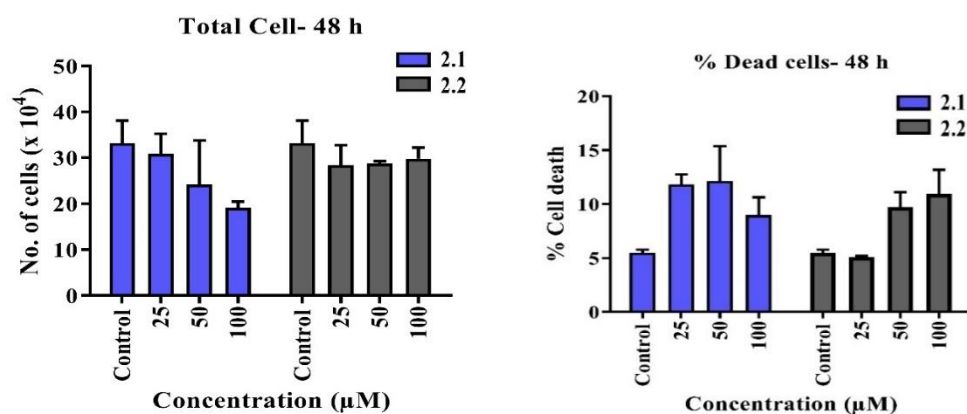


**Figure 2.71:** Trypan blue assay was performed to check the effect of **2.1** and **2.2** at 25, 50, and 100  $\mu\text{M}$  doses on A549 cells. Graphs represent the percent cell death and the total number of cells for (A) 24 h and (B) 48 h.



### 2.9.3.3. Compounds 2.1 and 2.2 induced apoptotic cell death in A549 adenocarcinoma cells

Normal cells, apoptotic cells, and necrotic cells can be differentiated by acridine orange–ethidium bromide staining. Normal cells appear in circular size with green color due to acridine orange stain. Ethidium bromide stains the cell's nucleus in red color, having compromised cellular membrane. Treatment of A549 cells with 100  $\mu\text{M}$  of **2.1** and **2.2** exhibited apoptotic characteristics like a blebbed membrane, nuclear fragmentation, and apoptotic body formation after 24 and 48 h treatment (Figure 2.72). These results indicate the apoptosis-inducing ability of **2.1** and **2.2** in A549 cells.

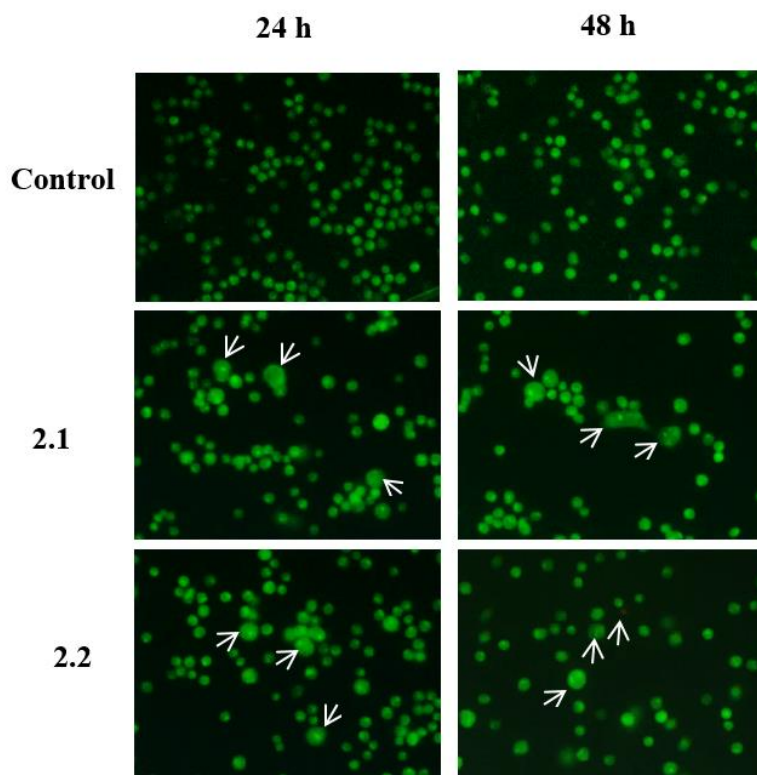


**Figure 2.72:** A549 adenocarcinoma cells were treated with 100  $\mu\text{M}$  **2.1** and **2.2** compounds for 24 and 48 h and stained with acridine orange and ethidium bromide.

#### 2.9.3.4. Compounds 2.1 and 2.2 increased nuclear fragmentation in A549 adenocarcinoma cells

Nuclear fragmentation, chromatin condensation, and nuclear shrinkage are the characteristics of apoptotic cells that could be observed by Hoechst stain under a fluorescent microscope. Hoechst 33342 stain is permeable through a normal cell membrane. It stains the normal cell nucleus in homogenous light blue color, and the apoptotic cell nucleus appears in bright blue. In the 2.1 and 2.2 treatment group (100  $\mu$ M), DNA fragmentation was observed, which indicated apoptosis (Figure 2.73). These results corresponded to the acridine orange-ethidium bromide staining and confirmed the 2.1 and 2.2 mediated apoptosis induction in A549 cells.

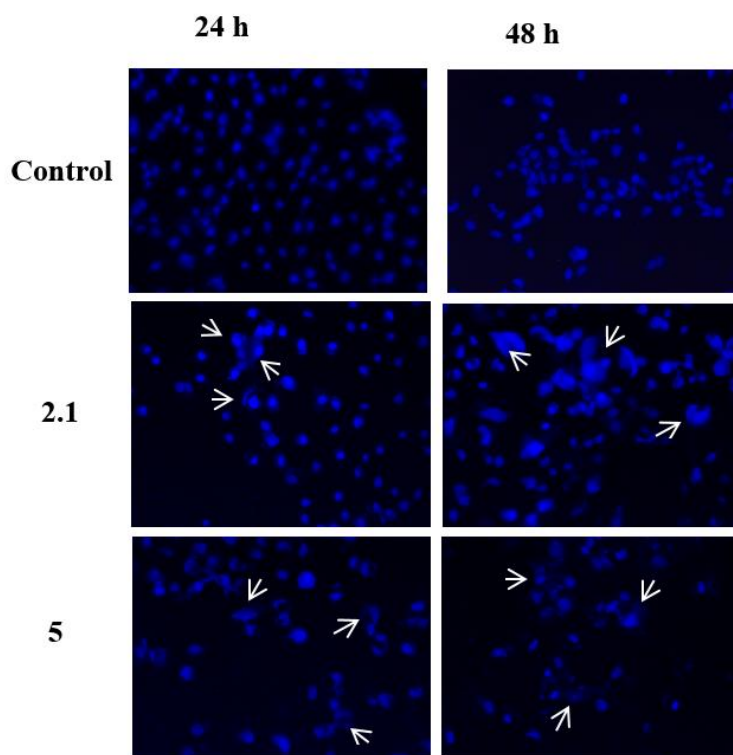


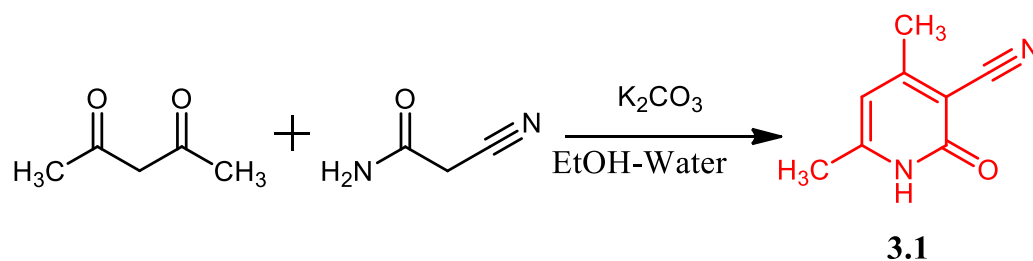
**Figure 2.73:** A549 adenocarcinoma cells were treated with 100  $\mu$ M 2.1 and 2.2 compounds for 24 and 48 h and stained with Hoechst stain, and cell death was assessed by fluorescence microscope, and images were taken at 200X magnification with 100  $\mu$ M, 2.1, and 2.2 compounds.

Among the dihydro-2-pyridone (DHP) series of compounds, intracellular oxidation can be induced in the redox cycle to resulting in both cytotoxicity and genotoxicity in cancer cells. These may induce an imbalance in cellular antioxidant/oxidant status and causes DNA damage. This phenomenon can further trigger molecular events, which might eventually cause alterations in the tumor cell cycle and initiate apoptosis. These can also reduce migration ability and could inhibit tumor growth and reduce the size of migration ability of A549 cells. These findings suggest that **2.1** and **2.2** might be anticancer drug candidates. Its analogues are promising agents for treating different types of cancers, particularly for cancer of the lung.

### 2.10. Scheme 3: Heterocyclic moiety is linked via substituted phenyl ring system through methylene linkers

In **Scheme 3**, molecules are synthesized based on six-membered heterocyclic moiety, **4,6-dimethyl-2-oxo-1,2-dihydropyridine-3-carbonitrile**. The heterocyclic moiety is linked via a substituted phenyl ring system through methylene linkers. Here we have synthesized such molecules in which there are chances to polarize charges to understand the electrostatic phenomenon in the self-assembly of molecules assisted through weak interactions. Towards this effort, model molecules with various electron-rich as well as electron-deficient combinations have been synthesized.

#### 2.10.1. Experimental



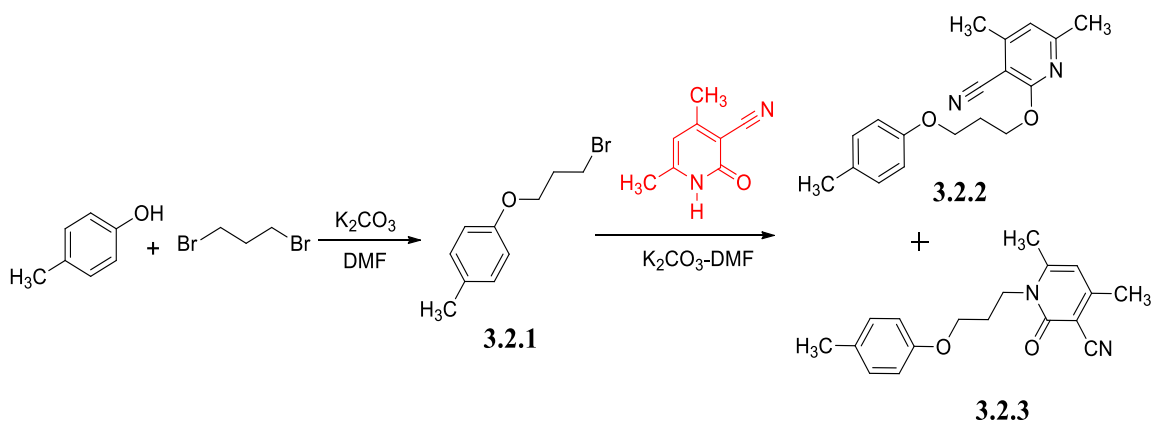
**Scheme 3.1**

### 2.10.1.1. Synthesis of 4,6-dimethyl-2-oxo-1,2-dihydropyridine-3-carbonitrile (3.1)

In a 100 mL round bottom flask, cyanoacetamide (4.2 g, 50 mmol) was taken in ethanol. Potassium carbonate (2.0 g, 50 mmol) dissolved in water and added to the reaction mixture and stirred it. Acetyl acetone (5.0 g, 50 mmol) was added slowly with stirring after 20 min. The reaction mixture was stirred for 2 h. The completion of the reaction was checked via TLC. Light yellow coloured precipitate appeared, which was filtered and washed with cold ethanol. Pure white coloured 4,6-dimethyl-2-oxo-1,2-dihydropyridine-3-carbonitrile (**3.1**) was then recrystallized with hot aqueous ethanol.

**Yield:** 6.40 g, 87%, m.p. 127-129°C.

**<sup>1</sup>H NMR 300 MHz, 25°C, Si(CH<sub>3</sub>)<sub>4</sub>, (CDCl<sub>3</sub>) (δ):** 2.409 (3H, s, CH<sub>3</sub>); 2.43 (3H, s, CH<sub>3</sub>); 6.07 (1H, s, Ar-H).



**Scheme 3.2**

### 2.10.1.2. Synthesis of 1-(3-bromopropoxy)-4-methylbenzene (3.2.1):

In a 100 mL round bottom flask, p-cresol (3 g, 28 mmol) and potassium carbonate (3.84 g, 28 mmol) were taken in DMF and stirred it. After 20 min. 1, 3-dibromopropane (16.5 mL, 180 mmol) was added and stirred for 12 h. Completion of the reaction was checked via TLC (20% EtOAc & Hexane). After completing the reaction, DMF was removed under reduced pressure through a rotary evaporator, and the reaction

mixture was extracted with CHCl<sub>3</sub>/ H<sub>2</sub>O (200/ 200 X 3 mL). The CHCl<sub>3</sub> layer was dried with anhydrous Na<sub>2</sub>SO<sub>4</sub> and filtered. Chloroform was removed, and the product was purified via column chromatography.

**Yield:** 5.4 g (85%), m.p. 235-237°C

**(2.2.1); <sup>1</sup>H NMR 300 MHz, 25°C, Si(CH<sub>3</sub>)<sub>4</sub>, (CDCl<sub>3</sub>) (δ):** 2.13(2H, m, CH<sub>2</sub>); 2.27(3H, s, CH<sub>3</sub>); 3.50-3.51(2H, t, CH<sub>2</sub>); 4.05-4.06(2H, t, CH<sub>2</sub>); 6.87(2H, d, Ar-H), 7.12(2H, d, Ar-H)

### **2.10.1.3 Synthesis of 4,6-dimethyl-2-(3-(p-tolyloxy)propoxy) nicotinonitrile (3.2.2) and 4,6-dimethyl-2-oxo-1-(3-(p-tolyloxy)propyl)-1,2-dihydropyridine-3-carbonitrile (3.2.3)**

In a 100 mL round bottom flask, 4,6-dimethyl-2-oxo-1,2-dihydropyridine-3-carbonitrile (1 g, 6.8 mmol) and potassium carbonate (1 g, 7.2 moles) were taken in DMF and stirred. After 20 min, **1-(3-bromopropoxy)-4-methylbenzene** (1.56 g, 6.8 mmoles) was added and stirred for 12 h. Completion of the reaction was checked via TLC (30% EtOAc & Hexane). After completing the reaction, DMF was removed under reduced pressure through a rotary evaporator, and the reaction mixture was extracted with CHCl<sub>3</sub>/ H<sub>2</sub>O (200/ 200 X 3 mL). The CHCl<sub>3</sub> layer was dried with anhydrous Na<sub>2</sub>SO<sub>4</sub> and filtered. Chloroform was removed, and the product was purified via SiO<sub>2</sub>-column chromatography. The first fraction collected at 8 % and the second one at 25 % ethyl acetate-hexane was characterized as compound **3.2.2** & **3.2.3**, it was recrystallized by hexane and ethyl acetate separately (5:95) and (10:90) respectively.

**(3.2.2); Yield:** 0.35 g (33%); m.p. 257-259°C.

**<sup>1</sup>H NMR 300 MHz, 25°C, Si(CH<sub>3</sub>)<sub>4</sub>, (CDCl<sub>3</sub>) (δ):** 2.20-2.30 (5H, m, CH<sub>2</sub>CH<sub>2</sub>CH<sub>2</sub>, CH<sub>3</sub>); 2.45 (6H, s, CH<sub>3</sub>); 4.13-4.20 (2H, t, OCH<sub>2</sub>, *J*= 12 Hz, 9 Hz); 4.58-4.64 (2H, t, OCH<sub>2</sub>, *J*= 9 Hz, *J*= 9 Hz); 6.66 (1H, s, Ar-H); 6.83-6.86 (2H, d, Ar-H, *J*= 9 Hz); 7.10-7.13 (2H, d, Ar-H, *J*= 9 Hz). **<sup>13</sup>C NMR (75MHz, CDCl<sub>3</sub>): (δ):** 63.88, 63.94, 64.44, 93.52, 114.39, 115.55, 117.57, 130.21, 131.99, 155.37, 157.08, 161.96, 163.28. **MS**

(*m/z*): 297.36(*M*+1). **Element analysis: (i). Calculated:** C=72.95%; H=6.80%; N=9.45%; **(ii). Found:** C=72.77%; H=6.68%; N=9.14%.

**(3.2.3); Yield:** 0.65 g (63%); m.p. 262-265°C.

**<sup>1</sup>H NMR 300 MHz, 25°C, Si(CH<sub>3</sub>)<sub>4</sub>, (CDCl<sub>3</sub>) (δ):** 2.20-2.26 (2H, p, CH<sub>2</sub>CH<sub>2</sub>CH<sub>2</sub>); 2.32 (3H, s, CH<sub>3</sub>); 2.40 (3H, s, CH<sub>3</sub>); 2.46 (3H, s, CH<sub>3</sub>); 3.99-4.03 (2H, t, NCH<sub>2</sub>, *J*= 5.4 Hz, 5.7 Hz); 4.22-4.26 (2H, t, OCH<sub>2</sub>, *J*= 7.2 Hz, 7.2 Hz); 6.14 (1H, s, Ar-H); 6.79-7.82 (2H, d, Ar-H, *J*= 8.4 Hz); 7.10-7.13 (1H, d, Ar-H, *J*= 8.4 Hz). **<sup>13</sup>C NMR (75MHz, CDCl<sub>3</sub>): (δ):** 20.66, 20.79, 21.3, 27.62, 42.48, 65.44, 101.59, 109.55, 109.57, 114.62, 115.31, 130.21, 131.99, 150.37, 158.08, 160.96, 161.21, 163.28. **MS (*m/z*):** 297.36(*M*+1). **Element analysis: (i). Calculated:** C=72.95%; H=6.80%; N=9.45%; **(ii). Found:** C=72.59%; H=6.27%; N=9.66%.

## 2.10.2. X-Ray Crystallographic studies and Hirshfeld surface analysis of 3.2.2 and 3.3.3

### 2.10.2.1. X-ray crystal structure of 3.2.2

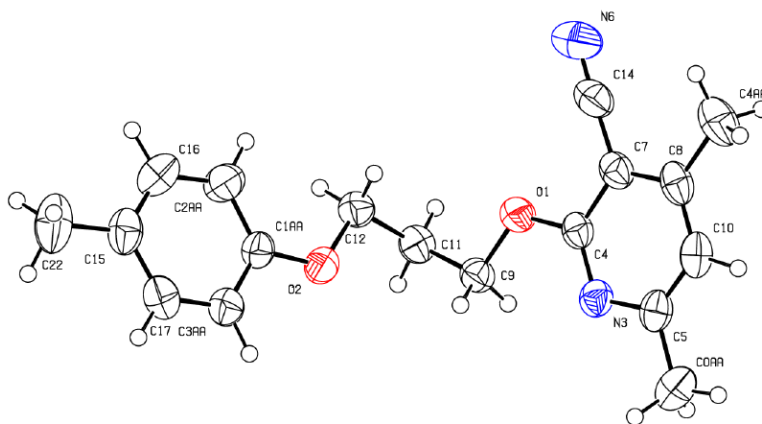


**Figure 2.74:** ORTEP diagram of 3.2.2

**2.10.2.2. Table 2.19.** Crystal data of compounds **3.2.2** and **3.2.3**

Compound	3.2.2	3.2.3
Identification code	1996721	1907079
Empirical formula	C18H20N2O2	C18H20N2O2
Formula weight	296.36	296.36
Temperature(K)	296(2) K	293(2)K
Crystal system	<i>P2<sub>1</sub>/c</i>	<i>P21/n</i>
Space group	monoclinic	triclinic
a(Å)	7.2627(4)	7.2535(4)
b(Å)	8.2928(4)	8.7640(6)
c(Å)	27.0765(13)	25.238(13)
α(°)	90	90
β(°)	90.358(3)	90.966(4)
γ(°)	90	90
Volume(Å <sup>3</sup> )	1630.73	1604.18 Å <sup>3</sup>
Z	4	4
ρ (g/cm <sup>3</sup> )	1.207	1.227
μ(mm <sup>-1</sup> )	0.079	0.081
F(000)	632.2852	632.2852
Crystal size(mm <sup>3</sup> )	0.24 x 0.22 x 0.18	0.24 x 0.22 x 0.18
Radiation	MoKα	MoKα
2θ range for data collection(°)	1.50 to 28.75	3.2 to 29.1
Reflections collected	53301	7159
Independent reflections	4206	3646
Data/restraints/parameters	4206/0/279	3646/0/279
Goodness-of-fit on F2	1.109	1.044
Final R indexes [I>=2σ(I)]	R <sub>1</sub> = 0.0558 , wR <sub>2</sub> = 0.1474	R <sub>1</sub> = 0.0599, wR <sub>2</sub> = 0.1513
Final R indexes [all data]	R <sub>1</sub> = 0.0920, wR <sub>2</sub> = 0.1777	R <sub>1</sub> = 0.0911, wR <sub>2</sub> = 0.1777
Largest diff. peak/hole / e Å <sup>-3</sup>	0.28/-0.37	0.36/-0.41

**2.10.2.3. Table 2.20.** Intermolecular and intramolecular interactions in **3.2.2**

D-H...A	D-H (Å)	H...A (Å)	D...A (Å)	D-H...A (°)
C10-H10...O2	0.999	2.615	3.522	151.11
C11a-H3aa...N6	0.982	2.605	3.447	143.88
C2aa-H2aa...π (C1aa, C2aa, C3aa, C15, C16, C17)	0.987	2.991	3.916	156.46
C10-H10...π (C1aa, C2aa, C3aa, C15, C16, C17)	0.999	3.812	4.745	156.51
C12-H12a...π (C1aa, C2aa, C3aa, C15, C16, C17)	0.945	3.694	4.247	120.03
C12-H12b...π (C1aa, C2aa, C3aa, C15, C16, C17)	0.993	3.862	4.247	106.13
π (N3, C4, C5, C7, C8, C10)...π (N3, C4, C5, C7, C8, C10)		3.622		
N3... π (N3, C4, C5, C7, C8, C10)		3.437		

Compound **3.2.2** was crystallized in ethyl acetate solution at room temperature by the slow evaporation method. Compound **3.2.2** having  $Z = 4$  in crystal packing. The perspective view of the compound **3.2.2** ORTEP diagram at a 50% probability along (010) view is shown in Figure 2.74. The packing diagram of a unit cell of compound **3.2.2** is shown in Figure 2.75. The summary of crystallographic information is listed in Table 2.19.

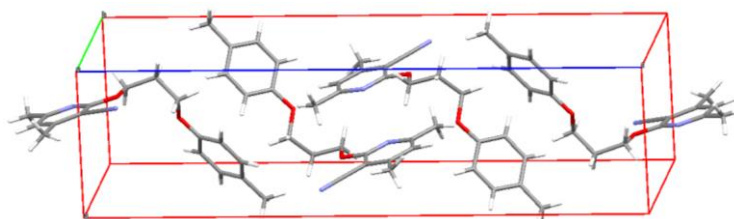


**Figure 2.75:** Packing diagram of a unit cell of compound **3.2.2** along the b axis.

The hydrogen-bonding network for **3.2.2** and crystal packing in Compound **3.2.2** exists in an unsymmetrical pattern in crystal packing. Unsymmetrical packing in the crystal lattice is the cause of uneven electronic distribution in the crystal lattice. Both rings exist in gauche conformation in crystal lattice rather than staggered conformation. Packing patterns in solid-state compounds exist in the ABAB pattern due to alternate C-H... $\pi$  and  $\pi$ ... $\pi$  interactions. In compound **3.2.2**, only one linker oxygen of the molecule is involved in hydrogen bonding.

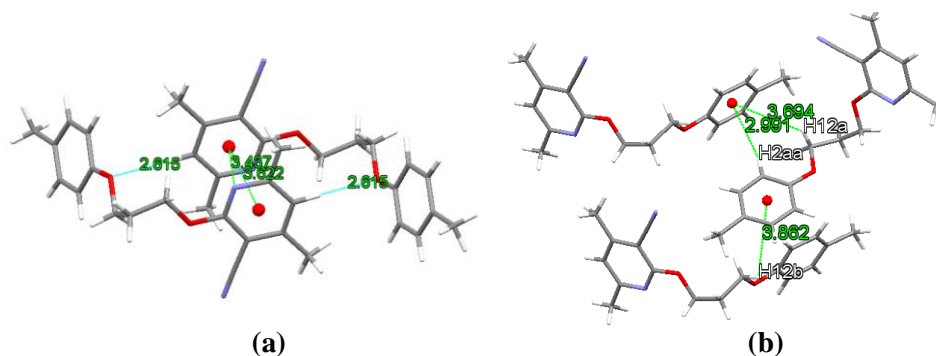


**Figure 2.76:** (a)  $\pi$ ... $\pi$  interactions and (b) C-H... $\pi$  interactions in compound **3.2.2**.

In addition to C-H...O interactions in the extended structure of compound **3.2.2** are also having intermolecular C-H... $\pi$  interactions in the crystal packing between C2aa-



H2aa, C10-H10, C12-H12a, C12-H12b and  $\pi$  electrons of the ring of an adjacent molecule (Table 2.20). Compound **3.2.2** also exhibit intermolecular  $\pi\dots\pi$  interactions among the adjacent ring of neighbor molecules (Figure 2.76). In  $\pi\dots\pi$  interactions, both rings' orientation is opposite due to the oppositely polarized structure (Figure 2.76 (a)). The compound has displaced face to face  $\pi$  (N3, C4, C5, C7, C8, C10) $\dots\pi$  (N3, C4, C5, C7, C8, C10) and lone pair $\dots\pi$  (N3 $\dots$ N3, C4, C5, C7, C8, C10) interactions in the crystal packing of the molecule. The dihedral between both rings in the compound **3.2.2** is  $77.16^\circ$ . This dihedral angle is close to the gauche conformation angle. It is not precisely in gauche confirmation concerning the ethylene linker.

#### 2.10.2.4. Hirshfeld surface analysis of 3.2.2

The Hirshfeld surface mapped on  $d_{\text{norm}}$  of compound **3.2.2** is displayed in Figure 2.77 (a). The red color represents the more dominant non-covalent C-H $\dots$ O interactions involved in the crystal structure (Figure 2.77 (a)).

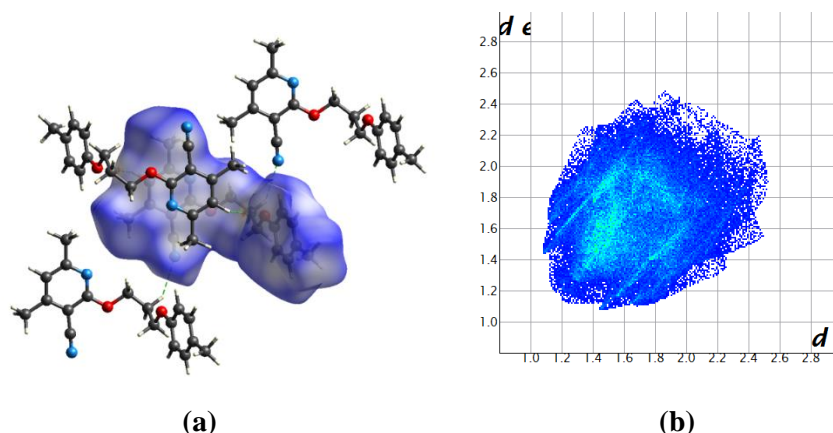


**Figure 2.77:** (a) Hirshfeld surface of compound **3.2.2**, (b) Two-dimensional fingerprint plot for compound **3.2.2**.

The fingerprint analysis of compound **3.2.2** shows the percentage contribution of intermolecular interactions are H-H for around 57.2 %, N-H for 12.6%, O-H for 4.9 %, N-C for 2.6%, C-H for 19.3%, C-O for 1.5%, and C-C for 1.7 % of the close contacts in the Hirshfeld surfaces (Figure 2.77(b)).

A prominent wing in the fingerprint indicates the vital contribution of C-H... $\pi$  interactions in the crystal lattice, which are prominent between  $d_i + d_e = 3.2-3.8 \text{ \AA}$ . There is a sharp peak in the fingerprint plots for C-H...O interactions in the crystal lattice, which are prominent in between  $d_i + d_e = 2.45-2.7 \text{ \AA}$  in the 2D plot of compound **3.2.2**. There is a sharp ridge to conform to the CH...N interactions in the fingerprint plot ( $d_i + d_e > 3.8 \text{ \AA}$ ) of compound **3.2.2**.

The strongest involves a pair of C-H... $\pi$  (C10-H10...C1aa, C2aa, C3aa, C15, C16, C17),  $\pi$ ... $\pi$  (N3, C4, C5, C7, C8, C10...N3, C4, C5, C7, C8,C10) interactions between molecules (Figure 2.78). The larger dispersion component was calculated for these interactions, presumably a result of the aromatic electronic distribution in the compound. Another interaction of interest is these weak H-bonds C11a-H3aa...N6 & loan pair...  $\pi$  (N3...N3, C4, C5, C7, C8,C10), making a non-covalent interaction among neighbor molecule ring due to electronic dispersion in the molecule. The larger electrostatic component is calculated for this interaction, presumably a result of the charge distribution in the cyano functional group and the polarization of the phenyl ring and pyridine by its substituents.

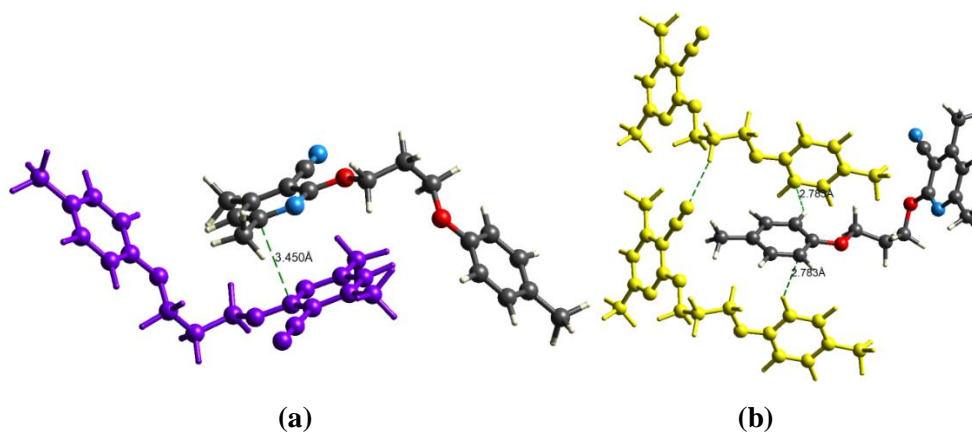


**Figure 2.78:** (a)  $\pi$ ... $\pi$  interaction and (b) C-H... $\pi$  and C-H...N interactions in compound **3.2.2** in Hirshfeld surface analysis.

Decomposed fingerprints of compound **3.2.2** are showing their characteristic distribution of colored bins for various interactions. The shape index of compound **3.2.2**

indicated the nature of interactions (i.e., donor and acceptor property) (Figure 2.79 (c) and (d)). The red and blue areas of the shape index indicated the acceptor and the donor property, respectively. The surface morphology of the shape index of compound **3.2.2** showed that the molecules were involved in an unsymmetrical way with neighboring molecules. Curvedness plots showed the presence of flat surface patches above the hetero-aromatic rings, and this is the evidence of planar stacking between the molecules (Figure 2.79 (a) and (b)). Red hollows over both aromatic rings were observed due to these rings' involvement in the C-H... $\pi$  interactions.

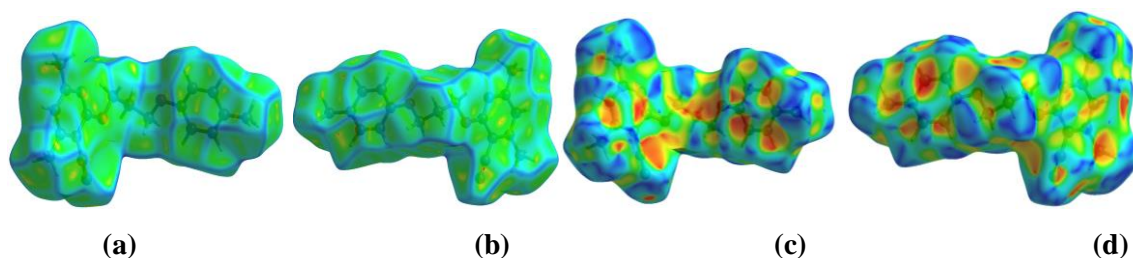


**Figure 2.79:** (a) and (b) Curvedness both side view of compound **3.2.2**, (c) and (d) Shape index both side view of compound **3.2.2**.

#### 2.10.2.5. X-ray crystal structure of **3.2.3**

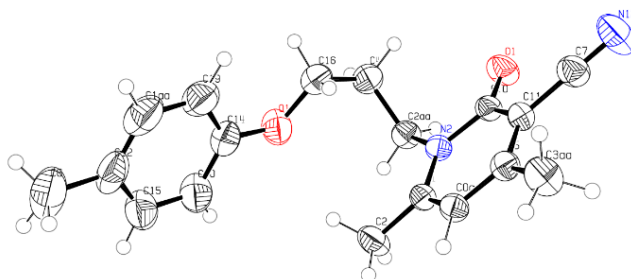


**Figure 2.80:** ORTEP diagram of **3.2.3**

#### 2.10.2.6. Table 2.21. Intermolecular and intramolecular interactions in **3.2.3**

D-H...A	D-H (Å)	H...A (Å)	D...A (Å)	D-H...A (°)
C0aa-H0aa....O1	0.998	2.436	3.344	150.93
C2-H2c....O1	0.970	2.438	3.376	162.70
C6-H6b....O1	0.909	2.499	3.398	170.52
C3aa-H3aa...N12	1.007	2.711	3.680	161.55
C3aa-H3ac...N12	0.946	2.732	3.672	171.97

O1... $\pi$ (C0aa, C1, C5, C10, C11, N2)		3.268		
C6-H6c... $\pi$ (C1aa, C12, C14, C15, C19, C20)		3.699		
C15-H15... $\pi$ (C1aa, C12, C14, C15, C19, C20)		3.537		
C19-H19... $\pi$ (C1aa, C12, C14, C15, C19, C20)		3.573		
C16-H16a... $\pi$ (C1aa, C12, C14, C15, C19, C20)		3.525		
$\pi$ (C0aa, C1, C5, C10, C11, N2)...C10		3.540		
<b>Intramolecular</b>				
C2-H2a...O10	1.001	2.502	3.401	149.26
C4-H4a...O1	0.989	2.536	3.075	114.05
C2-H2a... $\pi$ (C1aa, C12, C14, C15, C19, C20)		3.805		

Compound **3.2.3** was crystallized in hexane: ethyl acetate (9:1) solution at room temperature by a slow evaporation method. The perspective view of compound **3.2.3** ORTEP diagram at a 50% probability along (010) and packing diagram of compound **3.2.2** view is shown in Figure 2.80 and 2.81 (a), respectively.

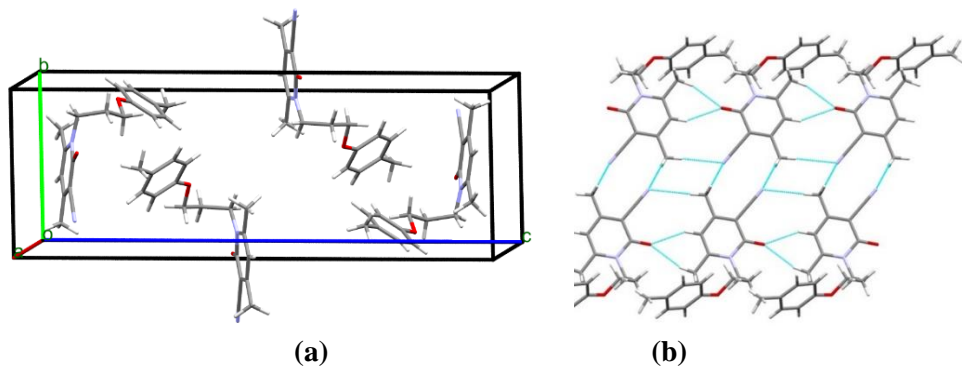


**Figure 2.81:** (a) Packing diagram of **3.2.3**, (b) C-H...O, and C-H...N interactions in **3.2.3**

Compound **3.2.2** has a folding pattern in crystal packing due to intra, and inter-molecular non-covalent interactions (Table 2.21), shown in Figure 2.32. The angle between the two planes of the pyridone ring and phenyl ring is  $65.96^\circ$ , reflecting the folding pattern of the fleximer. The packing of the crystal is stabilized by alternate  $\pi$ ... $\pi$ , O... $\pi$  and C-H... $\pi$  interactions. Aromatic  $\pi$ ... $\pi$  stacking layers are orthogonal to each

other, but C-H... $\pi$  layers are interlinked through the puckered structure. The compound exhibits parallel displaced  $\pi$ ... $\pi$  (3.32 Å) intermolecular stacking interactions between pyridone rings in the opposite orientation. This orientation is due to co-planarity and unequal electronic distribution over the ring's surface (Figure 2.82). C-H... $\pi$  layer B is having two alternative planes of four rings also strengthens the crystal packing. C-H... $\pi$  intermolecular interactions play a vital role in strengthening the system by four different C-H... $\pi$  interactions of 3.699, 3.537, 3.573 & 3.525 Å, respectively (Figure 2.82). C-H... $\pi$  intra-molecular interactions also strengthen the folded structure of 3.805 Å in the molecular system. C-H...O interactions are also playing an important role in the formation of self-assembly of the molecule. Intramolecular C-H...O interactions are also supporting the folded pattern of the crystal packing of 2.502 Å & 2.536 Å in the system with angle 149.26° and 114.05, respectively (Table 2.21).

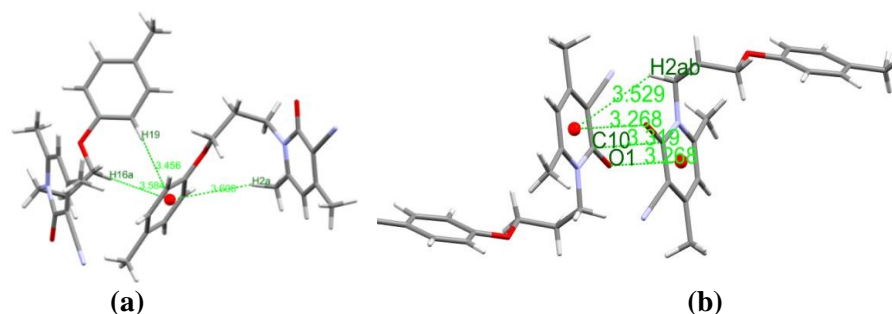


**Figure 2.82:** (a) C-H... $\pi$  interactions intermolecular and (b)  $\pi$ ... $\pi$  interactions in **3.2.3**.

#### 2.10.2.7. Hirshfeld surface analysis of **3.2.3**

The Hirshfeld surface mapped on  $d_{\text{norm}}$  of compound **3.2.3** is displayed in Figure 2.83 (a). The red color represents the more dominant non-covalent C-H...O interactions involved in the crystal structure (Figure 2.83 (a)).

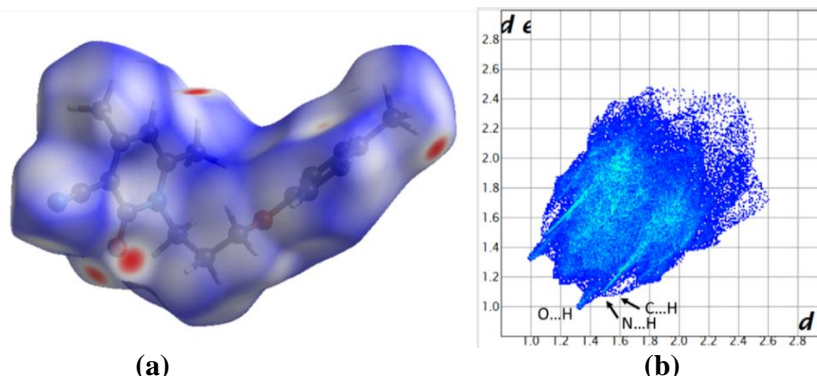


**Figure 2.83:** (a) Hirshfeld surface of compound **3.2.3**, (b) Two-dimensional fingerprint plot for compound **3.2.3**

The fingerprint analysis of compound **3.2.3** shows the contribution of intermolecular percentage interactions are H-H for around 52.8%, O-H for 8.9%, C-H for 21.8%, N-H for 13.4%, C-O for 1.6, and C-C for 0.5% of the close contacts in the Hirshfeld surfaces (Figure 2.83 (b)). A wing in the fingerprint plot indicates the significant contribution of C-H... $\pi$  interactions in the crystal lattice, which are prominent between  $d_i + d_e = 2.6\text{-}3.6$  Å. There is a sharp peak in the fingerprint plots for O...H interactions, which are prominent in between  $d_i + d_e = 2.3\text{-}3.4$  Å in the 2D plot of compound **3.2.3**. There is another sharp peak in the fingerprint plots for N...H interactions, which are prominent in between  $d_i + d_e = 2.6\text{-}3.4$  Å in the 2D plot of compound **3.2.3** (Figure 2.83 (b)).

The strongest interaction involves two C-O... $\pi$  contacts, as shown in Figure 2.84 (b), in which an inversion center relates molecules. This interaction is also responsible for the closest  $\pi$ ... $\pi$  interaction [4.2590(9) Å] (Figure 2.84 (a)).

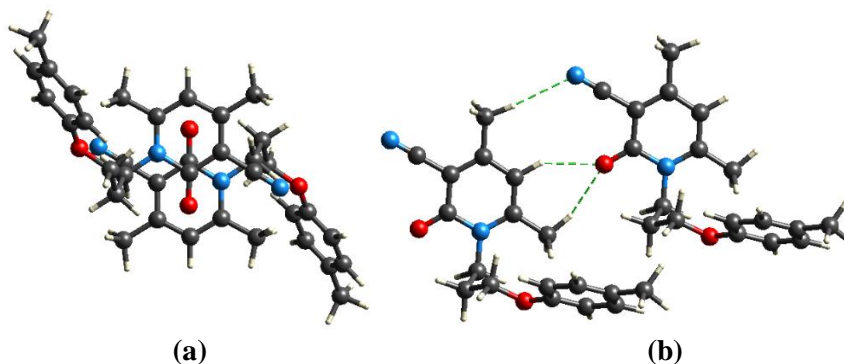


**Figure 2.84:** (a)  $\pi$ ... $\pi$  interactions and (b) C-H...O interactions in compound **3.2.3**

Decomposed fingerprints of compound **3.2.3** are showing their characteristic distribution of colored bins for various interactions. The shape index of compound **3.2.3** indicated the nature of interactions (i.e., donor and acceptor property) (Figure 2.85 (c) and (d)). The presence of red and blue colored triangles on the surface of rings of the molecule in the shape index plots also indicated the absence of weak  $\pi\cdots\pi$  stacking in the crystal structure. The surface morphology of the shape index of compound **3.2.3** showed that the molecules were involved in an unsymmetrical way with neighboring molecules. Curvedness plots showed the presence of flat surface patches above the hetero-aromatic rings, and this is the evidence of planar stacking between the molecules (Figure 2.85 (a) and (b)). The presence of green-colored flat regions in the curvedness plots indicated the presence of  $\pi\cdots\pi$  stacking in the crystal structure of compound **3.2.3** (Figure 2.85 (a) and (b)).

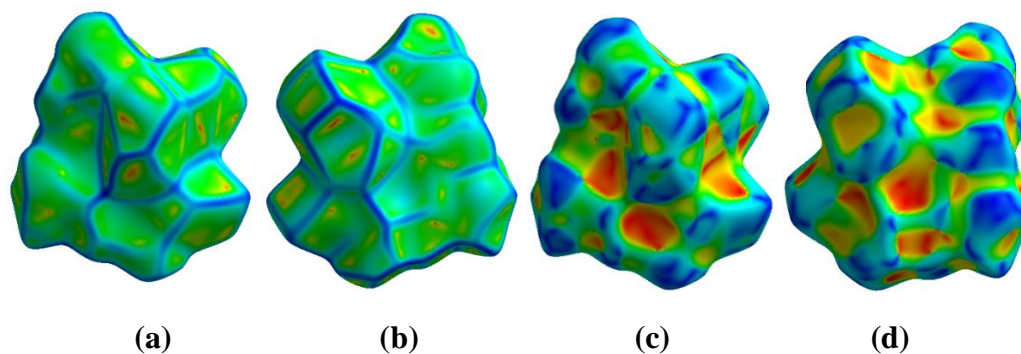


**Figure 2.85:** (a) and (b) Curvedness both side view of compound **3.2.3**, (c) and (d) Shape index both side view of compound **3.2.3**.

## 2.11. Conclusion

In conclusion, we have synthesized three series of fleximers based on 2-pyridones, 2-dihydropyridones, and dihydropyrimidinones derivatives with ester linked methylene containing small arm. For the first time, we have used *Citrus macroptera* juice to synthesize dihydropyrimidinones derivatives, which is a solvent-free reaction. The advantages of this procedure are good yield, short reaction time, and eco-friendly procedure. In Scheme two, we have synthesized 2-pyridones, 2-dihydropyridones



derivatives with methylene linked arm. Moreover, we have also studied X-ray crystallographic studies for these compounds. Aromatic interactions play an essential role in chemical and biological systems as they are ubiquitous. Aromatic interactions are different from simple interactions like hydrogen bonds; the difference is that they are just complicated because larger functional groups are involved in providing a large surface area of intermolecular contact. These interactions are very weak and very difficult to study with each and every tool. We have studied these interactions using the single-crystal X-ray diffraction (SCXRD) method and Hirshfeld surface analysis method. We found C-H... $\pi$ , C-H...O, C-H...N, C-H...C, lone pair... $\pi$ ,  $\pi$ ... $\pi$  interactions for synthesized compounds, which are very useful for the drug design, stabilization of DNA structure, protein folding, crystal engineering, material science, etc. Hirshfeld surface analysis analyzes the various intermolecular interactions in the crystal structures, supporting the single-crystal X-ray diffraction (SCXRD) study.

We have also carried out cytotoxicity and anticancer activity of these compounds. Most importantly, these compounds showed good anticancer activity, which is also supported by *in-silico* analysis. The anticancer activity was carried out in Human adenocarcinoma A549 cells, where two compounds (**1.2** and **1.5**) from Scheme 1 having better anticancer activity. Two compounds (**2.1** and **2.2**) from Scheme 2 also showed better anticancer activity. The anticancer activity results of these compounds (**1.2**, **1.5**, **2.1**, and **2.2**) were well supported by *in-silico* analysis, where these compounds showed better binding energy than standard drug monastrol. Anticancer studies suggested that our synthesized compounds could be better anticancer drugs.



### 3 SYNTHESIS AND STRUCTURAL STUDY OF POLY-AROMATIC FLEXIMERS

---

#### 3.1 Introduction

Nowadays, poly-aromatic heterocyclic fleximers represent important groups of compounds due to their biological and medical applications. Due to their flexible nature, it attracts many researchers, and much research has already been done. Conformationally flexible molecules have a high tendency to form polymorphs, which plays a pivotal role in improving relevant properties, such as hygroscopicity, stability, solubility, dissolution rates, and bioavailability. Analogues like pyridine, pyridone, pyrimidine, piperidine, piperazine, etc., already showed how important they are for the medicinal field. The fleximers of these analogues are an interesting topic for medicinal as well as for biological field. 2-pyridone analogues are particularly significant because the 2-pyridone structure present in many natural origin compounds acts as a potential framework for DNA and RNA, elucidating its importance in drug discovery and development. 2-pyridone analogues have been observed to possess different pharmacological activities such as antibacterial (Fujita et al., 2005; Li et al., 2000), antifungal (Fassihi et al., 2009), antiviral (Dragovich et al., 2002; Parreira et al., 2001), antitumor (Parlow et al., 2003; Parlow & South, 2003) and antiplatelet. Moreover, 2-pyridone analogues have also been used to manufacture paints (Mijin et al., 2014), pigments, additives for fuels and lubricants, acid-base indicators, stabilizers for polymers, and coatings (Litvinov et al., 1999). 2-pyridone based flexible dimers have also been reported as active anti-inflammatory agents (Dubey et al., 2014; Rai et al., 2016; Semple et al., 2003), since these structures are resemblance to celecoxib and the existence of a more significant number of rotatable dihedral angles.

Some marketed medications like milrinone (Figure 3.1) and amrinone (Figure 3.1) containing 2-pyridone are used for the treatment of heart failure (Pastelin et al., 1983), Pilocidines (Figure 3.1) used for the treatment of bacterial infections (Åberg & Almqvist, 2007), and perampanel (Figure 3.1), used as a non-competitive and selective antagonist of the  $\alpha$ -amino-3-hydroxy-5-methyl-4-isoxazolepropionic acid receptor. It improves motor symptoms in animal models of parkinson's disease (Eggert et al., 2010). Since 2-pyridone analogues possess various pharmacological properties, the synthesis, structural study, and biological activity of 2-pyridone analogues could be an exciting topic for developing different pharmaceutical agents. This chapter includes synthesis of 2-pyridone based poly-aromatic fleximers and studied through single crystal X-ray diffraction (SCXRD) and Hirshfeld surface analysis.

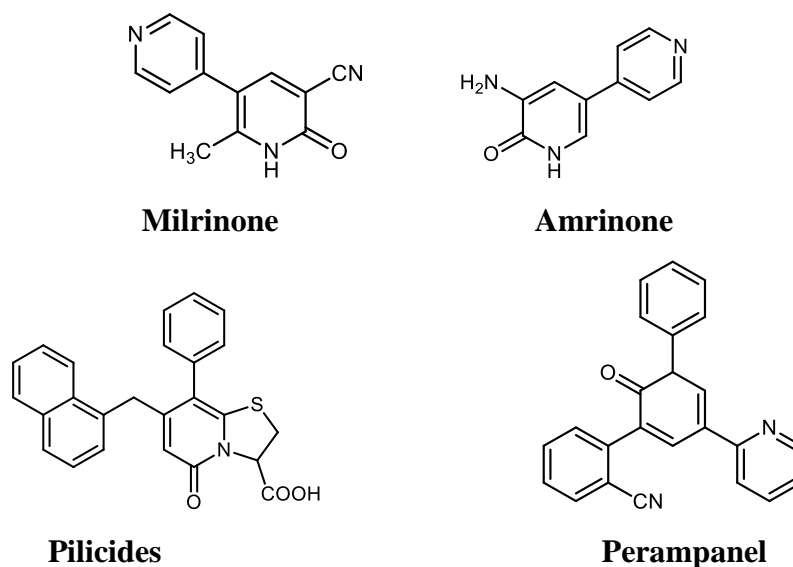


**Figure 3.1: 2-Pyridone** compounds which possess physiological activity

### 3.1.2 Molecular recognition in pyridones

Much research has been done on pyridone moiety to understand the molecular recognition and non-covalent interaction properties. Since the 2-pyridone structure is present in many natural origin compounds, it is also very similar to thymine and uracil. Both thymine and uracil have lactam-lactim tautomerization as present in pyridones.

Flexible dipyrindone (Figure 3.2) incorporates an extensive, self-complementary pattern of hydrogen-bond donors and acceptors. However, in the solid-state, dipyrindone (Figure 3.2) prefers a polymeric motif with intramolecular non-covalent interactions.

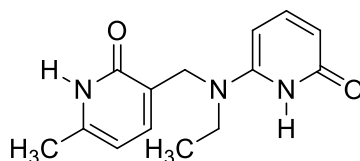


**Figure 3.2:** Flexible dipyrindone

Gallant et al. (Gallant, Phan Viet Minh Tan, and Wuest, 1991) proposed the extended structure of pyridone in solution as a dimer. The dimer is held together by two intermolecular hydrogen bonds strengthened by two intramolecular hydrogen bonds (Bertolasi *et al.*, 1998; Yan, Su, and Wu, 2007). They also studied aggregation in dipyrindones linked by flexible spacers. Wong et al. (Wong et al., 2006) studied the quadruple hydrogen-bonding core produced by dimeric 2-ureido-4-pyrimidinone. Williams and Kwast (Williams & Kwast, 1988) studied the dimerization of asymmetric dipyrindones and symmetrical isomers' polymerization. These studies incorporate an extensive, self-complementary pattern of hydrogen-bond donors and acceptors, behavior of pyridones.

### 3.2. Present work

Monastrol is the protagonist of the dihydropyrimidinones (DHPMs) class (Figure 3.3). The first dihydropyrimidinone based small molecule is identified as an inhibitor of mitotic spindle protein, Eg5, which helps spindle formation during mitosis. 2-pyridone derivatives also possess anticancer activity due to their ability to act as survivin inhibitors (Figure 3.1). We have designed and synthesized our compounds based on Monastrol kinesin inhibitor and Survivin inhibitor pharmacophore analysis and bioisoster group application (Figure 3.3). Our commitment towards the development of bioactive molecules and view of prominence as mentioned above of 2-pyridones groups

and synthetic feasibility. We proposed methylene-linked pyridone derivatives to introduce the phthalimide and phenol moiety to increase the intramolecular/intermolecular interactions and increase the interactions with respected protein residues.

The synthesis of desired derivatives **5.1-5.6** was depicted in **Scheme 4** and **Scheme 5**. In **Scheme 4**, we have synthesized methylene-linked Aromatic (phthalimide and phenol) with halide (**4.1-4.3**) by reaction with phthalimide, phenol and 1,2-dibromoethane and 1,3-dibromopropane in the presence of  $K_2CO_3$  in DMF. Then these compounds **4.1-4.3** used to react with 2-pyridone derivatives (**2.8**, **2.10**, **2.11** and **2.12**) (**Scheme 2**) in the presence of  $K_2CO_3$  in DMF to get the desired derivatives **5.1-5.6**.

This chapter has reported the synthesis and study of methylene-linked 2-pyridone derivatives to introduce the phthalimide and phenol moiety in **Scheme 4** and **Scheme 5**.

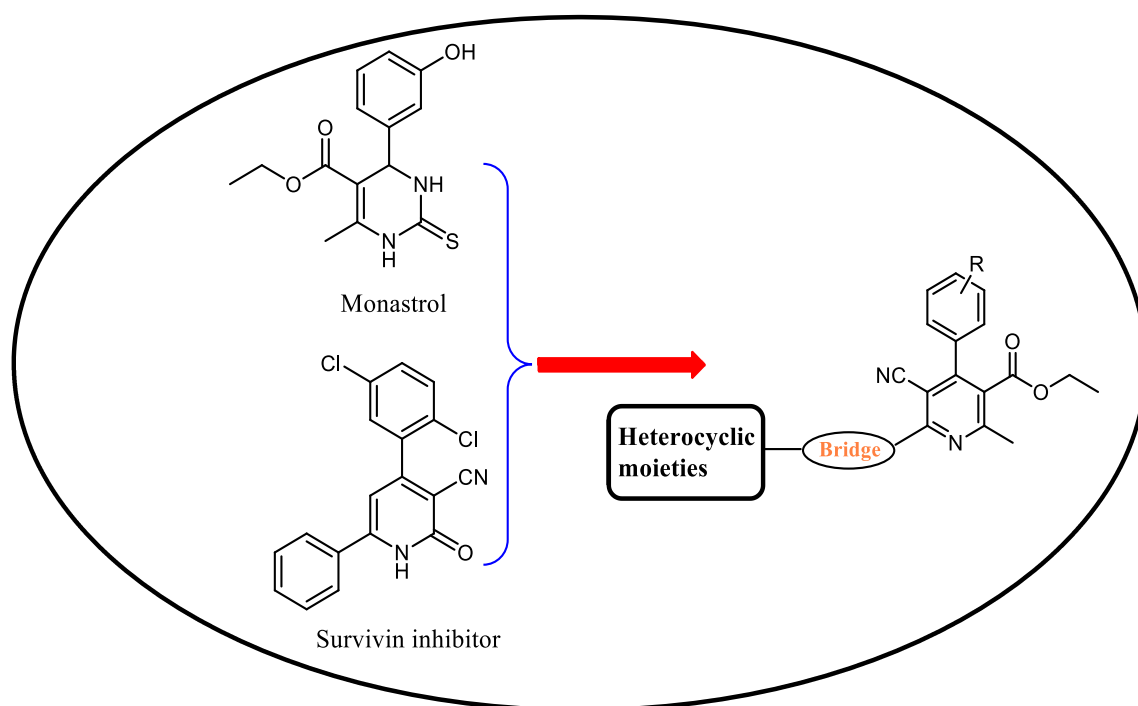
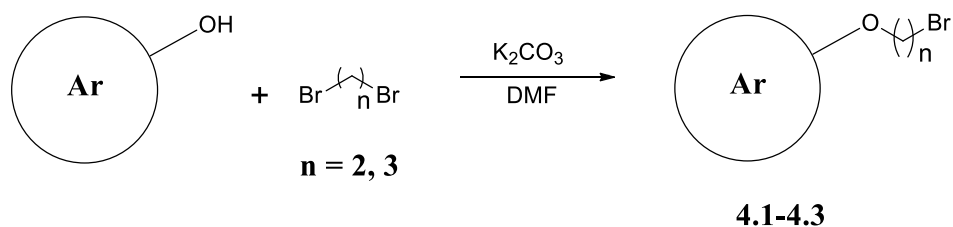


**Figure 3.3:** Design of heterocyclic moieties-linked dihydropyridone derivatives.

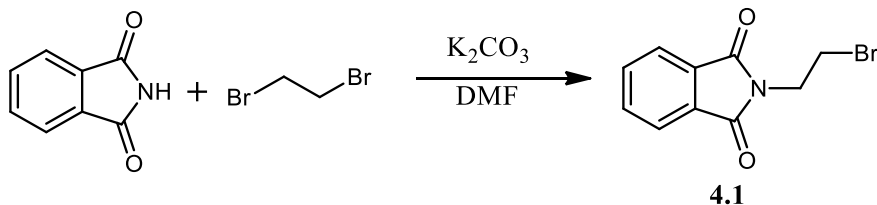
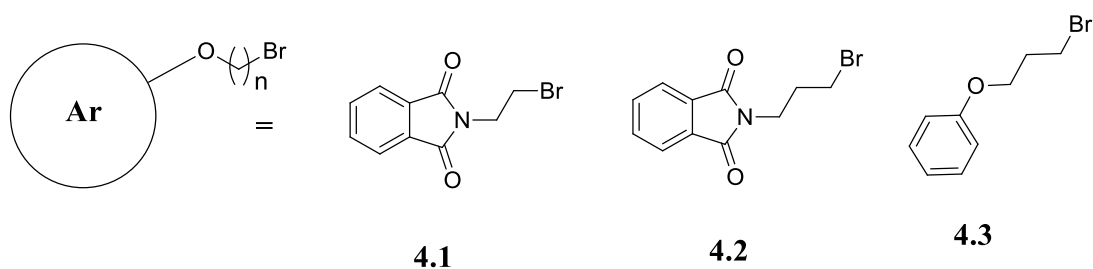
### 3.2.1. Experimental

$^1\text{H}$  NMR (300 MHz) and  $^{13}\text{C}$  (75 MHz) NMR spectra were recorded on **JEOL AL300 FTNMR** spectrometer using TMS as an internal reference, and chemical shift values are expressed in  $\delta$ , ppm units. Melting points of all the compounds were recorded on the electrically heated instrument and are uncorrected. All the reactions were monitored by thin-layer chromatography (TLC) on pre-coated aluminum sheets of Merck using an appropriate solvent system, and chromatograms were visualized under UV light. For column chromatography and flash chromatography, silica gel (60-120 and 230-400 mesh) was employed, and eluents were ethyl acetate/hexane mixtures.

### 3.3. Scheme 4: Methylene-linked Aromatic ring with bromide



Scheme 4



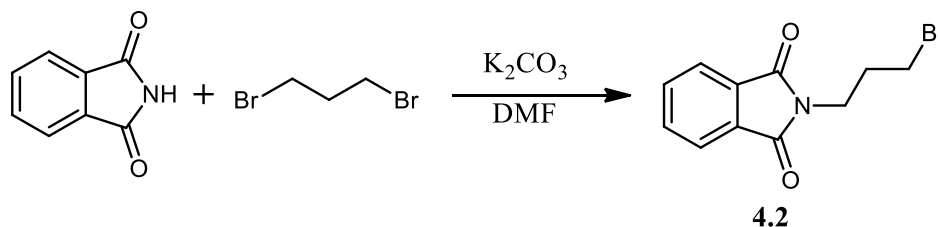
Scheme 4.1

### 3.3.1 Synthesis of 2-(2-bromoethyl)isoindoline-1,3-dione (4.1)

In a 100 mL round bottom flask, phthalimide (40.98 mmol) and potassium carbonate (40.98 mmol) were dissolved in 25 mL of dimethylformamide (DMF), and the reaction mixture was stirred for 30 minutes at room temperature. After 30 minutes of the reaction, 1,2-dibromoethane (204.8 mmol) was added to the reaction mixture, and the reaction was continued for 12 h. TLC monitored the completion of the reaction. Solvent DMF was removed by rotary evaporator, and the residue was extracted with chloroform (3 × 200 mL) and washed with water (3 × 100 mL). The combined organic layer was collected and dried over anhydrous sodium sulfate. The crude solid product was then mixed with silica gel (230-440 mesh) to make a slurry and subjected to flash chromatography using ethyl acetate and hexane as eluent. The pure compounds (**4.1**) were collected at 10 % EtOAc/Hexane.

**Yield:** 0.42 g (85%); m.p. 154-156°C.

**<sup>1</sup>H NMR 300 MHz, 25°C, Si(CH<sub>3</sub>)<sub>4</sub>, (CDCl<sub>3</sub>) (δ):** 4.06-4.08 (2H, t, CH<sub>2</sub>); 4.22-4.25 (2H, t, CH<sub>2</sub>); 7.78-7.82 (1H, d, CH); 7.78-7.82 (1H, d, CH); 7.88-7.92 (1H, dd, CH); 7.88-7.92 (1H, dd, CH).



**Scheme 4.2**

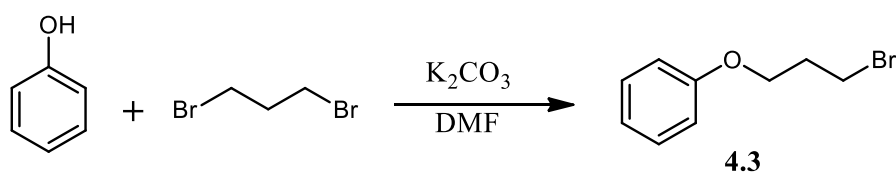
### 3.3.2 Synthesis of 2-(3-bromopropyl) isoindoline-1,3-dione (4.2)

In a 100 mL round bottom flask, phthalimide (40.98 mmol) and potassium carbonate (40.98 mmol) were dissolved in 25 mL of dimethylformamide (DMF), and the reaction mixture was stirred for 30 minutes at room temperature. After 30 minutes of the reaction, 1,3-dibromopropane (204.8 mmol) was added to the reaction mixture, and the

reaction was continued for 12 h. TLC monitored the completion of the reaction. Solvent DMF was removed by rotary evaporator, and the residue was extracted with chloroform (3 × 200 mL) and washed with water (3 × 100 mL). The combined organic layer was collected and dried over anhydrous sodium sulfate. The crude solid product was then mixed with silica gel (230-440 mesh) to make a slurry and subjected to flash chromatography using ethyl acetate and hexane as eluent. The pure compounds (**4.2**) were collected at 10 % EtOAc/Hexane.

**Yield:** 0.42 g (82%); m.p. 159-163°C.

**<sup>1</sup>H NMR 300 MHz, 25°C, Si(CH<sub>3</sub>)<sub>4</sub>, (CDCl<sub>3</sub>) (δ):** 2.55-2.58 (2H, m, CH<sub>2</sub>); 4.06-4.08 (2H, t, CH<sub>2</sub>); 4.22-4.25 (2H, t, CH<sub>2</sub>); 7.78-7.82 (1H, d, CH); 7.78-7.82 (1H, d, CH); 7.88-7.92 (1H, dd, CH); 7.88-7.92 (1H, dd, CH).



**Scheme 4.3**

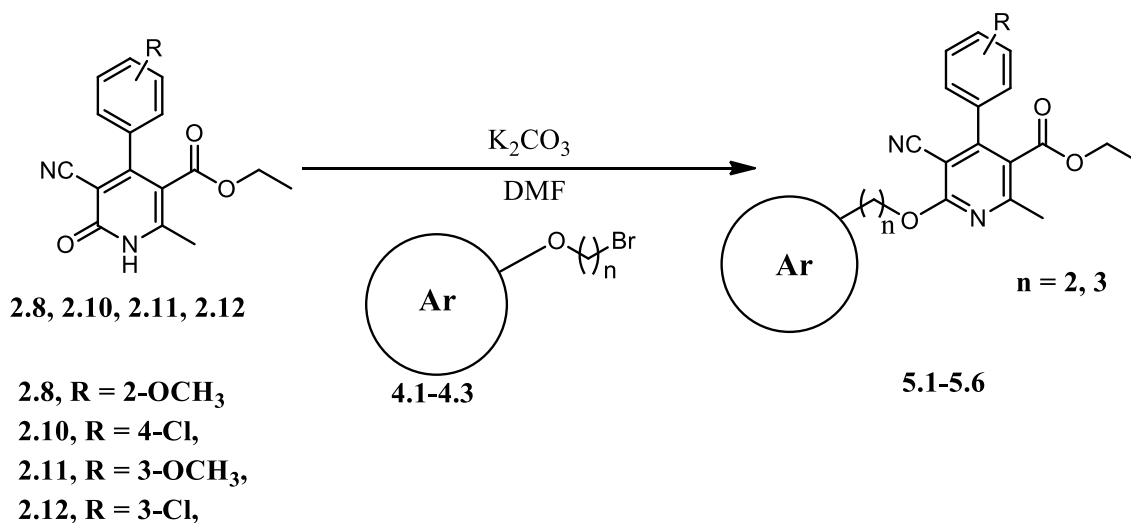
### 3.3.3 Synthesis of (3-bromopropoxy)benzene (**4.3**)

In a 100 mL round bottom flask, phenol (40.98 mmol) and potassium carbonate (40.98 mmol) were dissolved in 25 mL of dimethylformamide (DMF), and the reaction mixture was stirred for 30 minutes at room temperature. After 30 minutes of the reaction, 1,3-dibromopropane (204.8 mmol) was added to the reaction mixture, and the reaction was continued for 12 h. TLC monitored the completion of the reaction. Solvent DMF was removed by rotary evaporator, and the residue was extracted with chloroform (3 × 200 mL) and washed with water (3 × 100 mL). The combined organic layer was collected and dried over anhydrous sodium sulfate. The crude solid product was then mixed with silica gel (230-440 mesh) to make a slurry and subjected to flash chromatography using ethyl acetate and hexane as eluent. The pure compounds (**4.3**) were collected at 10 % EtOAc/Hexane.

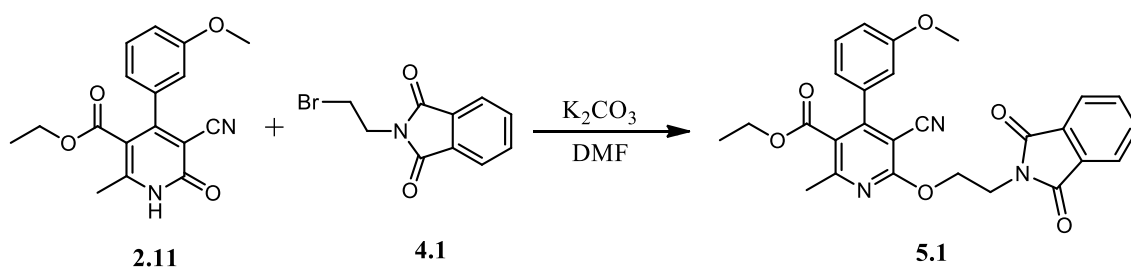
**Yield:** 0.42 g (79%); Liquid in nature

**<sup>1</sup>H NMR 300 MHz, 25°C, Si(CH<sub>3</sub>)<sub>4</sub>, (CDCl<sub>3</sub>) (δ):** 2.10-2.13 (2H, m, CH<sub>2</sub>); 3.75-3.77 (2H, t, CH<sub>2</sub>); 4.06-4.08 (2H, t, CH<sub>2</sub>); 6.88-6.91 (1H, d, CH); 6.89-6.92 (1H, d, CH); 7.10-7.13 (1H, dd, CH); 7.38-7.42 (1H, dd, CH); 7.38-7.42 (1H, dd, CH).

### 3.4. Scheme 5: Methylene-linked 2-pyridone derivatives with aromatic system



**Scheme 5**



**Scheme 5.1**

#### 3.4.1. Synthesis of ethyl 5-cyano-6-(2-(1,3-dioxisoindolin-2-yl)ethoxy)-4-(3-methoxyphenyl)-2-methylnicotinate (5.1)

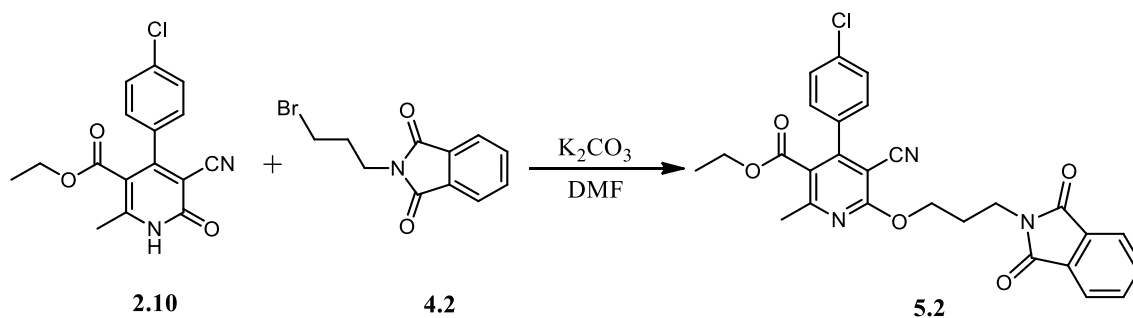
In a 100 ml round bottom flask, 2-pyridone derivative, **2.11** (2 g, 6.8 mmol) and potassium carbonate (1 g, 7.2 mmole) were taken in DMF and stirred for 20 min. After



20 min, 2-(2-bromoethyl)isoindoline-1,3-dione (**4.1**) (1.56 g, 6.8 mmole) was added and stirred it for 12 h. Completion of reaction was checked via TLC (30% EtOAc & Hexane). After completion of reaction DMF was removed under reduced pressure through rotary evaporator and the reaction mixture was extracted with EtOAc/ H<sub>2</sub>O (200/ 200 X 3 mL). The EtOAc layer was dried with anhydrous Na<sub>2</sub>SO<sub>4</sub> and filtered. EtOAc was removed and the product was purified via SiO<sub>2</sub>-flash chromatography. The pure compound (**5.1**) were collected at 15 % EtOAc/Hexane.

**Yield:** 2.1 g (65%); m.p. 217-219°C.

**<sup>1</sup>H NMR 300 MHz, 25°C, Si(CH<sub>3</sub>)<sub>4</sub>, (DMSO) (δ):** 0.98-1.00 (3H, t, CH<sub>3</sub>, *J*=7.2); 2.55 (3H, s, CH<sub>3</sub>); 3.83 (3H, s, CH<sub>3</sub>); 4.06-4.08 (2H, t, CH<sub>2</sub>, *J*=6.6); 4.22-4.25 (2H, q, CH<sub>2</sub>, *J*=6.9); 4.65-4.68 (2H, t, CH<sub>2</sub>, *J*=7.8); 6.95-6.99 (1H, d, CH, *J*=1.8); 7.08-7.11 (1H, d, CH, *J*=7.8); 7.36 (1H, s, CH); 7.45-7.48 (1H, t, CH, *J*=3); 7.78-7.82 (2H, dd, CH, *J*=3.3); 7.88-7.92 (2H, dd, CH, *J*=3.6); **<sup>13</sup>C NMR (75MHz, DMSO): (δ):** 14.1, 22.0, 26.7, 38.8, 60.9, 65.3, 91.6, 109.5, 114.6, 123.7, 125.5, 129.3, 129.5, 132.2, 134.8, 139.4, 154.5, 164.7, 169.7, 166.0, 167.9. **MS (m/z):** 486.16(M+1). **Element analysis:** (i). **Calculated:** C=66.80%; H=4.78%; N=8.66%; (ii). **Found:** C=66.65%; H=4.54%; N=8.47%.



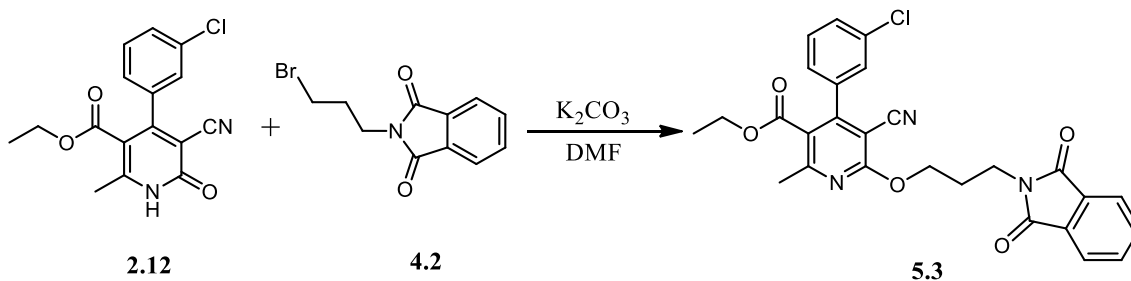
**Scheme 5.2**

### 3.4.2. Synthesis of ethyl 4-(4-chlorophenyl)-5-cyano-6-(3-(1,3-dioxisoindolin-2-yl)propoxy)-2-methylnicotinate (5.2)

In a 100 ml round bottom flask, 2-pyridone derivative, **2.10** (2 g, 6.8 mmol) and potassium carbonate (1 g, 7.2 mmole) were taken in DMF and stirred for 20 min. After 20 min, 2-(3-bromopropyl)isoindoline-1,3-dione (**4.2**) (1.56 g, 6.8 mmole) was added and stirred it for 12 h. Completion of reaction was checked via TLC (30% EtOAc & Hexane). After completion of reaction DMF was removed under reduced pressure through rotary evaporator and the reaction mixture was extracted with EtOAc/ H<sub>2</sub>O (200/ 200 X 3 mL). The EtOAc layer was dried with anhydrous Na<sub>2</sub>SO<sub>4</sub> and filtered. EtOAc was removed and the product was purified via SiO<sub>2</sub>-flash chromatography. The pure compound (**5.2**) were collected at 15 % EtOAc/Hexane.

**Yield:** 2.01 g (61%); m.p. 235-237°C.

**<sup>1</sup>H NMR 300 MHz, 25°C, Si(CH<sub>3</sub>)<sub>4</sub>, (DMSO) (δ):** 1.29-1.31 (3H, t, CH<sub>3</sub>, *J*=7.2); 2.18-2.22 (2H, m, CH<sub>2</sub>, *J*=6.3); 2.55 (3H, s, CH<sub>3</sub>); 4.06-4.08 (2H, t, CH<sub>2</sub>, *J*=6.6); 4.22-4.25 (2H, q, CH<sub>2</sub>, *J*=6.9); 4.65-4.68 (2H, t, CH<sub>2</sub>, *J*=7.8); 7.33-7.37 (2H, dd, CH, *J*=7.8); 7.55-7.59 (2H, dd, CH, *J*=3); 7.78-7.82 (2H, dd, CH, *J*=3.3); 7.88-7.92 (2H, dd, CH, *J*=3.6); **<sup>13</sup>C NMR (75MHz, DMSO) (δ):** 14.1, 22.0, 26.7, 38.8, 60.9, 65.3, 91.6, 109.5, 114.6, 123.7, 125.5, 129.3, 129.5, 132.2, 134.8, 139.4, 154.5, 164.7, 169.7, 166.0, 167.9. **MS (m/z):** 504.12(M+1). **Element analysis: (i). Calculated:** C=64.35%; H=4.40%; N=8.34%; **(ii). Found:** C=64.56%; H=4.23%; N=8.46%.



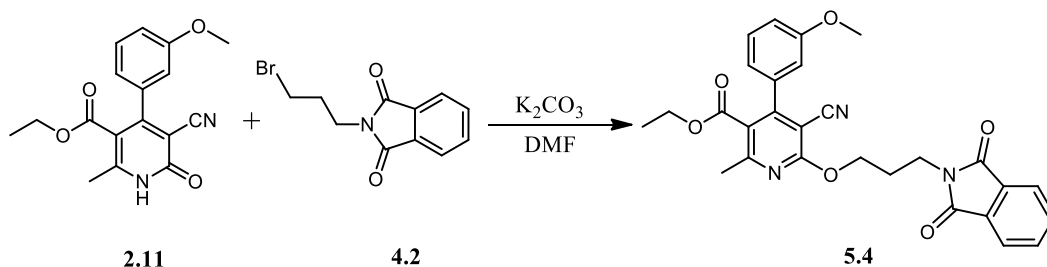
### Scheme 5.3

#### 3.4.3. Synthesis of ethyl 4-(3-chlorophenyl)-5-cyano-6-(3-(1,3-dioxoisindolin-2-yl)propoxy)-2-methylnicotinate (5.3)

In a 100 ml round bottom flask, 2-pyridone derivative, **2.12** (1 g, 6.8 mmol) and potassium carbonate (1 g, 7.2 mmole) were taken in DMF and stirred for 20 min. After 20 min, 2-(3-bromopropyl)isindoline-1,3-dione (**4.2**) (1.56 g, 6.8 mmole) was added and stirred it for 12 h. Completion of reaction was checked via TLC (30% EtOAc & Hexane). After completion of reaction DMF was removed under reduced pressure through rotary evaporator and the reaction mixture was extracted with EtOAc/ H<sub>2</sub>O (200/ 200 X 3 mL). The EtOAc layer was dried with anhydrous Na<sub>2</sub>SO<sub>4</sub> and filtered. EtOAc was removed and the product was purified via SiO<sub>2</sub>-flash chromatography. The pure compound (**5.3**) were collected at 15 % EtOAc/Hexane.

**Yield:** 1.99 g (58%); m.p. 213-216°C.

**<sup>1</sup>H NMR 300 MHz, 25°C, Si(CH<sub>3</sub>)<sub>4</sub>, (DMSO) (δ):** 1.29-1.31 (3H, t, CH<sub>3</sub>, *J*=7.2); 2.18-2.22 (2H, m, CH<sub>2</sub>, *J*=6.3); 2.55 (3H, s, CH<sub>3</sub>); 4.06-4.08 (2H, t, CH<sub>2</sub>, *J*=6.6); 4.22-4.25 (2H, q, CH<sub>2</sub>, *J*=6.9); 4.65-4.68 (2H, t, CH<sub>2</sub>, *J*=7.8); 7.40-7.43 (1H, d, CH, *J*=7.6); 7.45-7.48 (1H, t, CH, *J*=3); 7.48-7.451 (1H, d, CH, *J*=6.6); 7.78-7.82 (2H, dd, CH, *J*=3.3); 7.88-7.92 (2H, dd, CH, *J*= 3.6); 8.01-8.05 (1H, s, CH). **<sup>13</sup>C NMR (75MHz, DMSO): (δ):** 14.1, 22.0, 26.7, 38.8, 60.9, 65.3, 91.6, 109.5, 114.6, 123.7, 125.5, 129.3, 129.5, 132.2, 134.8, 139.4, 154.5, 164.7, 169.7, 166.0, 167.9. **MS (m/z):** 504.12(M+1). **Element analysis: (i). Calculated:** C=64.35%; H=4.40%; N=8.34%; **(ii). Found:** C=64.19%; H=4.66%; N=8.12%.



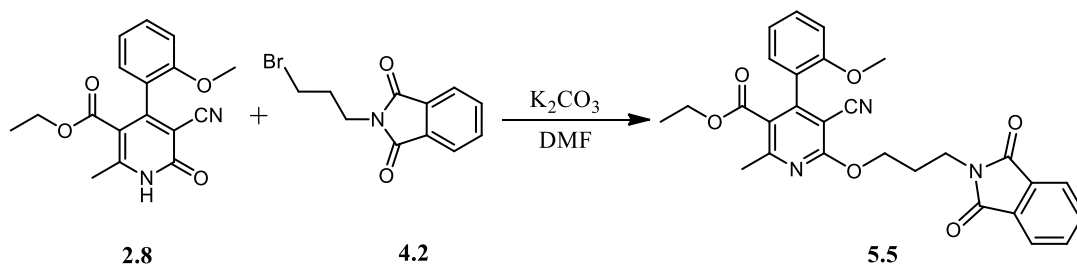
## Scheme 5.4

### 3.4.4. Synthesis of ethyl 5-cyano-6-(3-(1,3-dioxoisindolin-2-yl)propoxy)-4-(3-methoxyphenyl)-2-methylnicotinate (5.4)

In a 100 ml round bottom flask, 2-pyridone derivative, **2.11** (1 g, 6.8 mmol) and potassium carbonate (1 g, 7.2 mmole) were taken in DMF and stirred for 20 min. After 20 min, 2-(3-bromopropyl)isoindoline-1,3-dione (**4.2**) (1.56 g, 6.8 mmole) was added and stirred it for 12 h. Completion of reaction was checked via TLC (30% EtOAc & Hexane). After completion of reaction DMF was removed under reduced pressure through rotary evaporator and the reaction mixture was extracted with EtOAc/ H<sub>2</sub>O (200/ 200 X 3 mL). The EtOAc layer was dried with anhydrous Na<sub>2</sub>SO<sub>4</sub> and filtered. EtOAc was removed and the product was purified via SiO<sub>2</sub>-flash chromatography. The pure compound (**5.4**) were collected at 15 % EtOAc/Hexane.

**Yield:** 2.15 g (62%); m.p. 228-230°C.

**<sup>1</sup>H NMR 300 MHz, 25°C, Si(CH<sub>3</sub>)<sub>4</sub>, (DMSO) (δ):** 1.29-1.31 (3H, t, CH<sub>3</sub>, *J*=7.2); 2.18-2.22 (2H, m, CH<sub>2</sub>, *J*=6.3); 2.55 (3H, s, CH<sub>3</sub>); 3.83 (3H, s, CH<sub>3</sub>); 4.06-4.08 (2H, t, CH<sub>2</sub>, *J*=6.6); 4.22-4.25 (2H, q, CH<sub>2</sub>, *J*=6.9); 4.65-4.68 (2H, t, CH<sub>2</sub>, *J*=7.8); 6.95-6.99 (1H, d, CH, *J*=1.8); 7.08-7.11 (1H, d, CH, *J*=7.8); 7.36 (1H, s, CH); 7.45-7.48 (1H, t, CH, *J*=3.1); 7.78-7.82 (2H, dd, CH, *J*=3.5); 7.88-7.92 (2H, dd, CH, *J*=3.5); **<sup>13</sup>C NMR (75MHz, DMSO): (δ):** 14.1, 22.0, 26.7, 38.8, 60.9, 65.3, 91.6, 109.5, 114.6, 123.7, 125.5, 129.3, 129.5, 132.2, 134.8, 139.4, 154.5, 164.7, 169.7, 166.0, 167.9. **MS (m/z):** 500.17(M+1). **Element analysis: (i). Calculated:** C=67.33%; H=5.04%; N=8.41%; **(ii). Found:** C=67.56%; H=5.19%; N=8.69%.



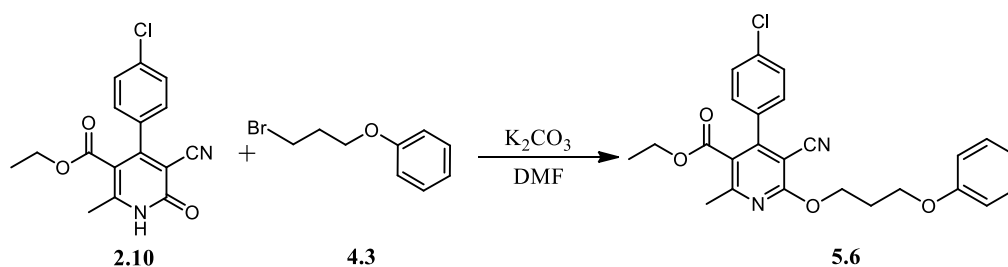
### Scheme 5.5

#### 3.3.5. Synthesis of ethyl 5-cyano-6-(3-(1,3-dioxoisindolin-2-yl)propoxy)-4-(2-methoxyphenyl)-2-methylnicotinate (5.5)

In a 100 mL round bottom flask, 2-pyridone derivative, **2.8** (1 g, 6.8 mmol) and potassium carbonate (1 g, 7.2 mmole) were taken in DMF and stirred for 20 min. After 20 min, 2-(3-bromopropyl)isoindoline-1,3-dione (**4.2**) (1.56 g, 6.8 mmole) was added and stirred it for 12 h. Completion of reaction was checked via TLC (30% EtOAc & Hexane). After completion of reaction DMF was removed under reduced pressure through rotary evaporator and the reaction mixture was extracted with EtOAc/ H<sub>2</sub>O (200/ 200 X 3 mL). The EtOAc layer was dried with anhydrous Na<sub>2</sub>SO<sub>4</sub> and filtered. EtOAc was removed and the product was purified via SiO<sub>2</sub>-flash chromatography. The pure compound (**5.5**) were collected at 15 % EtOAc/Hexane.

**Yield:** 2.2 g (69%); m.p. 217-219°C.

**<sup>1</sup>H NMR 300 MHz, 25°C, Si(CH<sub>3</sub>)<sub>4</sub>, (DMSO) (δ):** 1.27-1.29 (3H, t, CH<sub>3</sub>, *J*=7.1); 2.04-2.06 (2H, m, CH<sub>2</sub>, *J*=6.3); 2.53 (3H, s, CH<sub>3</sub>); 3.83 (3H, s, CH<sub>3</sub>); 4.05-4.07 (2H, t, CH<sub>2</sub>, *J*=6.7); 4.29-4.31 (2H, q, CH<sub>2</sub>, *J*=6.9); 4.54-4.55 (2H, t, CH<sub>2</sub>, *J*=7.6); 7.05-7.06 (1H, d, Ar-H, *J*=7.7); 7.07-7.11 (1H, m, Ar-H, *J*= 3.7); 7.30-7.31(1H, m, Ar-H, *J*=3.1); 7.67-7.68 (1H, d, Ar-H, *J*=3.3); 7.85-7.87 (2H, d, Ar-H, *J*=3.6); 7.88-7.90 (2H, d, Ar-H, *J*=3.8); **<sup>13</sup>C NMR (75MHz, DMSO): (δ):** 14.1, 22.0, 26.7, 38.8, 56.1, 60.9, 65.3, 91.6, 109.5, 114.6, 116.6, 121.5, 123.7, 127.1, 130.2, 130.3, 132.0, 154.5, 164.7, 164.9, 166.0, 167.9. **MS (m/z):** 500.17(M+1). **Element analysis: (i). Calculated:** C=67.33%; H=5.04%; N=8.41%; **(ii). Found:** C=67.89%; H=5.29%; N=8.19%.



## Scheme 5.6

### 3.4.6. Synthesis of ethyl 4-(4-chlorophenyl)-5-cyano-2-methyl-6-(3-phenoxypropoxy) nicotinate (5.6)

In a 100 ml round bottom flask, 2-pyridone derivative, **2.10** (1 g, 6.8 mmol) and potassium carbonate (1 g, 7.2 mmole) were taken in DMF and stirred for 20 min. After 20 min, (3-bromopropoxy)benzene (**4.3**) (1.56 g, 6.8 mmole) was added and stirred it for 12 h. Completion of reaction was checked via TLC (30% EtOAc & Hexane). After completion of reaction DMF was removed under reduced pressure through rotary evaporator and the reaction mixture was extracted with EtOAc/ H<sub>2</sub>O (200/ 200 X 3 mL). The EtOAc layer was dried with anhydrous Na<sub>2</sub>SO<sub>4</sub> and filtered. EtOAc was removed and the product was purified via SiO<sub>2</sub>-flash chromatography. The pure compound (**5.6**) were collected at 15 % EtOAc/Hexane.

**Yield:** 1.98 g (59%); m.p. 217-219°C.

**<sup>1</sup>H NMR 300 MHz, 25°C, Si(CH<sub>3</sub>)<sub>4</sub>, (DMSO) (δ):** 1.01-1.04 (3H, t, CH<sub>3</sub>, *J*=7.3); 2.18-2.22 (2H, m, CH<sub>2</sub>, 6.5); 2.51 (3H, s, CH<sub>3</sub>); 2.53 (3H, s, CH<sub>3</sub>); 2.55 (3H, s, CH<sub>3</sub>); 4.06-4.08 (2H, t, CH<sub>2</sub>, *J*=6.7); 4.22-4.25 (2H, q, CH<sub>2</sub>, *J*=7.1); 4.65-4.68 (2H, t, CH<sub>2</sub>, *J*=7.9); 6.12 (1H, s, CH); 7.33-7.37 (2H, dd, CH, *J*=3.4); 7.55-7.59 (2H, dd, CH, *J*=3.9); **<sup>13</sup>C NMR (75MHz, DMSO): (δ):** 14.1, 22.0, 26.7, 38.8, 60.9, 65.3, 91.6, 109.5, 114.6, 123.7, 125.5, 129.3, 129.5, 132.2, 134.8, 139.4, 154.5, 164.7, 169.7, 166.0, 167.9. **MS (m/z):** 451.13(M+1). **Element analysis: (i). Calculated:** C=66.59%; H=5.14%; N=6.21%; **(ii). Found:** C=66.25%; H=5.57%; N=6.42%.

## 3.5. Results and discussions

The compounds described in this chapter are synthesized to understand the effect of substitution of different electronic environments and the effect of the heteroaromatic ring in stacking flexible compounds' interactions, which changes electronic distribution on the system. The compounds were isolated at ≤20% EtOAc: Hexane by flash

chromatography. In this study, mainly intermolecular interactions have been observed. Not only stacking interaction but also many other weak interactions like CN... $\pi$ , CH...O, CH...N, etc., are stabilizing the network. Stacking interaction is a very weak interaction, so it is challenging to study weak interactions. It is studied with single-crystal X-ray diffraction and Hirshfeld surface analysis methods.

### 3.5.1. X-ray crystallographic studies and Hirshfeld surface analysis of compounds 5.1-5.6

Out of many single crystals, a suitable single crystal has been selected from each compound (5.1-5.6) for single-crystal X-ray diffraction. The structure of compound **5.1-5.6** have been solved by direct methods using SHELXTL, and all the non-hydrogen atoms were refined anisotropically by full-matrix least-squares on  $F^2$  using SHELXL2018. **Mercury 3.3** has been used for 3D structure visualization and packing diagrams. Carbon atoms were represented by grey color, hydrogen atoms white, oxygen atoms red, nitrogen atoms light blue, etc., in the packing diagram.

#### 3.5.1.1 X-ray crystal structure of compound 5.1

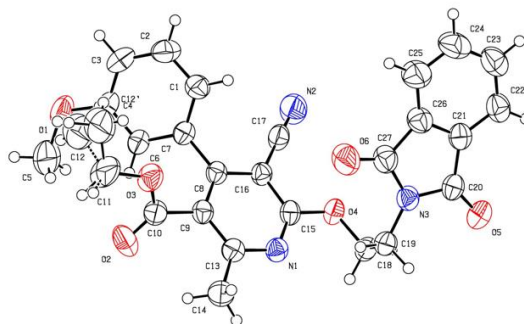


**Figure 3.4:** ORTEP diagram of compound **5.1**

#### 3.5.1.2. Table 3.1. Crystal data of compounds **5.1** and **5.2**

Compound	<b>5.1</b>	<b>5.2</b>
Identification code	2064031	2064032
Empirical formula	$C_{27}H_{22}N_3O_6$	$C_{27}H_{22}ClN_3O_5$
Formula weight	484.47	503.92
Temperature(K)	296.15	296.15
Crystal system	triclinic	monoclinic

Space group	<i>P</i> -1	<i>P</i> 21/ <i>c</i>
a(Å)	8.137(3)	23.437(10)
b(Å)	12.607(5)	8.357(4)
c(Å)	13.389(5)	12.600(6)
α(°)	70.173(5)	90
β(°)	77.494(5)	96.306(6)
γ(°)	75.410(5)	90
Volume(Å <sup>3</sup> )	1237.3(8)	2453(2)
Z	2	4
ρ (g/cm <sup>3</sup> )	1.300	1.365
μ(mm <sup>-1</sup> )	0.093	0.200
F(000)	506.0	1048.0
Crystal size(mm <sup>3</sup> )	0.22 × 0.17 × 0.14	0.19 × 0.17 × 0.12
Radiation	MoKα (λ = 0.71073)	MoKα (λ = 0.71073)
2θ range for data collection(°)	5.462 to 54.818	3.496 to 54.94
Reflections collected	10644	38462
Independent reflections	5375	5566
Data/restraints/parameters	5375/3/333	5566/0/335
Goodness-of-fit on F2	0.993	0.918
Final R indexes [I>=2σ (I)]	R1 = 0.0678, wR2 = 0.1788	R1 = 0.0642, wR2 = 0.1505
Final R indexes [all data]	R1 = 0.0962, wR2 = 0.2016	R1 = 0.1442, wR2 = 0.2022
Largest diff. peak/hole / e Å <sup>-3</sup>	0.40/-0.43	0.23/-0.31

### 3.5.1.3 Table 3.2. Intermolecular and intramolecular interactions in 5.1

D-H...A	D-H (Å)	H...A (Å)	D...A (Å)	D-H...A (°)
C25-H25...O1	0.930	2.682	3.520	150.29
C24-H24...O2	0.930	2.461	3.306	151.07
C1-H1... π (C1-C4, C6, C7)	0.930	3.642		
C18-H18... π (N1, C8, C9, C13, C15, C16)	0.970	3.290		
C23-H23... π (N3, C21, C22, C26, C27)	0.930	3.614		
C22-H22...π (N3, C21, C22, C26, C27)	0.930	3.897		
C22-H22...π (C21- C26)	0.930	3.667		
O4...π (N1, C8, C9, C13, C15, C16)		3.371		
C15... π (N1, C8, C9, C13, C15, C16)		3.366		
<b>Intramolecular</b>				
C18-H18A...O5	0.970	2.954	3.421	110.80
C6-H6...O2	0.930	2.850	3.414	120.16
C12-H12A... π (C1-C4, C6, C7)	0.930	3.029		
π (N3, C21, C22, C26, C27)...O4		3.593		

### Crystal analysis of 5.1



Single-crystal X-ray data for compound **5.1** were collected with an Oxford Diffraction Xcalibur CCD diffractometer. Crystallographic data of compound **5.1** have given in Table 3.1. The ORTEP diagram at a 50% probability along (010) of compound **5.1** is shown in Figure 3.4.

Compound **5.1** was crystallized with (15%) ethyl acetate: hexane mixture at room temperature. It possesses a triclinic crystal system having a, b, and c values of 8.137(3), 12.607(5), and 13.389(5) Å, respectively (Table 3.1). Intermolecular network ( $\pi$ ... $\pi$ , C-H...N, C-H...O interactions) leads to stabilizing self-assembly of molecules (Table 3.2). These were shown in Figures 3.5 and 3.6, as well as the packing diagram through different axes. **D** is the donor, and **A** is the acceptor in non-covalent interactions in Table 3.2.

All rings of compound **5.1** are in a different plane in the crystal structure. Compound **5.1** is an asymmetrical molecule in which the two rings are linked through a dimethylene linker.

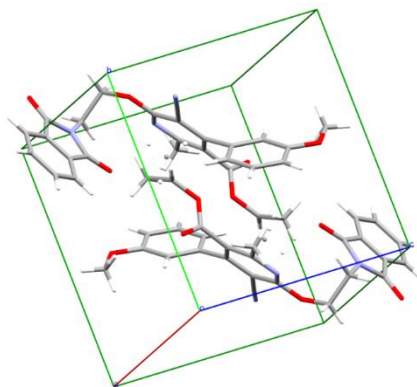


**Figure 3.5:** Packing diagram of molecule **5.1**

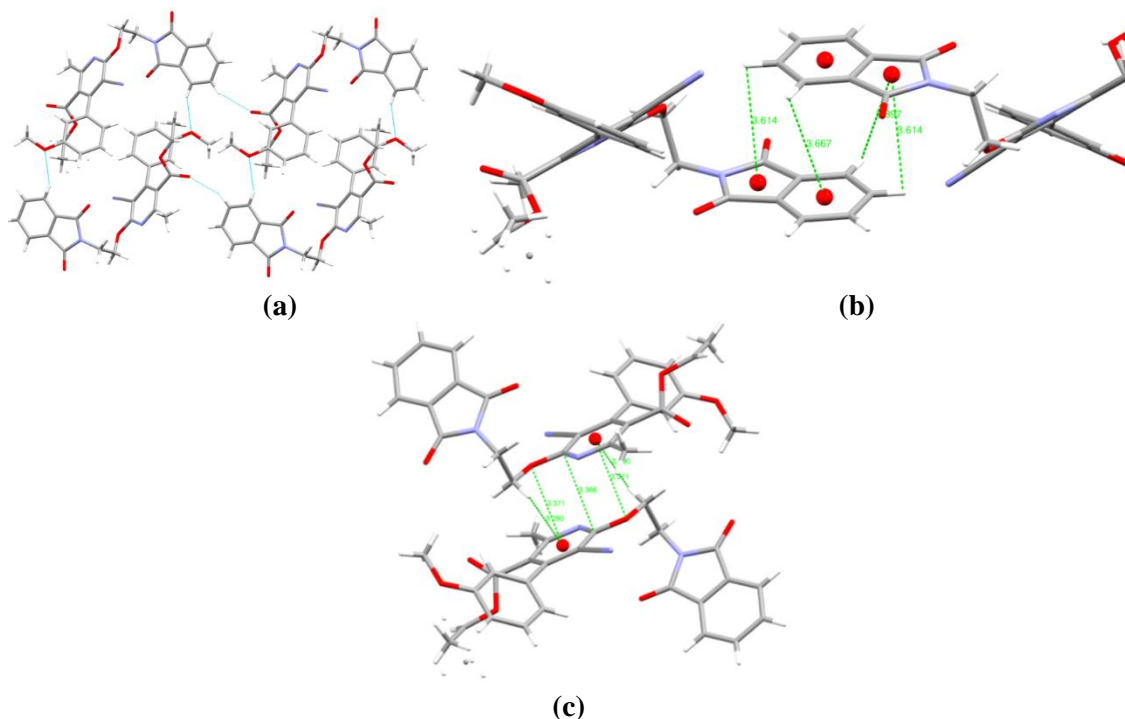


**Figure 3.6:** (a), (b) and (c) diagram showing non-covalent interactions in molecule **5.1**

The molecule is folded structure and exists in an AB pattern. C-H...O, C-H... $\pi$ , lone pair... $\pi$  intra-molecular weak interactions are present in this molecule, and the distance between the O...H is 2.954 and 2.850 Å, while aromatic interactions are 3.029 and 3.593 Å respectively.

The packing of compound **5.1** represented an interesting pattern of symmetrically arranged molecules. The overall intermolecular network is stabilized mainly through parallel/ off-set displaced C-H... $\pi$  interactions between the centroids of the tail of one molecule and the centroid of the head of another molecule. This will generate a stacked structure of compound **5.1** in which each molecule is stacked over each other generating a ladder-like formation that stabilizes the overall architecture. The distance between the parallel displaced C-H... $\pi$  interaction is 3.642, 3.290, 3.614, 3.897 Å, and 3.667 Å, respectively (Figure 3.7).

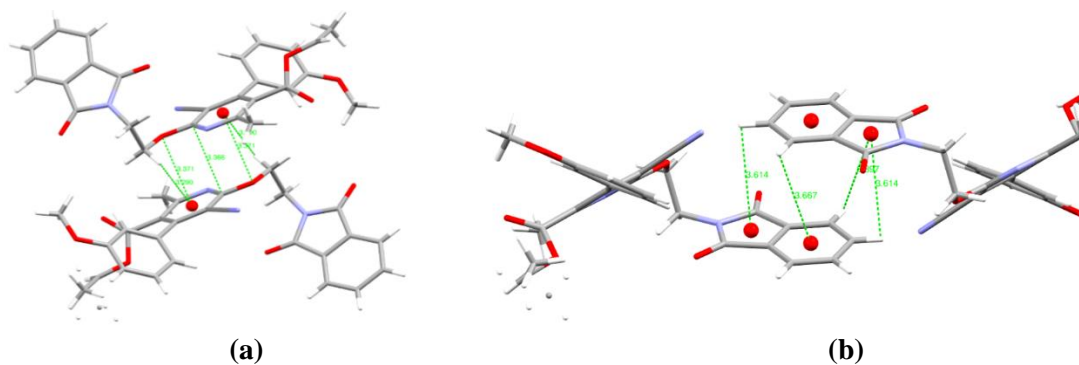
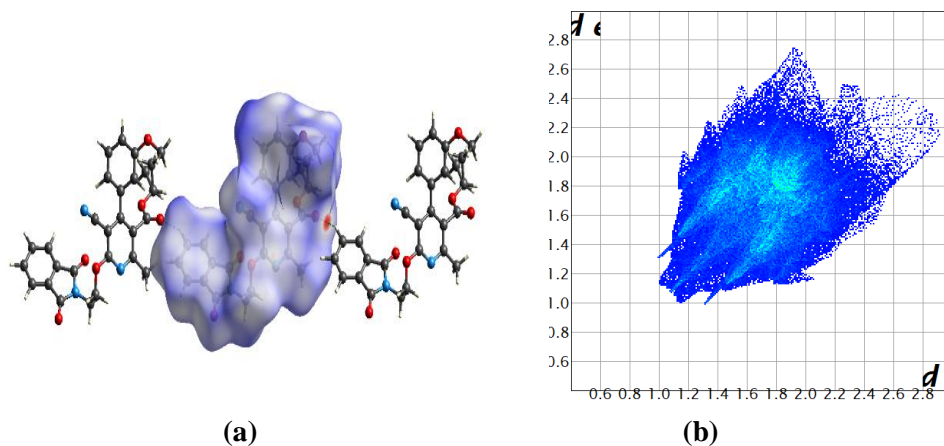


**Figure 3.7:** (a) and (b) C-H... $\pi$  and C-O- $\pi$  interactions in molecule **5.1**

The network is also supported by other non-covalent interactions in the form of lone pair... $\pi$  interactions. The distance between the O4 of one molecule and the centroid of the pyridone ring of another molecule is 3.371 Å. The distance between the 15<sup>th</sup> carbon of the tail and pyridone ring is found 3.366 Å, respectively. These weak interactions suggest that lone pairs and heads of one ring fall under the influence of the pyridone ring's electronic environment. This stacked architecture and different aromatic interactions are well visualized in Figures 3.6 and 3.7 of compound **5.1**.

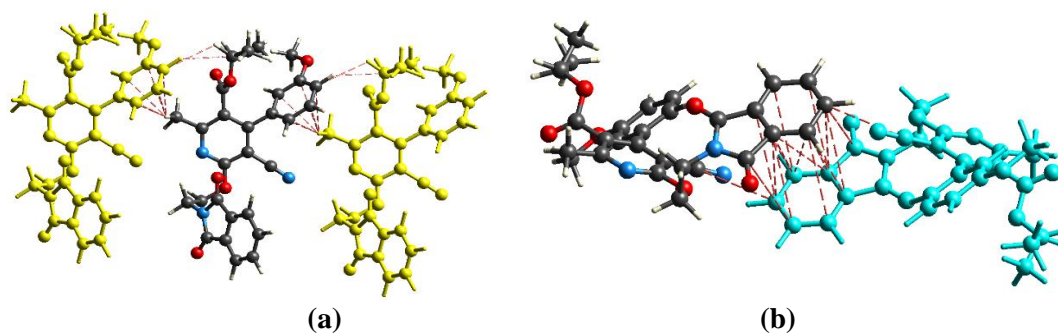
#### 3.5.1.4. Hirshfeld surface analysis of **5.1**

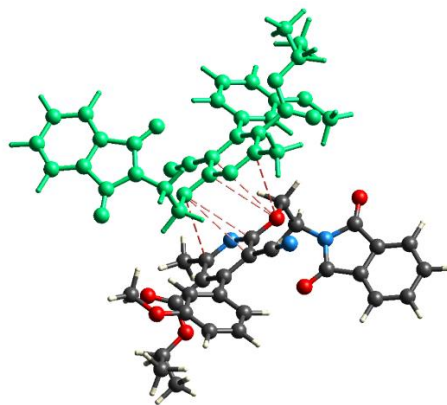
The Hirshfeld surface mapped on  $d_{\text{norm}}$  of compound **5.1** is displayed in Figure 3.8 (a). The red color represents the more dominant non-covalent C-H...O interactions involved in the crystal structure (Figure 3.8 (a)).



**Figure 3.8:** (a) Hirshfeld surface mapped on  $d_{\text{norm}}$  for compound **5.1**, (b) Two-dimensional fingerprint plot for compound **5.1**.

The 2D fingerprint plots represent the summary of weak intermolecular interactions in the crystal structure and provide information about the percentage contribution of a 3D Hirshfeld surface. The 2D fingerprint plots of compound **5.1** are shown in Figure 3.8 (b). The fingerprint analysis of compound **5.1** shows the percentage contribution of intermolecular interactions are C-C for around 2.7%, C-H for 15.7%, C-N for 1.0%, C-O for 2.8%, H-H for 43.5%, H-N for 10.2%, H-O for 23.0%, N-O for 0.7% and O-O for 0.4% of the close contacts in the Hirshfeld surfaces. The yellowish-red bin on the fingerprint plots is present in compound **5.1**, which means the presence of weak  $\pi$ - $\pi$  stacking interactions in the crystal packing (Figure 3.8 (b)). The spike-like pattern in the fingerprint plots of **5.1** represents the C-H...O interactions in the crystal lattice in the region of  $d_i + d_e = 2.3\text{-}2.9\text{\AA}$  (Figure 3.8 (b)). The C-H... $\pi$  interactions in **5.1** can be seen as a pair of unique blue-colored wings in the region of  $d_i + d_e = 3.0\text{-}3.6\text{\AA}$  (Figure 3.8 (b)). The C-H...N pair of contacts is also reflected as two characteristic wings occupied in the  $d_i + d_e = 2.9\text{-}3.4\text{\AA}$  in **5.1**. Figure 3.9 is showing Hirshfeld calculated weak non-covalent interactions of compound **5.1**. The Hirshfeld weak interactions calculation also supports the presence of weak non-covalent intermolecular interactions as in crystal packing. C-H... $\pi$  interactions, C-H...N, and C-H...O interactions of compound **5.1** in the crystal packing structure are in Figure 3.9. The C-H... $\pi$  and lone pair... $\pi$  weak interaction calculations of **5.1** are shown in Figures 3.9 (a), (b), and (c).





(c)

**Figure 3.9:** (a) C-H... $\pi$  interaction, (b)  $\pi$ ... $\pi$  interaction and (c) lone pair... $\pi$  interactions forming in Hirshfeld analysis of compound **5.1**

The curvedness plots and the Shape index plots of 3D Hirshfeld also reveal the various weak intermolecular interactions in compound **5.1**. Yellow spots represent the crystal structure's weak interactions, shown in Figure 3.10. The presence of green-colored flat regions in the curvedness plots indicated the presence of  $\pi$ ... $\pi$  stacking in the crystal structure of compound **5.1** (Figure 3.10 (a) and (b)). The red-yellow colored spots in curvedness plots show strong hydrogen-bonding interactions in the crystal structure.

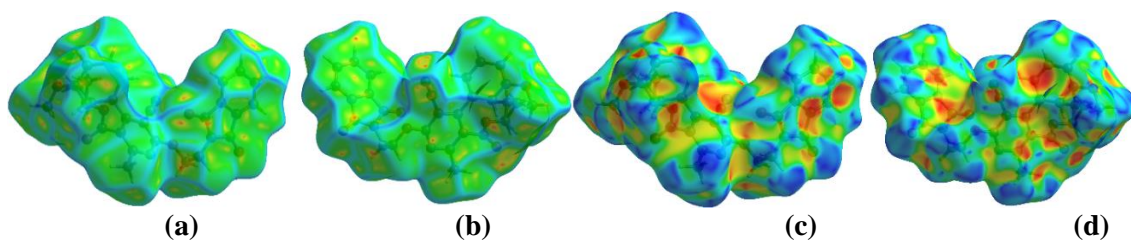


**Figure 3.10:** (a) and (b) Curvedness both side view of compound **5.1**, (c) and (d) Shape index both side view of compound **5.1**.

Red and blue areas represent the acceptor and the donor property, respectively, in the shape index of compound **5.1** (Figure 3.10 (c) and (d)). Yellowish-red colored concave regions indicate the presence of weak intermolecular interactions in the shape index plots. The presence of red and blue colored triangles on the surface of rings of the

molecule in the shape index plots also indicated the absence of weak  $\pi\cdots\pi$  stacking in the crystal structure (Figure 3.10 (c) and (d)).

### 3.5.1.5. X-ray crystal structure of compound 5.2

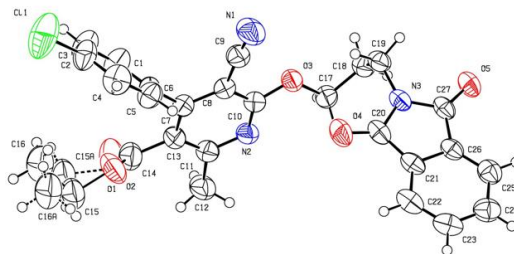


Figure 3.11: ORTEP diagram of compound 5.2

### 3.5.1.6 Table 3.3. Intermolecular and intramolecular interactions in 5.2

D-H...A	D-H (Å)	H...A (Å)	D...A (Å)	D-H...A (°)
C18-H18...O4	0.970	2.595	3.358	135.68
C24-H24...O5	0.970	2.521	3.386	148.52
C22-H22...O5	0.930	2.552	3.366	146.19
C23-H23...N2	0.930	2.735	3.577	151.01
C18-H18A... $\pi$ (C21-C16)	0.970	3.480		
C22-H22... $\pi$ (N3, C20, C21, C26, C27)	0.930	3.973		
C22-H22... $\pi$ (C21-C16)	0.930	3.835		
C23-H23... $\pi$ (N2, C7, C8, C10, C11, C13)	0.930	3.327		
C24-H24... $\pi$ (N2, C7, C8, C10, C11, C13)	0.970	3.441		
C15-H15A... $\pi$ (C1-C6)	0.930	3.548		
C15-H15B... $\pi$ (C1-C6)	0.930	3.788		
C16-H16A... $\pi$ (C1-C6)	0.970	3.833		
C16-H16B... $\pi$ (C1-C6)	0.970	3.278		
O5... $\pi$ (N3, C20, C21, C26, C27)		3.170		
<b>Intramolecular</b>				
C17-H17B...O(4)	0.970	2.856	3.335	111.44
C17-H17B... $\pi$ (N3, C20, C21, C26, C27)	0.970	3.477		
C16-H16A... $\pi$ (C1-C6)	0.970	3.278		
C16-H16B... $\pi$ (C1-C6)	0.970	3.833		

### Crystal analysis of 5.2

Compound 5.2 was crystallized with (5%) ethyl acetate: hexane mixture at room temperature. It possesses a monoclinic crystal system having a, b, and c values of

23.437(10), 8.357(4), and 12.600(6) Å, respectively (Table 3.1), ORTEP diagram in Figure 3.11. The summary of crystallographic information of compound **5.2** is listed in Table 3.1. Intermolecular network (lone pair... $\pi$ , C-H...  $\pi$ , C-H...N, C-H...O interactions) leads to stabilizing self-assembly of molecules (Table 3.3). These non-covalent interactions (Figure 3.13) and packing diagram (Figure 3.12) through different axes of compound **5.2** are shown below.

The heterocyclic pyridine ring (head) lies in one plane, and the benzaldehyde ring (tail) lies in another plane. Compound **5.2** is an asymmetrical molecule in which the two rings are separated through a dimethylene spacer.

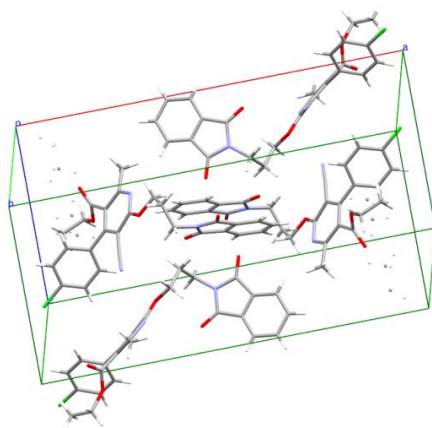


**Figure 3.12:** Packing diagram of molecule **5.2**

The molecule is folded structure and exists in two orthogonal planes in an AB pattern. C-H...O, C-H... $\pi$ , lone pair... $\pi$  intra-molecular weak interactions are present in this molecule, and the distance between the O...H is 2.856 Å. In contrast, aromatic interactions are 3.477, 3.278, and 3.833 Å respectively (Figure 3.13 and Table 3.3).

The packing of compound **5.2** represented an interesting three dimensional pattern of symmetrically arranged molecules. The overall intermolecular network is stabilized mainly through parallel/ off-set displaced C-H... $\pi$  interactions between the centroids of the different ring and another molecule's centroid. This will generate a stacked structure of compound **5.2** in which each molecule is stacked over each other



generating a spiral-like structure that stabilizes the overall architecture. The distance between the parallel displaced C-H... $\pi$  interaction is found 3.480, 3.973, 3.835, 3.327, 3.441, 3.548, 3.788, 3.833 Å and 3.278 Å, respectively (Figure 3.13 and Table 3.3).

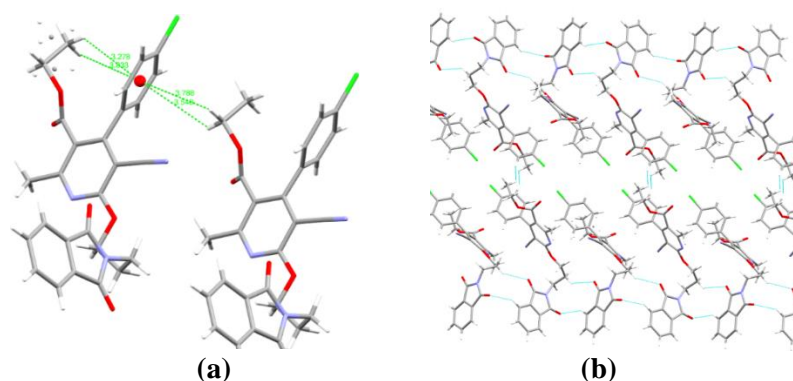


**Figure 3.13:** (a) and (b) diagram showing C-H... $\pi$  and C-N... $\pi$ , C-H...N, C-H...O interactions in molecule **5.2**

The network is also supported by other non-covalent interactions in the form of lone pair... $\pi$  interactions. The distance between O5 one molecule and centroid of phthalimide ring of the neighbour molecule is found 3.170 Å. Lone pairs of O5 and head of one ring fall under the influence of the pyridone ring's electronic environment. This stacked architecture and different aromatic interactions are well visualized in compound **5.2**.

### 3.5.1.7. Hirshfeld surface analysis of **5.2**

The Hirshfeld surface mapped on  $d_{\text{norm}}$  of compound **5.2** is displayed in Figure 3.14 (a). The red color represents the more dominant non-covalent C-H...O interactions involved in the crystal structure (Figure 3.14 (a)).



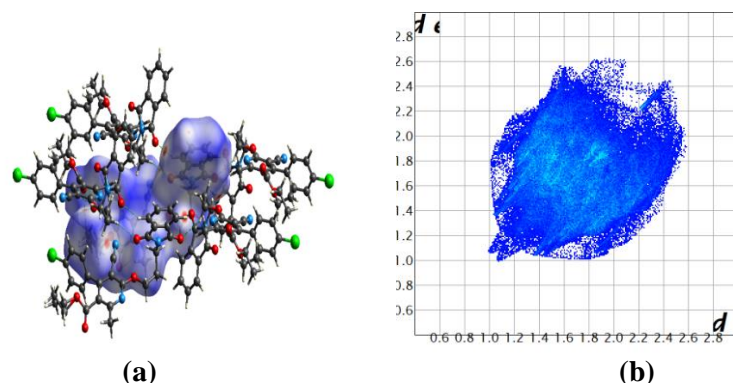


**Figure 3.14:** (a) Hirshfeld surface mapped on  $d_{\text{norm}}$  for compound **5.2**, (b) Two-dimensional fingerprint plot for compound **5.2**

The 2D fingerprint plots of compound **5.2** are shown in Figure 3.14 (b). The fingerprint analysis of compound **5.2** shows the percentage contribution of intermolecular interactions are C-C for around 1.4%, C-H for 19.5%, C-N for 0.8%, C-O for 2.4%, H-H for 36.3%, H-Cl for 10.4%, H-N for 9.8%, H-O for 17.2%, Cl-Cl for 0.5%, Cl-O for 0.2%, N-N for 0.5%, N-O for 0.8% and O-O for 0.1% of the close contacts in the Hirshfeld surfaces. The yellowish-red bin on the fingerprint plots is absent in compound **5.2**, which means the absence of weak  $\pi\cdots\pi$  stacking in the crystal structure (Figure 3.14 (b)). The spoke-like pattern in the fingerprint plots of **5.2** represents the C-H...O interactions in the crystal lattice in the region of  $d_i + d_e = 2.1\text{-}3.6$  Å (Figure 3.14 (b)). The C-H... $\pi$  interactions in **5.2** can be seen as a pair of unique blue-colored wings in the region of  $d_i + d_e = 2.8\text{-}3.6$  Å (Figure 3.14 (b)). The C-H...N pair of contacts is also reflected as two characteristic wings occupied in the  $d_i + d_e = 2.6\text{-}3.4$  Å in **5.2**. In addition, the C-H...Cl pair of contacts is also reflected as two characteristic wings occupied in the  $d_i + d_e = 3.2\text{-}3.8$  Å in **5.2**. Figure 3.15 represents the Hirshfeld calculated weak non-covalent interactions of compound **5.2**.

The Hirshfeld weak interactions calculation also supports the presence of weak non-covalent intermolecular interactions as in crystal packing. Where C-H... $\pi$  interactions, C...N and lone pair... $\pi$  interactions of compound **5.2** in the crystal packing structure are in Figures 3.15 (a), (b), and (c).

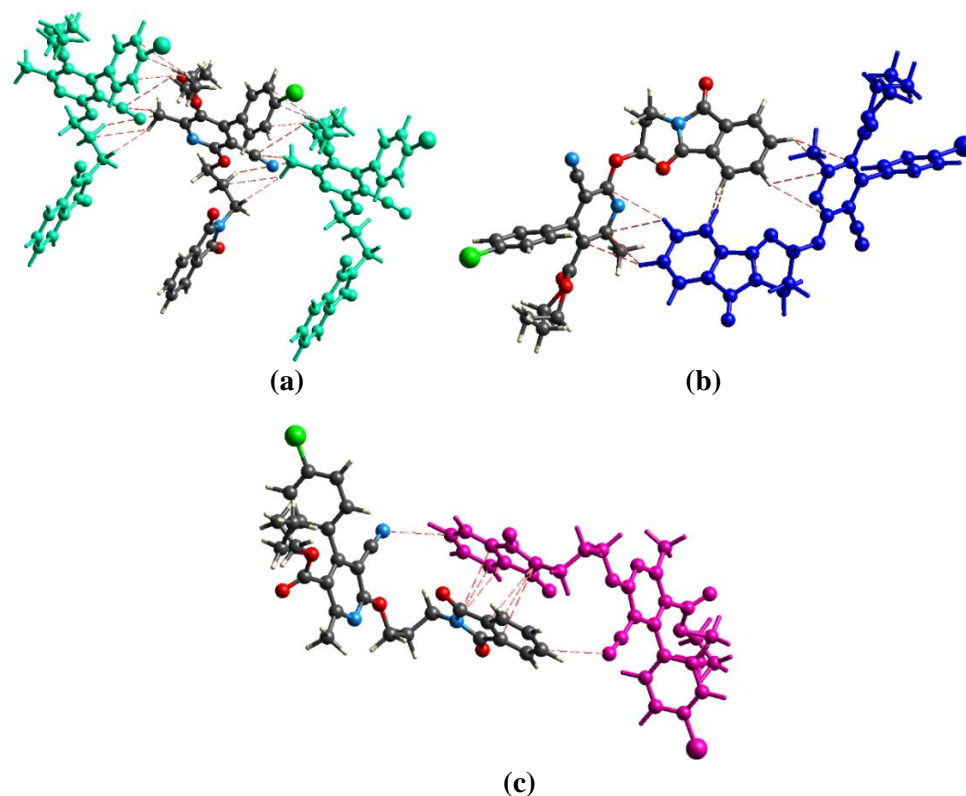


**Figure 3.15:** (a) and (b) C-H... $\pi$  interaction, (c) lone pair... $\pi$  interactions, and N...C interaction forming in Hirshfeld analysis of compound **5.2**.

The 3D Hirshfeld surface on Curvedness plots for compound **5.2** is shown in Figures 3.16 (a) and (b). In the Curvedness plots, very weak intermolecular interactions are seen inside the contours by yellow spots. The absence of green-colored flat regions provided the absence of  $\pi$ - $\pi$  stacking interaction in the crystal packing in Figures 3.16 (a) and (b). The shape index of compound **5.2** indicated the nature of interactions (i.e., donor and acceptor property) (Figure 3.16 (c) and (d)). The red and blue areas of the shape index indicated the acceptor and the donor property, respectively. In the Shape index plots of compound **5.2**, the missing red and blue colored triangles on the surface of rings of the molecule indicated the absence of  $\pi$ ... $\pi$  stacking interaction in the crystal packing. The yellowish-red colored concave regions on the Hirshfeld surface of compound **5.2** represent the weak intermolecular interactions in the crystal packing.

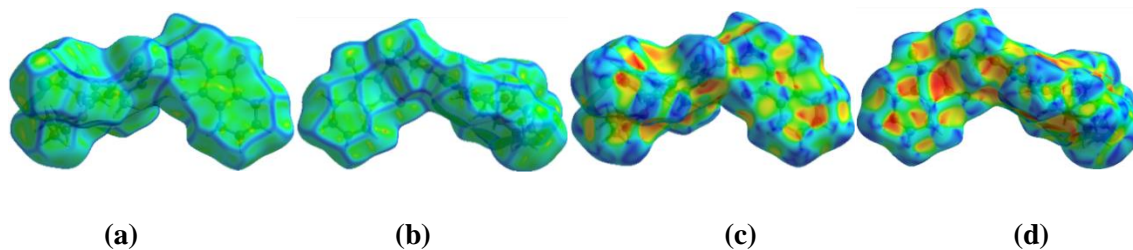


**Figure 3.16:** (a) and (b) Curvedness both side view of compound **5.2**, (c) and (d) Shape index both side view of compound **5.2**.

### 3.5.1.8. X-ray crystal structure of compound **5.3**

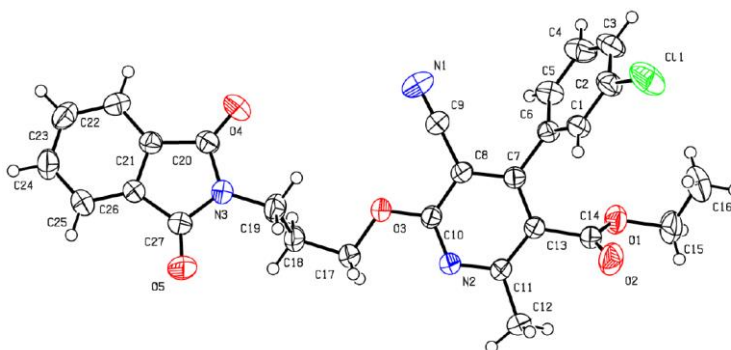


**Figure 3.17:** ORTEP diagram of compound **5.3**

### 3.5.1.9. Table 3.4. Crystal data of compounds **5.3** and **5.4**

Compound	<b>5.3</b>	<b>5.4</b>
Identification code	2064029	2062952
Empirical formula	$C_{27}H_{22}ClN_3O_5$	$C_{28}H_{25}N_3O_6$
Formula weight	503.92	499.51
Temperature(K)	296.15	296
Crystal system	Triclinic	Triclinic
Space group	<i>P-1</i>	<i>P-1</i>
a(Å)	8.334(3)	8.296(8)
b(Å)	12.154(4)	12.579(12)
c(Å)	14.031(5)	23.36(2)
$\alpha$ (°)	64.354(4)	87.172(10)
$\beta$ (°)	88.856(5)	83.908(10)
$\gamma$ (°)	80.732(8)	89.644(11)
Volume(Å <sup>3</sup> )	1262(8)	2421(4)
Z	2	4
$\rho$ (g/cm <sup>3</sup> )	1.326	1.370

$\mu(\text{mm}^{-1})$	0.194	0.098
F(000)	524.0	1048.0
Crystal size( $\text{mm}^3$ )	$0.23 \times 0.19 \times 0.13$	$0.22 \times 0.18 \times 0.14$
Radiation	MoK $\alpha$ ( $\lambda = 0.71073$ )	MoK $\alpha$ ( $\lambda = 0.71073$ )
2 $\Theta$ range for data collection( $^\circ$ )	2.85 to 27.26	0.878 to 26.158
Reflections collected	21353	30582
Independent reflections	5626	9376
Data/restraints/parameters	5626/0/327	9376/3/673
Goodness-of-fit on F2	1.038	1.028
Final R indexes [ $I \geq 2\sigma(I)$ ]	R1 = 0.0510, wR2 = 0.1345	R1 = 0.1183, wR2 = 0.3168
Final R indexes [all data]	R1 = 0.0652, wR2 = 0.1479	R1 = 0.1186, wR2 = 0.3935
Largest diff. peak/hole / $e \text{ \AA}^{-3}$	0.45/-0.48	0.60/-0.63

**3.5.1.10. Table 3.5.** Intermolecular and intramolecular interactions in **5.3**

D-H...A	D-H ( $\text{\AA}$ )	H...A ( $\text{\AA}$ )	D...A ( $\text{\AA}$ )	D-H...A ( $^\circ$ )
C1-H1...N2	0.930	2.652	3.534	158.37
C23-H23...N1	0.930	2.581	3.499	169.28
C22-H22...O4	0.930	2.436	3.362	173.87
C18-H18B...O4	0.970	2.686	3.346	125.69
C22-H22...N2	0.930	3.114	3.471	104.83
C12-H12C...O4	0.960	3.228	3.937	132.18
C15-H15A...N1	0.970	3.527	3.811	99.60
C12-H12B...N1	0.960	2.829	3.729	156.60
C17-H17A...O2	0.970	2.898	3.443	116.55
C19-H19A...O2	0.970	3.135	3.503	104.31
C17-H17A...C11	0.970	3.162	3.847	128.98
C5-H5... $\pi$ (C25, C24, C23, C22, C21, CC26)	0.930	3.441		
C8... $\pi$ (C25, C24, C23, C22, C21, CC26)		3.704		
$\pi$ (C25, C24, C23, C22, C21, CC26)... $\pi$ (C8, C7, C13, C11, N2, C10)		3.882		
C23-H23... $\pi$ (C8, C7, C13, C11, N2, C10)	0.930	3.651		
C22-H22... $\pi$ (C8, C7, C13, C11, N2, C10)	0.930	3.430		
C22... $\pi$ (C8, C7, C13, C11, N2, C10)		3.428		
C23... $\pi$ (C8, C7, C13, C11, N2, C10)		3.572		
C11... $\pi$ (C20, N3, C26, C27, C21)		3.399		
<b>Intramolecular</b>				
C22-H22...O4	0.930	3.032	3.152	88.78
C19-H19B...O4	0.970	2.553	2.900	101.03
C18-H18A...N3	0.970	2.648	2.462	68.37
C18-H18A...O5	0.970	2.900	3.404	113.43
C19-H19B...O3	0.970	2.617	2.946	100.07
C17-H17A...N2	0.970	2.593	2.658	83.20

C17-H17B...N2	0.970	2.623	2.658	81.49
C16-H16A... $\pi$ (C1-C6)	0.970	3.748		
C16-H16B... $\pi$ (C1-C6)	0.970	3.486		

### Crystal analysis of 5.3

Crystallographic data of compound **5.3** demonstrated in Table 3.4. The ORTEP diagram at a 50% probability along (010) of compound **5.3** is in Figure 3.17, and the packing diagram of compound **5.3** views is shown in Figure 3.18. Compound **5.3** was crystallized with (15%) ethyl acetate: hexane mixture at room temperature. It possesses a triclinic crystal system having a, b, and c values of 8.334(3), 12.154(4), and 14.031(5) Å<sup>o</sup>, respectively (Table 3.4). The compound **5.3** crystallizes in the P-1 space group. The molecular structure of compound **5.3** is non-planar.

In the crystal structure, molecules are linked together by different inter and intramolecular non-covalent interactions such as C-H...O, C-H... $\pi$ ,  $\pi$ ... $\pi$ , C-H...N, C-H...C, etc.(Table 3.5, Figure 3.19 and 3.20). These weak non-covalent interactions stabilize the crystal packing structure of compound **5.3**, shown in Figures 3.19 and 3.20. The heterocyclic pyridine ring and phthalimide ring lie in one plane, and the substituted phenyl ring lies in another plane. Compound **5.3** is an asymmetrical molecule in which the two rings are separated through a dimethylene linker.

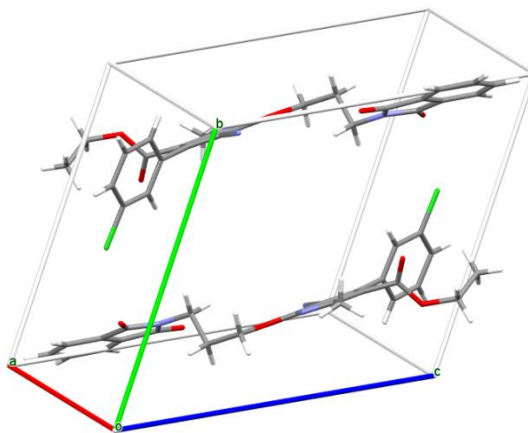


**Figure 3.18:** Packing diagram of molecule **5.3**

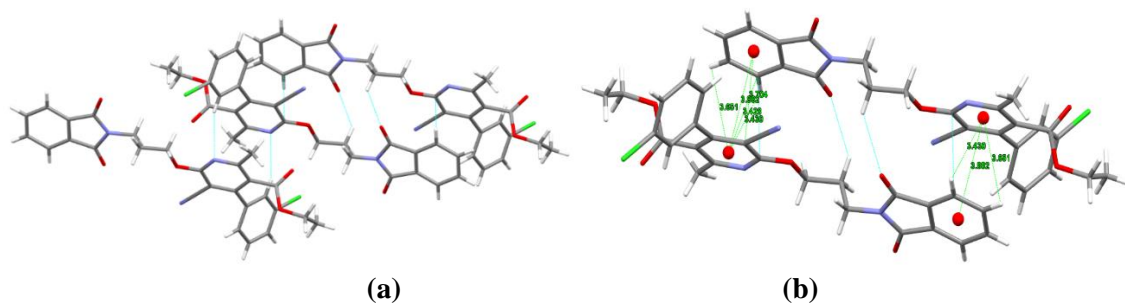


**Figure 3.19:** (a) C-H...O, C-H...N, N...C interactions in molecule **5.3**, (b) C-H... $\pi$  interactions of compound **5.3**

The molecule is folded structure and exists in two orthogonal planes in an AB pattern. C-H...O, C-H...N, C-H... $\pi$  intra-molecular weak interactions are present in this molecule. There are four C-H...O intra-molecular weak interactions are present in this molecule, and the distance between the O...H are 3.032, 2.553, 2.900, and 2.617 Å, respectively (Table 3.5). The distance between N...H of three C-H...N intra-molecular weak interactions are 2.648, 2.593, and 2.623 Å, respectively. The aromatic C-H... $\pi$  intra-molecular interaction of **5.3** is also observed with the distance of 3.486 and 3.748 Å, respectively (Table 3.5).

The packing of compound **5.3** represented an interesting pattern of symmetrically arranged molecules. The overall intermolecular network is stabilized mainly through parallel/ off-set displaced C-H... $\pi$  interactions between the centroids of the different ring and the other molecule's centroid. These interactions generate a stacked structure of compound **5.3** in which each molecule is piled over each other generating a helical structure that stabilizes the overall architecture. The distance between the parallel displaced C-H... $\pi$  interaction is found to be 3.441, 3.651, and 3.430 Å, respectively (Figure 3.19 (b) and Table 3.5). The extended structure of compound **5.3** is also having three intermolecular C... $\pi$  interactions in the crystal packing between C8, C22, C23, and  $\pi$ -electrons of the ring of an adjacent molecule of **5.3** structure with the distances of 3.704, 3.428, and 3.572 Å, respectively (Table 3.5).

The network is also supported by other non-covalent interactions in the form of lone pair... $\pi$  interactions. The distance between the Cl of one molecule and the centroid of the other molecule's phthalimide ring is 3.399 Å. It suggests that these lone pairs and heads of one ring fall under the electronic environment pyridone ring's influence. This stacked architecture and different aromatic interactions are well visualized in Figure 3.20 (b) of compound **5.3**.

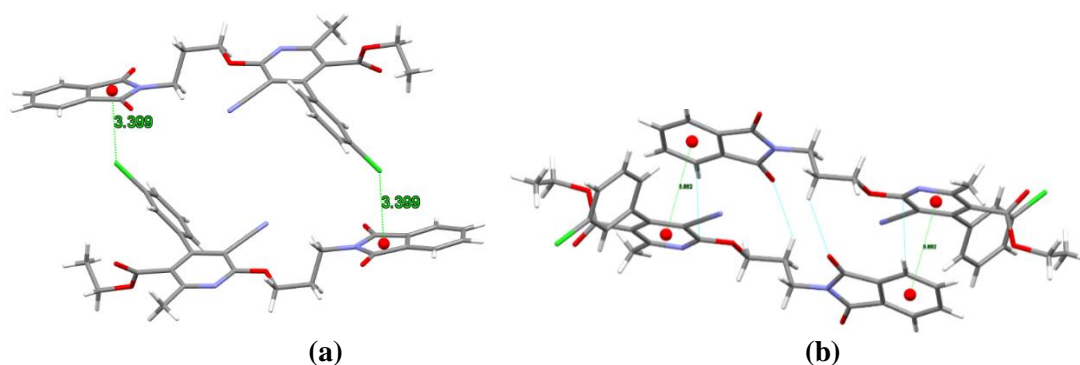


**Figure 3.20:** (a) lone pair... $\pi$  interactions of **5.3** and (b)  $\pi$ - $\pi$  interactions of **5.3**

The compound **5.3** also exhibited  $\pi$ - $\pi$  stacking between phenyl ring of phthalimide moiety and pyridine planes in the same orientation due to the planarity and unequal electronic distribution of the ring's surface (Figure 3.20 (b)). The observed  $\pi$ - $\pi$  stacking with the distance of 3.882 Å is shown in Figure 3.20 (b).

#### 3.5.1.11. Hirshfeld analysis for **5.3**

The Hirshfeld surface mapped on  $d_{\text{norm}}$  of compound **5.3** is displayed in Figure 3.21 (a). The red color represents the more dominant non-covalent C-H...O interactions involved in the crystal structure (Figure 3.21 (a)).

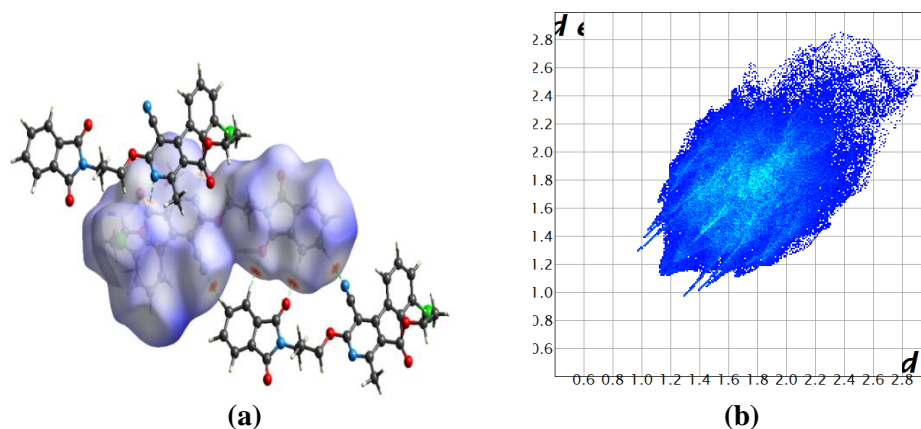


**Figure 3.21:** (a) Hirshfeld surface mapped on  $d_{\text{norm}}$  for compound **5.3**, (b) Two-dimensional fingerprint plot for compound **5.3**.

The 2D fingerprint plots of compound **5.3** are shown in Figure 3.21 (b). The fingerprint analysis of compound **5.3** shows the percentage contribution of intermolecular interactions, and those are C-C for around 3.9%, C-H for 13.9%, C-Cl for 3.2%, C-N for 1.0%, C-O for 1.9%, H-H for 39.2%, H-Cl for 6.5%, H-N for 10.1%, H-O for 18.1%, Cl-N for 0.6%, N-O for 0.9% and O-O for 0.7% of the close contacts in the Hirshfeld surfaces (Figure 3.21 (b)). There are prominent yellowish-red bins in the fingerprint plots indicating the presence of weak  $\pi\cdots\pi$  stacking (Figure 3.21 (b)). The spoke-like pattern in the fingerprint plots of **5.3** represents the C-H...O interactions in the crystal lattice in the region of  $d_i + d_e = 2.3\text{-}2.9\text{ \AA}$  (Figure 3.21 (b)). The second spoke-like pattern in the fingerprint plots of **5.3** represents the C-H...Cl interactions in the crystal lattice in the region of  $d_i + d_e = 2.4\text{-}4.0\text{ \AA}$  (Figure 3.21 (b)). The C-H... $\pi$  interactions in **5.3** can be seen as a pair of unique blue-colored wings in the region of  $d_i + d_e = 3.2\text{-}3.6\text{ \AA}$  (Figure 3.21 (b)). The C-H...N pair of contacts is also reflected as two characteristic wings occupied in the  $d_i + d_e = 2.9\text{-}4.0\text{ \AA}$  in **5.3**. Figure 3.22 is showing Hirshfeld calculated weak non-covalent interactions of compound **5.3**.

The Hirshfeld weak interactions calculation also supports the presence of weak non-covalent intermolecular interactions as in crystal packing. Aromatic  $\pi\text{-}\pi$  stacking,



C-H... $\pi$  interactions, C-H...N, lone pair... $\pi$  and C-H...O interactions of compound **5.3** in the crystal packing structure are in Figure 3.22.

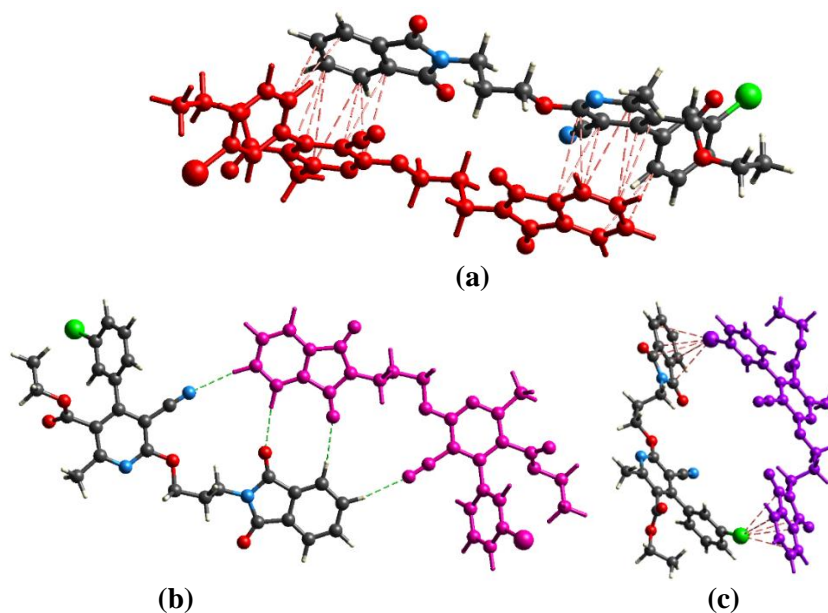


**Figure 3.22:** (a)  $\pi$ ... $\pi$  and C-H... $\pi$  interactions of **5.3**, (b) C-H...N and C-H...O interactions of compound **5.3**, and (c) lone pair... $\pi$  forming in Hirshfeld analysis of compound **5.3**

The 3D Hirshfeld surface on Curvedness plots for compound **5.3** is shown in Figures 3.23 (a) and (b). In the Curvedness plots, very weak intermolecular interactions are seen inside the contours by yellow spots. The presence of green-colored flat regions in the curvedness plot shows  $\pi$ - $\pi$  stacking interaction in the crystal packing. The red-yellow colored spots in curvedness plots show strong hydrogen-bonding interactions in the crystal structure of **5.3**.

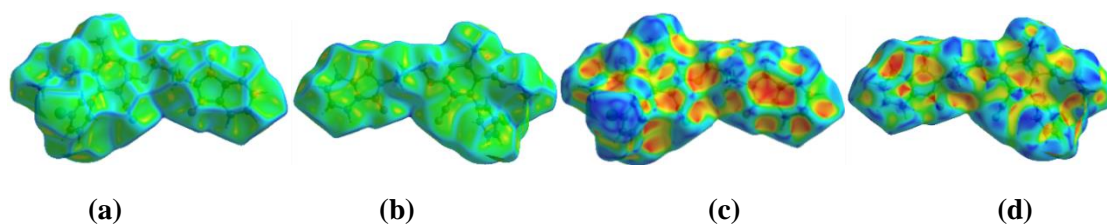


**Figure 3.23:** (a) and (b) Curvedness both side view of compound **5.3**, (c) and (d) Shape index both side view of compound **5.3**.

The shape index of compound **5.3** indicated the nature of interactions (i.e., donor and acceptor property) (Figure 3.23 (c) and (d)). The red and blue areas of the shape index indicated the acceptor and the donor property, respectively. In the shape index plots of compound **5.3**, the yellowish-red colored concave regions on the Hirshfeld surface represent the weak intermolecular interactions in the crystal packing. The presence of red and blue colored triangles on the surface of rings of the molecule indicated that there is  $\pi$ - $\pi$  stacking interaction in the crystal packing.

#### 3.5.1.12. X-ray crystal structure of compound **5.4**

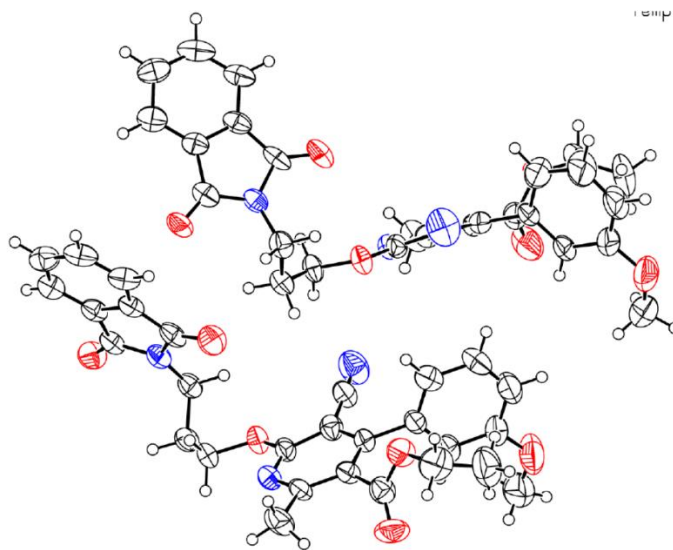


**Figure 3.24:** ORTEP diagram of compound **5.4**

#### 3.5.1.13. Table 3.6. Intermolecular and intramolecular interactions in **5.4**

D-H...A	D-H (Å)	H...A (Å)	D...A (Å)	D-H...A (°)
C52-H52...N5	0.930	2.741	3.586	151.53
C46-H46B...O6	0.970	2.469	3.340	149.35
C52-H52...O11	0.930	3.106	3.511	108.37
C52-H52...O10	0.930	3.706	4.589	159.78
C51-H51...O11	0.929	3.530	3.715	94.18
C51-H51...O6	0.929	2.539	3.344	145.03
C19-H19A...O11	0.970	2.601	3.385	138.05

C53-H53...N5	0.931	3.603	4.014	109.72
C47-H47B...O5	0.970	2.649	3.378	132.16
C23-H23...O12	0.930	2.585	3.365	144.44
C24-H24...O12	0.929	3.338	3.753	109.63
C47-H47A...O5	0.971	3.557	3.378	71.57
C47-H47A... $\pi$ (C22-C27)	0.971	3.310		
C47-H47B... $\pi$ (C22-C27)	0.971	3.365		
C48-H48A... $\pi$ (C22-C27)	0.970	3.362		
C52-H52... $\pi$ (C40, N5, C39, C37, C36, C42)	0.930	3.308		
C53-H53... $\pi$ (C40, N5, C39, C37, C36, C42)	0.931	3.438		
C16-H16A... $\pi$ (C1, C2, C4, C5, C6, C7)	0.970	3.465		
C16-H16B... $\pi$ (C1, C2, C4, C5, C6, C7)	0.970	3.613		
O12... $\pi$ (N3, C28, C27, C22, C21)		3.180		
C47... $\pi$ (C22-C27)		3.710		
<b>Intramolecular</b>				
C48-H48B...O11	0.970	2.874	3.351	111.37
C13-H13A...O2	0.960	2.425	3.091	126.25
C20-H20A...O4	0.970	2.462	2.845	103.19
C18-H18B...N2	0.971	2.630	2.711	84.26
C20-H20A...N1	0.970	3.613	4.562	166.25
C17-H17B... $\pi$ (C1, C2, C4, C5, C6, C7)	0.970	3.207		
C17-H17C... $\pi$ (C1, C2, C4, C5, C6, C7)	0.970	3.785		
O3... $\pi$ (C1, C2, C4, C5, C6, C7)		3.613		
C17... $\pi$ (C1, C2, C4, C5, C6, C7)		3.870		

#### Crystal analysis of 5.4

The ORTEP diagram at a 50% probability along (010) of compound **5.4** is shown in Figure 3.24, and the packing diagram of compound **5.4** views is shown in Figure 3.25. Compound **5.4** was crystallized with (15%) ethyl acetate: hexane mixture at room temperature. It possesses a triclinic crystal system having a, b, and c values of 8.296(8), 12.579(12), and 23.36(2) Å, respectively (Table 3.6). The compound **5.4** crystallizes in the P-1 space group. The summary of crystallographic information of compound **5.4** is listed in Table 3.4. The molecular structure of compound **5.4** is non-planar.

In the crystal structure, molecules are linked together by different inter and intramolecular non-covalent interactions such as C-H...O, C-H... $\pi$ ,  $\pi$ ... $\pi$ , C-H...N, C-H...C, etc. (Table 3.6 and Figure 3.26). All these weak non-covalent interactions stabilize the crystal packing structure of compound **5.4**. Inter-molecular network ( $\pi$ ... $\pi$ , C-H...N, C-H...O interactions) leads to stabilizing self-assembly of molecules (Table 3.6).

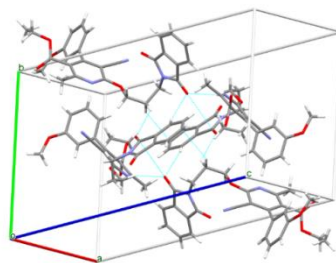


**Figure 3.25:** Packing diagram of molecule **5.4**

In the packing diagram, all the rings, pyridone, phthalimide ring, and the substituted phenyl ring, lies in a different plane. There are some C-H...O interactions, and one C...O interaction has been observed in the packing diagram of compound **5.4** (Figure 3.25). Compound **5.4** is an asymmetrical molecule in which the two rings are separated through a dimethylene spacer.

The packing of compound **5.4** represented an interesting pattern of symmetrically arranged molecules. The overall intermolecular network is stabilized mainly through parallel/ off-set displaced C-H... $\pi$  interactions between the centroids of the different ring and another molecule's centroid. This will generate a stacked structure of compound **5.4**, where each molecule is linked with each other, like a DNA helical structure that stabilizes the overall architecture. The extended structure of compound **5.4** is also having seven intermolecular, C-H... $\pi$  interactions in the crystal packing between C47-H47A, C47-H47B, C48-H48A, C52-H52, C53-H53, C16-H16A, C16-H16B, and  $\pi$ -electrons of the ring of an adjacent molecule with the distance of 3.3.310, 3.365, 3.362, 3.308, 3.438, 3.465 Å and 3.613 Å, respectively (Figure 3.26 and Table 3.6).

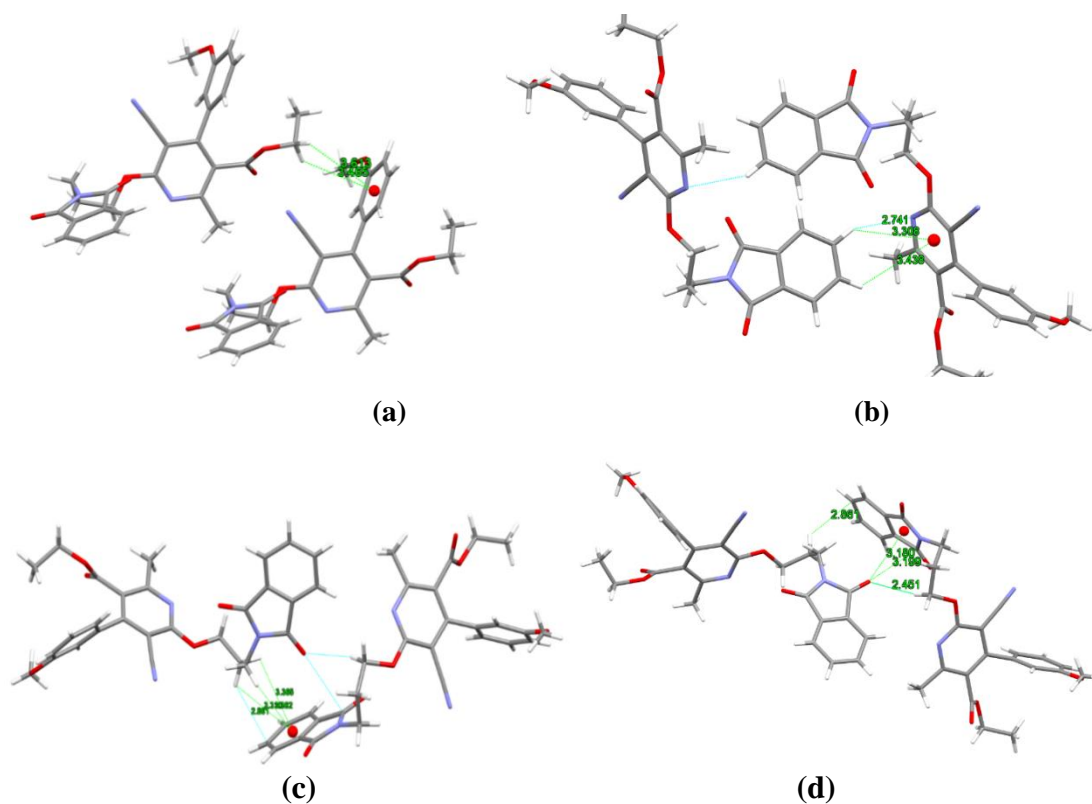


**Figure 3.26:** (a), (b) and (b) C-H... $\pi$ , C-H...O, and C-H...N interactions of **5.4**, and (d) Lone pair... $\pi$  interaction of **5.4**

The molecule is folded structure and exists in two orthogonal planes in an ABC pattern. C-H...O, C-H...N, C-H... $\pi$  intra-molecular weak interactions are present in this molecule. There are four C-H...O intra-molecular weak interactions present in this molecule. The distance between O...H of C-H...O intramolecular interactions is found 2.874, 2.425, and 2.462 Å, respectively (Table 3.6). The distance between N...H of two C-H...N intra-molecular weak interactions are 2.630 and 2.613 Å, respectively. The aromatic C-H... $\pi$  intra-molecular interaction of **5.4** is also observed with the distance of 3.207 and 2.785 Å, respectively (Table 3.6). A lone pair- $\pi$  intra-molecular interaction is also observed between the O3 and  $\pi$  system of substituted phenyl ring with a distance of 3.613 Å.

The network is also supported by other non-covalent interactions in lone pair- $\pi$  intermolecular interactions. The distance between the O12 one molecule and the centroid of the other molecule's phthalimide ring is found to be 3.180 Å. It suggests that these lone pairs and heads of one ring fall under the influence of the electronic environment pyridone ring (Figure 3.26 (d)). This stacked architecture and different aromatic interactions are well visualized in Figure 3.26 of compound **5.4**.

#### 3.5.1.14. Hirshfeld analysis for **5.4**

The Hirshfeld surface and fingerprint plots for compound **5.4** are shown in Figures 3.27 (a) and (b), respectively. The red color in the Hirshfeld surface represents the more dominant non-covalent C-H...O interactions involved in the crystal structure of **5.4** (Figure 3.27 (a)).

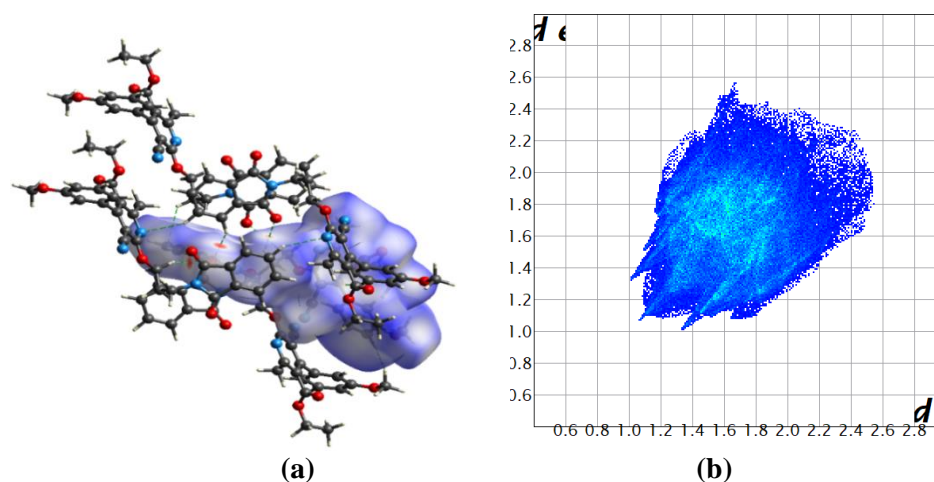


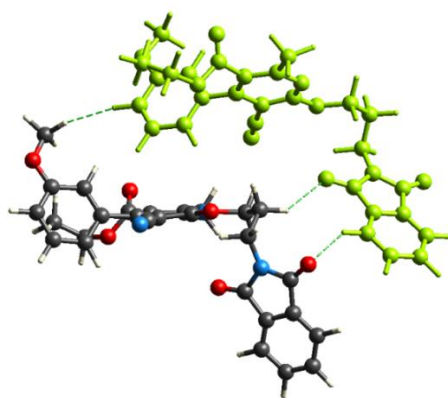
**Figure 3.27:** (a) Hirshfeld surface mapped on  $d_{\text{norm}}$  for compound **5.4**, (b) Two-dimensional fingerprint plot for compound **5.4**.

The yellowish-red bin on the fingerprint plots is absent in **5.4**, which means the absence of weak  $\pi$ ... $\pi$  stacking in the crystal structure (Figure 3.27 (b)). The spoke-like

pattern in the fingerprint plots of **5.4** represents the C-H...O interactions in the crystal lattice in the region of  $d_i + d_e = 2.3\text{-}2.9\text{\AA}$  (Figure 3.27 (b)). The C-H... $\pi$  interactions in **5.4** can be seen as a pair of unique blue-colored wings in the region of  $d_i + d_e = 2.9\text{-}3.6\text{\AA}$  (Figure 3.27 (b)). The C-H...N pair of contacts is also reflected as two characteristic wings occupied in the  $d_i + d_e = 2.8\text{-}3.4\text{\AA}$  in **5.4**.

Hirshfeld's surface view exactly explained the pattern of molecule conformation that exists in the solid-state. Electronic distribution within the compound also explained non-covalent interactions (Figure 3.27 (b)). The fingerprint analysis of compound **5.4** shows the percentage contribution of intermolecular interactions, and those are C-C for around 1.5%, C-H for 17.6%, C-N for 0.9%, C-O for 2.1%, H-H for 45.1%, H-N for 9.7%, H-O for 21.7%, N-N for 0.5%, N-O for 1.0%, and O-O for 0.1% of the close contacts in the Hirshfeld surfaces.

The Hirshfeld weak interactions calculation also supports the presence of weak non-covalent intermolecular interactions as in crystal packing. The C-H...O interactions of compound **5.4** in the crystal packing structure are in Figure 3.28 (a). The C-H... $\pi$  and lone pair- $\pi$  weak interaction calculations of **5.4** are shown in Figures 3.28 (b) and (c).



(a)

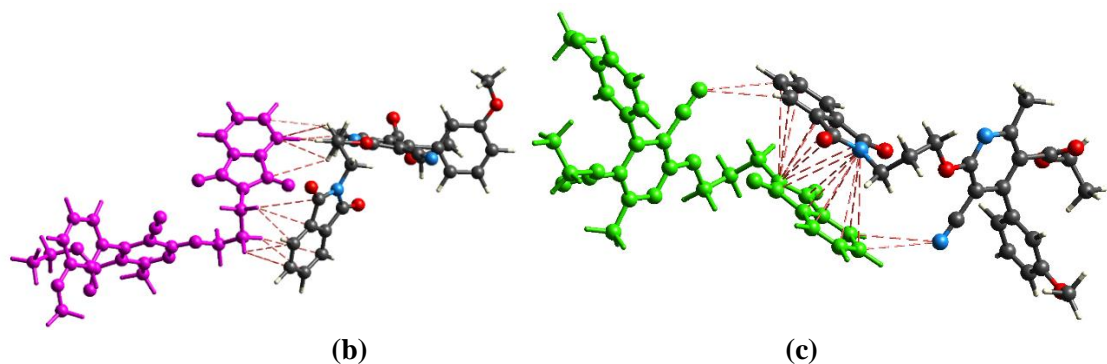


**Figure 3.28:** (a) C-H...O interaction and (b) C-H... $\pi$  and C-H...C (c) lone pair... $\pi$  interactions forming in Hirshfeld analysis of compound **5.4**

In the 3D curvedness plots of compound **5.4**, yellow spots represent the crystal structure's weak interactions, shown in Figures 3.29 (a) and (b). The absence of green-colored flat regions in the curvedness plots indicated the absence of  $\pi$ ... $\pi$  stacking in the crystal structure of compound **5.4**. The red-yellow colored spots in curvedness plots show strong hydrogen-bonding interactions in the crystal structure.

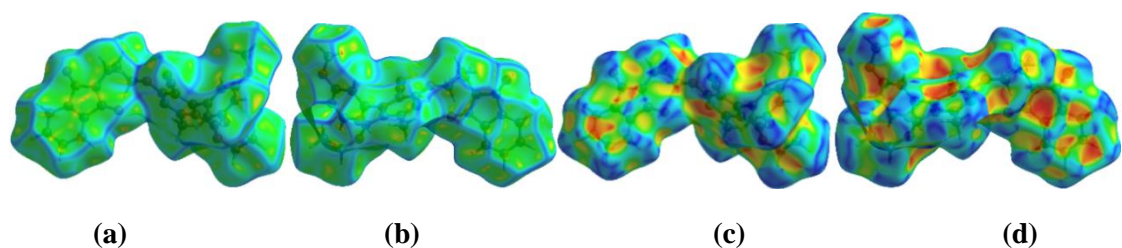


**Figure 3.29:** (a) and (b) Curvedness both side view of compound **5.4**, (c) and (d) Shape index both side view of compound **5.4**.

Red and blue areas represent the acceptor and the donor property, respectively, in the shape index of compound **5.4** (Figure 3.29 (c) and (d)). Yellowish-red colored concave regions indicate the presence of weak intermolecular interactions in the shape index plots. The absence of red and blue colored triangles on the surface of rings of the molecule in the shape index plots also indicated the absence of weak  $\pi$ - $\pi$  stacking in the crystal structure (Figure 3.29 (c) and (d)). Hirshfeld surface analysis gives evidence



about weak intermolecular interactions, and all these weak interactions stabilize and strengthen the crystal packing structure of compound **5.4**.

### 3.5.1.15. X-ray crystal structure of compound **5.5**

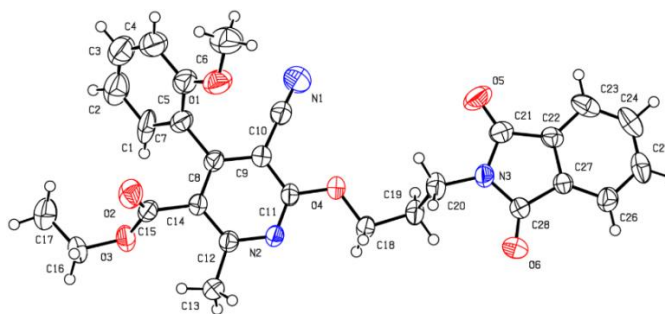


**Figure 3.30:** ORTEP diagram of compound **5.5**

### 3.5.1.16. Table 3.7. Crystal data of compounds **5.5** and **5.6**

Compound	<b>5.5</b>	<b>5.6</b>
Identification code	2062947	2062949
Empirical formula	C <sub>28</sub> H <sub>25</sub> N <sub>3</sub> O <sub>6</sub>	C <sub>25</sub> H <sub>23</sub> ClN <sub>2</sub> O <sub>4</sub>
Formula weight	499.51	450.90
Temperature(K)	296.15	296.15
Crystal system	Monoclinic	Monoclinic
Space group	<i>P2<sub>1</sub>/c</i>	<i>P2<sub>1</sub>/n</i>
a(Å)	21.003(5)	8.036(3)
b(Å)	8.333(2)	22.982(8)
c(Å)	14.842(4)	12.764(4)
α(°)	90	90
β(°)	106.465(3)	105.589(4)
γ(°)	90	90
Volume(Å <sup>3</sup> )	2491.3(11)	2270.6(13)
Z	4	4
ρ (g/cm <sup>3</sup> )	1.332	1.319
μ(mm <sup>-1</sup> )	0.095	0.202
F(000)	1048.0	944.0
Crystal size(mm <sup>3</sup> )	0.24 x .021 x .018	0.22 × 0.18 × 0.15
Radiation	MoKα (λ = 0.71073)	MoKα (λ = 0.71073)
2θ range for data collection(°)	5.29 to 55.4	6.266 to 54.624
Reflections collected	41186	37999
Independent reflections	5733	5091

Data/restraints/parameters	5733/0/337	5091/0/291
Goodness-of-fit on F2	1.027	0.984
Final R indexes [ $I \geq 2\sigma(I)$ ]	R1 = 0.0735, wR2 = 0.2032	R <sub>1</sub> = 0.0498, wR <sub>2</sub> = 0.1508
Final R indexes [all data]	R1 = 0.1140, wR2 = 0.2304	R <sub>1</sub> = 0.0695, wR <sub>2</sub> = 0.1689
Largest diff. peak/hole / e Å <sup>-3</sup>	0.85/-0.41	0.23/-0.28

**3.5.1.17. Table 3.8.** Intermolecular and intramolecular interactions in **5.5**

D-H...A	D-H (Å)	H...A (Å)	D...A (Å)	D-H...A (°)
C26-H26...O6	0.930	2.588	3.235	127.00
C4-H4...O2	0.930	2.610	3.526	168.43
C6-H6B...O2	0.959	2.662	3.339	127.90
C13-H13B...O5	0.970	2.622	3.346	125.69
C6-H6B... $\pi$ (C1, C2, C3, C4, C5, C7)	0.959	2.916		
C18-H18A... $\pi$ (C22-C27)	0.970	3.262		
C19-H19B... $\pi$ (C22-C27)	0.970	3.407		
C17-H17A... $\pi$ (N2, C8, C9, C11, C12, C14)	0.959	3.262		
$\pi$ (C22-C27)... $\pi$ (N2, C8, C9, C11, C12, C14)		3.792		
$\pi$ (C22-C27)... $\pi$ (C22-C27)		3.672		
$\pi$ (N2, C8, C9, C11, C12, C14)... $\pi$ (N3, C21, C22, C27, C28)		3.779		
O4... $\pi$ (C22-C27)		3.749		
O4... $\pi$ (N3, C21, C22, C27, C28)		3.859		
<b>Intramolecular</b>				
C13-H13B...O3	0.960	2.505	3.092	119.48
C19-H19A... $\pi$ (N3, C21, C22, C27, C28)	0.970	3.475		
C19-H19B... $\pi$ (N3, C21, C22, C27, C28)	0.970	3.576		
O2... $\pi$ (C1, C2, C3, C4, C5, C7)		3.841		

### Crystal analysis of **5.5**

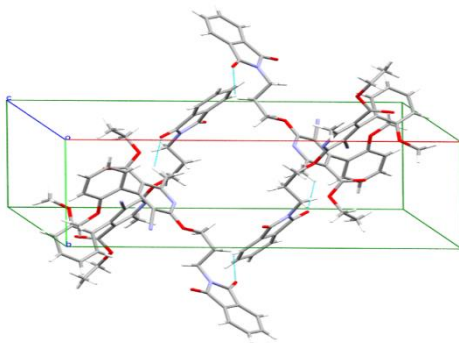
Crystallographic data of compound **5.5** demonstrated in Table 3.7. The ORTEP diagram at a 50% probability along (010) of compound **5.5** is in Figure 3.30, and the packing diagram of compound **5.5** views is shown in Figure 3.31.

Compound **5.5** was crystallized with (15%) ethyl acetate: hexane mixture at room temperature. It possesses a monoclinic crystal system having a, b, and c values of 21.003(5), 8.333(2), and 14.842(4) Å<sup>o</sup>, respectively (Table 3.7). The compound **5.5**

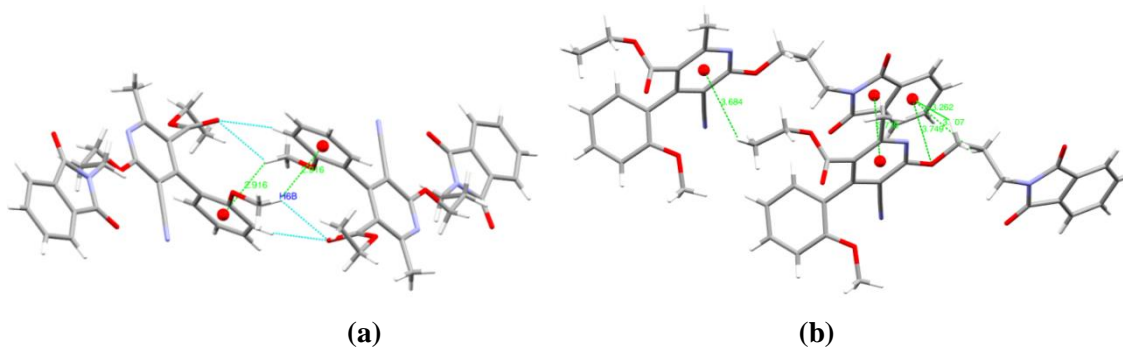
crystallizes in the  $P2_1/c$  space group. The molecular structure of compound **5.5** is non-planar.

In the crystal structure, molecules are linked together by different inter as well as intra-molecular non-covalent interactions such as C-H...O, C-H... $\pi$ ,  $\pi$ ... $\pi$  and lone pair (O)... $\pi$ , etc.(Table 3.8 and Figure 3.32). All these weak non-covalent interactions stabilize the crystal packing structure of compound **5.5**. Intermolecular network ( $\pi$ ... $\pi$ , C-H...N, C-H...O interactions) leads to stabilizing self-assembly of molecules (Table 3.8). These are shown in Figure 3.32.

The heterocyclic pyridine ring and phthalimide ring lie in one plane, and the substituted phenyl ring lies in another plane. Compound **5.5** is an asymmetrical molecule in which phthalimide rings are separated through a trimethylene spacer.



**Figure 3.31:** Packing diagram of molecule **5.5**



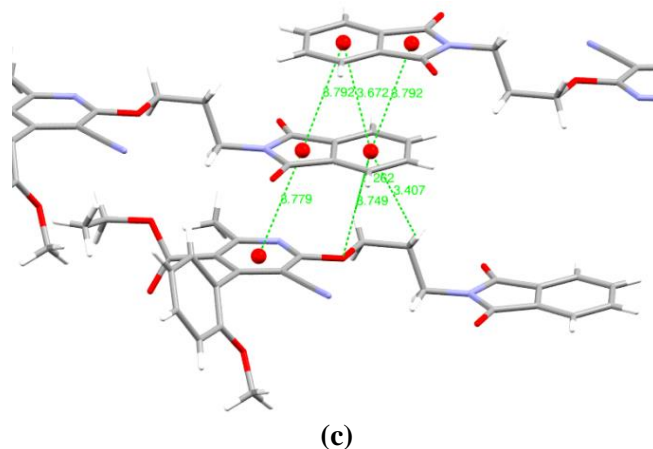


**Figure 3.32:** (a) C-H...O and C-H... $\pi$  interactions, (b) C-H...O, C-H... $\pi$ , lone pair... $\pi$  and  $\pi$ ... $\pi$ , and (c) C-H... $\pi$ , lone pair... $\pi$  and  $\pi$ ... $\pi$  interactions in molecule **5.5**

The molecule is folded structure and exists in an ABC pattern. C-H...O, C-H... $\pi$ , and lone pair... $\pi$  intra-molecular weak interactions are present in this molecule. C-H...O intra-molecular weak interactions are present in this molecule, and the distance between the O...H is 2.505 Å. The aromatic C-H... $\pi$  intra-molecular interaction of **5.5** is also observed with the distance of 3.475 and 3.576 Å, respectively (Table 3.8).

The packing of compound **5.5** represented an interesting zig-zag pattern of symmetrically arranged molecules. The overall intermolecular network is stabilized mainly through parallel/ off-set displaced/ T-shaped C-H... $\pi$  interactions between the centroids of the different ring and the other molecule's centroid. This will generate a stacked structure of compound **5.5** in which each molecule is stacked in ABBA pattern over each other generating a helical structure that stabilizes the overall architecture. The distance between the parallel displaced C-H... $\pi$  interaction is found at 2.916, 3.262, 3.407, and 3.262 Å, respectively (Figure 3.32).

The network is also supported by other non-covalent interactions in the form of lone pair... $\pi$  interactions. Distance between the oxygen of one molecule and the centroid of both rings of phthalimide of the other molecule is 3.749 and 3.859 Å. It indicates that

lone pairs and heads of one ring fall under the influence of the phthalimide ring's electronic environment (Figure 3.32).

The compound **5.5** also exhibited  $\pi\cdots\pi$  stacking between phenyl rings, phenyl-pyridine rings, and pyridine-pyridine rings in the same orientation due to the planarity and un-equal electronic distribution of the surface of the ring (Figure 3.32). The observed  $\pi\cdots\pi$  stacking with the distance of 3.792, 3.672, and 3.779 Å is shown in Figure 3.32.

### 3.5.1.18. Hirshfeld analysis for **5.5**

The Hirshfeld surface mapped on  $d_{\text{norm}}$  of compound **5.5** is displayed in Figure 3.33 (a). The red color represents the more dominant non-covalent C-H...O interactions involved in the crystal structure (Figure 3.33 (a)).

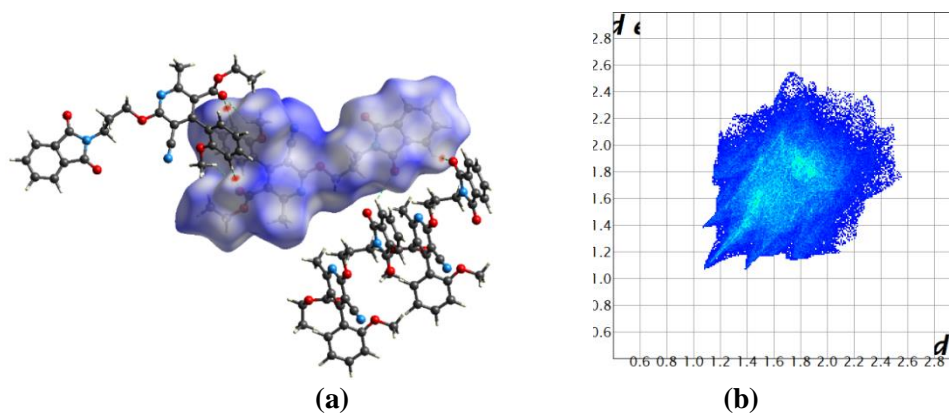
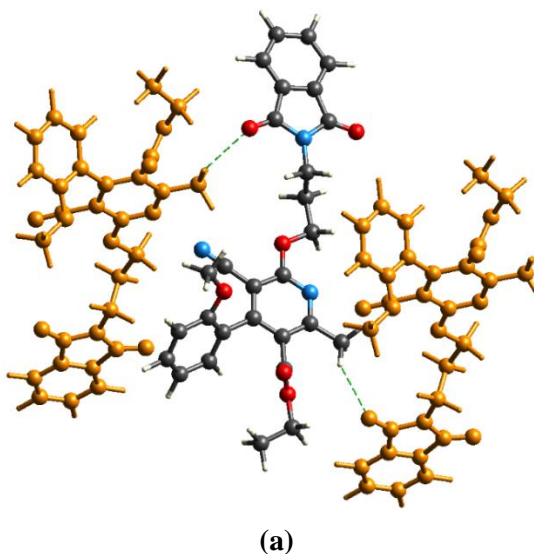


**Figure 3.33:** (a) Hirshfeld surface mapped on  $d_{\text{norm}}$  for compound **5.5**, (b) Two-dimensional fingerprint plot for compound **5.5**

The 2D fingerprint plots of compound **5.5** are shown in Figure 3.33 (b). The fingerprint analysis of compound **5.5** shows the percentage contribution of intermolecular interactions. Those are C-C for around 4.0%, C-N for 1.6%, C-O for 2.3%, H-H for 42.8%, N-H for 10.0%, O-H for 22.4%, N-N for 0.3%, O-N for 0.5% and C-H for 16.1% of the close contacts in the Hirshfeld surfaces (Figure 3.33 (b)).

There are prominent yellowish-red bins in the fingerprint plots indicating the presence of weak  $\pi\cdots\pi$  stacking (Figure 3.33 (b)). The spoke-like pattern in the fingerprint plots of **5.5** represents the C-H...O interactions in the crystal lattice in the region of  $d_i + d_e = 2.6\text{-}3.6 \text{ \AA}$  (Figure 3.33 (b)). The second spoke-like pattern in the fingerprint plots of **5.5** represents the C-H...N interactions in the crystal lattice in the region of  $d_i + d_e = 2.8\text{-}3.8 \text{ \AA}$  (Figure 3.33 (b)). The C-H... $\pi$  interactions in **5.5** can be seen as a pair of unique blue-colored wings in the region of  $d_i + d_e = 3.0\text{-}3.8 \text{ \AA}$  (Figure 3.33 (b)). Figure 3.34 is showing Hirshfeld calculated weak non-covalent interactions of compound **5.5**.

The Hirshfeld weak interactions calculation also supports the presence of weak non-covalent intermolecular interactions as in crystal packing. Where  $\pi\cdots\pi$  stacking, C-H... $\pi$  interactions, C-H...N, lone pair... $\pi$  and C-H...O interactions of compound **5.5** in the crystal packing structure is in Figures 3.34 (a), (b) and (c). The  $\pi\cdots\pi$  weak interaction calculations of **5.5** are shown in Figure 3.34 (c).



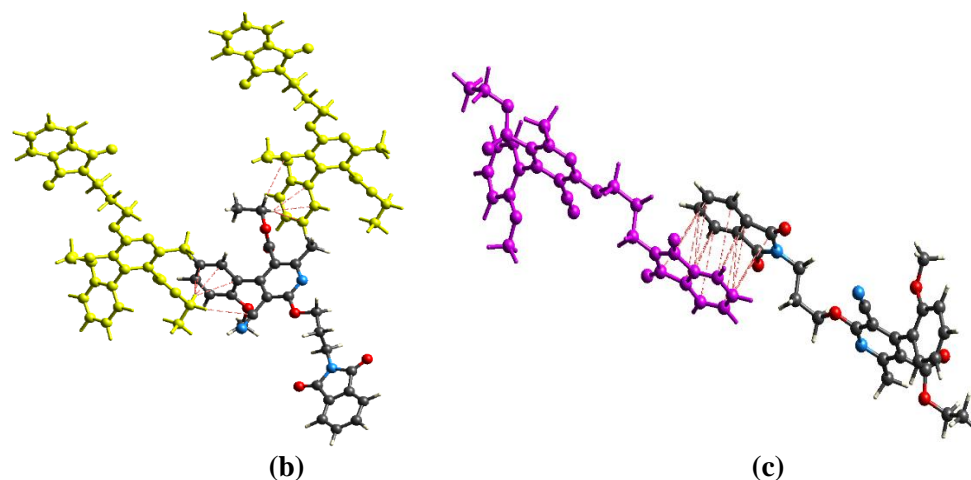


**Figure 3.34:** (a) C-H...O interaction, (b) C-H... $\pi$  interactions (c)  $\pi$ ... $\pi$  interaction forming in Hirshfeld analysis of compound **5.5**.

The 3D Hirshfeld surface on Curvedness plots for compound **5.5** is shown in Figures 3.35 (a) and (b). In the Curvedness plots, very weak intermolecular interactions are seen inside the contours by yellow spots. The presence of green-colored flat regions in the curvedness plot shows the presence of  $\pi$ ... $\pi$  stacking interaction in the crystal packing. The red-yellow colored spots in curvedness plots show strong hydrogen-bonding interactions in the crystal structure of **5.5**.

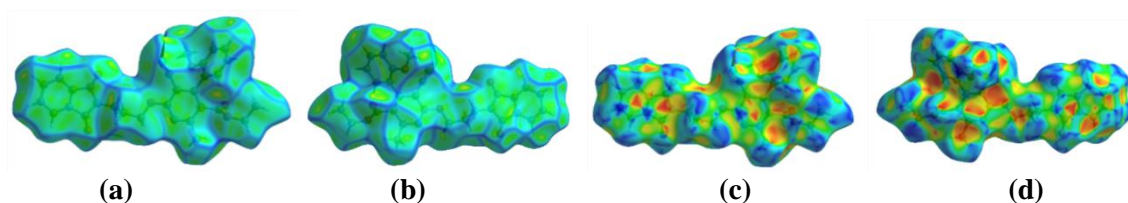


**Figure 3.35:** (a) and (b) Curvedness both side view of compound **5.5**, (c) and (d) Shape index both side view of compound **5.5**.

The shape index of compound **5.5** indicated the nature of interactions (i.e., donor and acceptor property) (Figure 3.35 (c) and (d)). The red and blue areas of the shape index indicated the acceptor and the donor property, respectively. In the Shape index plots of compound **5.5**, the yellowish-red colored concave regions on the Hirshfeld surface represent weak intermolecular interactions in the crystal packing. The presence

of red and blue colored triangles on the surface of rings of the molecule indicated that there is  $\pi \dots \pi$  stacking interaction in the crystal packing.

### 3.5.1.19. X-ray crystal structure of compound 5.6

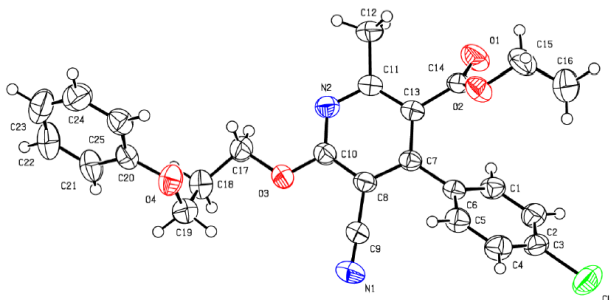


**Figure 3.36:** ORTEP diagram of compound 5.6

### 3.5.1.20. Table 3.9. Intermolecular and intramolecular interactions in 5.6

D-H...A	D-H (Å)	H...A (Å)	D...A (Å)	D-H...A (°)
C5-H5...O4	0.930	2.477	3.307	148.76
C22-H22...O4	0.930	2.671	3.379	168.43
C25-H25...N1	0.930	2.708	3.416	133.51
C24-H24... $\pi$ (C7, C8, C10, C11, C13, N2)	0.930	3.864		
C12-H12A... $\pi$ (C7, C8, C10, C11, C13, N2)	0.960	3.568		
C25-H25... $\pi$ (C7, C8, C10, C11, C13, N2)	0.930	3.649		
C21-H21... $\pi$ (C1-C6)	0.970	3.505		
C22-H22... $\pi$ (C1-C6)	0.930	3.861		
C12... $\pi$ (C7, C8, C10, C11, C13, N2)		3.924		
$\pi$ (C20-C25)... $\pi$ (C7, C8, C10, C11, C13, N2)		3.808		
O1... $\pi$ (C7, C8, C10, C11, C13, N2)		3.775		
<b>Intramolecular</b>				
C12-H12B...O1	0.960	2.881	3.037	90.00
C12-H12B...O1	0.960	2.760	3.037	97.36
C17-H17B...O4	0.970	2.623	2.947	99.83
O2... $\pi$ (C1-C6)		3.642		

### Crystal analysis of 5.6



Crystallographic data of compound **5.6** demonstrated in Table 3.7. The ORTEP diagram at a 50% probability along (010) of compound **5.6** is in Figure 3.36, and the packing diagram of compound **5.6** views is shown in Figure 3.37.

Compound **5.6** was crystallized with (15%) ethyl acetate: hexane mixture at room temperature. It possesses a monoclinic crystal system having a, b, and c values of 8.036(3), 22.982(8), and 12.764(4) Å, respectively (Table 3.7). The compound **5.6** crystallizes in the  $P2_1/n$  space group. The molecular structure of compound **5.6** is non-planar.

In the crystal structure, molecules are linked together by different inter as well as intra-molecular non-covalent interactions such as C-H...O, C-H...N, C-H... $\pi$ ,  $\pi$ ... $\pi$  and lone pair (O)... $\pi$ , etc.(Table 3.9 and Figure 3.38). All these weak non-covalent interactions stabilize the crystal packing structure of compound **5.6**. Intermolecular network (lone pair... $\pi$  and C-H...O interactions) leads to stabilizing self-assembly of molecules (Table 3.9).

The heterocyclic pyridine ring and phthalimide ring lie in one plane, and the substituted phenyl ring lies in another plane. Compound **5.6** is an asymmetrical molecule in which phthalimide rings are separated through a trimethylene linker.

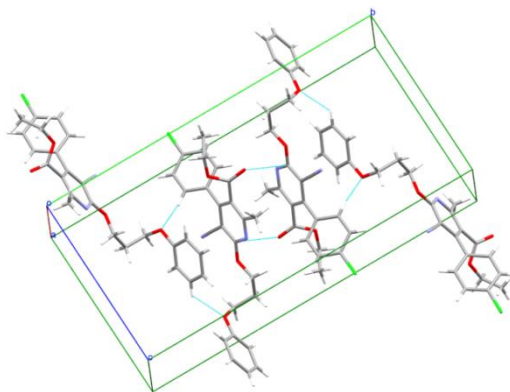


**Figure 3.37:** Packing diagram of molecule **5.6**

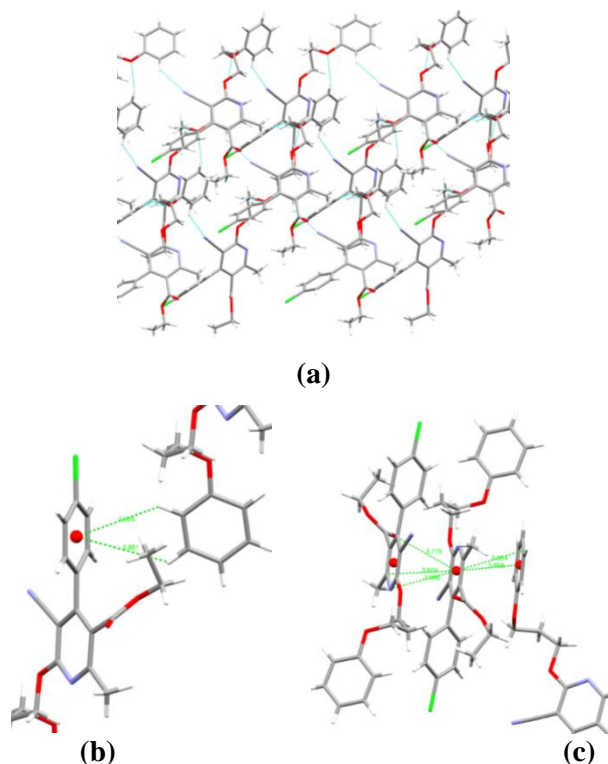


**Figure 3.38:** (a) C-H...O and C-H...N interactions, (b) C-H... $\pi$  interactions, and (c) C-H... $\pi$ , lone pair... $\pi$  and  $\pi$ - $\pi$  interactions in molecule **5.6**

The molecule is folded structure and exists in an AB pattern. C-H...O, C-H... $\pi$  and lone pair... $\pi$  intra-molecular weak interactions are present in this molecule. C-H...O intra-molecular weak interactions are present in this molecule, and the distances between the O...H are 2.881, 2.760, and 2.623 Å. The aromatic lone pair... $\pi$  intra-molecular interaction of **5.6** is also observed with the distance of 3.642 Å (Table 3.9).

The packing of compound **5.6** represented an interesting pattern of symmetrically arranged molecules. The overall intermolecular network is stabilized mainly through parallel/ off-set displaced/ T-shaped C-H... $\pi$  interactions. This generates a stacked structure of compound **5.6** in which each molecule is interlinked through non-covalent interactions over each other generating a helical structure that stabilizes the overall architecture. The distance between C-H and  $\pi$  system is 3.864, 3.649, 3.568, 3.505, and 3.861 Å, respectively in C-H...  $\pi$  interactions (Figure 3.38 (b)).

The network is also supported by other non-covalent interactions in the form of lone pair... $\pi$  interactions. The distance between the oxygen of one molecule and the centroid of the pyridine rings of the neighbour molecule is found at 3.775 Å, suggesting that these lone pairs and head of one ring fall under the influence of the electronic environment of the heterocyclic ring (Table 3.9).

The compound **5.6** also exhibited  $\pi$ ... $\pi$  stacking between phenyl rings, phenyl-pyridine rings, and pyridine-pyridine rings in the same orientation due to the planarity and un-equal electronic distribution of the surface of the ring (Figure 3.38 (c)). The observed  $\pi$ ... $\pi$  stacking with the distance of 3.924 and 3.808 Å is shown in Figure 3.38 (c).

#### 3.5.1.21. Hirshfeld analysis for **5.6**

The Hirshfeld surface and fingerprint plots for compound **5.6** are shown in Figures 3.39 (a) and (b), respectively. The red color in the Hirshfeld surface represents the more dominant non-covalent C-H...O interactions involved in the crystal structure of **5.6** (Figure 3.39 (a)).

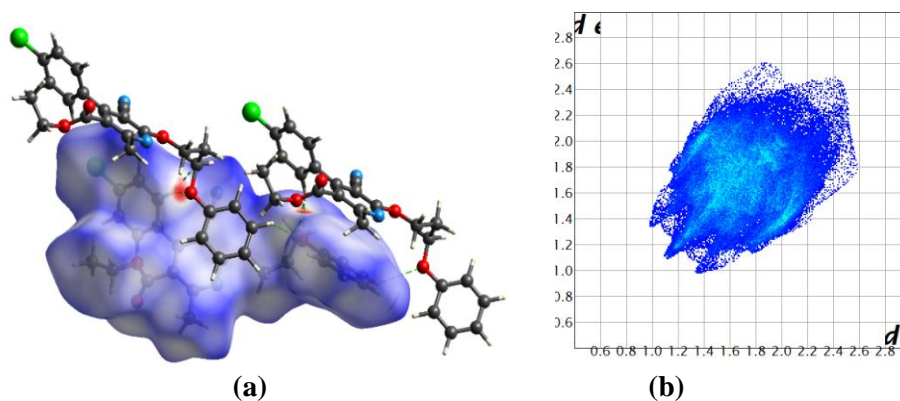


**Figure 3.39:** (a) Hirshfeld surface mapped on  $d_{\text{norm}}$  for compound **5.6**, (b) Two-dimensional fingerprint plot for compound **5.6**.

Hirshfeld's surface view exactly explained the pattern of molecule conformation that exists in the solid-state. Electronic distribution within the compound also explained

non-covalent interactions (Figure 3.39 (b)). The fingerprint analysis of compound **5.6** shows the percentage contribution of intermolecular interactions, and those are H-H for around 46.1%, Cl-N for 0.2%, Cl-H for 11.0%, O-O for 0.6%, O-N for 0.9%, O-C for 1.7%, O-H for 8.7%, C-N for 1.0%, N-H for 10.2%, C-C for 3.5% and C-H for 16.2% of the close contacts in the Hirshfeld surfaces. The small yellowish-red bin on the fingerprint plots is present in **5.6**, which means weak  $\pi\cdots\pi$  stacking in the crystal structure (Figure 3.39 (b)). The spoke-like pattern in the fingerprint plots of **5.6** represents the C-H...O interactions in the crystal lattice in the region of  $d_i + d_e = 2.4\text{-}3.2$  Å (Figure 3.39 (b)). The C-H... $\pi$  interactions in **5.6** can be seen as a pair of unique blue-colored wings in the region of  $d_i + d_e = 3.0\text{-}3.6$  Å (Figure 3.39 (b)). The C-H...N pair of contacts is also reflected as two characteristic wings occupied in the  $d_i + d_e = 2.8\text{-}3.8$  Å in **5.6**.

The Hirshfeld weak interactions calculation also supports the presence of weak non-covalent intermolecular interactions as in crystal packing. The C-H...N, C-H...C, and C-H...O interactions of compound **5.6** in the crystal packing structure are in Figure 3.40. The CH... $\pi$  and  $\pi\cdots\pi$  weak interaction calculations of **5.6** are shown in Figures 3.40 (a) and (b).

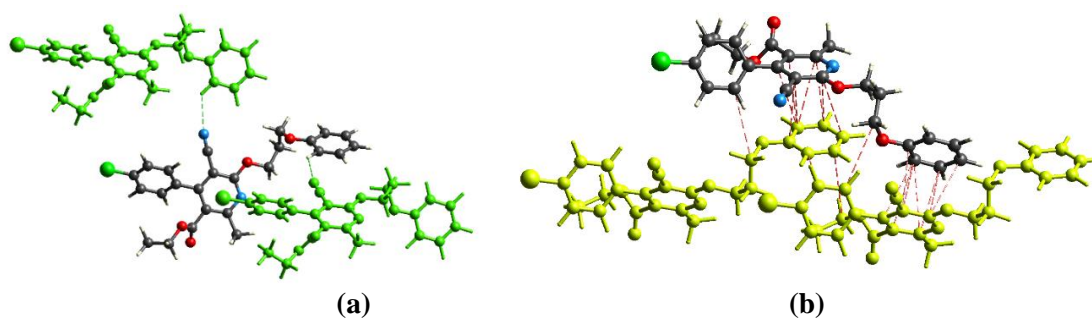


**Figure 3.40:** (a) C-H...N interaction and (b) CH... $\pi$  and  $\pi\cdots\pi$  interactions forming in Hirshfeld analysis of compound **5.6**.

In the 3D curvedness plots of compound **5.6**, yellow spots represent the crystal structure's weak interactions, shown in Figures 3.41 (a) and (b). The presence of green-colored flat regions in the curvedness plots indicated  $\pi\text{-}\pi$  stacking in the crystal structure

of compound **5.6**. The red-yellow colored spots in curvedness plots show strong hydrogen-bonding interactions in the crystal structure.

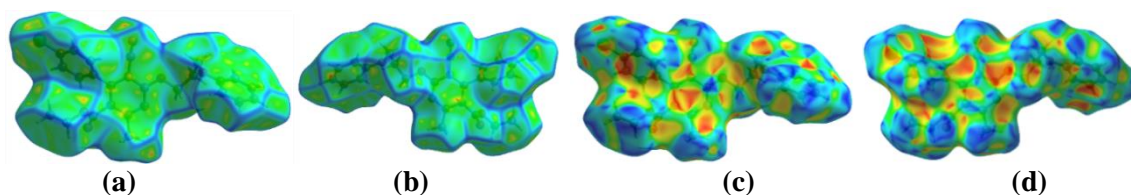


**Figure 3.41:** (a) and (b) Curvedness both side view of compound **5.6**, (c) and (d) Shape index both side view of compound **5.6**.

Red and blue areas represent the acceptor and the donor property, respectively; in the shape index of compound **5.6** (Figure 3.41 (c) and (d)). Yellowish-red colored concave regions indicate the presence of weak intermolecular interactions in the Shape index plots. The presence of red and blue colored triangles on the surface of rings of the molecule in the Shape index plots also indicated the presence of weak  $\pi$ - $\pi$  stacking in the crystal structure (Figure 3.41 (c) and (d)). Hirshfeld surface analysis gives evidence about weak intermolecular interactions, and all these weak interactions stabilize and strengthen the crystal packing structure of compound **5.6**.

### 3.6. Conclusion:

This chapter has successfully synthesized six (**5.1**, **5.2**, **5.3**, **5.4**, **5.5**, and **5.6**) 2-pyridone based poly-aromatic fleximers, and all of these six fleximers (**5.1**, **5.2**, **5.3**, **5.4**, **5.5** and **5.6**) have been formed single crystal. We have studied single-crystal X-ray crystallography study of these six fleximers (**5.1**, **5.2**, **5.3**, **5.4**, **5.5** and **5.6**) and found that all these crystal showed C-H... $\pi$ , lone pair... $\pi$ , C-H...O, C-H...N, C-H...C, etc. weak non-covalent interactions. Fleximer **5.1**, **5.3**, **5.5**, and **5.6** also showed  $\pi$ - $\pi$  stacking interactions. Aromatic interactions are very weak interactions, so its study in the solvent is callous task. We have studied these interactions in the solid-state with single-crystal X-ray diffraction and Hirshfeld surface analysis method. Hirshfeld surface analysis also

supported the presence of weak non-covalent interactions like  $\pi$ - $\pi$  stacking, C-H... $\pi$ , lone pair... $\pi$ , C-H...O, C-H...N, C-H...C, etc. in crystal packing of all the six fleximers (**5.1**, **5.2**, **5.3**, **5.4**, **5.5** and **5.6**). From the Hirshfeld surface analysis, we can say that it is an excellent tool to study aromatic  $\pi$ - $\pi$  stacking.

Our present study has given clear experimental evidence of the intermolecular aromatic interactions in the models containing poly-aromatic fleximers. We have also observed that the interaction between two electron-rich systems is less than that of two electron-deficient systems. The X-ray crystallography analysis of **5.3** fleximer shows that the  $\pi$ - $\pi$  interaction between two rings is found by the phenyl ring of phthalimide moiety stacked with a heteroaromatic ring system pyridone with face to face stacking. Whereas, in fleximer **5.5**,  $\pi$ - $\pi$  interaction occurred between two phenyl rings of phthalimide moiety. However, in fleximer **5.6**,  $\pi$ - $\pi$  interaction occurred between two heteroaromatic rings with face-to-face stacking.

\

## **CHAPTER-4**

### **4 SYNTHESIS AND STUDY OF ROSIGLITAZONE BASED BIO-ACTIVE MOLECULES**

---

#### **4.1. Introduction**

Diabetes is one of the largest worldwide health emergencies of this century and is the third major cause of death in the USA after heart disease and cancer (Singh, 2016). Thousands of new anti-diabetes drugs are synthesized each year, but it is challenging to eliminate this deadly disease. Diabetes has a significant consequence on fatality and

mortality and is a worldwide non-communicable disease. According to the International Diabetes Federation (IDF) Diabetes Atlas data, diabetes currently affected an estimated 463 million people worldwide in 2019. This trend will rise to 700 million by the end of 2045 (International Diabetes Federation, 2019). There are several complications of diabetes, such as cardiovascular disease (Bugger & Abel, 2014), retinopathy (Kostev & Rathmann, 2013), nephropathy (Gray & Cooper, 2011), neuropathy (Martin et al., 2014), food disorders (Wukich et al., 2013), complications during pregnancy (“Hyperglycemia and Adverse Pregnancy Outcomes,” 2008), dental disease, kidney disease (International Diabetes Federation, 2017), etc. Diabetes can also interfere with wound healing (Brem & Tomic-Canic, 2007). Some other complications of diabetes are ketoacidosis, hyperosmolar coma, reduced immunity to pneumonia, and influenza.

#### **4.1.1. Type 1 diabetes mellitus**

This type of diabetes accounts for 5–10% of all cases of diabetes. Type 1 diabetes is also known as insulin-dependent diabetes mellitus, or youthful-onset, since it is diagnosed in children, teenagers, and young adults; however, it has been discovered in the previous decade that it can develop at any age (Leslie, 2010). In type 1 diabetes, beta cells are unable to produce insulin in the pancreas because of the autoimmune response of the body, where antibodies destroy beta cells, causing a lack of insulin (Bluestone et al., 2010; Rother, 2007; Todd, 2010; Van Belle et al., 2011). Insulin injection or continuous infusions of insulin via an insulin pump are essential to maintaining health for type 1 diabetics.

#### **4.1.2. Type 2 diabetes mellitus**

Overall, type 2 diabetes is the most common, accounting for around 85–90% of all cases; it is also known as non-insulin-dependent or adult-onset diabetes. It is most often diagnosed in people aged 45 years or older (Wild et al., 2004) but is also found in younger generations. In type-2 diabetes, the production of insulin takes place in the  $\beta$  cells of the pancreas, but insulin receptors or insulin-responsive cells in the cell

membrane do not normally respond to insulin. There is an inadequate response to receptors, known as "insulin resistant," thus increasing blood glucose levels.

#### **4.1.3. Gestational diabetes**

Gestational diabetes is another type of diabetes observed in pregnant women, usually during advanced stages of pregnancy. Treatments of gestational diabetes include unique dietary plans and regular physical activity. A few antidiabetic drugs are sometimes required to maintain normal blood glucose levels (Kim, Newton, and Knopp, 2002). The risk factors associated with developing gestational diabetes mellitus include a previous diagnosis of gestational diabetes mellitus, overweight, obesity, etc. (Kim, Newton, and Knopp, 2002; Chu *et al.*, 2007).

#### **4.1.4. Insulin action or the role of insulin in the body**

Insulin is also called the principal hormone, which controls blood glucose levels by transferring glucose from the blood to the tissue. Insulin production occurs in the pancreas' beta cells (Mane, Antre, and Oswal, 2012) and is stored in the body in six molecules' units; the active form is a monomer. The main action of insulin is to control the circulating blood glucose coming from carbohydrates throughout the body, especially entering tissues via insulin receptors or insulin-responsive cells. If beta cells cannot synthesize insulin, type-1 diabetes occurs, while type-2 diabetes occurs if insulin receptors or insulin-responsive cells cannot respond to insulin. From the UK Prospective diabetes study, insulin and its analogues are used as a standard treatment for type 1, gestational, and some forms of type-2 diabetes (Auer, 2004; Ivanova et al., 2009).

#### **4.1.5. Peroxisome proliferator-activated receptor (PPAR) agonist**

PPA receptors are mostly found in adipose tissues. They are members of the nuclear hormone receptor superfamily, including retinoid-X receptors (RXRs), thyroid hormone receptors, retinoic acid receptors (RARs), and oestrogen receptors (Mangelsdorf et al., 1995). Like other nuclear hormone receptors, PPAR is a ligand-



activated transcription factor that controls different target genes' expression. PPAR regulates fatty acid storage and controls glucose digestion by altering the expression of the genes involved; it consists of three different genes: PPAR $\alpha$ , PPAR $\beta/\delta$ , and PPAR- $\gamma$  (Mirza et al., 2019). PPAR also reduces gluconeogenesis and increases lipogenesis, which further increases glucose utilization (Day, 1999).

PPAR- $\gamma$  has been involved in glucose homeostasis's critical function, making it a viable target in T2DM management (Berger et al., 2002). Synthetic Thiazolidinediones (TZDs) have a high affinity for PPAR- $\gamma$  and are used clinically to treat type 2 diabetes since they can sensitize tissues to insulin. That's why PPAR- $\gamma$  is also recognized as a glitazone receptor or NR1C3 (nuclear receptor subfamily 1, group C, member 3) (Di Marzio, 2008). PPAR- $\gamma$  may also be considered the biochemical target of TZDs (Lehmann et al., 1995). A central DNA-binding and carboxy-terminal region, as a common structural aspect, influences ligand binding, dimerization, and transactivation functions.

#### **4.1.6. Thiazolidinedione scaffolds target different diabetic enzymes**

It has been reported that thiazolidinedione (TZD) derivatives are having the potential to treat diabetes. Thiazolidinedione (TZD) targets many targets of diabetic enzyme receptors. Thiazolidinedione (TZD) scaffolds serve as a potent protein tyrosine phosphatase 1B (PTP1B) enzyme inhibitor, aldose reductase inhibitors, and provide pharmacologically new drugs in direct treatment for diabetic complications and also help to design structurally new aldose reductase inhibitors. But most importantly, Thiazolidinedione (TZD) scaffolds act as PPAR- $\gamma$  agonists due to their high binding affinity for PPAR- $\gamma$  receptor, which leads to the development of a new class of drugs for diabetes. To date, many Thiazolidinedione derivatives have been reported as potent Protein tyrosine phosphatase 1B (PTP1B) enzyme inhibitors and aldose reductase inhibitors. Mahapatra et al. reported 5-benzylidene-thiazolidine-2,4-dione derivatives and examined their PTP1B inhibition activity (Mahapatra et al., 2017). From the series, two compounds **4.0.1** and **4.0.2** (Figure 4.1) emerged as the most active PTP1B inhibitor

with  $IC_{50}$  values of 7.31 and 8.73  $\mu\text{M}$ . SAR revealed that phenyl sulfonate and methanesulfonate groups increase PTP1B inhibition activity compared to bulky substituents such as 2,4,6-trimethylphenyl, phenylmethane. Molecular docking simulations demonstrated that both active compounds (**4.0.1** and **4.0.2**) occupied the enzyme's active site and formed hydrogen bonds with amino acid residues Ser216, Ala217, and Arg221. *In vivo* studies showed that compounds **4.0.1** and **4.0.2** reduced the blood glucose level to 32.13% and 30.22%, respectively (with seven days of duration), comparable to standard pioglitazone drug.

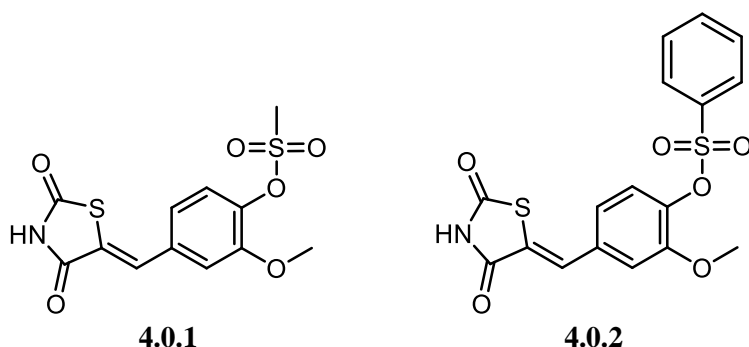


**Figure 4.1:** Thiazolidinedione derivatives **4.0.1** and **4.0.2** as potent PTP1B inhibitors

Maccari et al. developed other 5-arylidene-4-thiazolidinone derivatives and evaluated their inhibitory activity against aldose reductase (Maccari et al., 2014). Acetic acid derivatives of the benzylidene-2-oxo/thioxo-4-thiazolidinone series were found superior to the standard drugs with  $IC_{50}$  values of 0.11  $\mu\text{M}$  to 0.13  $\mu\text{M}$ . The acetic acid analogue compound **4.0.3** (Figure 4.2) proved to be the most active aldose reductase inhibitor ( $IC_{50} = 0.13 \mu\text{M}$ ) of the series and showed the potential to diminished NF-kB activation and iNOS expression.

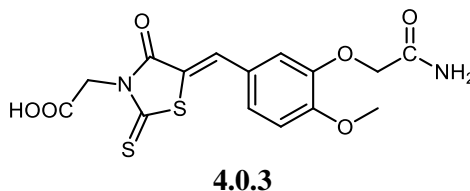
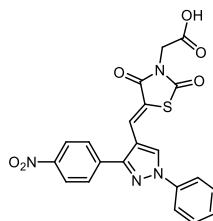


**Figure 4.2:** 5-arylidene-2,4-thiazolidinedione derivative **4.0.3** as potent aldose reductase inhibitor

Recently, Bansal et al. developed a new novel series of thiazolidine-2,4-dione-pyrazole conjugates and evaluated their PPAR- $\gamma$  agonistic activity (Bansal et al., 2019). *In silico* analysis stated that compound **4.0.4** (Figure 4.3) showed the best docking score (-17.44) with PPAR- $\gamma$  receptor, compared to standard pioglitazone (-12.605). *In vivo* studies showed that compound **4.0.4** was the most potent PPAR- $\gamma$  agonist with blood glucose-lowering effects  $134.46 \pm 0.49$  in C57BL/6J mice (14th-day duration), which compared to standard pioglitazone ( $136.56 \pm 0.64$ ). Structure activity relationship studies (SAR) revealed that this class of compounds' activity mostly depends on the substituents' nature present on the phenyl ring of pyrazole moiety. Generally, electron-donating groups on the phenyl ring improved the activity. Further studies reported that this class of compounds also found potent anti-inflammatory and antioxidant agents.



**4.0.4**

**Figure 4.3:** Pyrazole based thiazolidinedione derivative **4.0.4** as potent PPAR- $\gamma$  agonist

#### 4.1.7. Thiazolidinedione scaffolds as PPAR- $\gamma$ agonists

Thiazolidinediones (TZDs) are also known as glitazones. These are insulin sensitizer drugs used for the treatment of type 2 diabetes mellitus (T2DM). The thiazolidinedione series of drugs' primary mechanism of action is to binds with PPAR receptors in fat cells, making the cells progressively receptive to insulin. It has also been reported that the type 2 antidiabetic activity is due to their agonistic effect on the peroxisome proliferator-activated receptor (Thangavel et al., 2017). The mechanism action of TZD is in Figure 4.4.

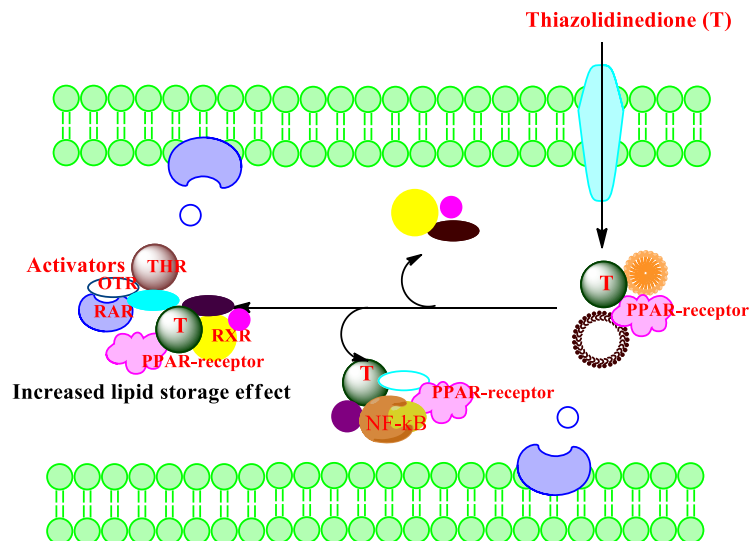
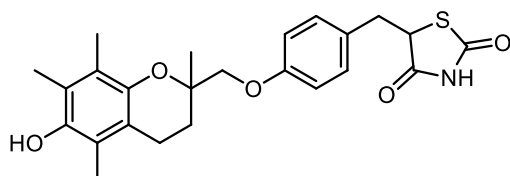
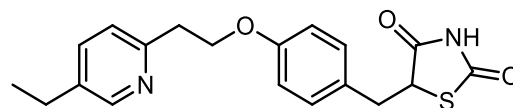


**Figure 4.4:** Mechanism action of TZD

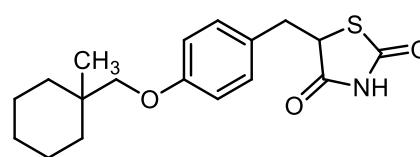
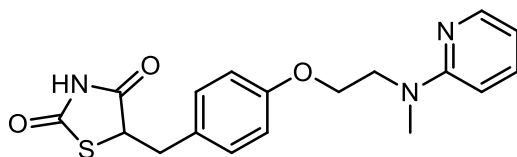
The TZD class of drugs includes troglitazone, rosiglitazone, pioglitazone, etc. (Figure 4.5). In 1997, among the class of TZD drugs, troglitazone was the first marketed drug for the treatment of T2DM (Rendell & Kirchain, 2000). Troglitazone was discontinued in March 2000 because of the involvement of extreme hepatic toxicity. Rosiglitazone and pioglitazone were approved in 1999 and act by activating PPAR- $\gamma$  to maximize insulin sensitivity in body muscle, adipose tissue, and liver. These are affecting gene regulations in the target cells (Day, 1999).



**Troglitazone**



**pioglitazone**



## Rosiglitazone

## Ciglitazone

**Figure 4.5:** Currently available, approved TZD class of drugs: **troglitazone**, **pioglitazone**, **rosiglitazone**, and **ciglitazone**.

It has been reported that rosiglitazone interacts with the PPAR- $\gamma$  amino acids in several ways and occupies about 40% of the catalytic site (Nolte et al., 1998) in the ternary complex. For example, two histidine residues, His323 and His449, of the PPAR- $\gamma$  protein form hydrogen bonds with the carbonyl group of TZD. The nitrogen atom of the TZD head group occupies the hydrogen-bonding region. Another secondary hydrogen bond is formed by a buried lysine residue, K367, with the rosiglitazone at residue His449. All of these hydrogen bond interactions enable the TZD head group to fit into the active site of PPAR- $\gamma$ . The oxygen atom between the phenyl moiety and the pyridine moiety provides essential structural features for the pyridine moiety, which occupies the pocket between H3 and the  $\beta$ -sheet. The TZD ring's sulfur atom is also occupied in a hydrophobic region of PPAR- $\gamma$  (Figure 4.6). Due to all of these interactions, the glitazone series can activate PPAR- $\gamma$ . After activation by these ligands, PPARs bind to the genes' regulatory regions, resulting in the transcription of genes involved in the glucose homeostasis pocket, formed by F282, Q286, F363, and L469.

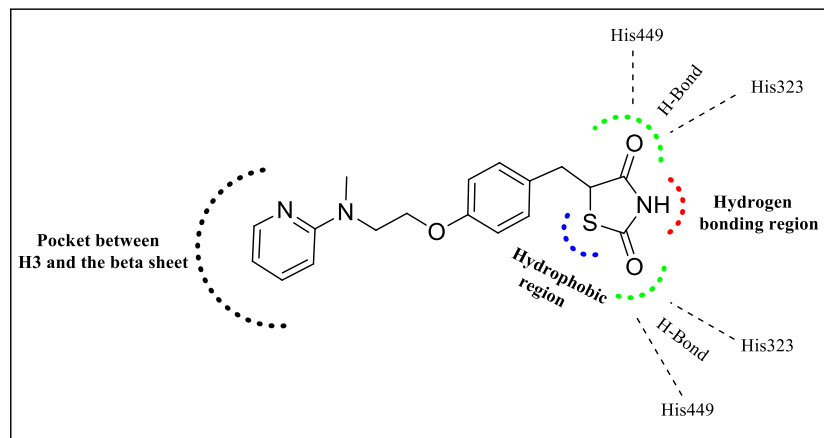


**Figure 4.6:** Key interactions between Rosiglitazone and the PPAR- $\gamma$  receptor

It has been seen that the first-line treatment of T2DM is oral metformin followed by oral sulfonylureas, dipeptidyl peptidase-IV-inhibitors, and Thiazolidinediones (TZDs). But there is not a single drug reported to cure T2DM properly. Moreover, these traditional therapies have so many complications, such as gastrointestinal discomfort with metformin, hypoglycemia, weight gain with sulfonylurea, edema, and increased risk of bone fractures, TZDs, etc. The main side effect of glitazones is water retention leading to edema, with significant water retention, leading to decompensation of potentially previously unrecognized heart failure (Singh et al., 2020). Therefore, there is an unmet need for new potent type 2 antidiabetic drugs with better pharmacological profiles.

#### 4.2. Present work

In recent years, heterocyclic scaffolds have been the basis of antidiabetic chemotherapies. There are currently several antidiabetic drugs available in the market, but their use is associated with various side effects. Therefore, necessitating the search for new potent antidiabetic agents with better pharmacological profiles. As TZDs scaffolds target different diabetic enzyme receptors, we have designed two series of compounds based on standard rosiglitazone's structural basis (**Figure 4.7**).

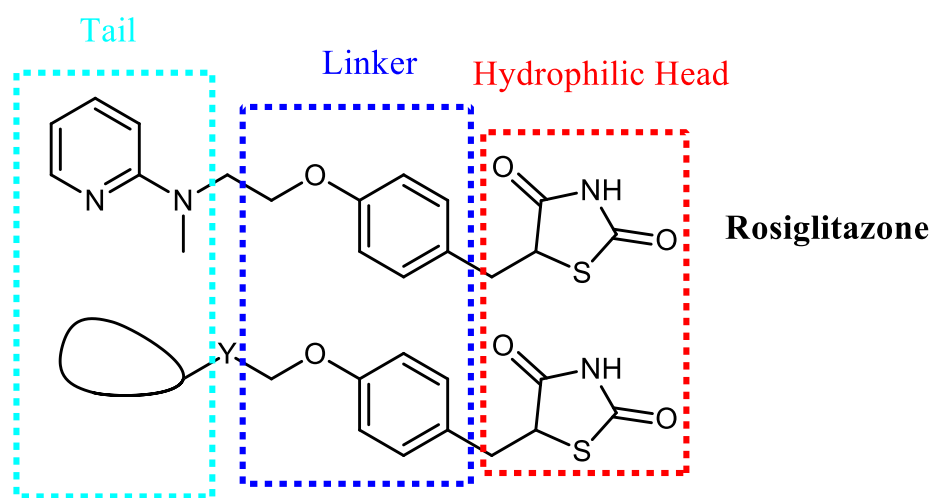


**Figure 4.7:** Designing the compounds on the structural basis of rosiglitazone

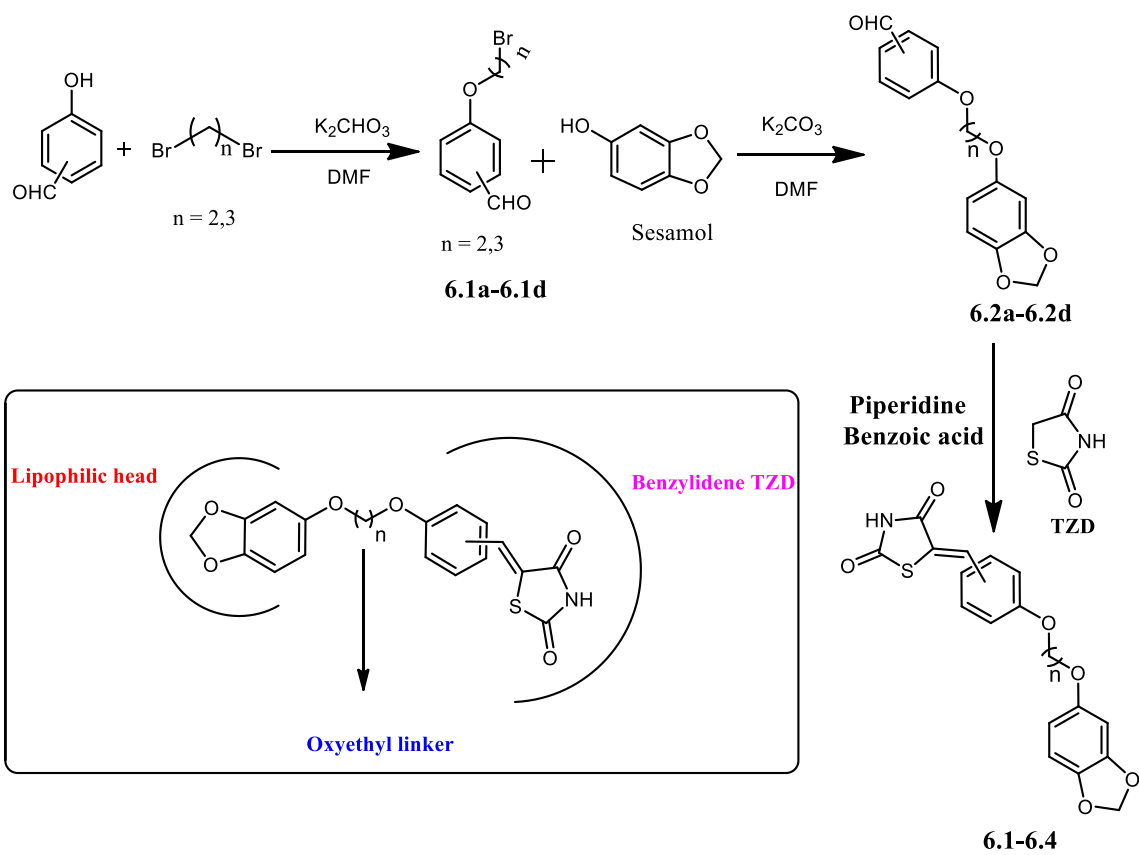
### 4.3. Experimental

$^1\text{H}$  NMR (300 MHz) and  $^{13}\text{C}$  (75 MHz) NMR spectra were recorded on **JEOL AL300 FTNMR** spectrometer using TMS as an internal reference, and chemical shift values are expressed in  $\delta$ , ppm units. Melting points of all the compounds were recorded on an electrically heated instrument and are uncorrected. All the reactions were monitored by thin-layer chromatography (TLC) on pre-coated aluminum sheets of Merck using an appropriate solvent system, and chromatograms were visualized under UV light. We have used flash chromatography with silica gel mesh size 230-400 with ethyl acetate/hexane mixtures to purify compounds.

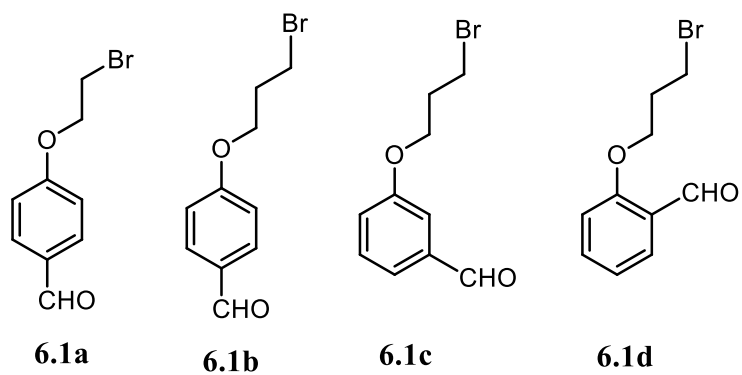
### 4.4. Results and discussions

We have designed and synthesized two series of compounds (**Scheme 6 and Scheme 7**) based on standard rosiglitazone's structural feature, an oxyethylene linker connecting the benzyl-TZD with a lipophilic head (Figure 4.7). It has been found that oxyethylene linker with aromatic rings as lipophilic heads was found less effective. Therefore, the aromatic lipophilic head was replaced with hetero-aromatic moieties, such as-sesamol, and 2-cyano pyridone, in two series of compounds. Here, the central benzylidene phenyl ring and the benzylidene-TZD group have been retained, essential for potency and antidiabetic activity. Additionally, we have also increased the carbon number or extended linker length by  $-\text{CH}_2-$  or  $-\text{CH}_2\text{-N-}$  to increase the potency or binding affinity with the PPAR- $\gamma$  receptor (Yasmin *et al.*, 2017). The structural feature of **Scheme 6** compounds are benzylidene-TZD-Linker with sesamol lipophilic head, whereas **Scheme 7** compounds are benzylidene-TZD-Linker with 2-cyano pyridone lipophilic head. We have performed *in silico* analysis on these two series of compounds to see the binding affinity with the active site of the PPAR- $\gamma$  receptor. We have also carried out the hypoglycemic activity in the animal model (rats) to see these compounds' antidiabetic activity.

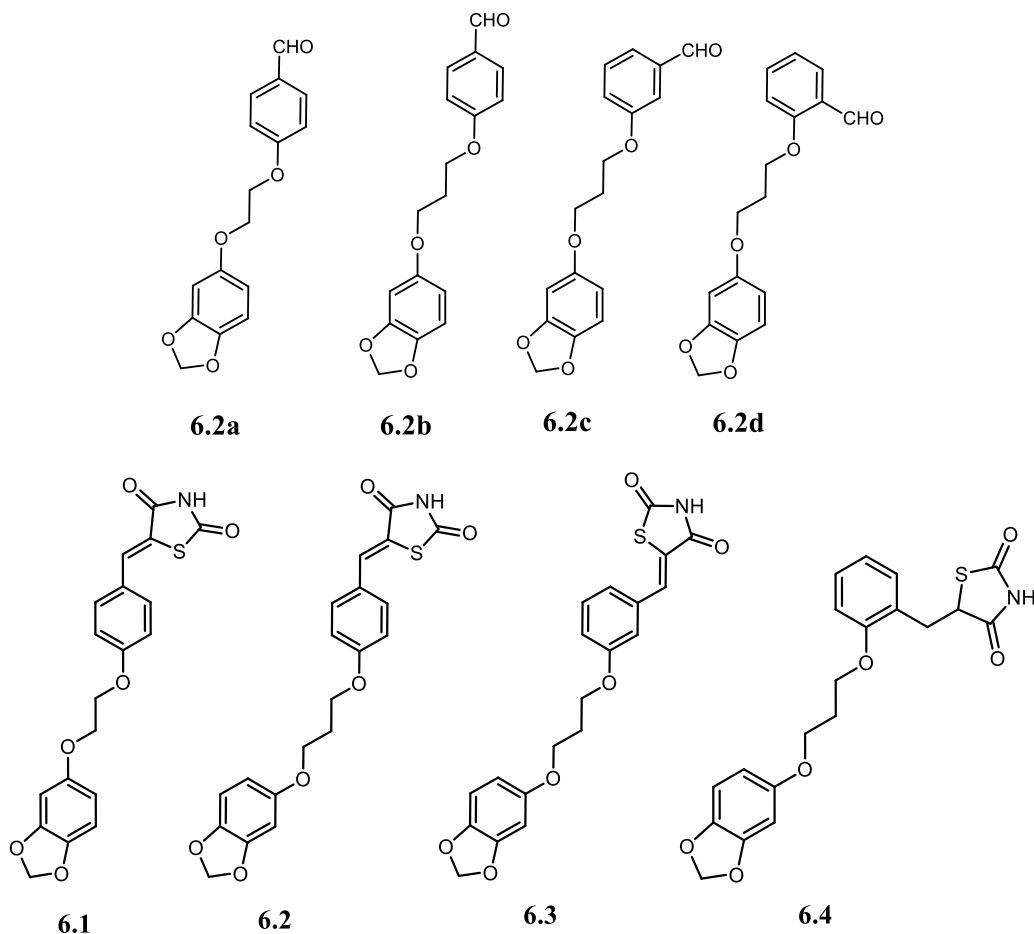
### 4.5. Scheme 6: Synthesis of benzylidene-TZD-Linker compounds with sesamol lipophilic head (6.1-6.4)



**Scheme 6**







#### 4.5.1. General procedure for the synthesis of 6.1a-6.1d

In a 100 mL round bottom flask, para- or meta- or ortho-substituted hydroxylbenzaldehydes (40.98 mmol) and potassium carbonate (40.98 mmol) was dissolved in 25 mL of dimethylformamide (DMF), and the reaction mixture was stirred for 30 minutes at room temperature. After 30 minutes, 1,2-dibromoethane (204.8 mmol)/1,3-dibromopropane (204.8 mmol) was added to the reaction mixture, and the reaction was continued for 12 h. TLC monitored the completion of the reaction. Solvent DMF was removed by rotary evaporator, and the residue was extracted with chloroform ( $3 \times 200$  mL) and washed with water ( $3 \times 100$  mL). The combined organic layer was collected and dried over anhydrous sodium sulfate. The crude product slurry was prepared with silica gel (230-440 mesh) and subjected to flash chromatography using ethyl acetate and hexane as eluent. The pure compounds (**6.1a-6.1d**) recovered at ~10 % EtOAc/Hexane.

#### 4.5.1.1. 4-(2-bromoethoxy) benzaldehyde (6.1a)

Yield: 62%. m.p. 80 – 82 °C.

$^1\text{H NMR 300 MHz, 25}^\circ\text{C, Si(CH}_3)_4, (\text{CDCl}_3) (\delta)$ : 3.66-3.69 (2H, t,  $\text{CH}_2\text{Br}$ ,  $J= 5.1$  Hz,  $J= 6$  Hz); 4.37-4.40 (2H, t,  $\text{OCH}_2$ ,  $J= 4.8$  Hz,  $J= 6$  Hz); 7.01-7.04 (2H, d,  $\text{ArH}$ ,  $J= 7.2$  Hz); 7.85-7.87 (2H, d,  $\text{ArH}$ ,  $J= 7.2$  Hz); 9.91 (1H, s,  $\text{CHO}$ ).

#### 4.5.1.2. 4-(3-bromopropoxy) benzaldehyde (6.1b)

Yield: 70%. Liquid in nature

$^1\text{H NMR 300 MHz, 25}^\circ\text{C, Si(CH}_3)_4, (\text{CDCl}_3) (\delta)$ : 2.18-2.22 (2H, m,  $\text{CH}_2$ ,  $J= 5.1$  Hz,  $J= 6$  Hz); 3.60-3.63 (2H, t,  $\text{CH}_2\text{Br}$ ,  $J= 5.1$  Hz,  $J= 6$  Hz); 4.12-4.15 (2H, t,  $\text{OCH}_2$ ,  $J= 4.8$  Hz,  $J= 6$  Hz); 7.01-7.04 (2H, d,  $\text{ArH}$ ,  $J= 7.2$  Hz); 7.85-7.87 (2H, d,  $\text{ArH}$ ,  $J= 7.2$  Hz); 9.88 (1H, s,  $\text{CHO}$ ).

#### 4.5.1.3. 3-(3-bromopropoxy) benzaldehyde (6.1c)

Yield: 66%. Liquid in nature

$^1\text{H NMR 300 MHz, 25}^\circ\text{C, Si(CH}_3)_4, (\text{CDCl}_3) (\delta)$ : 2.18-2.22 (2H, m,  $\text{CH}_2$ ,  $J= 5.1$  Hz,  $J= 6$  Hz); 3.66-3.69 (2H, t,  $\text{CH}_2\text{Br}$ ,  $J= 5.1$  Hz,  $J= 6$  Hz); 4.37-4.40 (2H, t,  $\text{OCH}_2$ ,  $J= 4.8$  Hz,  $J= 6$  Hz); 7.01-7.04 (2H, d,  $\text{ArH}$ ,  $J= 7.2$  Hz); 7.85-7.87 (2H, d,  $\text{ArH}$ ,  $J= 7.2$  Hz); 9.61 (1H, s,  $\text{CHO}$ ).

#### 4.5.1.4. 2-(3-bromopropoxy) benzaldehyde (6.1d)

Yield: 59%. Liquid in nature

$^1\text{H NMR 300 MHz, 25}^\circ\text{C, Si(CH}_3)_4, (\text{CDCl}_3) (\delta)$ : 2.18-2.22 (2H, m,  $\text{CH}_2$ ,  $J= 5.1$  Hz,  $J= 6$  Hz); 3.66-3.69 (2H, t,  $\text{CH}_2\text{Br}$ ,  $J= 5.1$  Hz,  $J= 6$  Hz); 4.37-4.40 (2H, t,  $\text{OCH}_2$ ,  $J= 4.8$  Hz,  $J= 6$  Hz); 7.01-7.04 (2H, d,  $\text{ArH}$ ,  $J= 7.2$  Hz); 7.85-7.87 (2H, d,  $\text{ArH}$ ,  $J= 7.2$  Hz); 10.31 (1H, s,  $\text{CHO}$ ).

#### 4.5.2. General procedure for the synthesis of 6.2a-6.2d

In a 100 mL round bottom flask, sesamol (40.98 mmol) and potassium carbonate (40.98 mmol) was dissolved in dimethylformamide (DMF), and the reaction mixture was stirred for 30 minutes at room temperature. After 30 minutes of the reaction, bromoethoxy/propoxy benzaldehyde (**6.1a-6.1d**) (40.98 mmol) was added to the reaction mixture, and the reaction was continued for 12 h. TLC monitored the completion of the reaction. Solvent DMF was removed by rotary evaporator, and the residue was extracted with ethyl acetate (3 × 200 mL) and washed with water (3 × 100 mL). The combined organic layer was collected and dried over anhydrous sodium sulfate. The crude product slurry was then prepared with silica gel (230-440 mesh) and subjected to flash chromatography using ethyl acetate and hexane as eluent. The pure compounds (**6.2a-6.2d**) were collected at 18% EtOAc/Hexane.

##### 4.5.2.1. 4-(2-(benzo[d][1,3]dioxol-5-yloxy)ethoxy)benzaldehyde (**6.2a**)

Yield: 88%. m.p. 180-183<sup>0</sup>C

<sup>1</sup>H NMR 300 MHz, 25<sup>o</sup>C, Si(CH<sub>3</sub>)<sub>4</sub>, (CDCl<sub>3</sub>) (δ): 3.72-3.69 (2H, t, CH<sub>2</sub>Br, *J*= 5.1 Hz); 4.37-4.40 (2H, t, OCH<sub>2</sub>, *J*= 4.8 Hz); 6.07 (2H, t, CH<sub>2</sub>O, *J*= 5.1 Hz); 6.44-6.47 (1H, d, ArH, *J*= 7.2 Hz); 6.47-6.51 (1H, s, ArH); 6.75-6.79 (1H, d, ArH, *J*= 7.2 Hz); 7.01-7.04 (1H, d, ArH, *J*= 7.2 Hz); 7.85-7.87 (1H, d, ArH, *J*= 7.2 Hz); 9.91 (1H, s, CHO).

##### 4.5.2.2. 4-(3-(benzo[d][1,3]dioxol-5-yloxy)propoxy)benzaldehyde (**6.2b**)

Yield: 89%. m.p. 192-196<sup>0</sup>C

<sup>1</sup>H NMR 300 MHz, 25<sup>o</sup>C, Si(CH<sub>3</sub>)<sub>4</sub>, (CDCl<sub>3</sub>) (δ): 2.18-2.22 (2H, m, CH<sub>2</sub>, *J*= 5.1 Hz, *J*= 6 Hz); 3.60-3.63 (2H, t, CH<sub>2</sub>Br, *J*= 5.1 Hz, *J*= 6 Hz); 4.12-4.15 (2H, t, OCH<sub>2</sub>, *J*= 4.8 Hz, *J*= 6 Hz); 6.07 (2H, t, CH<sub>2</sub>O, *J*= 5.1 Hz, *J*= 6 Hz); 6.44-6.47 (1H, d, ArH, *J*= 7.2 Hz);

6.47-6.51 (1H, s, ArH); 6.75-6.79 (1H, d, ArH,  $J = 7.2$  Hz); 7.01-7.04 (2H, d, ArH,  $J = 7.2$  Hz); 7.85-7.87 (2H, d, ArH,  $J = 7.2$  Hz); 9.88 (1H, s, CHO).

#### 4.5.2.3. 3-(3-(benzo[d][1,3]dioxol-5-yloxy)propoxy)benzaldehyde (6.2c)

Yield: 84%. m.p. 179-182<sup>0</sup>C

<sup>1</sup>H NMR 300 MHz, 25<sup>o</sup>C, Si(CH<sub>3</sub>)<sub>4</sub>, (CDCl<sub>3</sub>) (δ): 2.18-2.22 (2H, m, CH<sub>2</sub>,  $J = 5.1$  Hz,  $J = 6$  Hz); 3.60-3.63 (2H, t, CH<sub>2</sub>Br,  $J = 5.1$  Hz,  $J = 6$  Hz); 4.12-4.15 (2H, t, OCH<sub>2</sub>,  $J = 4.8$  Hz,  $J = 6$  Hz); 6.07 (2H, t, CH<sub>2</sub>O,  $J = 5.1$  Hz,  $J = 6$  Hz); 6.44-6.47 (1H, d, ArH,  $J = 7.2$  Hz); 6.47-6.51 (1H, s, ArH); 6.75-6.79 (1H, d, ArH,  $J = 7.2$  Hz); 7.01-7.04 (2H, d, ArH,  $J = 7.2$  Hz); 7.85-7.87 (2H, d, ArH,  $J = 7.2$  Hz); 9.61 (1H, s, CHO).

#### 4.5.2.4. 2-(3-(benzo[d][1,3]dioxol-5-yloxy)propoxy)benzaldehyde (6.2d)

Yield: 79%. m.p. 220-222<sup>0</sup>C

<sup>1</sup>H NMR 300 MHz, 25<sup>o</sup>C, Si(CH<sub>3</sub>)<sub>4</sub>, (CDCl<sub>3</sub>) (δ): 2.18-2.22 (2H, m, CH<sub>2</sub>,  $J = 5.1$  Hz,  $J = 6$  Hz); 3.60-3.63 (2H, t, CH<sub>2</sub>Br,  $J = 5.1$  Hz,  $J = 6$  Hz); 4.12-4.15 (2H, t, OCH<sub>2</sub>,  $J = 4.8$  Hz,  $J = 6$  Hz); 6.07 (2H, t, CH<sub>2</sub>O,  $J = 5.1$  Hz,  $J = 6$  Hz); 6.44-6.47 (1H, d, ArH,  $J = 7.2$  Hz); 6.47-6.51 (1H, s, ArH); 6.75-6.79 (1H, d, ArH,  $J = 7.2$  Hz); 7.01-7.04 (2H, d, ArH,  $J = 7.2$  Hz); 7.85-7.87 (2H, d, ArH,  $J = 7.2$  Hz); 10.31 (1H, s, CHO).

### 4.5.3. General procedure for the synthesis of 6.1-6.4

Appropriate benzaldehyde derivative (6.2a-6.2d) (2 g, 7 mmol) taken in toluene (50 mL), thiazolidine-2,4-dione (0.8 g, 7 mmol), benzoic acid (0.4g, 3.5 mmol), and piperidine (0.2 mL, 3.5 mmol) were added sequentially. The flask was connected to a Dean-Stark apparatus and refluxed at 180<sup>o</sup>C for 12 h. After that, the reaction mixture was cooled to room temperature and reduced in a rotary evaporator. The reaction suspension was then filtered, and the residue was washed with ice-cold water, EtOH, and hexane. The washed residue was dried under vacuum overnight, affording the desired products as (6.1-6.4) canary yellow residues.

#### 4.5.3.1. 5-(4-(2-(benzo[d][1,3]dioxol-5-yloxy)ethoxy)benzylidene)thiazolidine-2,4-dione (6.1)

**Yield:** 2.0 g (82%); m.p. 261-263°C.

**<sup>1</sup>H NMR 300 MHz, 25°C, Si(CH<sub>3</sub>)<sub>4</sub>, (DMSO) (δ):** 4.44-4.47 (2H, t, CH<sub>2</sub>, *J*= 6.2 Hz); 4.56-4.59 (2H, t, CH<sub>2</sub>, *J*= 6.3 Hz); 5.97 (2H, s, CH<sub>2</sub>); 6.43-6.46 (1H, d, CH, *J*= 2.4 Hz); 6.47 (1H, s, CH); 6.77-6.79 (1H, d, CH, *J*= 9.3 Hz); 6.90-6.92 (1H, d, CH, *J*= 8.7 Hz); 6.92-6.94 (1H, d, CH, *J*= 7.2 Hz); 7.56-7.58 (1H, d, CH, *J*= 8.7 Hz); 7.62-7.64 (1H, d, CH); 7.94 (1H, s, CH); 10.5 (1H, s, NH); **<sup>13</sup>C NMR (75MHz, CDCl<sub>3</sub>): (δ):** 68.9, 69.2, 101.2, 101.5, 107.7, 108.9, 114.3, 116.0, 126.8, 129.8, 143.3, 144.4, 149.4, 152.7, 161.6, 166.3, 167.1. **MS (m/z):** 386.06(M+1). **Element analysis: (i). Calculated:** C=59.21%; H=3.92%; N=3.63%; **(ii). Found:** C=59.86%; H=3.67%; N=3.82%.

**4.5.3.2. 5-(4-(3-(benzo[d][1,3]dioxol-5-yloxy)propoxy)benzylidene)thiazolidine-2,4-dione (6.2)**

**Yield:** 2.1 g (78%); m.p. 272-274°C.

**<sup>1</sup>H NMR 300 MHz, 25°C, Si(CH<sub>3</sub>)<sub>4</sub>, (DMSO) (δ):** 2.25-2.29 (2H, m, CH<sub>2</sub>, *J*= 6.2 Hz); 4.29-4.31 (2H, t, CH<sub>2</sub>, *J*= 6.2 Hz); 4.25-4.29 (2H, t, CH<sub>2</sub>, *J*= 6.2 Hz); 5.927 (2H, s, CH<sub>2</sub>); 6.33-6.36 (1H, dd, CH, *J*= 2.4 Hz); 6.37-6.41 (1H, dd, CH, *J*= 2.4 Hz); 6.77-6.79 (1H, d, CH, *J*= 2.4 Hz); 6.85-6.87 (1H, d, CH, *J*= 8.4 Hz); 6.87-6.89 (1H, d, CH, *J*= 6.9 Hz, *J*= 7.2 Hz); 7.56-7.58 (1H, d, CH, *J*= 8.4 Hz); 7.62-7.64 (1H, d, CH, *J*= 8.7 Hz); 7.94 (1H, s, CH); 10.5 (1H, s, NH). **<sup>13</sup>C NMR (75MHz, DMSO): (δ):** 29.0, 64.8, 65.1, 101.2, 101.5, 107.7, 108.9, 114.3, 116.0, 126.8, 129.8, 143.3, 144.4, 149.4, 152.7, 158.6, 166.3, 167.1. **MS (m/z):** 400.08(M+1). **Element analysis: (i). Calculated:** C=60.14%; H=4.29%; N=3.51% **(ii). Found:** C=60.33%; H=4.41%; N=3.63%.

**4.5.3.3. 5-(3-(3-(benzo[d][1,3]dioxol-5-yloxy)propoxy)benzylidene)thiazolidine-2,4-dione (6.3)**

**Yield:** 1.96 g (72%); m.p. 188-191°C.

**<sup>1</sup>H NMR 300 MHz, 25°C, Si(CH<sub>3</sub>)<sub>4</sub>, (DMSO) (δ):** 2.25-2.29 (2H, m, CH<sub>2</sub>, *J*= 6.3 Hz); 4.29-4.31 (2H, t, CH<sub>2</sub>, *J*= 2.4 Hz); 4.25-4.29 (2H, t, CH<sub>2</sub>, *J*= 2.4 Hz); 6.07 (2H, s, CH<sub>2</sub>); 6.43-6.46 (1H, dd, CH, *J*= 2.4 Hz); 6.47 (1H, s, CH); 6.77-6.79 (1H, d, CH, *J*= 2.4 Hz);

6.87-6.89 (1H, d,  $\underline{\text{CH}}$ ,  $J= 8.3$  Hz); 7.12 (1H, s,  $\underline{\text{CH}}$ ); 7.14-7.16 (1H, d,  $\underline{\text{CH}}$ ,  $J= 8.3$  Hz); 7.62-7.64 (1H, t,  $\underline{\text{CH}}$ ,  $J= 8.3$  Hz); 7.94 (1H, s,  $\underline{\text{CH}}$ ); 10.5 (1H, s,  $\underline{\text{NH}}$ ).  $^{13}\text{C}$  NMR (75MHz,  $\text{CDCl}_3$ ): ( $\delta$ ): 29.0, 64.8, 65.1, 101.2, 101.5, 107.7, 108.9, 113.3, 113.0, 116.0, 120.1, 129.2, 135.8, 143.3, 144.4, 149.4, 152.7, 164.4, 166.3, 167.1. MS (m/z): 400.08(M+1). Element analysis: (i). Calculated: C=60.14%; H=4.29%; N=3.51%. (ii). Found: C=60.26%; H=4.18%; N=3.61%.

#### 4.5.3.4. 5-(2-(3-(benzo[d][1,3]dioxol-5-yloxy)propoxy)benzylidene)thiazolidine-2,4-dione (6.4)

**Yield:** 2.0 g (76%); m.p. 210-212°C.

$^1\text{H}$  NMR 300 MHz, 25°C,  $\text{Si}(\text{CH}_3)_4$ , (DMSO) ( $\delta$ ): 2.25-2.29 (2H, m,  $\underline{\text{CH}_2}$ ,  $J= 6.2$  Hz); 4.29-4.31(2H, t,  $\underline{\text{CH}_2}$ ,  $J= 6.2$  Hz); 4.25-4.29 (2H, t,  $\underline{\text{CH}_2}$ ,  $J= 6.2$  Hz); 6.11 (2H, s,  $\underline{\text{CH}}$ ); 6.43-6.46 (1H, d,  $\underline{\text{CH}}$ ,  $J= 2.4$  Hz); 6.47-6.51 (1H, s,  $\underline{\text{CH}}$ ,  $J= 2.4$  Hz); 6.77-6.79 (1H, d,  $\underline{\text{CH}}$ ,  $J= 8.3$  Hz); 6.94-6.96 (1H, d,  $\underline{\text{CH}}$ ,  $J= 8.4$  Hz); 6.96-6.98 (1H, t,  $\underline{\text{CH}}$ ,  $J= 8.3$  Hz); 7.22-7.24 (1H, t,  $\underline{\text{CH}}$ ,  $J= 8.4$  Hz); 7.66-7.68 (1H, d,  $\underline{\text{CH}}$ ,  $J= 8.4$  Hz); 8.13 (1H, s,  $\underline{\text{CH}}$ ); 10.9 (1H, s,  $\underline{\text{NH}}$ ).  $^{13}\text{C}$  NMR (75MHz,  $\text{CDCl}_3$ ): ( $\delta$ ): 29.0, 64.8, 65.1, 101.2, 101.5, 107.7, 108.9, 114.3, 115.0, 116.0, 120.2, 128.1, 128.5, 143.3, 144.4, 149.4, 152.7, 154.4, 166.3, 167.1. MS (m/z): 400.08(M+1). Element analysis: (i). Calculated: C=60.14%; H=4.29%; N=3.51%. (ii). Found: C=60.08%; H=4.39%; N=3.55%.

#### 4.5.4. $^1\text{H}$ NMR spectra of compounds 6.1-6.4

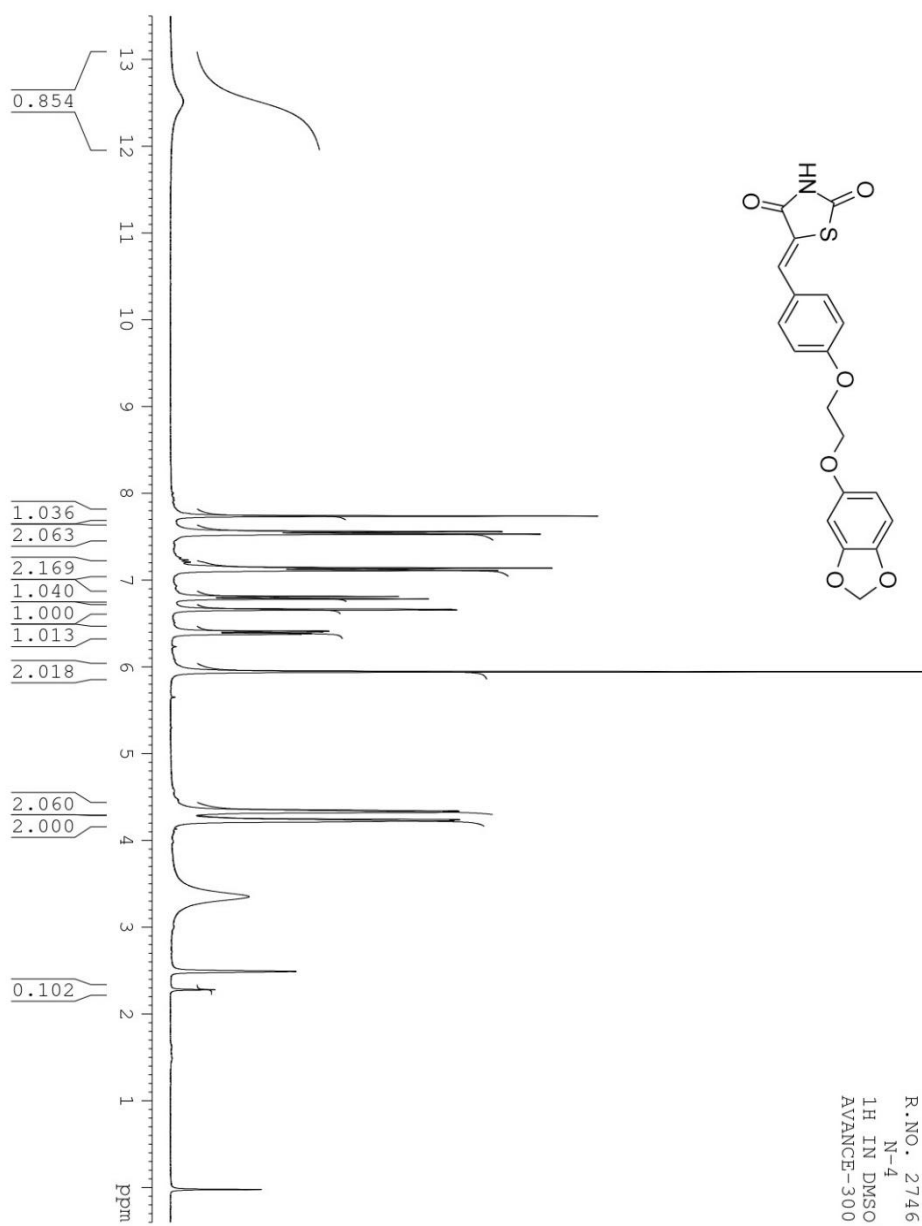


**Figure 4.8:** <sup>1</sup>H NMR of 5-(4-(2-(benzo[d][1,3]dioxol-5-yloxy)ethoxy)benzylidene)thiazolidine-2,4-dione (**6.1**)

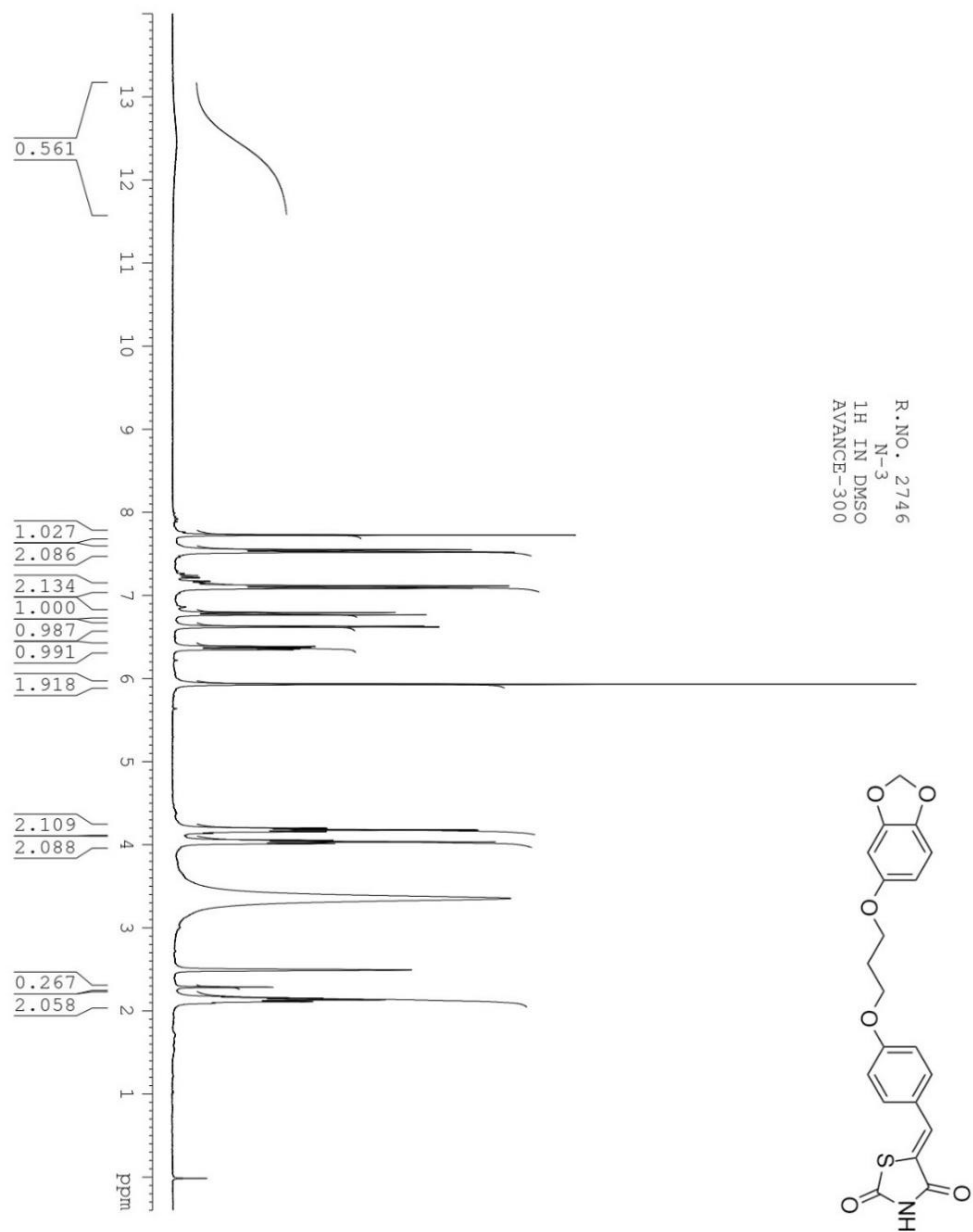


**Figure 4.9:**  $^1\text{H}$  NMR of 5-(4-(3-(benzo[d][1,3]dioxol-5-yloxy)propoxy)benzylidene)thiazolidine-2,4-dione (**6.2**)



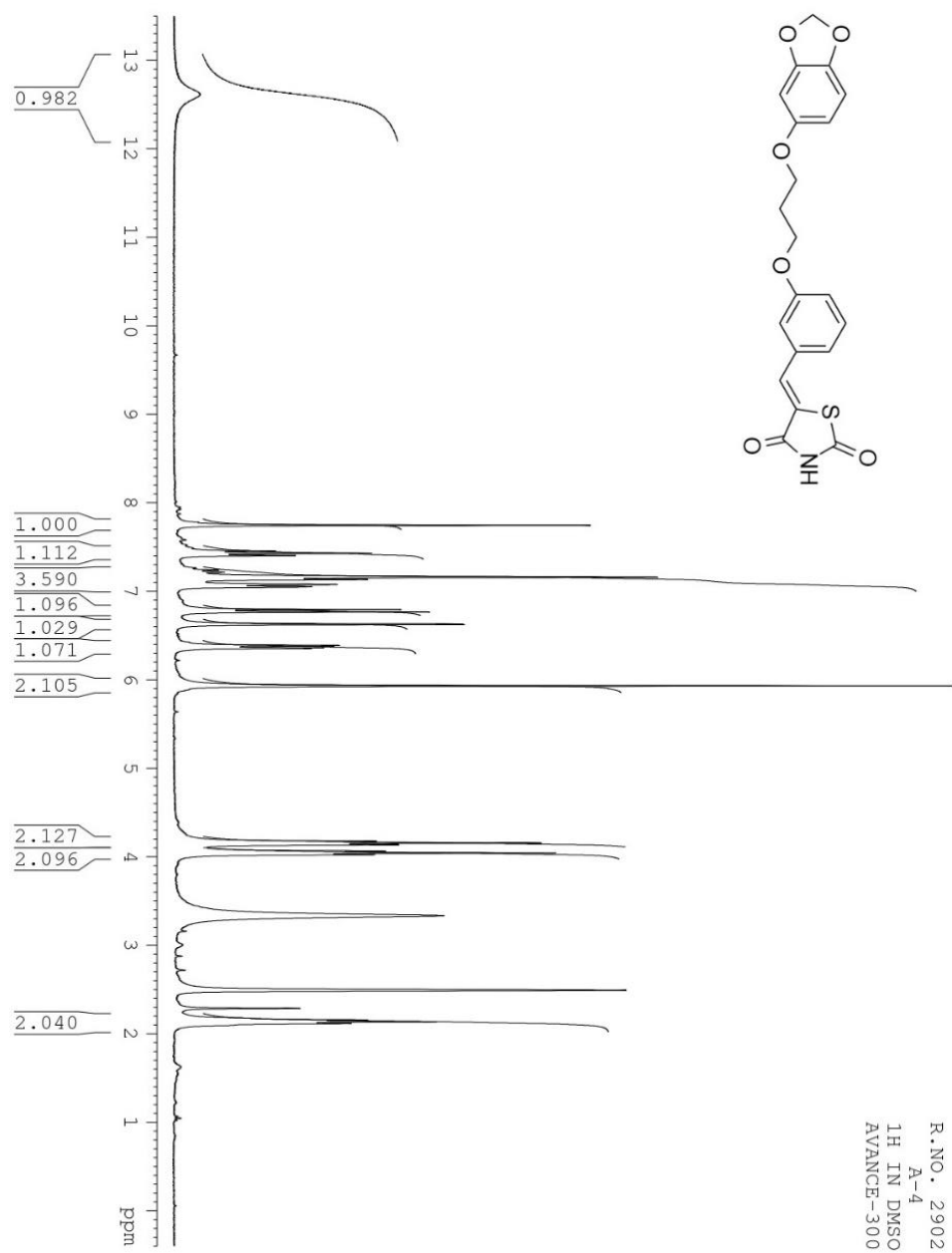


**Figure 4.10:** <sup>1</sup>H NMR of 5-(3-(3-(benzo[d][1,3]dioxol-5-yloxy)propoxy)benzylidene)thiazolidine-2,4-dione (**6.3**)

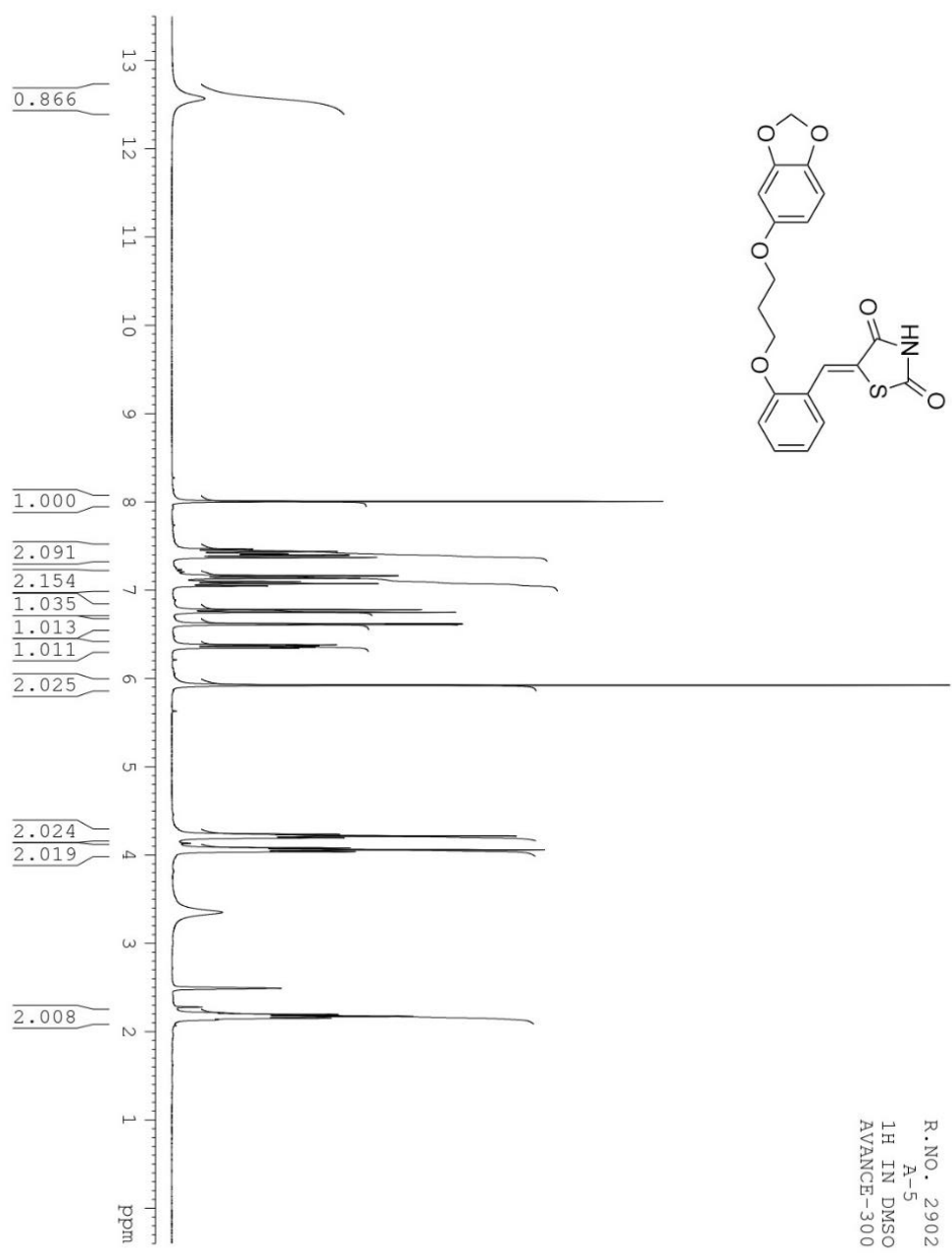
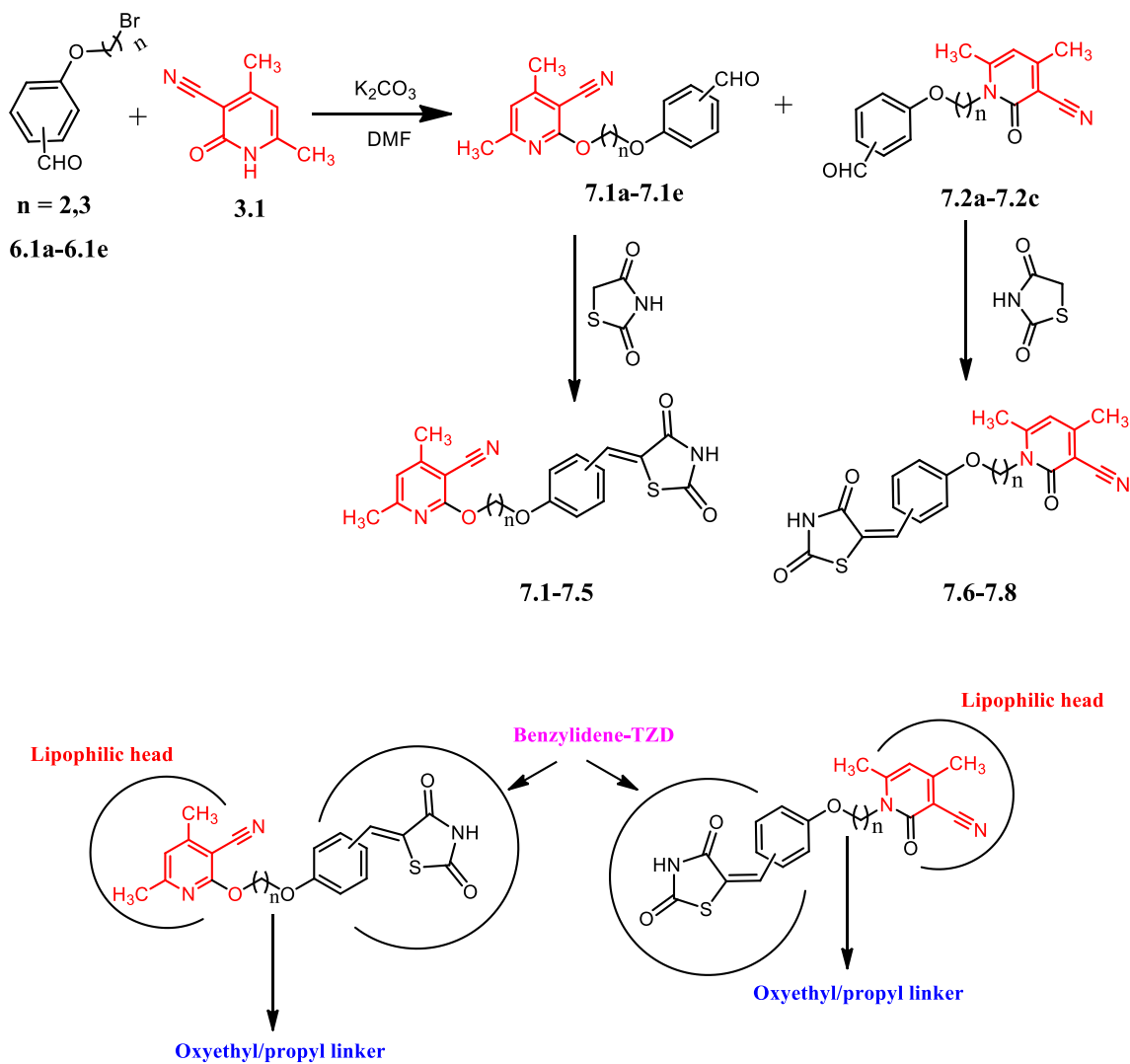


**Figure 4.11:** <sup>1</sup>H NMR of 5-(2-(3-(benzo[d][1,3]dioxol-5-yloxy)propoxy)benzylidene)thiazolidine-2,4-dione (**6.4**)

**4.6. Scheme 7: Synthesis of benzylidene-TZD-Linker compounds with 2-cyano pyridone lipophilic head (7.1-7.8)**



**Scheme 7**

**4.6.1. Synthesis of 2-(2-bromoethoxy) benzaldehyde (6.1e)**

In a 100 mL round bottom flask, Salicylaldehyde (40.98 mmol) and potassium carbonate (40.98 mmol) was dissolved in 25 mL of dimethylformamide (DMF), and the reaction mixture was stirred for 30 minutes at room temperature. After 30 minutes, 1,2-

dibromoethane (204.8 mmol) was added to the reaction mixture, and the reaction was continued for 12 h. TLC monitored the completion of the reaction. Solvent DMF was removed by rotary evaporator, and the residue was extracted with chloroform (3 × 200 mL) and washed with water (3 × 100 mL). The combined organic layer was collected and dried over anhydrous sodium sulfate. The crude product slurry was prepared with silica gel (230-440 mesh) and subjected to flash chromatography using ethyl acetate and hexane as eluent. The pure compounds (**6.1e**) recovered at ~10 % EtOAc/Hexane.

**Yield:** 62%. Liquid in nature.

**<sup>1</sup>H NMR 300 MHz, 25°C, Si(CH<sub>3</sub>)<sub>4</sub>, (CDCl<sub>3</sub>) (δ):** 3.66-3.69 (2H, t, CH<sub>2</sub>Br, *J*= 5.1 Hz, *J*= 6 Hz); 4.37-4.40 (2H, t, OCH<sub>2</sub>, *J*= 4.8 Hz, *J*= 6 Hz); 7.01-7.04 (2H, d, ArH, *J*= 7.2 Hz); 7.85-7.87 (2H, d, ArH, *J*= 7.2 Hz); 10.36 (1H, s, CHO).

#### 4.6.2. General procedure for the synthesis of 7.1a-7.1e

In a 100 mL round bottom flask, 4,6-dimethyl-2-oxo-1,2-dihydro-pyridine-3-carbonitrile (40.98 mmol) and potassium carbonate (40.98 mmol) was dissolved in dimethylformamide (DMF), and the reaction mixture was stirred for 30 minutes at room temperature. After 30 minutes of the reaction, bromo ethoxy/propoxy benzaldehyde (**6.1a-6.1e**) (40.98 mmol) was added to the reaction mixture, and the reaction was continued for 12 h. TLC monitored the completion of the reaction. Solvent DMF was removed by rotary evaporator, and the residue was extracted with ethyl acetate (3 × 200 mL) and washed with water (3 × 100 mL). The combined organic layer was collected and dried over anhydrous sodium sulfate. The crude product slurry was then prepared with silica gel (230-440 mesh) and subjected to flash chromatography using ethyl acetate and hexane as eluent. The pure compounds (**7.1a-7.1e**) were collected at 20% EtOAc/Hexane.

##### 4.6.2.1. 2-(2-(4-formylphenoxy) ethoxy)-4,6-dimethylnicotinonitrile (**7.1a**)

**Yield:** 35%. m.p. 154-157<sup>0</sup>C.

**<sup>1</sup>H NMR 300 MHz, 25°C, Si(CH<sub>3</sub>)<sub>4</sub>, (CDCl<sub>3</sub>) (δ):** 2.52-2.54 (3H, s, CH<sub>3</sub>); 2.54-2.57 (3H, s, CH<sub>3</sub>); 3.66-3.69 (2H, t, CH<sub>2</sub>Br, *J*= 5.1 Hz, *J*= 6 Hz); 4.37-4.40 (2H, t, OCH<sub>2</sub>, *J*=

4.8 Hz,  $J = 6$  Hz); 6.82 (1H, s, ArH); 7.01-7.04 (2H, d, ArH,  $J = 7.2$  Hz); 7.85-7.87 (2H, d, ArH,  $J = 7.2$  Hz); 9.91 (1H, s, CHO).

#### 4.6.2.2. 2-(3-(4-formylphenoxy) propoxy)-4,6-dimethylnicotinonitrile (7.1b)

**Yield:** 41%. m.p. 138-140°C.

**$^1\text{H}$  NMR 300 MHz, 25°C, Si(CH<sub>3</sub>)<sub>4</sub>, (CDCl<sub>3</sub>) ( $\delta$ ):** 2.18-2.22 (2H, m, CH<sub>2</sub>,  $J = 5.1$  Hz,  $J = 6$  Hz); 2.52-2.54 (3H, s, CH<sub>3</sub>); 2.54-2.57 (3H, s, CH<sub>3</sub>); 3.66-3.69 (2H, t, CH<sub>2</sub>Br,  $J = 5.1$  Hz,  $J = 6$  Hz); 4.37-4.40 (2H, t, OCH<sub>2</sub>,  $J = 4.8$  Hz,  $J = 6$  Hz); 6.82 (1H, s, ArH); 7.01-7.04 (2H, d, ArH,  $J = 7.2$  Hz); 7.85-7.87 (2H, d, ArH,  $J = 7.2$  Hz); 9.91 (1H, s, CHO).

#### 4.6.2.3. 2-(3-(3-formylphenoxy) propoxy)-4,6-dimethylnicotinonitrile (7.1c)

**Yield:** 39%. m.p. 144-146°C.

**$^1\text{H}$  NMR 300 MHz, 25°C, Si(CH<sub>3</sub>)<sub>4</sub>, (CDCl<sub>3</sub>) ( $\delta$ ):** 2.18-2.22 (2H, m, CH<sub>2</sub>,  $J = 5.1$  Hz,  $J = 6$  Hz); 2.52-2.54 (3H, s, CH<sub>3</sub>); 2.54-2.57 (3H, s, CH<sub>3</sub>); 3.66-3.69 (2H, t, CH<sub>2</sub>Br,  $J = 5.1$  Hz,  $J = 6$  Hz); 4.37-4.40 (2H, t, OCH<sub>2</sub>,  $J = 4.8$  Hz,  $J = 6$  Hz); 6.82 (1H, s, ArH); 7.01-7.04 (2H, d, ArH,  $J = 7.2$  Hz); 7.85-7.87 (2H, d, ArH,  $J = 7.2$  Hz); 9.61 (1H, s, CHO).

#### 4.6.2.4. 2-(3-(2-formylphenoxy) propoxy)-4,6-dimethylnicotinonitrile (7.1d)

**Yield:** 38%. m.p. 162-165°C.

**$^1\text{H}$  NMR 300 MHz, 25°C, Si(CH<sub>3</sub>)<sub>4</sub>, (CDCl<sub>3</sub>) ( $\delta$ ):** 2.18-2.22 (2H, m, CH<sub>2</sub>,  $J = 5.1$  Hz,  $J = 6$  Hz); 2.52-2.54 (3H, s, CH<sub>3</sub>); 2.54-2.57 (3H, s, CH<sub>3</sub>); 3.66-3.69 (2H, t, CH<sub>2</sub>Br,  $J = 5.1$  Hz,  $J = 6$  Hz); 4.37-4.40 (2H, t, OCH<sub>2</sub>,  $J = 4.8$  Hz,  $J = 6$  Hz); 6.82 (1H, s, ArH); 7.01-7.04 (2H, d, ArH,  $J = 7.2$  Hz); 7.85-7.87 (2H, d, ArH,  $J = 7.2$  Hz); 10.36 (1H, s, CHO).

#### 4.6.2.5. 2-(2-(2-formylphenoxy) ethoxy)-4,6-dimethylnicotinonitrile (7.1e)

**Yield:** 30%. m.p. 156-158°C.

**$^1\text{H}$  NMR 300 MHz, 25°C, Si(CH<sub>3</sub>)<sub>4</sub>, (CDCl<sub>3</sub>) ( $\delta$ ):** 2.52-2.54 (3H, s, CH<sub>3</sub>); 2.54-2.57 (3H, s, CH<sub>3</sub>); 3.66-3.69 (2H, t, CH<sub>2</sub>Br,  $J = 5.1$  Hz,  $J = 6$  Hz); 4.37-4.40 (2H, t, OCH<sub>2</sub>,  $J = 4.8$  Hz,  $J = 6$  Hz); 6.82 (1H, s, ArH); 7.01-7.04 (2H, d, ArH,  $J = 7.2$  Hz); 7.85-7.87 (2H, d, ArH,  $J = 7.2$  Hz); 10.36 (1H, s, CHO).

### 4.6.3. General procedure for the synthesis of 7.2a-7.2c

In a 100 mL round bottom flask, 4,6-dimethyl-2-oxo-1,2-dihydro-pyridine-3-carbonitrile (40.98 mmol) and potassium carbonate (40.98 mmol) was dissolved in dimethylformamide (DMF), and the reaction mixture was stirred for 30 minutes at room temperature. After 30 minutes of the reaction, bromo ethoxy/propoxy benzaldehyde (**6.1a**, **6.1b**, **6.1d**) (40.98 mmol) was added to the reaction mixture, and the reaction was continued for 12 h. TLC monitored the completion of the reaction. Solvent DMF was removed by rotary evaporator, and the residue was extracted with ethyl acetate (3 × 200 mL) and washed with water (3 × 100 mL). The combined organic layer was collected and dried over anhydrous sodium sulfate. The crude product slurry was then prepared with silica gel (230-440 mesh) and subjected to flash chromatography using ethyl acetate and hexane as eluent. The pure compounds (**7.2a-7.2c**) were collected at 55% EtOAc/Hexane.

#### 4.6.3.1. 1-(2-(4-formylphenoxy)ethyl)-4,6-dimethyl-2-oxo-1,2-dihydropyridine-3-carbonitrile (**7.2a**)

**Yield:** 62%. m.p. 156-158<sup>0</sup>C.

<sup>1</sup>H NMR 300 MHz, 25<sup>o</sup>C, Si(CH<sub>3</sub>)<sub>4</sub>, (CDCl<sub>3</sub>) (δ): 2.23-2.26 (3H, s, CH<sub>3</sub>); 2.27-2.30 (3H, s, CH<sub>3</sub>); 3.66-3.69 (2H, t, CH<sub>2</sub>Br, *J*= 5.1 Hz, *J*= 6 Hz); 4.37-4.40 (2H, t, OCH<sub>2</sub>, *J*= 4.8 Hz, *J*= 6 Hz); 6.35 (1H, s, ArH); 7.01-7.04 (2H, d, ArH, *J*= 7.2 Hz); 7.85-7.87 (2H, d, ArH, *J*= 7.2 Hz); 9.91 (1H, s, CHO).

#### 4.6.3.2. 1-(3-(4-formylphenoxy)propyl)-4,6-dimethyl-2-oxo-1,2-dihydropyridine-3-carbonitrile (**7.2b**)

**Yield:** 61%. m.p. 156-158<sup>0</sup>C.

<sup>1</sup>H NMR 300 MHz, 25<sup>o</sup>C, Si(CH<sub>3</sub>)<sub>4</sub>, (CDCl<sub>3</sub>) (δ): 1.95-1.98 (2H, m, CH<sub>2</sub>, *J*= 5.1 Hz, *J*= 6 Hz); 2.23-2.26 (3H, s, CH<sub>3</sub>); 2.27-2.30 (3H, s, CH<sub>3</sub>); 3.66-3.69 (2H, t, CH<sub>2</sub>Br, *J*= 5.1 Hz, *J*= 6 Hz); 4.37-4.40 (2H, t, OCH<sub>2</sub>, *J*= 4.8 Hz, *J*= 6 Hz); 6.35 (1H, s, ArH); 7.01-7.04 (2H, d, ArH, *J*= 7.2 Hz); 7.85-7.87 (2H, d, ArH, *J*= 7.2 Hz); 9.91 (1H, s, CHO).

#### 4.6.3.3. 1-(3-(2-formylphenoxy)propyl)-4,6-dimethyl-2-oxo-1,2-dihydropyridine-3-carbonitrile (7.2c)

**Yield:** 58%. m.p. 156-158<sup>0</sup>C.

**<sup>1</sup>H NMR 300 MHz, 25<sup>o</sup>C, Si(CH<sub>3</sub>)<sub>4</sub>, (CDCl<sub>3</sub>) (δ):** 1.95-1.98 (2H, m, CH<sub>2</sub>, *J*= 5.1 Hz, *J*= 6 Hz); 2.23-2.26 (3H, s, CH<sub>3</sub>); 2.27-2.30 (3H, s, CH<sub>3</sub>); 3.66-3.69 (2H, t, CH<sub>2</sub>Br, *J*= 5.1 Hz, *J*= 6 Hz); 4.37-4.40 (2H, t, OCH<sub>2</sub>, *J*= 4.8 Hz, *J*= 6 Hz); 6.35 (1H, s, ArH); 7.01-7.04 (2H, d, ArH, *J*= 7.2 Hz); 7.85-7.87 (2H, d, ArH, *J*= 7.2 Hz); 10.36 (1H, s, CHO).

#### 4.6.4. General procedure for the synthesis of 7.1-7.5

Benzaldehyde derivative (7.1a-7.1e) (2 g, 7 mmol) taken in toluene (50 mL) and thiazolidine-2,4-dione (0.8 g, 7 mmol), benzoic acid (0.4 g, 3.5 mmol), and piperidine (0.2 mL, 3.5 mmol) were added sequentially. The flask was connected to a Dean-Stark apparatus and refluxed at 180<sup>o</sup>C for 12 h. After that, the reaction mixture was cooled to room temperature and reduced in a rotary evaporator. The reaction suspension was then filtered, and the residue was washed with cold water, EtOH, and hexane. The washed residue was dried under vacuum overnight, affording the desired products as (7.1-7.5) canary yellow residues.

##### 4.6.4.1. 2-(2-(4-((2,4-dioxothiazolidin-5-ylidene)methyl)phenoxy)ethoxy)-4,6-dimethyl-nicotinonitrile (7.1)

**Yield:** 2.1 g (78%); m.p. 210-213<sup>o</sup>C.

**<sup>1</sup>H NMR 300 MHz, 25<sup>o</sup>C, Si(CH<sub>3</sub>)<sub>4</sub>, (DMSO) (δ):** 2.44 (3H, s, CH<sub>3</sub>); 2.53 (3H, s, CH<sub>3</sub>); 4.52-4.55 (2H, t, CH<sub>2</sub>, *J*= 6.9 Hz, *J*= 6.3 Hz); 4.72-4.75 (2H, t, CH<sub>2</sub>, *J*= 6.3 Hz); 6.82 (1H, s, CH); 6.92-6.94 (1H, d, CH, *J*= 2.4 Hz); 6.94-6.96 (1H, d, CH, *J*= 2.3 Hz); 7.56-7.58 (1H, d, CH, *J*= 8.3 Hz); 7.62-7.64 (1H, d, CH, *J*= 8.3 Hz); 7.94 (1H, s, CH); 10.5 (1H, s, NH); **<sup>13</sup>C NMR (75MHz, CDCl<sub>3</sub>):** (δ): 20.7, 24.5, 68.4, 68.9, 93.8, 11.2, 114.5, 114.3, 115.6, 116.0, 126.8, 129.8, 129.8 143.3, 155.2, 160.5, 161.6, 164.3, 166.3, 167.1. **MS (m/z):** 396.09(M+1). **Element analysis: (i). Calculated:**C=60.75%; H=4.33%; N=10.63%. **(ii). Found:** C=60.63%; H=4.22%; N=10.51%.

**4.6.4.2. 2-(3-(4-((2,4-dioxothiazolidin-5-ylidene)methyl)phenoxy)propoxy)-4,6-dimethyl-nicotinonitrile (7.2)**

**Yield:** 2.2 g (79%); m.p. 189-191°C.

**<sup>1</sup>H NMR 300 MHz, 25°C, Si(CH<sub>3</sub>)<sub>4</sub>, (DMSO) (δ):** 2.25-2.27 (2H, m, CH<sub>2</sub>, *J*= 6.3 Hz); 2.47 (3H, s, CH<sub>3</sub>); 2.50 (3H, s, CH<sub>3</sub>); 4.06-4.09 (2H, t, CH<sub>2</sub>, *J*= 6.3 Hz); 4.26-4.29 (2H, t, CH<sub>2</sub>, *J*= 6.3 Hz); 6.85 (1H, s, CH); 6.92-6.94 (1H, d, CH, *J*= 8.4 Hz); 6.94-6.96 (1H, d, CH, *J*= 8.3 Hz); 7.56-7.58 (1H, d, CH, *J*= 8.4 Hz); 7.62-7.64 (1H, d, CH, *J*= 8.3 Hz); 7.94 (1H, s, CH); 10.5 (1H, s, NH); **<sup>13</sup>C NMR (75MHz, CDCl<sub>3</sub>): (δ):** 20.7, 24.5, 29.0, 68.4, 68.9, 93.8, 11.2, 114.5, 114.3, 115.6, 116.0, 126.8, 129.8, 129.8 143.3, 155.2, 160.5, 161.6, 164.3, 166.3, 167.1. **MS (m/z):** 410.11(M+1). **Element analysis: (i). Calculated:** C=61.60%; H=4.68%; N=10.26%. **(ii). Found:** C=60.63%; H=4.52%; N=10.11%.

**4.6.4.3. 2-(3-(3-((2,4-dioxothiazolidin-5-ylidene)methyl)phenoxy)propoxy)-4,6-dimethyl-nicotinonitrile (7.3)**

**Yield:** 2.3 g (82%); m.p. 222-224°C.

**<sup>1</sup>H NMR 300 MHz, 25°C, Si(CH<sub>3</sub>)<sub>4</sub>, (DMSO) (δ):** 2.25-2.27 (2H, m, CH<sub>2</sub>, *J*= 6.4 Hz); 2.46 (3H, s, CH<sub>3</sub>); 2.50-2.53 (3H, s, CH<sub>3</sub>); 4.06-4.09 (2H, t, CH<sub>2</sub>, *J*= 6.3 Hz); 4.26-4.29 (2H, t, CH<sub>2</sub>, *J*= 6.3 Hz); 6.84 (1H, s, CH); 6.92-6.94 (1H, d, CH, *J*= 2.4 Hz); 6.94-6.96 (1H, d, CH, *J*= 2.4 Hz); 7.56-7.58 (1H, d, CH, *J*= 8.4 Hz); 7.62-7.64 (1H, d, CH, *J*= 8.4 Hz); 7.95 (1H, s, CH); 10.7 (1H, s, NH); **<sup>13</sup>C NMR (75MHz, CDCl<sub>3</sub>): (δ):** 20.7, 24.5, 29.0, 68.4, 68.9, 93.8, 11.2, 114.5, 114.3, 115.6, 116.0, 126.8, 129.8, 129.8 143.3, 155.2, 160.5, 161.6, 164.3, 166.3, 167.1. **MS (m/z):** 410.11(M+1). **Element analysis: (i). Calculated:** C=61.60%; H=4.68%; N=10.26%. **(ii). Found:** C=60.77%; H=4.52%; N=10.17%.

**4.6.4.4. 2-(3-(2-((2,4-dioxothiazolidin-5-ylidene)methyl)phenoxy)propoxy)-4,6-dimethyl-nicotinonitrile (7.4)**

**Yield:** 2.05 g (72%); m.p. 197-199°C.



**<sup>1</sup>H NMR 300 MHz, 25°C, Si(CH<sub>3</sub>)<sub>4</sub>, (DMSO) (δ):** 2.25-2.27 (2H, m, CH<sub>2</sub>, *J*= 6.3 Hz); 2.40 (3H, s, CH<sub>3</sub>); 2.52 (3H, s, CH<sub>3</sub>); 4.06-4.09 (2H, t, CH<sub>2</sub>, *J*= 6.2 Hz); 4.26-4.29 (2H, t, CH<sub>2</sub>, *J*= 6.3 Hz); 6.87 (1H, s, CH); 6.92-6.94 (1H, d, CH, *J*= 8.4 Hz); 6.94-6.96 (1H, d, CH, *J*= 8.3 Hz); 7.56-7.58 (1H, d, CH, *J*= 8.3 Hz); 7.62-7.64 (1H, d, CH, *J*= 8.4 Hz); 7.97 (1H, s, CH); 10.4 (1H, s, NH); **<sup>13</sup>C NMR (75MHz, CDCl<sub>3</sub>): (δ):** 20.7, 24.5, 29.0, 68.4, 68.9, 93.8, 11.2, 114.5, 114.3, 115.6, 116.0, 126.8, 129.8, 129.8 143.3, 155.2, 160.5, 161.6, 164.3, 166.3, 167.1. **MS (m/z):** 410.11(M+1). **Element analysis: (i). Calculated:** C=61.60%; H=4.68%; N=10.26. **(ii). Found:** C=60.51%; H=4.56%; N=10.19%.

#### **4.6.4.5. 2-(2-(2-((2,4-dioxothiazolidin-5-ylidene)methyl)phenoxy)ethoxy)-4,6-dimethyl-nicotinonitrile (7.5)**

**Yield:** 2.0 g (70%); m.p. 235-237°C.

**<sup>1</sup>H NMR 300 MHz, 25°C, Si(CH<sub>3</sub>)<sub>4</sub>, (DMSO) (δ):** 2.42 (3H, s, CH<sub>3</sub>); 2.52 (3H, s, CH<sub>3</sub>); 4.52-4.55 (2H, t, CH<sub>2</sub>, *J*= 6.3 Hz); 4.72-4.75 (2H, t, CH<sub>2</sub>, *J*= 6.3 Hz); 6.84 (1H, s, CH); 6.92-6.94 (1H, d, CH, *J*= 2.3 Hz); 6.94-6.96 (1H, d, CH, *J*= 2.4 Hz); 7.56-7.58 (1H, d, CH, *J*= 8.4 Hz); 7.62-7.64 (1H, d, CH, *J*= 8.3 Hz); 7.97 (1H, s, CH); 12.5 (1H, s, NH); **<sup>13</sup>C NMR (75MHz, CDCl<sub>3</sub>): (δ):** 20.7, 24.5, 68.4, 68.9, 93.8, 11.2, 114.5, 114.3, 115.6, 116.0, 126.8, 129.8, 129.8 143.3, 155.2, 160.5, 161.6, 164.3, 166.3, 167.1. **MS (m/z):** 396.09(M+1). **Element analysis: (i). Calculated:** C=60.75%; H=4.33%; N=10.63%; **(ii). Found:** C=60.55%; H=4.18%; N=10.45%.

#### 4.6.5. $^1\text{H}$ NMR spectra of compounds 7.1-7.5

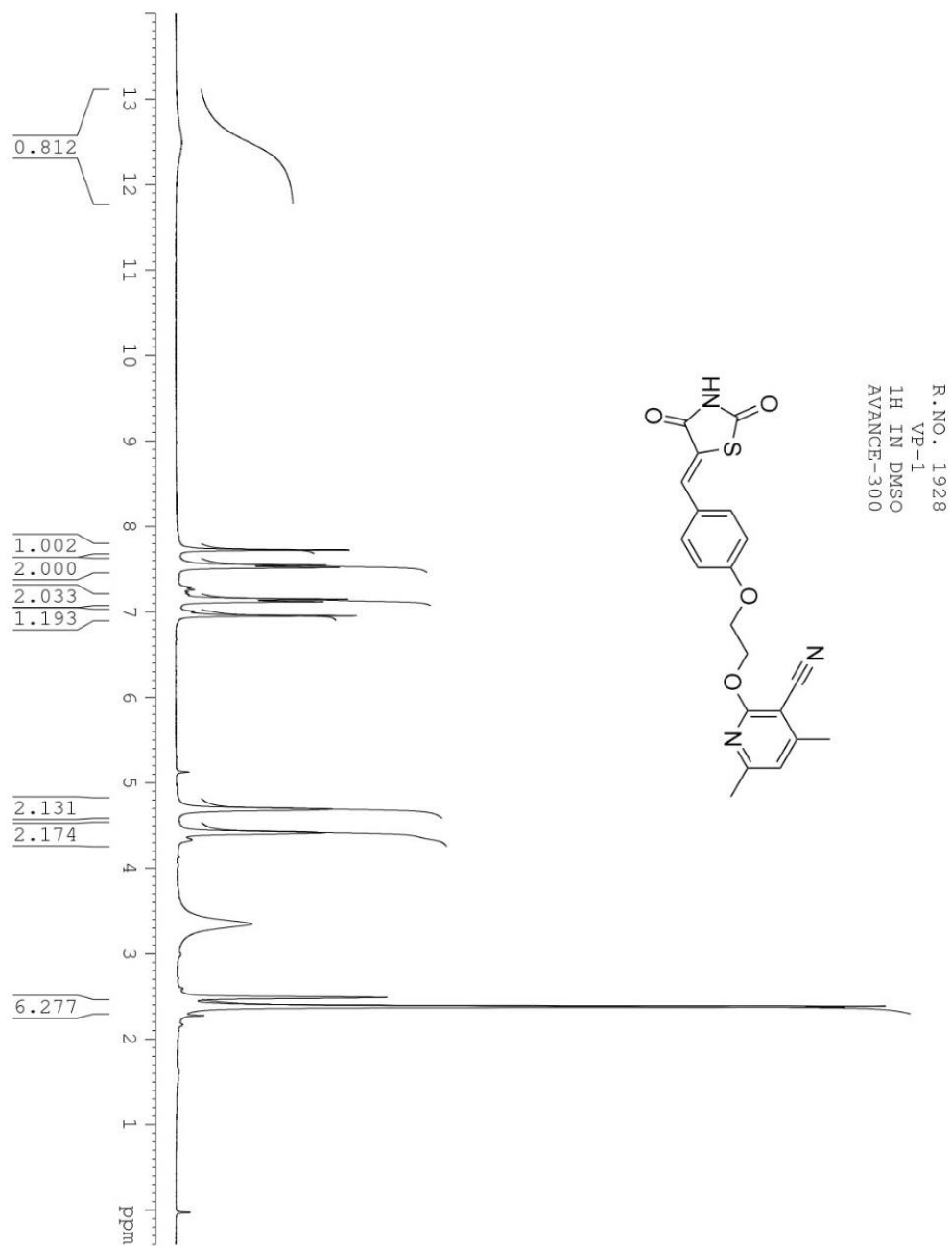


**Figure 4.12:**  $^1\text{H}$  NMR of 2-(2-(4-((2,4-dioxothiazolidin-5-ylidene)methyl) phenoxy) ethoxy)-4,6-dimethyl-nicotinonitrile (**7.1**)

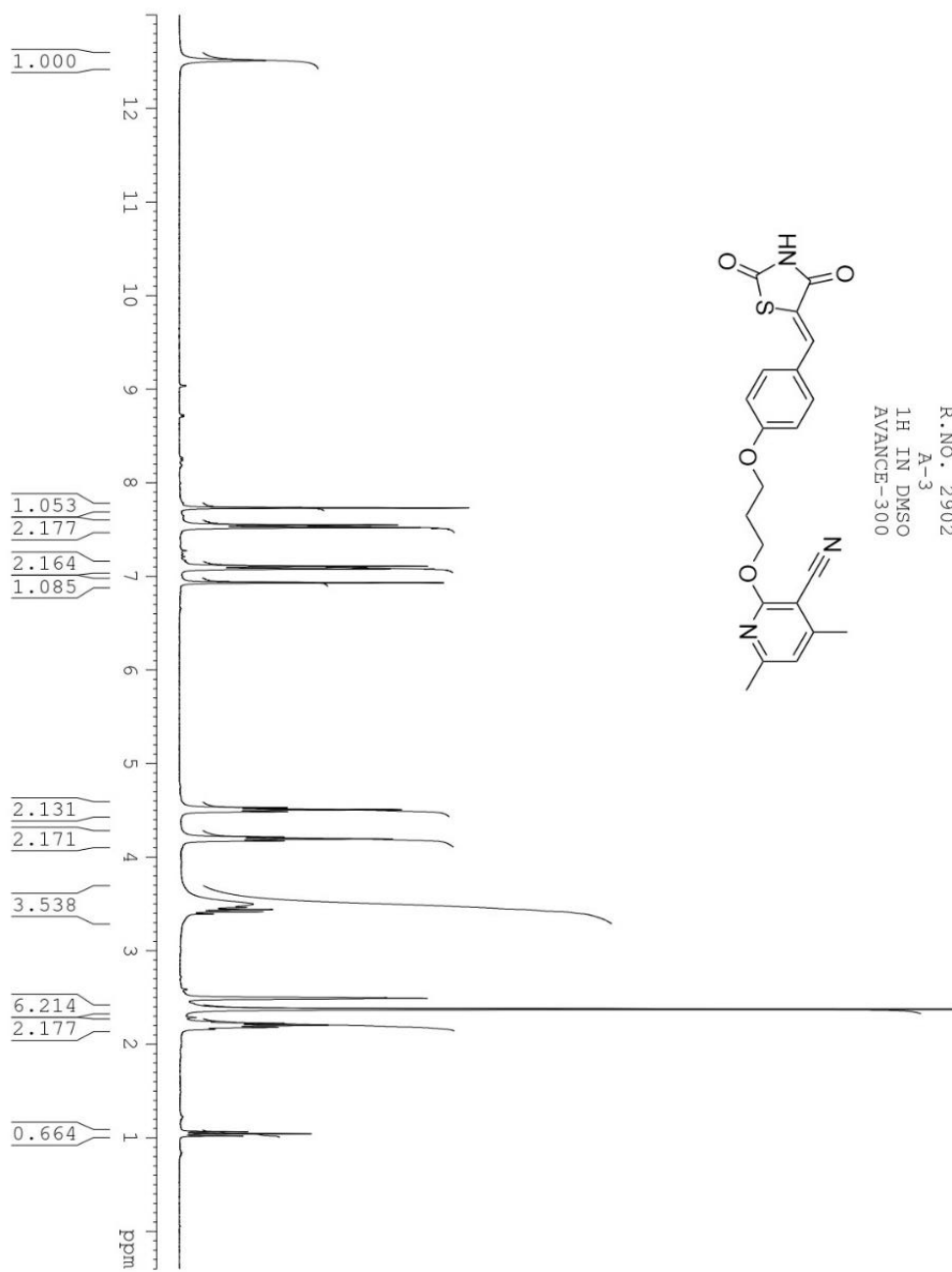


**Figure 4.13:**  $^1\text{H}$  NMR of 2-(3-(4-((2,4-dioxothiazolidin-5-ylidene)methyl)phenoxy)propoxy)-4,6-dimethyl-nicotinonitrile (**7.2**)

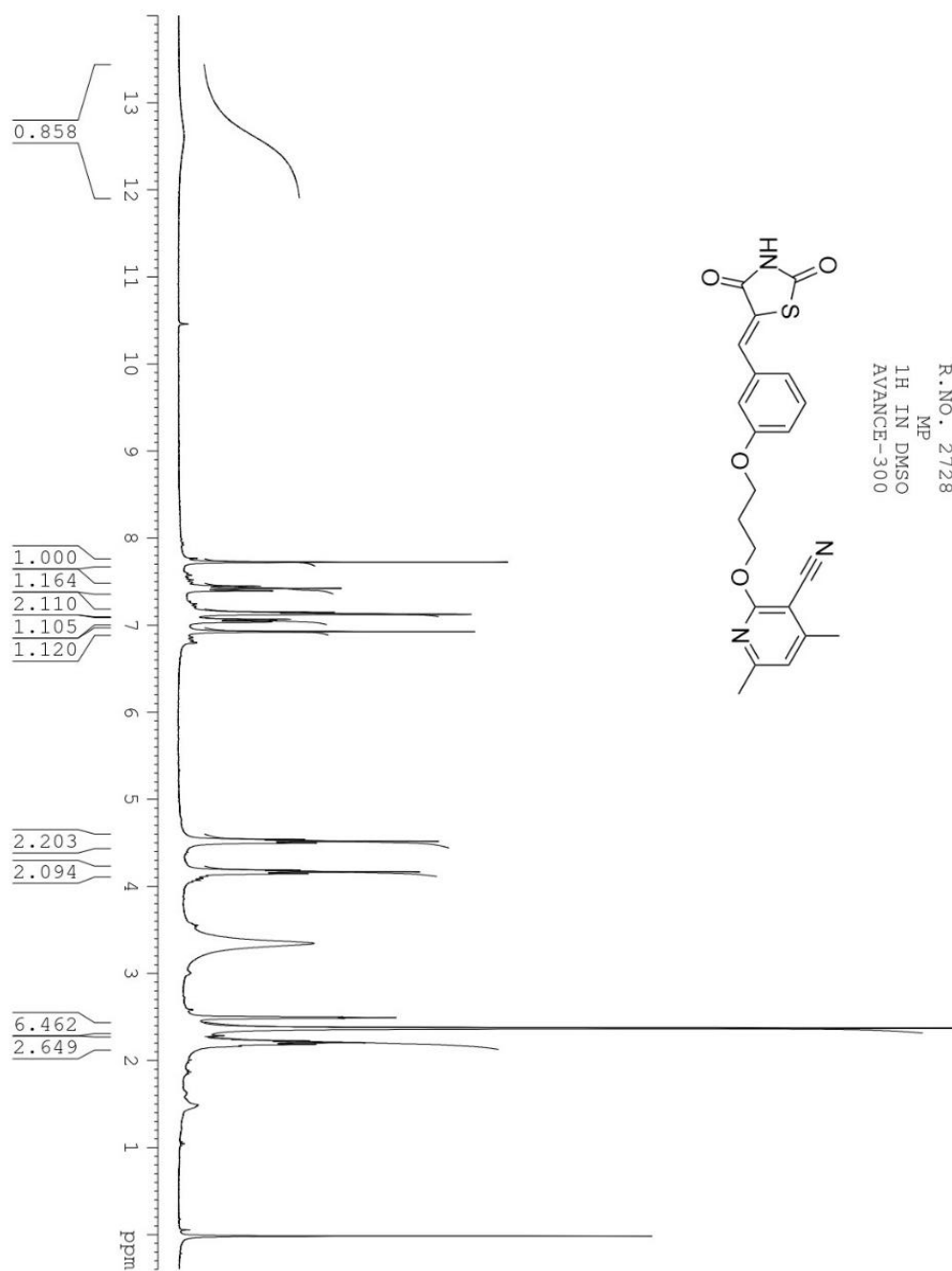


**Figure 4.14:**  $^1\text{H}$  NMR of 2-(3-(3-((2,4-dioxothiazolidin-5-ylidene)methyl)phenoxy)propoxy)-4,6 dim ethyl-nicotinonitrile (**7.3**)

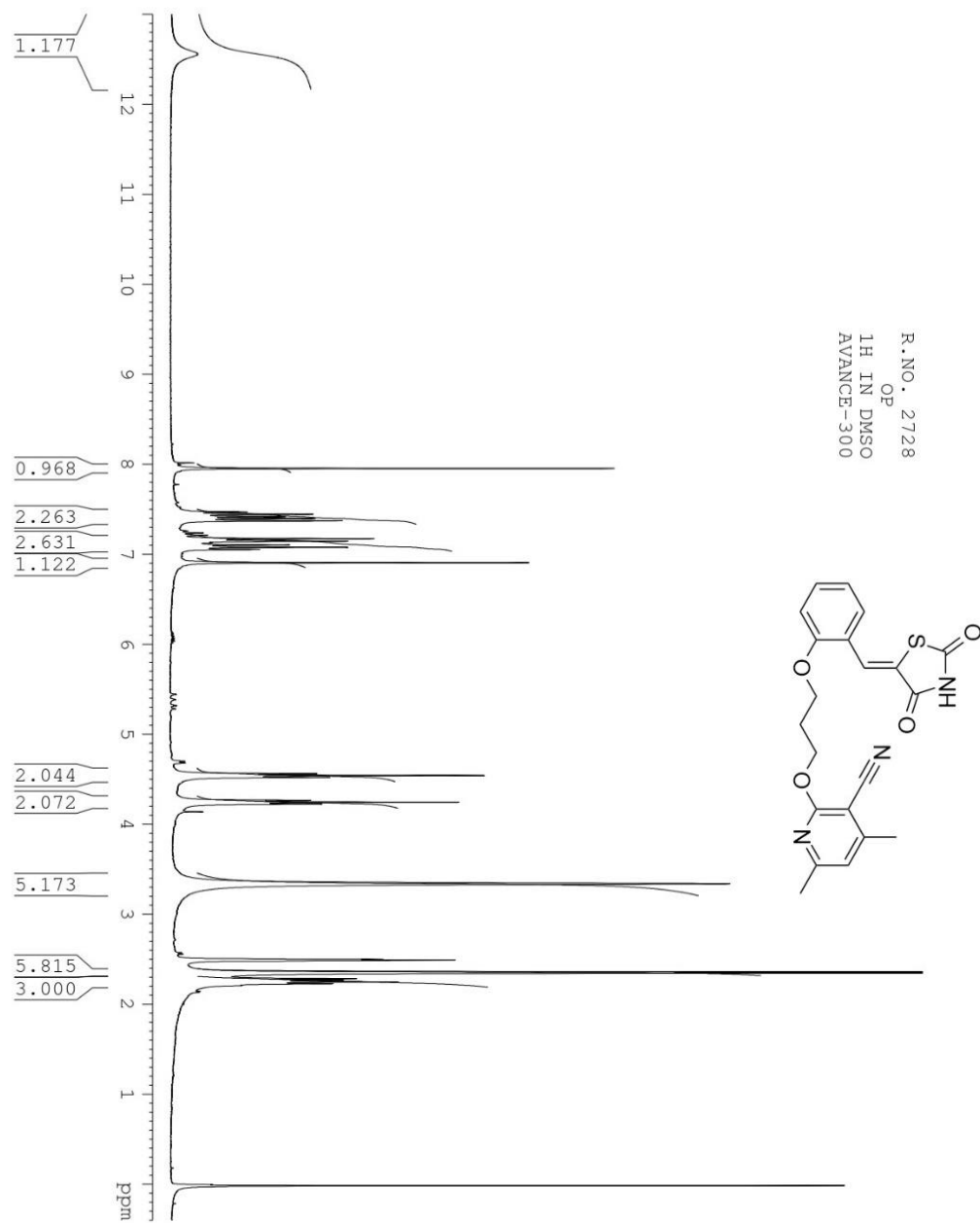


**Figure 4.15:**  $^1\text{H}$  NMR of 2-(3-(2-((2,4-dioxothiazolidin-5-ylidene)methyl)phenoxy)propoxy)-4,6-dimethyl-nicotinonitrile (**7.4**)

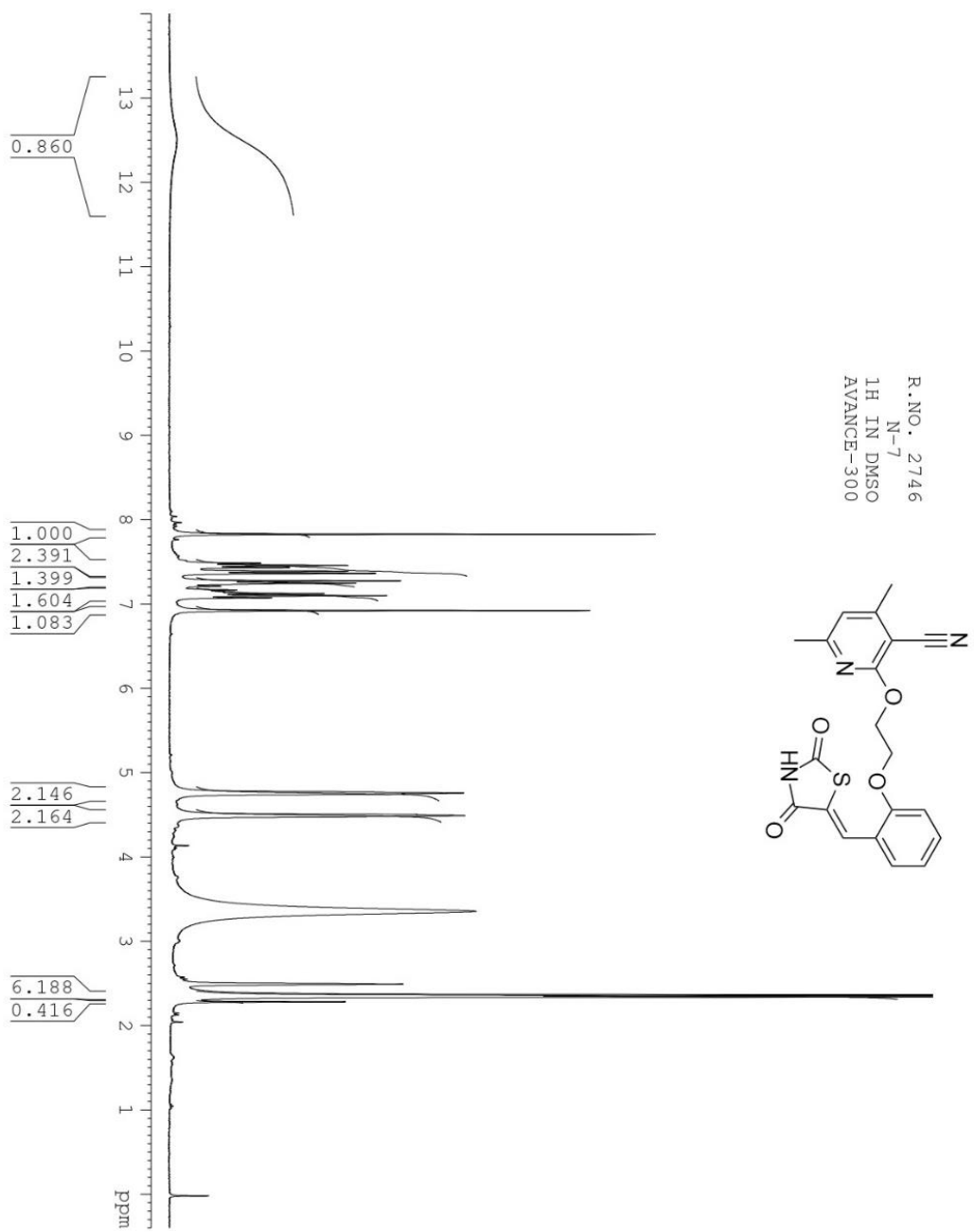


**Figure 4.16:**  $^1\text{H}$  NMR of 2-(2-(2-((2,4-dioxothiazolidin-5-ylidene)methyl)phenoxy)ethoxy)-4,6-dimethyl-nicotinonitrile (**7.5**)

#### 4.6.6. General procedure for the synthesis of 7.6-7.8

Appropriate benzaldehyde derivative (**7.2a-7.2c**) (2 g, 7 mmol) taken in toluene (50 mL) and thiazolidine-2,4-dione (0.8 g, 7 mmol), benzoic acid (0.4 g, 3.5 mmol), and piperidine (0.2 mL, 3.5 mmol) were added sequentially. The flask was connected to a Dean-Stark apparatus and refluxed at 180°C for 12 h. After that, the reaction mixture was cooled to room temperature and reduced in a rotary evaporator. The reaction suspension was then filtered, and the residue was washed with cold water, EtOH, and hexane. The washed residue was dried under vacuum overnight, affording the desired products as (**7.6-7.8**) canary yellow residues.

##### 4.6.6.1. 1-(2-(4-((2,4-dioxothiazolidin-5-ylidene)methyl)phenoxy)ethyl)-4,6-dimethyl-2-oxo-1,2-dihydropyridine-3-carbonitrile (**7.6**)

**Yield:** 1.95 g (72%); m.p. 213-215°C.

**<sup>1</sup>H NMR 300 MHz, 25°C, Si(CH<sub>3</sub>)<sub>4</sub>, (DMSO) (δ):** 2.18-2.22 (3H, s, CH<sub>3</sub>); 2.40-2.43 (3H, s, CH<sub>3</sub>); 4.22-4.25 (2H, t, CH<sub>2</sub>, *J*= 6.3 Hz); 4.44-4.47 (2H, t, CH<sub>2</sub>, *J*= 6.3 Hz); 6.32-6.35 (1H, s, CH); 6.92-6.94 (1H, d, CH, *J*= 2.4 Hz); 6.94-6.96 (1H, d, CH, *J*= 2.3 Hz); 7.56-7.58 (1H, d, CH, *J*= 8.5 Hz); 7.62-7.64 (1H, d, CH, *J*= 8.3 Hz); 7.94-7.96 (1H, s, CH); 12.3-12.6 (1H, s, NH); **<sup>13</sup>C NMR (75MHz, CDCl<sub>3</sub>): (δ):** 20.7, 24.5, 68.4, 68.9, 93.8, 11.2, 114.5, 114.3, 115.6, 116.0, 126.8, 129.8, 129.8, 143.3, 155.2, 160.5, 161.6, 164.3, 166.3, 167.1; **MS (m/z):** 396.09(M+1); **Element analysis: (i). Calculated:** C=60.75%; H=4.33%; N=10.63%; **(ii). Found:** C=60.56%; H=4.17%; N=10.71%.

##### 4.6.6.2. 1-(3-(4-((2,4-dioxothiazolidin-5-ylidene)methyl)phenoxy)propyl)-4,6-dimethyl-2-oxo-1,2-dihydropyridine-3-carbonitrile (**7.7**)

**Yield:** 2.35 g (82%); m.p. 228-230 °C.

**<sup>1</sup>H NMR 300 MHz, 25°C, Si(CH<sub>3</sub>)<sub>4</sub>, (DMSO) (δ):** 2.12-2.14 (2H, m, CH<sub>2</sub>, *J*= 6.3 Hz); 2.29-2.32 (3H, s, CH<sub>3</sub>); 2.40-2.43 (3H, s, CH<sub>3</sub>); 4.06-4.09 (2H, t, CH<sub>2</sub>, *J*= 6.3 Hz); 4.26-4.29 (2H, t, CH<sub>2</sub>, *J*= 6.3 Hz); 6.32-6.36 (1H, s, CH); 6.92-6.94 (1H, d, CH, *J*= 2.4 Hz); 6.94-6.96 (1H, d, CH, *J*= 8.3 Hz); 7.56-7.58 (1H, d, CH, *J*= 8.4 Hz); 7.62-7.64 (1H, d, CH, *J*= 8.2 Hz); 7.94-7.96 (1H, s, CH); 12.3-12.7 (1H, s, NH); **<sup>13</sup>C NMR (75MHz,**

**CDCl<sub>3</sub>**: (δ): 20.7, 24.5, 29.0, 68.4, 68.9, 93.8, 11.2, 114.5, 114.3, 115.6, 116.0, 126.8, 129.8, 129.8 143.3, 155.2, 160.5, 161.6, 164.3, 166.3, 167.1; **MS (m/z)**: 410.11(M+1).  
**Element analysis: (i). Calculated:** C=61.60%; H=4.68%; N=10.26%; **(ii). Found:** C=61.77%; H=4.51%; N=10.33%.

**4.6.6.3. 1-(3-(2-((2,4-dioxothiazolidin-5-ylidene)methyl)phenoxy)propyl)-4,6-dimethyl-2-oxo-1,2-dihydropyridine-3-carbonitrile (7.8)**

**Yield:** 2.02 g (71%); m.p. 228-230 °C.

**<sup>1</sup>H NMR 300 MHz, 25°C, Si(CH<sub>3</sub>)<sub>4</sub>, (DMSO) (δ):** 2.10-2.13 (2H, m, CH<sub>2</sub>, *J*= 6.2 Hz); 2.30-2.32 (3H, s, CH<sub>3</sub>); 2.55-2.58 (3H, s, CH<sub>3</sub>); 4.10-4.12 (2H, t, CH<sub>2</sub>, *J*= 6.3 Hz); 4.12-4.15 (2H, t, CH<sub>2</sub>, *J*= 6.3 Hz); 6.30-6.32 (1H, s, CH); 7.10-7.12 (1H, d, CH, *J*= 8.4 Hz); 7.12-7.14 (1H, d, CH, *J*= 8.4 Hz); 7.50-7.52 (1H, d, CH, *J*= 8.3 Hz); 7.58-7.60 (1H, d, CH, *J*= 8.4 Hz); 7.98-8.00 (1H, s, CH); 12.3-12.7 (1H, s, NH); **<sup>13</sup>C NMR (75MHz, CDCl<sub>3</sub>): (δ):** 20.7, 24.5, 29.0, 68.4, 68.9, 93.8, 11.2, 114.5, 114.3, 115.6, 116.0, 126.8, 129.8, 129.8 143.3, 155.2, 160.5, 161.6, 164.3, 166.3, 167.1; **MS (m/z)**: 410.11(M+1).  
**Element analysis: (i). Calculated:** C=61.60%; H=4.68%; N=10.26%; **(ii). Found:** C=61.77%; H=4.51%; N=10.33%.



#### 4.6.7. $^1\text{H}$ NMR spectra of compounds 7.6-7.8

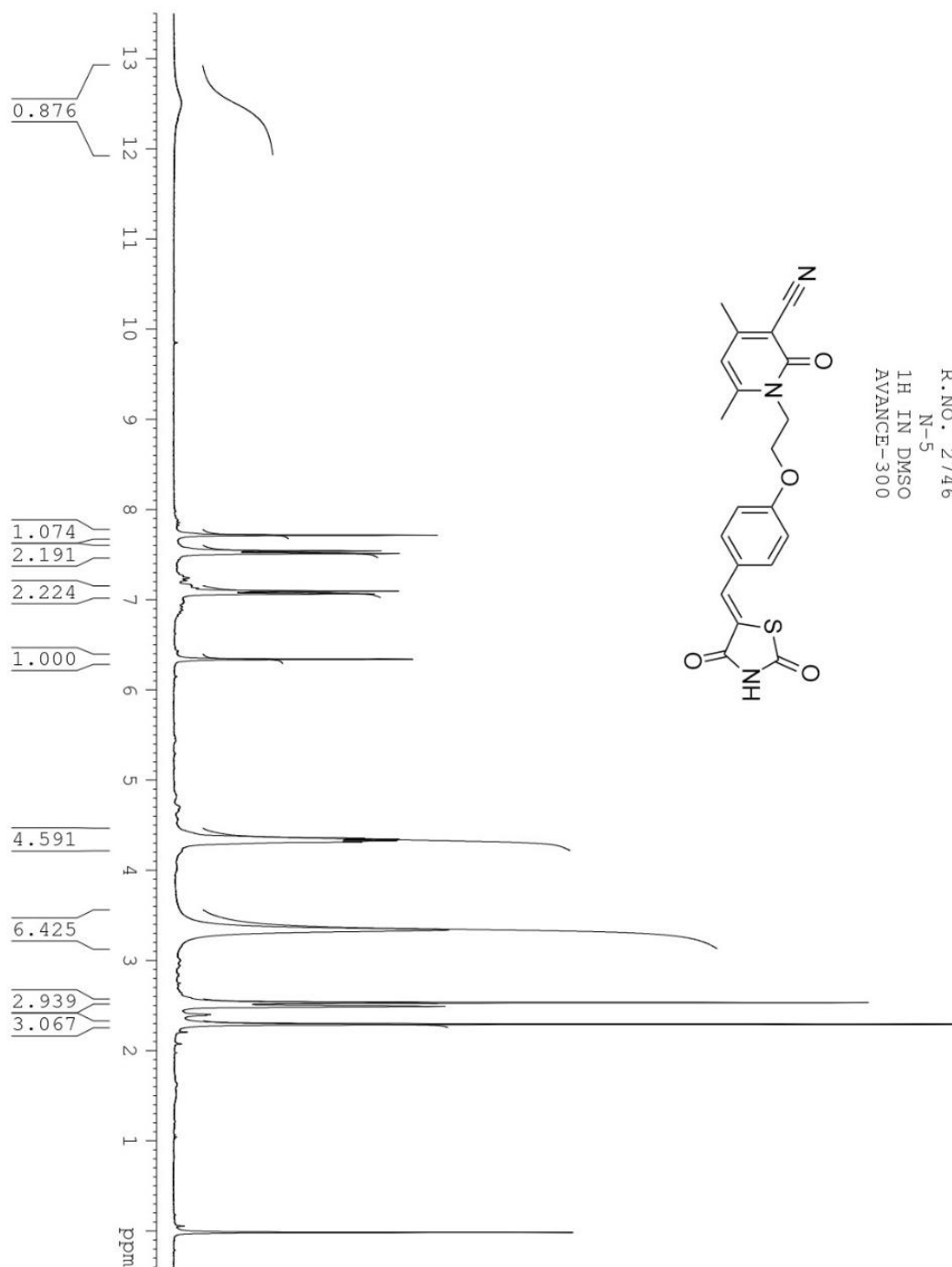


**Figure 4.17:**  $^1\text{H}$  NMR of 1-(2-(4-((2,4-dioxothiazolidin-5-ylidene)methyl)phenoxy)ethyl)-4,6-dimethyl-2-oxo-1,2-dihydropyridine-3-carbonitrile (**7.6**)

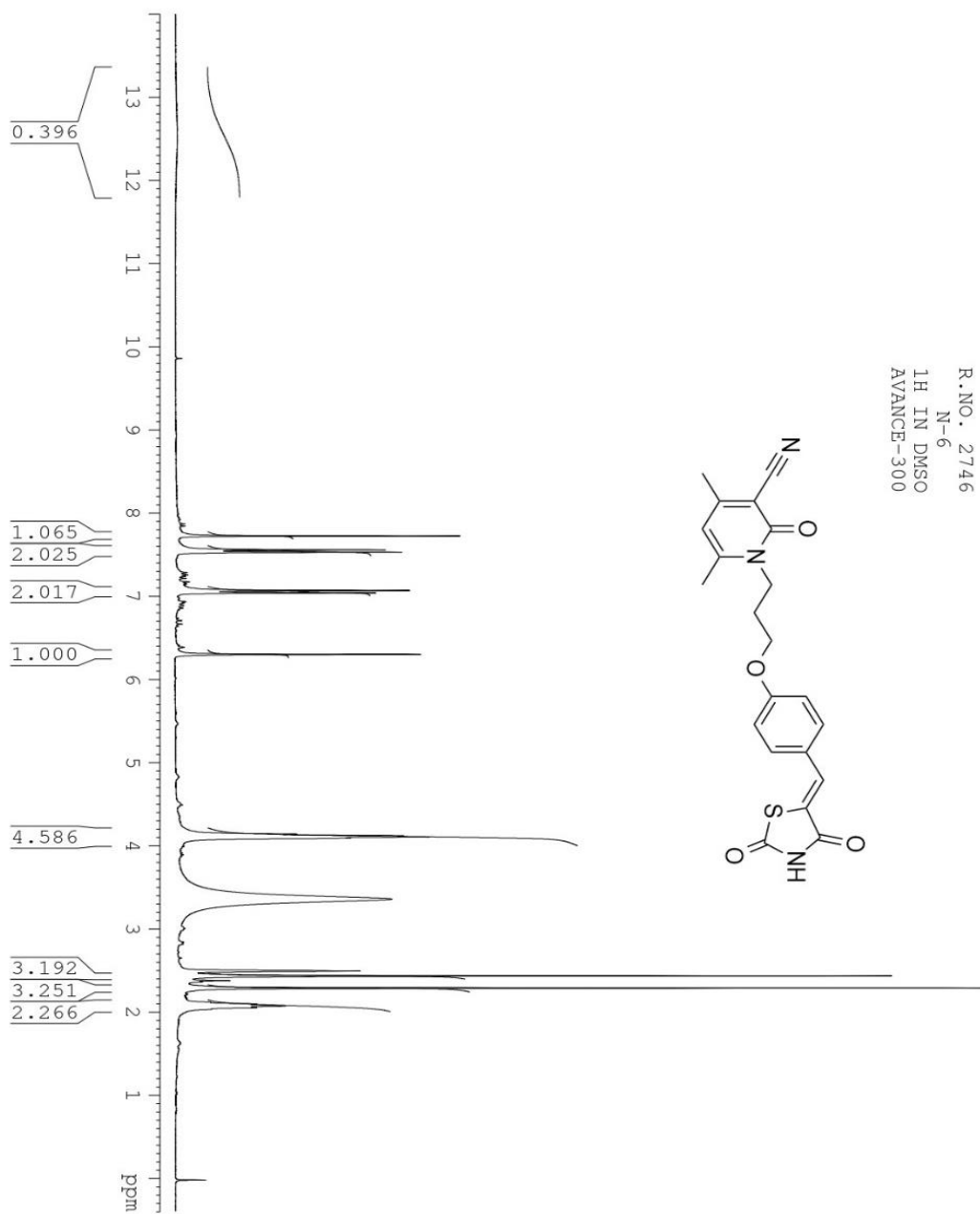


**Figure 4.18:**  $^1\text{H}$  NMR of 1-(3-(4-((2,4-dioxothiazolidin-5-ylidene)methyl)phenoxy)propyl)-4,6-dimethyl-2-oxo-1,2-dihydropyridine-3-carbonitrile (**7.7**)

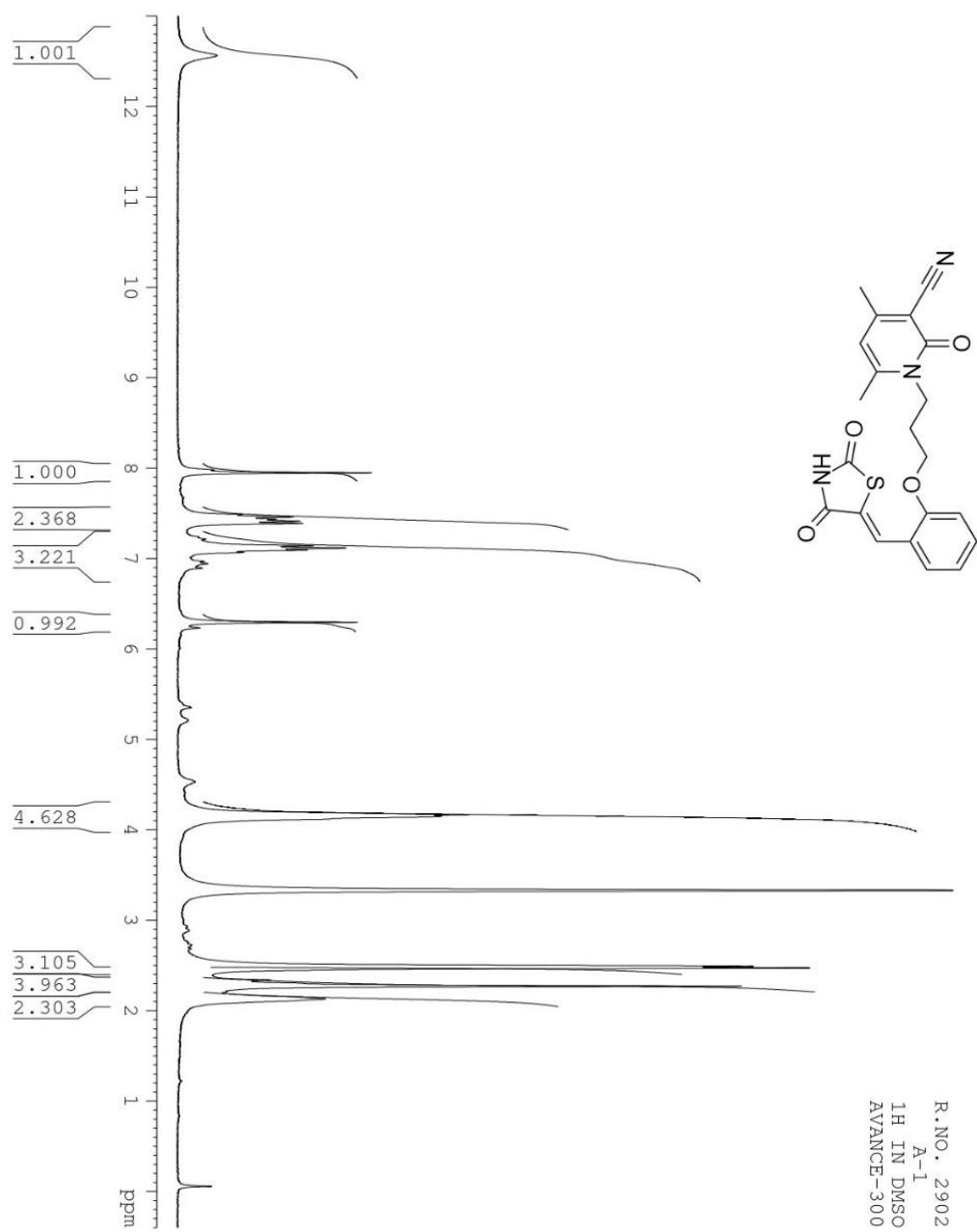


**Figure 4.19:**  $^1\text{H}$  NMR of 1-(3-(2-((2,4-dioxothiazolidin-5-ylidene)methyl)phenoxy)propyl)-4,6-dimethyl-2-oxo-1,2-dihydropyridine-3-carbonitrile (**7.8**)

## 4.7. Antidiabetic activity of synthesized compounds 6.1-6.4 and 7.1-7.8

### 4.7.1. *In-silico* analysis of 6.1-6.4 and 7.1-7.8

*In-silico* analysis or molecular docking analysis is an essential or very important tool to know the host-guest chemistry of compounds. The ability of compounds to interact with the PPAR- $\gamma$  enzyme was assessed by *in-silico* or molecular docking studies. Molecular docking analysis was carried out using the autodock-Vina (Trott & Olson, 2009) to see the binding affinity of these synthesized compounds (6.1-6.4 and 7.1-7.8) at the PPAR- $\gamma$  enzyme active site. PPAR- $\gamma$  PDB id: 5YCP was used and retrieved from the protein data bank. The exhaustiveness parameter for analyzing the binding affinity was set into nine modes. Finally, the processed protein structure was then subjected to docking with the thirteen compounds. The docked results were visualized using the pymol, chimera, and Discovery studio.

#### 4.7.1.1. *In-silico* analysis of compounds 6.1-6.4

4.7.1.1.1. **Table 4.1:** Docking score and the residues involved in the interaction of compounds (6.1-6.4) with PPAR- $\gamma$  enzyme

Compounds	Docking score (Kcal/mol)	Residues involved in H-bond	Residues involved in other interactions ( $\pi$ -anion, $\pi$ - $\sigma$ , $\pi$ - $\pi$ , $\pi$ -alkyl, and alkyl)
6.1	-8.7	Ser289, Tyr473	Gly284, Cys285, Arg288, Leu330, Ile341, Met364
6.2	-9.0	Tyr327, Ser342	Cys285, Arg288, Leu330, Val339, Ile341, Met364, His449
6.3	-9.1	Tyr327, Ser342	Phe282, Gly284, Cys285, Arg288, Leu330, Val339, Ile341, Met364, His449
6.4	-8.8	Ser289, Tyr473	Cys285, Gly284, Arg288, Leu330, Ile341, Met364

Compounds 6.1-6.4 have a binding energy of 8.7-9.1 kcal/mol, higher than rosiglitazone's binding energy (8.3 kcal/mol) (Table 4.1). The ligand-binding pocket of PPAR- $\gamma$  has a sizeable Y-shaped cavity and is comprised of three sub-pockets viz. Arm I, Arm II, and Arm III. Arm I is the most polar pocket, occupied by most polar group TZD of compounds 6.1-6.4, much like standard rosiglitazone. On the other hand, Arm III is the less polar pocket that was occupied by sesamol moiety. The Arm II was

remained unoccupied, just like standard rosiglitazone. Figure 4.24 representing the overlapped diagram of compounds **6.1-6.4** with standard rosiglitazone, which indicated that all these compounds occupied the active site of the PPAR- $\gamma$  enzyme, much like standard rosiglitazone. Therefore, these compounds could be a potent antidiabetic drug. Docking images of compounds **6.1-6.4** with PPAR- $\gamma$  enzyme active site are shown in the following Figures 4.20-4.24.

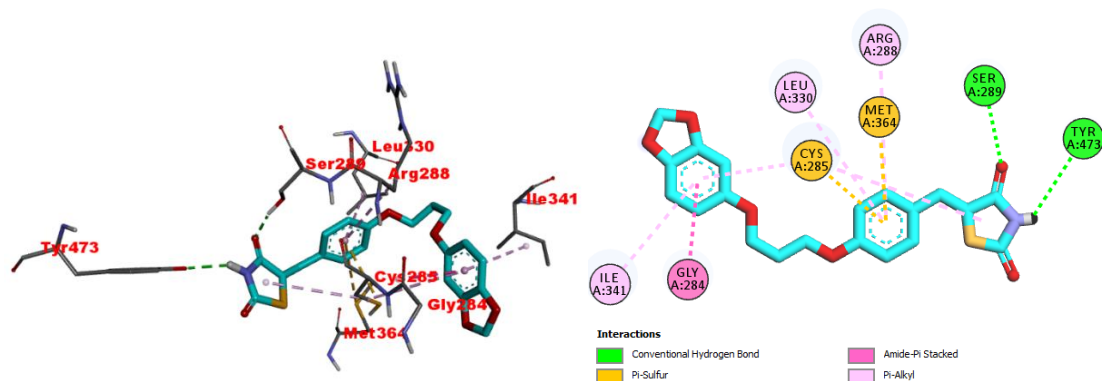


**Figure 4.20:** Binding mode of compound **6.1** in the active site cavity of PPAR- $\gamma$  enzyme

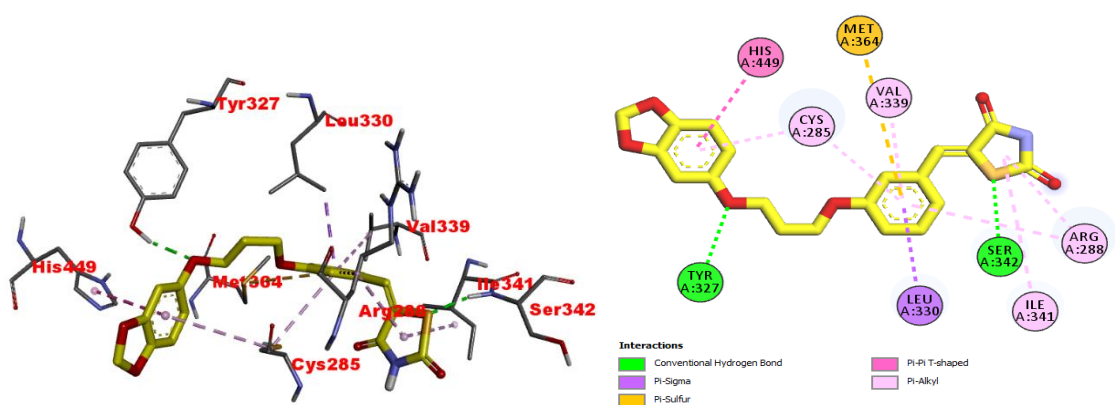


**Figure 4.21:** Binding mode of compound **6.2** in the active site cavity of PPAR- $\gamma$  enzyme

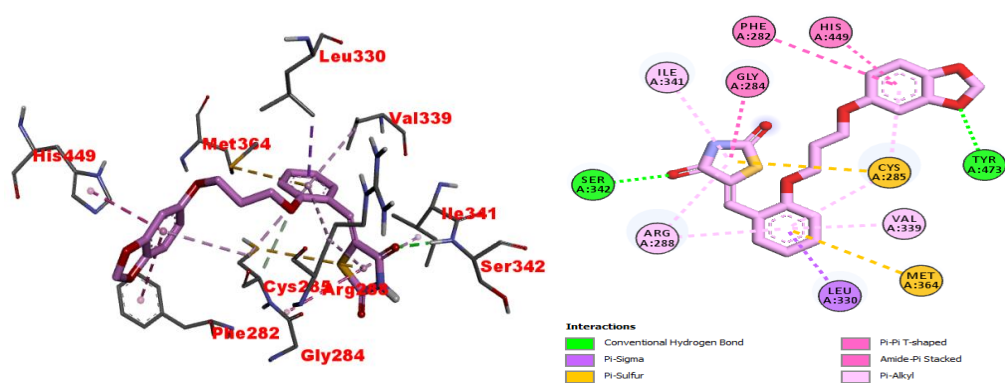


**Figure 4.22:** Binding mode of compound 6.3 in the active site cavity of PPAR- $\gamma$  enzyme

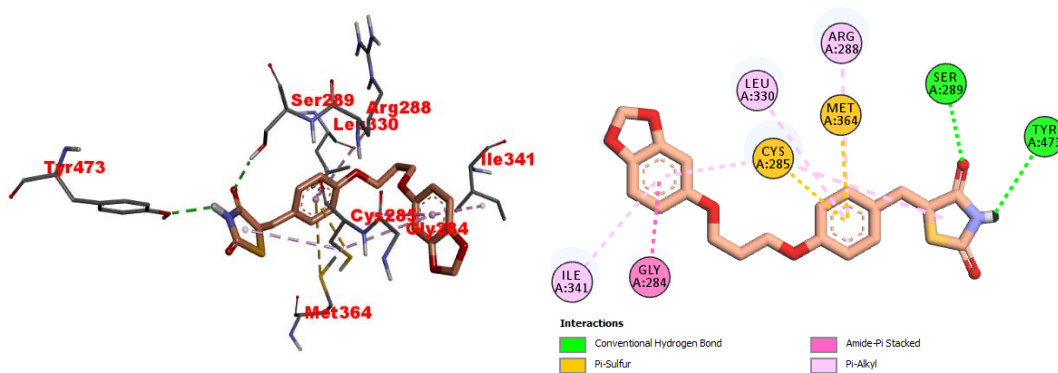


**Figure 4.23:** Binding mode of compound 6.4 in the active site cavity of PPAR- $\gamma$  enzyme

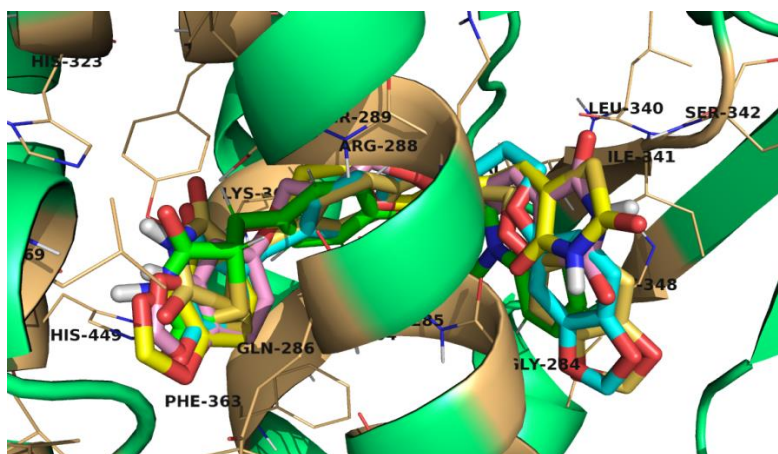


**Figure 4.24:** Compounds 6.1, 6.2, 6.3 & 6.4 with rosiglitazone (blue) overlapped at the active site of PPAR- $\gamma$  enzyme

#### 4.7.1.2 *In-silico* analysis of compounds 7.1-7.8

4.7.1.2.1. **Table 4.2.** Docking score and the residues involved in the interaction of compounds (7.1-7.8) with PPAR- $\gamma$  enzyme

Compounds	Docking score (Kcal/mol)	Residues involved in H-bond	Residues involved in other interactions ( $\pi$ -anion, $\pi$ - $\sigma$ , $\pi$ - $\pi$ , $\pi$ -alkyl, and alkyl)
7.1	-9.0	Tyr473	Gln284, Cys285, Arg288, Leu330, Ile341, Met364
7.2	-9.2	His323, Tyr473	Cys285, Gln286, Phe287, Arg288, Ser289, Leu330, Ile341, Met364
7.3	-9.3	Ser289, Tyr327, Tyr473	Ile281, Phe282, Gly284, Cys285, Gln286, Arg288, Leu330, Ile341, Met348, Met364
7.4	-8.1	Ser289, Ser342	Phe282, Cys285, Gln286, Arg288, His323, Leu330, Val339, Ile341, Phe363, Met364, His449, Leu469, Tyr473
7.5	-8.3	Ser289, Tyr473	Phe282, Cys285, Gln286, Arg288, Tyr327, Val339, Ile341, Met348, Leu353, Met364, His449, Leu469
7.6	-9.2	Tyr327, Tyr473	Phe282, Cys285, Phe287, Arg288, Gln286, Leu330, Leu340, Ile341, Ser342, Met364, His449
7.7	-9.1	Ser289, Tyr473	Cys285, Arg288, Leu330, Ile341, Met364
7.8	-8.1	Ser289	Phe282, Gly284, Cys285, Arg288, His323, Tyr327, Leu330, Val339, Ile341, Phe363, Met364, His449

Most of the **Scheme 7** compounds, i.e., **7.1-7.8** have higher binding energy than rosiglitazone's binding energy (8.3 kcal/mol) (Table 4.2). Out of these, three compounds, **7.2**, **7.3**, and **7.6** showed the highest binding energy of 9.2-9.3 kcal/mol. Much like rosiglitazone, these compounds also occupied Arm I and Arm II of the ligand-binding pocket, and the arm-III pocket remains unoccupied. The more hydrophilic group of these compounds, i.e., TZD, occupied the most polar pocket Arm I, while the cyano-pyridone moiety is directed towards the Arm II pocket. The overlapped diagram of compounds **7.2**, **7.3**, and **7.6** with standard rosiglitazone was shown in Figure 4.28, which indicated that all these compounds occupied the active site of PPAR- $\gamma$  enzyme, much like standard rosiglitazone. This docking analysis found that compounds **7.2**, **7.3**, and **7.6** could be potent as antidiabetic drugs. Docking images of compounds **7.2**, **7.3**, and **7.6** with PPAR- $\gamma$  enzyme active site are shown in the following Figures 4.25-4.28.

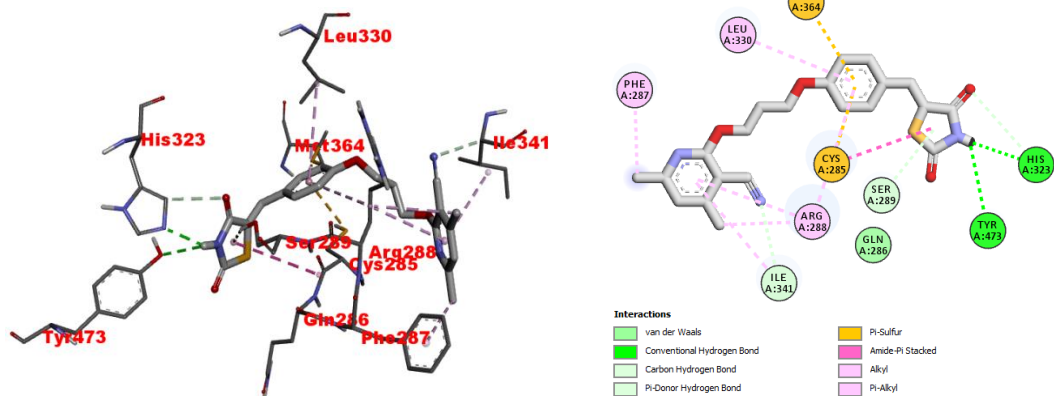


Figure 4.25: Binding mode of compound 7.2 in the active site cavity of PPAR- $\gamma$  enzyme

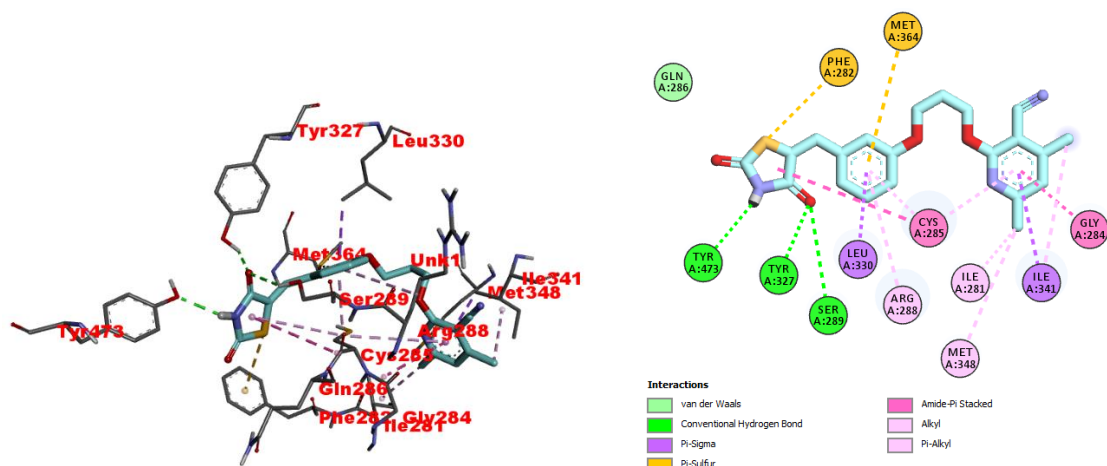


Figure 4.26: Binding mode of compound 7.3 in the active site cavity of PPAR- $\gamma$  enzyme

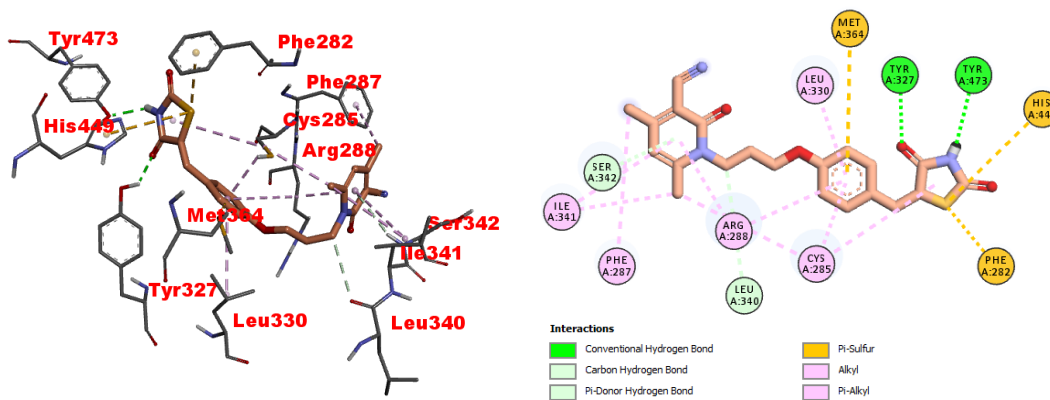
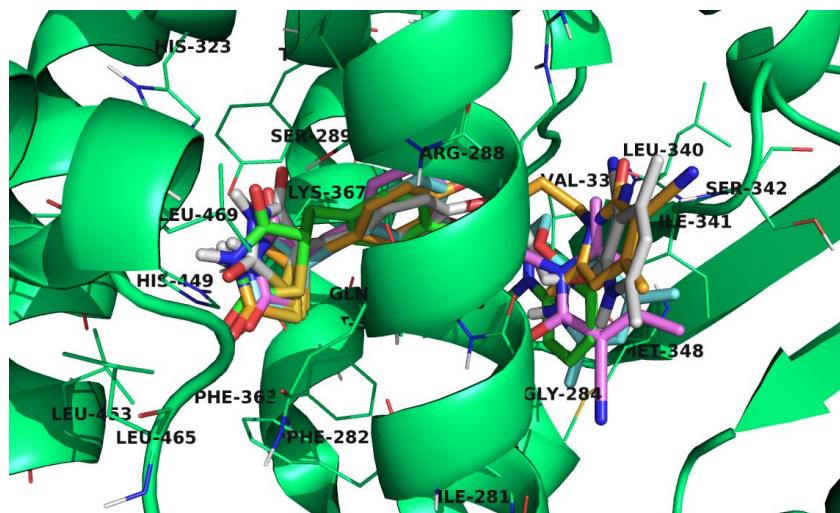


Figure 4.27: Binding mode of compound 7.6 in the active site cavity of PPAR- $\gamma$  enzyme





**Figure 4.28:** Overlapped diagram of compound 7.2 (grey), 7.3 (pink), 7.6 (bright orange) and rosiglitazone (blue) at the active site activity of PPAR- $\gamma$  enzyme.

#### 4.7.2. Biological activity of 6.1-6.4 and 7.1-7.8

##### 4.7.2.1 Materials and Methods

**Animals:** Charles foster rats of either sex (body weight:  $180 \pm 10$  g) were obtained from Animal house, department of Zoology, Mizoram University, Aizawl. All animals were allowed free access to tap water and pellet diet and maintained at room temperature in plastic cages.

##### 4.7.2.2 Experimental Method

Diabetes was induced chemically by alloxan. Rats were injected 120 mg/kg body weight alloxan intra-peritoneal after overnight fasting (Lenzen, 2008). These animals were kept for a week to stabilize the diabetic condition. Animals showing fasting blood glucose levels more than 80 mg/dl were considered as diabetic [Rawat (2006)] and used for the study. Animals were divided into five groups, each containing six rats as a group I (normal control), Group II (diabetic control), Group III (diabetic rats treated with glibenclamide, 10 mg/kg/day, p.o.), Group IV (diabetic rats treated with compounds (6.1-6.4 and 7.1-7.8), 50 mg/kg/day, p.o.) and Group V (diabetic rats treated with

compound(6.1-6.4 and 7.1-7.8), 80 mg/kg/day, p.o.). Compounds (6.1-6.4 and 7.1-7.8) were orally administered as a suspension in 0.3% carboxymethylcellulose (CMC) for seven days. Animals of Group I & II were given an equal volume of vehicle (0.3% CMC suspension). Blood samples were collected at 0 and 7th day (1 hour after the last dose) from orbital sinus, and blood glucose was estimated by commercially available kit (Span Diagnostics Ltd., Surat, India). The bodyweight of rats was measured before and after the treatment.

#### **4.7.2.3 Statistical analysis**

All the experimental results' values were expressed as mean  $\pm$  Standard Error of Mean (SEM). Statistical analyses were performed by one-way analysis of variance (ANOVA) followed by Dunnett Multiple Comparisons Test. The student's t-test was used for comparison within the same group before and after treatment. Graph Pad in Stat (version 3.06) software was used for all statistical analyses.

#### **4.7.2.4 Effect on blood glucose**

The fasting blood glucose levels of diabetic control rats (Group II) were significantly higher than those of normal control rats (Group I). There was a significant fall in blood glucose level ( $p < 0.01$ , compared to diabetic control) in compound treated groups (80 mg/kg, p.o.). In the untreated animals (Group II), blood glucose levels did not change significantly throughout the study period (Table 4.3). There was a significant ( $p < 0.05$  and  $p < 0.001$ ) fall in blood glucose level in compound (80 mg/kg), and glibenclamide treated rats (Table 4.3).

#### **4.7.2.5 Effect on body weight**

There was a significant loss in body weight in diabetic control animals (Group II). Alloxan induced body weight loss was reversed significantly by glibenclamide 10 mg/kg ( $p < 0.01$ ) and compounds 80 mg/kg ( $p < 0.001$ ) (Table 4.3).

**4.7.2.6 Table 4.3.** Effect of different compounds treatment on blood glucose level and body weight

Group	Fasting blood glucose level (mg/dl)		Bodyweight (g)	
	0 day	7 <sup>th</sup> day	0 day	7 <sup>th</sup> day
Normal control	77.10±3.4	77.83±2.9	175.5±3.1	184±2.8
Diabetic control	220.10±16.12	285±13.11	176.8±2.1	170.9±3.1
Diabetic +glibenclamide	250.55±20.11	178.8±9.12	177.80±3.14	181.20±2.81
6.1	244.30±24.21	180.84±10.11	174.55±4.25	178.32±3.66
<b>6.2</b>	<b>255.39±21.43</b>	<b>171.8±7.38</b>	<b>177.64±4.87</b>	<b>180.43±5.18</b>
6.3	259.67±26.18	188.44±8.98	176.56±6.13	179.86±3.89
6.4	249.63±18.68	177.65±10.13	173.54±4.34	179.88±5.13
7.1	244.43±20.28	188.72±9.15	176.65±4.23	181.44±4.21
<b>7.2</b>	<b>241.98±21.81</b>	<b>170.90±11.32</b>	<b>175.84±6.12</b>	<b>176.88±5.11</b>
<b>7.3</b>	<b>251.62±20.33</b>	<b>168.8±4.89</b>	<b>179.21±4.81</b>	<b>183.51±3.92</b>
7.4	251.28±22.32	198.68±4.48	177.80±3.84	176.38±3.19
7.5	254.86±14.11	210.54±9.46	178.12±5.12	181.21±4.78
<b>7.6</b>	<b>250.69±16.11</b>	<b>168.50±7.87</b>	<b>174.4±3.94</b>	<b>171.26±2.68</b>
7.7	241.30±21.13	180.21±12.12	171.51±4.89	178.59±5.28
7.8	254.69±16.16	221.50±7.83	173.4±3.94	182.26±2.681

#### 4.8. Conclusion

This chapter has successfully synthesized twelve compounds (**6.1-6.4** and **7.1-7.8**) based on standard rosiglitazone's structural feature. We have shown that these compounds maintained the standard prototype structural features of PPAR- $\gamma$  agonist, i.e., benzyl/benzylidene-TZD-Linker-Lipophilic Head, where sesamol and cyano-pyridone moiety acted as lipophilic head in these compounds. We have also extended the oxymethylene linker length by  $-\text{CH}_2-$  or  $-\text{CH}_2\text{-N-}$  to increase the potency or binding affinity with the PPAR- $\gamma$  receptor. Molecular docking simulations demonstrated that

these compounds occupied the active site of the PPAR- $\gamma$  enzyme, much like standard rosiglitazone. These analogues exhibited higher binding energy than standard rosiglitazone. The present series of compounds **6.1, 6.2, 6.3, 6.4, 7.1, 7.2, 7.3, 7.4, 7.5, 7.6, 7.7, and 7.8** anti-diabetic activity studied in rats to validate these compounds in the treatment of diabetes scientifically. Administration of alloxan (120 mg/kg, i.p.) led to about 3-fold elevation of fasting blood glucose levels maintained for seven days. Seven days of daily treatment with these compounds (**6.1-6.4** and **7.1-7.8**) caused a significant fall in elevated blood glucose levels. Especially, compounds **6.2, 7.2, 7.3, and 7.6** showed excellent anti-diabetic activity and caused a significant fall in rats' elevated blood glucose levels. Synthesized compounds **6.1-6.4** and **7.1-7.8** showed good experimental results, and docking scores also support our experimental results. Therefore, we can conclude that compounds **6.2, 7.2, 7.3, and 7.6** could be potent type-2 anti-diabetic drugs. However, detailed studies are needed to clarify the mechanism(s) of these newly synthesized derivatives' anti-diabetic effects.

## 5. SUMMARY AND CONCLUSION

---

Molecular recognition lies in the complementarity of interacting surfaces by non-covalent interactions, and non-covalent interactions play an important role in chemical and biological systems as they are ubiquitous. All these interactions are surface-dependent phenomena. In aromatic interactions, larger functional groups are involved in providing a large surface area of intermolecular contact. There are many more contact points in aromatic interactions where electrostatic interactions have to be considered, making it difficult to understand and study these interactions. Generally, molecules tend to orient in a way to minimize energy and to generate stable geometry. Therefore, the study of aromatic or non-covalent interactions is important to know how molecules orient within the system (intra-molecular) and when it forms a complex with a receptor (biological systems). It is not adequately clear that whether molecules interact through face-to-face stacking or edge to face stacking. Hence, new models have been synthesized to study the orientation preferences and role of weak/ aromatic interactions in biological systems. We have successfully synthesized a hetero-aromatic system with methylene-linked fleximers and poly-aromatic 2-pyridones fleximers with methylene and ethylene linkers in the present studies. We have also synthesized rosiglitazone-based fleximers to study aromatic interactions in biological systems by *in-silico* analysis.

Chapter 2 has designed, synthesized, and studied the structural studies of 2-pyridones, 2-dihydropyridones, and dihydropyrimidinones derivatives. We have used *Citrus macroptera* juice for the first time to synthesized dihydropyrimidinones derivatives, which is an eco-friendly procedure. This method also showed good yield and shorter reaction time. These compounds gave suitable single crystals, which were studied by the single-crystal X-ray diffraction method and Hirshfeld surface analysis method. The single-crystal X-ray diffraction method and Hirshfeld surface analysis method are beneficial for studying weak non-covalent interactions. The single-crystal X-

ray diffraction method determined the 3-D self-assemblies of compounds. It analyzed the various intermolecular and intramolecular interactions, supported by the Hirshfeld surface analysis method. Cytotoxicity and anticancer activity of the compounds of schemes 1 and 2 are studied, which revealed that monastrol-based synthesized compounds exhibited better cytotoxicity and anticancer activity. Chapter 2 also synthesized 3-cyano-2-pyridone based unsymmetrical fleximers and studied the structural properties by using the single-crystal X-ray diffraction method, Hirshfeld surface analysis method to know the orientation preferences and weak/aromatic interactions.

Chapter 3 has designed and synthesized 2-pyridone based poly-aromatic unsymmetrical fleximers with methylene and n-methylene linkers. We have studied the structural properties or how these molecules orient within the system and weak non-covalent interactions by using the single-crystal X-ray diffraction method and Hirshfeld surface analysis method. Our present study showed clear experimental evidence of the intermolecular aromatic interactions in the models containing poly-aromatic fleximers.

In chapter 4, twelve compounds were synthesized based on rosiglitazone's structural features and studied the anti-diabetic activity in rats. Alloxan was administrated orally (120 mg/kg, i.p.), which induced diabetes, which led to about 3-fold elevation of fasting blood glucose levels maintained for seven days. Compounds **6.2**, **7.2**, **7.3**, and **7.6** showed excellent anti-diabetic activity and caused a significant fall in rats' elevated blood glucose levels after seven days. *In-silico* analysis also supported the experimental results of these compounds. Therefore, these synthesized compounds could be potent type-2 anti-diabetic drugs, but detailed studies must clarify the mechanism.

As per objective one, we have synthesized new polyaromatic and heteroaromatic fleximers using bio-catalyst and weak base-catalyzed simple reactions.

Chapters 2 and 3 deal with the study of molecular recognition through non-covalent interactions. All compounds of chapter 2 and 3 have different types of

interactions. We can say that non-covalent interactions are very much influenced by surface area, volume, heteroatom, and nature of the supramolecular system. These studies fulfill the goal of objective two to understand weak interactions in supramolecular systems.

Chapters 2 and 4 deal with the study of drug-receptor interactions of new analogs with selected receptors through *in silico* analysis. Chapter 2 molecular docking investigation of Scheme 1 and 2 compounds was carried out with kinesin Eg5 receptor to study drug-receptor complex interactions. Chapter 4 molecules were used to study drug-receptor interactions through *in silico* analysis with PPAR-gamma receptor. These studies fulfill the third objective of the research work done to complete the present work's goal.

## REFERENCES

- Abadi, A., Al-Deeb, O., Al-Afify, A., & El-Kashef, H. (1999). Synthesis of 4-alkyl (aryl)-6-aryl-3-cyano-2(1H)-pyridinones and their 2-imino isosteres as nonsteroidal cardiotonic agents. *Il Farmaco*, *54*(4), 195–201. [https://doi.org/10.1016/S0014-827X\(99\)00004-X](https://doi.org/10.1016/S0014-827X(99)00004-X)
- Abadi, A. H., Abouel-Ella, D. A., Lehmann, J., Tinsley, H. N., Gary, B. D., Piazza, G. A., & Abdel-Fattah, M. A. O. (2010). Discovery of colon tumor cell growth inhibitory agents through a combinatorial approach. *European Journal of Medicinal Chemistry*, *45*(1), 90–97. <https://doi.org/10.1016/j.ejmech.2009.09.029>
- Abassi, Y. A., Xi, B., Zhang, W., Ye, P., Kirstein, S. L., Gaylord, M. R., Feinstein, S. C., Wang, X., & Xu, X. (2009). Kinetic Cell-Based Morphological Screening: Prediction of Mechanism of Compound Action and Off-Target Effects. *Chemistry & Biology*, *16*(7), 712–723. <https://doi.org/10.1016/j.chembiol.2009.05.011>
- Åberg, V., & Almqvist, F. (2007). Pilicides—Small molecules targeting bacterial virulence. *Org. Biomol. Chem.*, *5*(12), 1827–1834. <https://doi.org/10.1039/B702397A>
- Aliev, A. E., Arendorf, J. R. T., Pavlakos, I., Moreno, R. B., Porter, M. J., Rzepa, H. S., & Motherwell, W. B. (2014). Surfing  $\pi$  Clouds for Noncovalent Interactions: Arenes versus Alkenes. *Angewandte Chemie International Edition*, n/a-n/a. <https://doi.org/10.1002/anie.201409672>
- An introduction to hydrogen bonding (1997 edition) | Open Library.* (n.d.). Retrieved December 16, 2020, from [https://openlibrary.org/books/OL988608M/An\\_introduction\\_to\\_hydrogen\\_bonding](https://openlibrary.org/books/OL988608M/An_introduction_to_hydrogen_bonding)
- Aqui, N. A., & Vonderheide, R. H. (2008). Survivin as a universal tumor antigen for novel cancer immunotherapy: Functions of a killer clone. *Cancer Biology & Therapy*, *7*(12), 1888–1889. <https://doi.org/10.4161/cbt.7.12.7219>



- Auer, R. N. (2004). Hypoglycemic brain damage. *Forensic Science International*, 146(2–3), 105–110. <https://doi.org/10.1016/j.forsciint.2004.08.001>
- Avasthi, K., Chandra, T., Rawat, D. S., & Bhakuni, D. S. (1998). Synthesis and high resolution proton NMR studies on isomeric N-1-N-2-,5,7-trisubstituted-4,6-dioxo-4,5,6,7-tetrahydropyrazole [3,4-d] pyrimidines *Indian J. Chem. Indian J. Chem*, 37B, 1228–1233.
- Bansal, G., Singh, S., Monga, V., Thanikachalam, P. V., & Chawla, P. (2019). Synthesis and biological evaluation of thiazolidine-2,4-dione-pyrazole conjugates as antidiabetic, anti-inflammatory and antioxidant agents. *Bioorganic Chemistry*, 92, 103271. <https://doi.org/10.1016/j.bioorg.2019.103271>
- Barlow, W. (1883). Probable Nature of the Internal Symmetry of Crystals. *Nature*, 29(738), 186–188. <https://doi.org/10.1038/029186a0>
- Bertolasi, V., Gilli, P., Ferretti, V., & Gilli, G. (1998). Intermolecular N-H...O Hydrogen Bonding Assisted by Resonance. II. Self Assembly of Hydrogen-Bonded Secondary Enaminones in Supramolecular Catemers. *Acta Crystallographica Section B Structural Science*, 54(1), 50–65. <https://doi.org/10.1107/S0108768197008677>
- Bluestone, J. A., Herold, K., & Eisenbarth, G. (2010). Genetics, pathogenesis and clinical interventions in type 1 diabetes. *Nature*, 464(7293), 1293–1300. <https://doi.org/10.1038/nature08933>
- Boys, S. F., & Bernardi, F. (1970). The calculation of small molecular interactions by the differences of separate total energies. Some procedures with reduced errors. *Molecular Physics*, 19(4), 553–566. <https://doi.org/10.1080/00268977000101561>
- Bragg, S. W. H. (1921). The Structure of Organic Crystals. *Proceedings of the Physical Society of London*, 34(1), 33–50. <https://doi.org/10.1088/1478-7814/34/1/306>
- Bravais, A. (1850). *Mémoire sur les systèmes formés par des points distribués régulièrement sur un plan ou dans l'espace*,. Bachelier.

- Brem, H., & Tomic-Canic, M. (2007). Cellular and molecular basis of wound healing in diabetes. *Journal of Clinical Investigation*, *117*(5), 1219–1222. <https://doi.org/10.1172/JCI32169>
- Buckingham, A. D., Fowler, P. W., & Hutson, J. M. (1988). Theoretical studies of van der Waals molecules and intermolecular forces. *Chemical Reviews*, *88*(6), 963–988. <https://doi.org/10.1021/cr00088a008>
- Bugger, H., & Abel, E. D. (2014). *Molecular mechanisms of diabetic cardiomyopathy*. *57*(4), 660–671. <https://doi.org/10.1007/s00125-014-3171-6>.Molecular
- Burley, S. K., & Petsko, G. A. (1986). Dimerization energetics of benzene and aromatic amino acid side chains. *Journal of the American Chemical Society*, *108*(25), 7995–8001. <https://doi.org/10.1021/ja00285a019>
- Cheney, I. W., Yan, S., Appleby, T., Walker, H., Vo, T., Yao, N., Hamatake, R., Hong, Z., & Wu, J. Z. (2007). Identification and structure–activity relationships of substituted pyridones as inhibitors of Pim-1 kinase. *Bioorganic & Medicinal Chemistry Letters*, *17*(6), 1679–1683. <https://doi.org/10.1016/j.bmcl.2006.12.086>
- Chu, S. Y., Callaghan, W. M., Kim, S. Y., Schmid, C. H., Lau, J., England, L. J., & Dietz, P. M. (2007). Maternal Obesity and Risk of Gestational Diabetes Mellitus. *Diabetes Care*, *30*(8), 2070–2076. <https://doi.org/10.2337/dc06-2559a>
- Chudinov, M. V. (2020). Nucleoside Analogs with Fleximer Nucleobase. *Chemistry of Heterocyclic Compounds*, *56*(6), 636–643. <https://doi.org/10.1007/s10593-020-02713-5>
- Cocco, M. (2003). New bis(pyridyl)methane derivatives from 4-hydroxy-2-pyridones: Synthesis and antitumoral activity. *European Journal of Medicinal Chemistry*, *38*(1), 37–47. [https://doi.org/10.1016/S0223-5234\(02\)00002-8](https://doi.org/10.1016/S0223-5234(02)00002-8)
- Cox, E. G., Cruickshank, D. W. J., & Smith, J. a. S. (1958). The crystal structure of benzene at  $-3^{\circ}\text{C}$ . *Proceedings of the Royal Society of London. Series A. Mathematical and Physical Sciences*, *247*(1248), 1–21. <https://doi.org/10.1098/rspa.1958.0167>

- Cozzi, F., Cinquini, M., Annunziata, R., Dwyer, T., & Siegel, J. S. (1992). Polar/ $\pi$  Interactions between stacked aryls in 1,8-diarylnaphthalenes. *Journal of the American Chemical Society*, *114*(14), 5729–5733. <https://doi.org/10.1021/ja00040a036>
- Cozzi, F., Cinquini, M., Annunziata, R., & Siegel, J. S. (1993). Dominance of polar/ $\pi$  Over charge-transfer effects in stacked phenyl interactions. *Journal of the American Chemical Society*, *115*(12), 5330–5331. <https://doi.org/10.1021/ja00065a069>
- Day, C. (1999). Thiazolidinediones: A new class of antidiabetic drugs. *Diabetic Medicine*, *16*(3), 179–192. <https://doi.org/10.1046/j.1464-5491.1999.00023.x>
- Desiraju, G. R. (1989). *Crystal engineering: The design of organic solids*. Elsevier.
- Desiraju, Gautam R. (1995). Supramolecular Synthons in Crystal Engineering—A New Organic Synthesis. *Angewandte Chemie International Edition in English*, *34*(21), 2311–2327. <https://doi.org/10.1002/anie.199523111>
- Di Marzio, D. (2008). Peroxisome proliferator-activated receptor- $\gamma$  agonists and diabetes: Current evidence and future perspectives. *Vascular Health and Risk Management*, *Volume 4*, 297–304. <https://doi.org/10.2147/VHRM.S993>
- Diamond, R. (1974). Real-space refinement of the structure of hen egg-white lysozyme. *Journal of Molecular Biology*, *82*(3), 371–391. [https://doi.org/10.1016/0022-2836\(74\)90598-1](https://doi.org/10.1016/0022-2836(74)90598-1)
- Dowarah, J., Marak, B. N., Lalhruaizela, Sran, B. S., & Singh, V. P. (2020). Design, Synthesis, In Silico Analysis, and Structural Study of 4,6-Dimethyl-2-(3-(p-tolyloxy)propoxy)nicotinonitrile Fleximer. *Crystal Research and Technology*, 2000100. <https://doi.org/10.1002/crat.202000100>
- Dragovich, P. S., Prins, T. J., Zhou, R., Brown, E. L., Maldonado, F. C., Fuhrman, S. A., Zalman, L. S., Tuntland, T., Lee, C. A., Patick, A. K., Matthews, D. A., Hendrickson, T. F., Kosa, M. B., Liu, B., Batugo, M. R., Gleeson, J.-P. R., Sakata, S. K., Chen, L., Guzman, M. C., ... Worland, S. T. (2002). Structure-based design, synthesis, and biological evaluation of irreversible human

- rhinovirus 3C protease inhibitors. 6. Structure-activity studies of orally bioavailable, 2-pyridone-containing peptidomimetics. *Journal of Medicinal Chemistry*, 45(8), 1607–1623. <https://doi.org/10.1021/jm010469k>
- Duan, L., Wang, T.-Q., Bian, W., Liu, W., Sun, Y., & Yang, B.-S. (2015). Centrin: Another target of monastrol, an inhibitor of mitotic spindle. *Spectrochimica Acta Part A: Molecular and Biomolecular Spectroscopy*, 137, 1086–1091. <https://doi.org/10.1016/j.saa.2014.08.050>
- Dubey, R., Singh, P., Singh, A. K., Yadav, M. K., Swati, D., Vinayak, M., Puerta, C., Valerga, P., Ravi Kumar, K., Sridhar, B., & Tewari, A. K. (2014). Polymorphic Signature of the Anti-inflammatory Activity of 2,2'-{[1,2-Phenylenebis(methylene)]bis(sulfanediyl)}bis(4,6-dimethylnicotinonitrile). *Crystal Growth & Design*, 14(3), 1347–1356. <https://doi.org/10.1021/cg401842y>
- Editor, B. (2001). The weak hydrogen bond in structural chemistry and biology. By Gautam R Desiraju and Thomas Steiner. Pp. xiv + 507. New York: Oxford University Press/International Union of Crystallography, 2001. Price US\$55.00. ISBN 0 19 850970 7 (paper). *Acta Crystallographica Section B: Structural Science*, 57(5), 723–723. <https://doi.org/10.1107/S0108768101013118>
- Eggert, K., Squillacote, D., Barone, P., Dodel, R., Katzenschlager, R., Emre, M., Lees, A. J., Rascol, O., Poewe, W., Tolosa, E., Trenkwalder, C., Onofrj, M., Stocchi, F., Nappi, G., Kostic, V., Potic, J., Ruzicka, E., & Oertel, W. (2010). Safety and efficacy of perampanel in advanced Parkinson's disease: A randomized, placebo-controlled study. *Movement Disorders*, 25(7), 896–905. <https://doi.org/10.1002/mds.22974>
- Fassihi, A., Abedi, D., Saghiaie, L., Sabet, R., Fazeli, H., Bostaki, G., Deilami, O., & Sadinpour, H. (2009). Synthesis, antimicrobial evaluation and QSAR study of some 3-hydroxypyridine-4-one and 3-hydroxypyran-4-one derivatives. *European Journal of Medicinal Chemistry*, 44(5), 2145–2157. <https://doi.org/10.1016/j.ejmech.2008.10.022>

- Fleming, F. F., Yao, L., Ravikumar, P. C., Funk, L., & Shook, B. C. (2010). Nitrile-Containing Pharmaceuticals: Efficacious Roles of the Nitrile Pharmacophore. *Journal of Medicinal Chemistry*, 53(22), 7902–7917. <https://doi.org/10.1021/jm100762r>
- Fujita, Y., Oguri, H., & Oikawa, H. (2005). Biosynthetic studies on the antibiotics PF1140: A novel pathway for a 2-pyridone framework. *Tetrahedron Letters*, 46(35), 5885–5888. <https://doi.org/10.1016/j.tetlet.2005.06.115>
- Gallant, M., Phan Viet Minh Tan, & Wuest, J. D. (1991). Use of hydrogen bonds to control molecular aggregation. Association of dipyridones joined by flexible spacers. *The Journal of Organic Chemistry*, 56(7), 2284–2286. <https://doi.org/10.1021/jo00007a007>
- Gazit, E. (2002). A possible role for pi-stacking in the self-assembly of amyloid fibrils. *FASEB Journal: Official Publication of the Federation of American Societies for Experimental Biology*, 16(1), 77–83. <https://doi.org/10.1096/fj.01-0442hyp>
- Goud, N. R., Babu, N. J., & Nangia, A. (2011). Sulfonamide–Pyridine-N-oxide Cocrystals. *Crystal Growth & Design*, 11(5), 1930–1939. <https://doi.org/10.1021/cg200094x>
- Gray, S. P., & Cooper, M. E. (2011). Alleviating the burden of diabetic nephropathy. *Nature Reviews Nephrology*, 7(2), 71–73. <https://doi.org/10.1038/nrneph.2010.176>
- Griffiths, K. E., & Stoddart, J. F. (2008). Template-directed synthesis of donor/acceptor [2]catenanes and [2]rotaxanes. *Pure and Applied Chemistry*, 80(3), 485–506. <https://doi.org/10.1351/pac200880030485>
- Hobza, P., Selzle, H. L., & Schlag, E. W. (1990). Floppy structure of the benzene dimer: Ab initio calculation on the structure and dipole moment. *The Journal of Chemical Physics*, 93(8), 5893–5897. <https://doi.org/10.1063/1.459587>
- Hobza, Pavel, & Šponer, J. (1999). Structure, Energetics, and Dynamics of the Nucleic Acid Base Pairs: Nonempirical Ab Initio Calculations. *Chemical Reviews*, 99(11), 3247–3276. <https://doi.org/10.1021/cr9800255>

- Hunter, C. A. (1993). Arene—Arene Interactions: Electrostatic or Charge Transfer? *Angewandte Chemie International Edition in English*, 32(11), 1584–1586. <https://doi.org/10.1002/anie.199315841>
- Hunter, C. A., & Sanders, J. K. M. (1990). The nature of  $\pi$ - $\pi$  Interactions. *Journal of the American Chemical Society*, 112(14), 5525–5534. <https://doi.org/10.1021/ja00170a016>
- Hurst, E. W., & Hull, R. (1961). Two New Synthetic Substances Active against Viruses of the Psittacosis-Lymphogranuloma-Trachoma Group. *Journal of Medicinal and Pharmaceutical Chemistry*, 3(2), 215–229. <https://doi.org/10.1021/jm50015a002>
- Hyperglycemia and Adverse Pregnancy Outcomes. (2008). *New England Journal of Medicine*, 358(19), 1991–2002. <https://doi.org/10.1056/NEJMoa0707943>
- International Diabetes Federation. (2019). *IDF DIABETES ATLAS* (Eight). International Diabetes Federation.
- Ivanova, M. I., Sievers, S. A., Sawaya, M. R., Wall, J. S., & Eisenberg, D. (2009). Molecular basis for insulin fibril assembly. *Proceedings of the National Academy of Sciences*, 106(45), 18990–18995. <https://doi.org/10.1073/pnas.0910080106>
- Jain, A., Purohit, C. S., Verma, S., & Sankararamkrishnan, R. (2007). Close Contacts between Carbonyl Oxygen Atoms and Aromatic Centers in Protein Structures:  $\Pi \cdots \pi$  or Lone-Pair  $\cdots \pi$  Interactions? *The Journal of Physical Chemistry B*, 111(30), 8680–8683. <https://doi.org/10.1021/jp0727421>
- Jennings, W. B., Farrell, B. M., & Malone, J. F. (2001). Attractive Intramolecular Edge-to-Face Aromatic Interactions in Flexible Organic Molecules. *Accounts of Chemical Research*, 34(11), 885–894. <https://doi.org/10.1021/ar0100475>
- Johnson, S. N., Ellington, T. L., Ngo, D. T., Nevarez, J. L., Sparks, N., Rheingold, A. L., Watkins, D. L., & Tschumper, G. S. (2019). Probing non-covalent interactions driving molecular assembly in organo-electronic building blocks. *CrystEngComm*, 21(20), 3151–3157. <https://doi.org/10.1039/C9CE00219G>

- Kannan, N., & Vishveshwara, S. (2000). Aromatic clusters: A determinant of thermal stability of thermophilic proteins. *Protein Engineering*, 13(11), 753–761. <https://doi.org/10.1093/protein/13.11.753>
- Kapoor, T. M., Mayer, T. U., Coughlin, M. L., & Mitchison, T. J. (2000). Probing Spindle Assembly Mechanisms with Monastrol, a Small Molecule Inhibitor of the Mitotic Kinesin, Eg5. *Journal of Cell Biology*, 150(5), 975–988. <https://doi.org/10.1083/jcb.150.5.975>
- Kazantsev, R. V., Dannenhoffer, A. J., Aytun, T., Harutyunyan, B., Fairfield, D. J., Bedzyk, M. J., & Stupp, S. I. (2018). Molecular Control of Internal Crystallization and Photocatalytic Function in Supramolecular Nanostructures. *Chem*, 4(7), 1596–1608. <https://doi.org/10.1016/j.chempr.2018.04.002>
- Kim, C., Newton, K. M., & Knopp, R. H. (2002). Gestational Diabetes and the Incidence of Type 2 Diabetes: A systematic review. *Diabetes Care*, 25(10), 1862–1868. <https://doi.org/10.2337/diacare.25.10.1862>
- Klärner, F.-G., & Schrader, T. (2013). Aromatic Interactions by Molecular Tweezers and Clips in Chemical and Biological Systems. *Accounts of Chemical Research*, 46(4), 967–978. <https://doi.org/10.1021/ar300061c>
- Klein, E., DeBonis, S., Thiede, B., Skoufias, D. A., Kozielski, F., & Lebeau, L. (2007). New chemical tools for investigating human mitotic kinesin Eg5. *Bioorganic & Medicinal Chemistry*, 15(19), 6474–6488. <https://doi.org/10.1016/j.bmc.2007.06.016>
- Kool, null, Morales, null, & Guckian, null. (2000). Mimicking the Structure and Function of DNA: Insights into DNA Stability and Replication. *Angewandte Chemie (International Ed. in English)*, 39(6), 990–1009. [https://doi.org/10.1002/\(sici\)1521-3773\(20000317\)39:6<990::aid-anie990>3.0.co;2-0](https://doi.org/10.1002/(sici)1521-3773(20000317)39:6<990::aid-anie990>3.0.co;2-0)
- Kool, E. T. (2001). Hydrogen Bonding, Base Stacking, and Steric Effects in DNA Replication. *Annual Review of Biophysics and Biomolecular Structure*, 30(1), 1–22. <https://doi.org/10.1146/annurev.biophys.30.1.1>

- Kostev, K., & Rathmann, W. (2013). Diabetic retinopathy at diagnosis of type 2 diabetes in the UK: a database analysis. *Diabetologia*, 56, 109–111. <https://doi.org/10.1007/s00125-012-2742-7>
- Kryger, G., Silman, I., & Sussman, J. L. (1998). Three-dimensional structure of a complex of E2020 with acetylcholinesterase from *Torpedo californica*. *Journal of Physiology, Paris*, 92(3–4), 191–194. [https://doi.org/10.1016/s0928-4257\(98\)80008-9](https://doi.org/10.1016/s0928-4257(98)80008-9)
- Lehmann, J. M., Moore, L. B., Smith-Oliver, T. A., Wilkison, W. O., Willson, T. M., & Kliewer, S. A. (1995). An Antidiabetic Thiazolidinedione Is a High Affinity Ligand for Peroxisome Proliferator-activated Receptor  $\gamma$  (PPAR $\gamma$ ). *Journal of Biological Chemistry*, 270(22), 12953–12956. <https://doi.org/10.1074/jbc.270.22.12953>
- Lenzen, S. (2008). The mechanisms of alloxan- and streptozotocin-induced diabetes. *Diabetologia*, 51(2), 216–226. <https://doi.org/10.1007/s00125-007-0886-7>
- Leslie, R. D. (2010). Predicting Adult-Onset Autoimmune Diabetes: Clarity From Complexity. *Diabetes*, 59(2), 330–331. <https://doi.org/10.2337/db09-1620>
- Li, Q., Mitscher, L. A., & Shen, L. L. (2000). The 2-pyridone antibacterial agents: Bacterial topoisomerase inhibitors. *Medicinal Research Reviews*, 20(4), 231–293. [https://doi.org/10.1002/1098-1128\(200007\)20:4<231::AID-MED1>3.0.CO;2-N](https://doi.org/10.1002/1098-1128(200007)20:4<231::AID-MED1>3.0.CO;2-N)
- Litvinov, V. P., Krivokolysko, S. G., & Dyachenko, V. D. (1999). Synthesis and properties of 3-cyanopyridine-2(1H)-chalcogenones. Review. *Chemistry of Heterocyclic Compounds*, 35(5), 509–540. <https://doi.org/10.1007/BF02324634>
- Lundstrom, K. (2006). Structural genomics for membrane proteins. *Cellular and Molecular Life Sciences*, 63(22), 2597–2607. <https://doi.org/10.1007/s00018-006-6252-y>
- Maccari, R., Vitale, R. M., Ottanà, R., Rocchiccioli, M., Marrazzo, A., Cardile, V., Graziano, A. C. E., Amodeo, P., Mura, U., & Del Corso, A. (2014). Structure-activity relationships and molecular modelling of new 5-arylidene-4-



- thiazolidinone derivatives as aldose reductase inhibitors and potential anti-inflammatory agents. *European Journal of Medicinal Chemistry*, *81*, 1–14. <https://doi.org/10.1016/j.ejmech.2014.05.003>
- Mackenzie, C. F., Spackman, P. R., Jayatilaka, D., & Spackman, M. A. (2017). *CrystalExplorer* model energies and energy frameworks: Extension to metal coordination compounds, organic salts, solvates and open-shell systems. *IUCrJ*, *4*(5), 575–587. <https://doi.org/10.1107/S205225251700848X>
- Mahapatra, M. K., Kumar, R., & Kumar, M. (2017). Synthesis, biological evaluation and in silico studies of 5-(3-methoxybenzylidene)thiazolidine-2,4-dione analogues as PTP1B inhibitors. *Bioorganic Chemistry*, *71*, 1–9. <https://doi.org/10.1016/j.bioorg.2017.01.007>
- Makin, O. S., Atkins, E., Sikorski, P., Johansson, J., & Serpell, L. C. (2005). Molecular basis for amyloid fibril formation and stability. *Proceedings of the National Academy of Sciences*, *102*(2), 315–320. <https://doi.org/10.1073/pnas.0406847102>
- Mane, P. B., Antre, R. V., & Oswal, R. J. (2012). *Antidiabetic Drugs: An Overview*. *1*, 6.
- Mangelsdorf, D. J., Thummel, C., Beato, M., Herrlich, P., Schütz, G., Umesono, K., Blumberg, B., Kastner, P., Mark, M., Chambon, P., & Evans, R. M. (1995). The nuclear receptor superfamily: The second decade. *Cell*, *83*(6), 835–839. [https://doi.org/10.1016/0092-8674\(95\)90199-X](https://doi.org/10.1016/0092-8674(95)90199-X)
- Martin, C. L., Albers, J. W., Pop-Busui, R., & for the DCCT/EDIC Research Group. (2014). Neuropathy and Related Findings in the Diabetes Control and Complications Trial/Epidemiology of Diabetes Interventions and Complications Study. *Diabetes Care*, *37*(1), 31–38. <https://doi.org/10.2337/dc13-2114>
- Mayer, T. U. (1999). Small Molecule Inhibitor of Mitotic Spindle Bipolarity Identified in a Phenotype-Based Screen. *Science*, *286*(5441), 971–974. <https://doi.org/10.1126/science.286.5441.971>
- Mazik, M. (2012). Recent developments in the molecular recognition of carbohydrates by artificial receptors. *RSC Advances*, *2*(7), 2630–2642. <https://doi.org/10.1039/C2RA01138G>

- McKinnon, J. J., Spackman, M. A., & Mitchell, A. S. (2004). Novel tools for visualizing and exploring intermolecular interactions in molecular crystals. *Acta Crystallographica Section B Structural Science*, 60(6), 627–668. <https://doi.org/10.1107/S0108768104020300>
- Meyer, E. A., Castellano, R. K., & Diederich, F. (2003). Interactions with Aromatic Rings in Chemical and Biological Recognition. *Angewandte Chemie International Edition*, 42(11), 1210–1250. <https://doi.org/10.1002/anie.200390319>
- Mijin, D., Markovic, J., Brkovic, D., & Marinkovic, A. (2014). Microwave assisted synthesis of 2-pyridone and 2-pyridone based compounds. *Hemijska Industrija*, 68(1), 1–14. <https://doi.org/10.2298/HEMIND121204021M>
- Mirkovic, J., Mijin, D., & Petrovic, S. (2013). Properties and synthesis of milrinone. *Hemijska industrija*, 67(1), 17–25. <https://doi.org/10.2298/HEMIND120410057M>
- Mirza, A. Z., Althagafi, I. I., & Shamshad, H. (2019). Role of PPAR receptor in different diseases and their ligands: Physiological importance and clinical implications. *European Journal of Medicinal Chemistry*, 166, 502–513. <https://doi.org/10.1016/j.ejmech.2019.01.067>
- Mooibroek, T. J., Gamez, P., & Reedijk, J. (2008). Lone pair– $\pi$  interactions: A new supramolecular bond? *CrystEngComm*, 10(11), 1501–1515. <https://doi.org/10.1039/B812026A>
- Morgan, R. S., Tatsch, C. E., Gushard, R. H., Mcadon, J. M., & Warne, P. K. (2009). CHAINS OF ALTERNATING SULFUR AND  $\pi$ -BONDED ATOMS IN EIGHT SMALL PROTEINS. *International Journal of Peptide and Protein Research*, 11(3), 209–217. <https://doi.org/10.1111/j.1399-3011.1978.tb02841.x>
- Müller-Dethlefs, K., & Hobza, P. (2000). Noncovalent Interactions: A Challenge for Experiment and Theory. *Chemical Reviews*, 100(1), 143–168. <https://doi.org/10.1021/cr9900331>

- Muraki, M. (2002). The Importance of CH /  $\pi$  Interactions to the Function of Carbohydrate Binding Proteins. *Protein & Peptide Letters*, 9(3), 195–209. <https://doi.org/10.2174/0929866023408751>
- Nishio, M., Umezawa, Y., Fantini, J., Weiss, M. S., & Chakrabarti, P. (2014). CH- $\pi$  hydrogen bonds in biological macromolecules. *Physical Chemistry Chemical Physics*, 16(25), 12648–12683. <https://doi.org/10.1039/C4CP00099D>
- Nolte, R. T., Wisely, G. B., Westin, S., Cobb, J. E., Lambert, M. H., Kurokawa, R., Rosenfeld, M. G., Willson, T. M., Glass, C. K., & Milburn, M. V. (1998). Ligand binding and co-activator assembly of the peroxisome proliferator-activated receptor- $\gamma$ . *Nature*, 395(6698), 137–143. <https://doi.org/10.1038/25931>
- Ono, K., Yoshizawa, M., Kato, T., & Fujita, M. (2008). Three-metal-center spin interactions through the intercalation of metal azaporphines and porphines into an organic pillared coordination box. *Chemical Communications*, 20, 2328–2330. <https://doi.org/10.1039/B801701H>
- Öztürk, G., Erol, D. D., Uzday, T., & Aytimir, M. D. (2001). Synthesis of 4(1H)-pyridinone derivatives and investigation of analgesic and antiinflammatory activities. *Il Farmaco*, 56(4), 251–256. [https://doi.org/10.1016/S0014-827X\(01\)01083-7](https://doi.org/10.1016/S0014-827X(01)01083-7)
- Pace, C. J., Kim, D., & Gao, J. (2012). Experimental Evaluation of CH- $\pi$  Interactions in a Protein Core. *Chemistry - A European Journal*, 18(19), 5832–5836. <https://doi.org/10.1002/chem.201200334>
- Parlow, J. J., Kurumbail, R. G., Stegeman, R. A., Stevens, A. M., Stallings, W. C., & South, M. S. (2003). Design, Synthesis, and Crystal Structure of Selective 2-Pyridone Tissue Factor VIIa Inhibitors. *Journal of Medicinal Chemistry*, 46(22), 4696–4701. <https://doi.org/10.1021/jm0301686>
- Parlow, J. J., & South, M. S. (2003). Synthesis of 2-pyridones as tissue factor VIIa inhibitors. *Tetrahedron*, 59(39), 7695–7701. [https://doi.org/10.1016/S0040-4020\(03\)01239-0](https://doi.org/10.1016/S0040-4020(03)01239-0)

- Parreira, R. L. T., Abrahão, O., & Galembeck, S. E. (2001). Conformational preferences of non-nucleoside HIV-1 reverse transcriptase inhibitors. *Tetrahedron*, *57*(16), 3243–3253. [https://doi.org/10.1016/S0040-4020\(01\)00193-4](https://doi.org/10.1016/S0040-4020(01)00193-4)
- Pastelin, G., Mendez, R., Kabela, E., & Farah, A. (1983). The search for a digitalis substitute II milrinone (Win 47203) its action on the heart-lung preparation of the dog. *Life Sciences*, *33*(18), 1787–1796. [https://doi.org/10.1016/0024-3205\(83\)90686-0](https://doi.org/10.1016/0024-3205(83)90686-0)
- Pettersen, E. F., Goddard, T. D., Huang, C. C., Couch, G. S., Greenblatt, D. M., Meng, E. C., & Ferrin, T. E. (2004). UCSF Chimera—A visualization system for exploratory research and analysis. *Journal of Computational Chemistry*, *25*(13), 1605–1612. <https://doi.org/10.1002/jcc.20084>
- Pollino, J. M., & Weck, M. (2005). Non-covalent side-chain polymers: Design principles, functionalization strategies, and perspectives. *Chemical Society Reviews*, *34*(3), 193. <https://doi.org/10.1039/b311285n>
- Rai, S. K., Singh, P., Khanam, S., & Tewari, A. K. (2016). Polymorphic study and anti-inflammatory activity of a 3-cyano-2-pyridone based flexible model. *New Journal of Chemistry*, *40*(6), 5577–5587. <https://doi.org/10.1039/C5NJ03683F>
- Ramesh, B., & Bhalgat, C. M. (2011). Novel dihydropyrimidines and its pyrazole derivatives: Synthesis and pharmacological screening. *European Journal of Medicinal Chemistry*, *46*(5), 1882–1891. <https://doi.org/10.1016/j.ejmech.2011.02.052>
- Rendell, M. S., & Kirchain, W. R. (2000). Pharmacotherapy of Type 2 Diabetes Mellitus. *Annals of Pharmacotherapy*, *34*(7–8), 878–895. <https://doi.org/10.1345/aph.19171>
- Ringer, A. L., Figgs, M. S., Sinnokrot, M. O., & Sherrill, C. D. (2006). Aliphatic C–H/ $\pi$  Interactions: Methane–Benzene, Methane–Phenol, and Methane–Indole Complexes. *The Journal of Physical Chemistry A*, *110*(37), 10822–10828. <https://doi.org/10.1021/jp062740l>

- Rother, K. I. (2007). Diabetes Treatment—Bridging the Divide. *New England Journal of Medicine*, 356(15), 1499–1501. <https://doi.org/10.1056/NEJMp078030>
- Rovnyak, G. C., Atwal, K. S., Hedberg, A., Kimball, S. D., Moreland, S., Gougoutas, J. Z., O'Reilly, B. C., Schwartz, J., & Malley, M. F. (1992). Dihydropyrimidine calcium channel blockers. 4. Basic 3-substituted-4-aryl-1,4-dihydropyrimidine-5-carboxylic acid esters. Potent antihypertensive agents. *Journal of Medicinal Chemistry*, 35(17), 3254–3263. <https://doi.org/10.1021/jm00095a023>
- Salonen, L. M., Ellermann, M., & Diederich, F. (2011). Aromatic Rings in Chemical and Biological Recognition: Energetics and Structures. *Angewandte Chemie International Edition*, 50(21), 4808–4842. <https://doi.org/10.1002/anie.201007560>
- Scapin, G. (2006). Structural Biology and Drug Discovery. *Current Pharmaceutical Design*, 12(17), 2087–2097. <https://doi.org/10.2174/138161206777585201>
- Seley, K. L., Zhang, L., & Hagos, A. (2001). “Fleximers”. Design and Synthesis of Two Novel Split Nucleosides. *Organic Letters*, 3(20), 3209–3210. <https://doi.org/10.1021/ol0165443>
- Seley-Radtke, K. (2018). Flexibility—Not just for yoga anymore! *Antiviral Chemistry and Chemotherapy*, 26, 204020661875678. <https://doi.org/10.1177/2040206618756788>
- Semple, G., Andersson, B. M., Chhajlani, V., Georgsson, J., Johansson, M. J., Rosenquist, A., & Swanson, L. (2003). Synthesis and Biological activity of kappa opioid receptor agonists. Part 2: Preparation of 3-aryl-2-pyridone analogues generated by solution- and solid-phase parallel synthesis methods. *Bioorganic & Medicinal Chemistry Letters*, 13(6), 1141–1145. [https://doi.org/10.1016/s0960-894x\(03\)00033-7](https://doi.org/10.1016/s0960-894x(03)00033-7)
- Shimizu, K., Murata, T., Okumura, K., Manganiello, V. C., & Tagawa, T. (2002). Expression and role of phosphodiesterase 3 in human squamous cell carcinoma KB cells: *Anti-Cancer Drugs*, 13(8), 875–880. <https://doi.org/10.1097/00001813-200209000-00014>

- Shinkai, S., Ikeda, M., Sugasaki, A., & Takeuchi, M. (2001). Positive Allosteric Systems Designed on Dynamic Supramolecular Scaffolds: Toward Switching and Amplification of Guest Affinity and Selectivity †. *Accounts of Chemical Research*, 34(6), 494–503. <https://doi.org/10.1021/ar000177y>
- Singh, V. P., Dowarah, J., Marak, B. N., & Tewari, A. K. (2020). Design, synthesis, in silico analysis with PPAR  $\gamma$  receptor and study of non-covalent interactions in unsymmetrical heterocyclic/phenyl fleximer. *Journal of the Chinese Chemical Society*, jccs.202000215. <https://doi.org/10.1002/jccs.202000215>
- Spek, A. L. (2009). Structure validation in chemical crystallography. *Acta Crystallographica Section D Biological Crystallography*, 65(2), 148–155. <https://doi.org/10.1107/S090744490804362X>
- Šponer, J., Riley, K. E., & Hobza, P. (2008). Nature and magnitude of aromatic stacking of nucleic acid bases. *Physical Chemistry Chemical Physics*, 10(19), 2595–2610. <https://doi.org/10.1039/B719370J>
- Steiner, T. (2002). The Hydrogen Bond in the Solid State. *Angewandte Chemie International Edition*, 41(1), 48–76. [https://doi.org/10.1002/1521-3773\(20020104\)41:1<48::AID-ANIE48>3.0.CO;2-U](https://doi.org/10.1002/1521-3773(20020104)41:1<48::AID-ANIE48>3.0.CO;2-U)
- Steno, N., Ferdinando, & Accademia della Crusca. (1669). *Nicolai Stenonis De solido intra solidum naturaliter contento dissertationis prodromus* (pp. 1–98). Ex typographia sub signo Stellae,. <https://doi.org/10.5962/bhl.title.148841>
- Storck, P., Aubertin, A.-M., & Grierson, D. S. (2005). Tosylation/mesylation of 4-hydroxy-3-nitro-2-pyridinones as an activation step in the construction of dihydropyrido[3,4-b] benzo[f][1,4]thiazepin-1-one based anti-HIV agents. *Tetrahedron Letters*, 46(16), 2919–2922. <https://doi.org/10.1016/j.tetlet.2005.02.128>
- Sudha, R., Kohtani, M., & Jarrold, M. F. (2005). Non-Covalent Interactions between Unsolvated Peptides: Helical Complexes Based on Acid–Base Interactions. *The Journal of Physical Chemistry B*, 109(13), 6442–6447. <https://doi.org/10.1021/jp045490m>

- Swierczynski, D., Luboradzki, R., Dolgonos, G., Lipkowski, J., & Schneider, H.-J. (2005). Non-Covalent Interactions of Organic Halogen Compounds with Aromatic Systems – Analyses of Crystal Structure Data. *European Journal of Organic Chemistry*, 2005(6), 1172–1177. <https://doi.org/10.1002/ejoc.200400446>
- Tewari, Ashish K., & Dubey, R. (2009). Conformational tuning of molecular network stabilized via C-H... $\pi$  &  $\pi$ - $\pi$  interaction in 2-[2-(3-cyano-4, 6-dimethyl-2-oxo-2H-pyridin-1-yl-methyl)-benzyloxy]-4, 6-dimethyl-nicotinonitrile. *Arkivoc*, 2009(10), 283–291. <https://doi.org/10.3998/ark.5550190.0010.a25>
- Tewari, Ashish Kumar, & Dubey, R. (2008). Emerging trends in molecular recognition: Utility of weak aromatic interactions. *Bioorganic & Medicinal Chemistry*, 16(1), 126–143. <https://doi.org/10.1016/j.bmc.2007.09.023>
- Thangavel, N., Al Bratty, M., Akhtar Javed, S., Ahsan, W., & Alhazmi, H. A. (2017). Targeting Peroxisome Proliferator-Activated Receptors Using Thiazolidinediones: Strategy for Design of Novel Antidiabetic Drugs. *International Journal of Medicinal Chemistry*, 2017, 1–20. <https://doi.org/10.1155/2017/1069718>
- Todd, J. A. (2010). Etiology of Type 1 Diabetes. *Immunity*, 32(4), 457–467. <https://doi.org/10.1016/j.immuni.2010.04.001>
- Trott, O., & Olson, A. J. (2009). AutoDock Vina: Improving the speed and accuracy of docking with a new scoring function, efficient optimization, and multithreading. *Journal of Computational Chemistry*, NA-NA. <https://doi.org/10.1002/jcc.21334>
- Tsuzuki, S., & Fujii, A. (2008). Nature and physical origin of CH/ $\pi$  interaction: Significant difference from conventional hydrogen bonds. *Physical Chemistry Chemical Physics*, 10(19), 2584. <https://doi.org/10.1039/b718656h>
- Tsuzuki, S., Honda, K., Uchimar, T., Mikami, M., & Tanabe, K. (1999). High-Level ab Initio Calculations of Interaction Energies of C<sub>2</sub>H<sub>4</sub>-CH<sub>4</sub> and C<sub>2</sub>H<sub>6</sub>-CH<sub>4</sub> Dimers: A Model Study of CH/ $\pi$  Interaction. *The Journal of Physical Chemistry A*, 103(41), 8265–8271. <https://doi.org/10.1021/jp9909309>

- Tsuzuki, S., Honda, K., Uchimarui, T., Mikami, M., & Tanabe, K. (2000). The Magnitude of the CH/ $\pi$  Interaction between Benzene and Some Model Hydrocarbons. *Journal of the American Chemical Society*, 122(15), 3746–3753. <https://doi.org/10.1021/ja993972j>
- Tsuzuki, S., Uchimarui, T., & Tanabe, K. (1994). Basis set effects on the intermolecular interaction of hydrocarbon molecules obtained by an ab initio molecular orbital method: Evaluation of dispersion energy. *Journal of Molecular Structure: THEOCHEM*, 307, 107–118. [https://doi.org/10.1016/0166-1280\(94\)80122-3](https://doi.org/10.1016/0166-1280(94)80122-3)
- Turner, M. J., Grabowsky, S., Jayatilaka, D., & Spackman, M. A. (2014). Accurate and Efficient Model Energies for Exploring Intermolecular Interactions in Molecular Crystals. *The Journal of Physical Chemistry Letters*, 5(24), 4249–4255. <https://doi.org/10.1021/jz502271c>
- Van Belle, T. L., Coppieters, K. T., & Von Herrath, M. G. (2011). Type 1 Diabetes: Etiology, Immunology, and Therapeutic Strategies. *Physiological Reviews*, 91(1), 79–118. <https://doi.org/10.1152/physrev.00003.2010>
- von Feilitzsch, T. (2006). Charge Transfer in DNA. From Mechanism to Application. Edited by Hans-Achim Wagenknecht. *Angewandte Chemie International Edition*, 45(3), 346–347. <https://doi.org/10.1002/anie.200585325>
- Walsh, R. D. B., Bradner, M. W., Fleischman, S., Morales, L. A., Moulton, B., Rodríguez-Hornedo, N., & Zaworotko, M. J. (2003). Crystal engineering of the composition of pharmaceutical phases. *Chemical Communications*, 2, 186–187. <https://doi.org/10.1039/b208574g>
- Wan, C.-Q., Chen, X.-D., & Mak, T. C. W. (2008). Supramolecular frameworks assembled via intermolecular lone pair-aromatic interaction between carbonyl and pyridyl groups. *CrystEngComm*, 10(5), 475–478. <https://doi.org/10.1039/B718823D>
- Wild, S., Roglic, G., Green, A., Sicree, R., & King, H. (2004). Global Prevalence of Diabetes: Estimates for the year 2000 and projections for 2030. *Diabetes Care*, 27(5), 1047–1053. <https://doi.org/10.2337/diacare.27.5.1047>



- Williams, R. M., & Kwast, A. (1988). Versatile new approach to the synthesis of monosubstituted and bicyclic piperazine-2,5-diones: Unusual in situ generation and enolate addition to a cumulene. *The Journal of Organic Chemistry*, *53*(24), 5785–5787. <https://doi.org/10.1021/jo00259a036>
- Wong, C.-H., Chow, H.-F., Hui, S.-K., & Sze, K.-H. (2006). Generation-Independent Dimerization Behavior of Quadruple Hydrogen-Bond-Containing Oligoether Dendrons. *Organic Letters*, *8*(9), 1811–1814. <https://doi.org/10.1021/ol0603716>
- Wu, R., & McMahon, T. B. (2008). Investigation of Cation- $\pi$  Interactions in Biological Systems. *Journal of the American Chemical Society*, *130*(38), 12554–12555. <https://doi.org/10.1021/ja802117s>
- Wukich, D. K., Armstrong, D. G., Attinger, C. E., Boulton, A. J. M., Burns, P. R., Frykberg, R. G., Hellman, R., Kim, P. J., Lipsky, B. A., Pile, J. C., Pinzur, M. S., & Siminerio, L. (2013). Inpatient Management of Diabetic Foot Disorders: A Clinical Guide. *Diabetes Care*, *36*(9), 2862–2871. <https://doi.org/10.2337/dc12-2712>
- Yamauchi, Y., Yoshizawa, M., & Fujita, M. (2008). Engineering Stacks of Aromatic Rings by the Interpenetration of Self-Assembled Coordination Cages. *Journal of the American Chemical Society*, *130*(18), 5832–5833. <https://doi.org/10.1021/ja077783+>
- Yan, C., Su, N., & Wu, S. (2007). The structure and spectra of H-bonded complexes formed by 2-pyridone. *Russian Journal of Physical Chemistry A*, *81*(12), 1980–1985. <https://doi.org/10.1134/S0036024407120138>
- Yoshizawa, M., Klosterman, J. K., & Fujita, M. (2009). Functional Molecular Flasks: New Properties and Reactions within Discrete, Self-Assembled Hosts. *Angewandte Chemie International Edition*, *48*(19), 3418–3438. <https://doi.org/10.1002/anie.200805340>
- Yoshizawa, M., Tamura, M., & Fujita, M. (2007). Chirality Enrichment through the Heterorecognition of Enantiomers in an Achiral Coordination Host. *Angewandte*

*Chemie International Edition*, 46(21), 3874–3876.  
<https://doi.org/10.1002/anie.200700103>

Zhu, L., Cheng, P., Lei, N., Yao, J., Sheng, C., Zhuang, C., Guo, W., Liu, W., Zhang, Y., Dong, G., Wang, S., Miao, Z., & Zhang, W. (2011). Synthesis and Biological Evaluation of Novel Homocamptothecins Conjugating with Dihydropyrimidine Derivatives as Potent Topoisomerase I Inhibitors. *Archiv Der Pharmazie*, 344(11), 726–734. <https://doi.org/10.1002/ardp.201000402>

## LIST OF PUBLICATIONS

1. Structural and non-covalent interactions study of 2-pyridone based flexible unsymmetrical dimer, Ved P. Singh, **J. Dowarah**, Lalhruaizela, david K. Geiger, December 2019, Crystal Research and Technology, DOI: 10.1002/crat.201900 136. (**IF: 1.639**)
2. Structural chemistry and anti-inflammatory activity of flexible/restricted phenyl dimers, Ved P. Singh, **J. Dowarah**, Ashish K. Tewari and David K. Geiger, January 2020, Journal of the Iranian Chemical Society, DOI: 10.1007/s13738-020-01853-x. (**IF: 2.019**)
3. Anti-diabetic drugs recent approaches and advancements, **J. Dowarah**, Ved P. Singh, January 2020, Bioorganic & Medicinal Chemistry 28(5):115263. (**IF: 3.641**)
4. A Comprehensive Insight on the Recent Development of Cyclic Dependent Kinase Inhibitors as Anticancer Agents, Brilliant N. Marak, Jayanta Dowarah, Dingtea Khiangte, Ved Prakash Singh\*, European Journal of Medicinal Chemistry, (**IF: 6.514**). (DOI: 10.1016/j.ejmech.2020.112571).
5. Design, synthesis, In silico analysis and structural study of 4,6-dimethyl-2-(3-(p-tolyloxy)propoxy)nicotinonitrile fleximer, **J. Dowarah**, Brilliant N. Marak Lalhruaizela, Balkaran S. Sran, Ved P. Singh, Accepted, Crystal Research and Technology, (**IF: 1.639**). (DOI: 10.1002/crat.202000100).
6. Design, synthesis, in silico analysis with PPAR- $\gamma$  receptor and study of non-covalent interactions in unsymmetrical heterocyclic/phenyl fleximer, Ved P. Singh, J. Dowarah, Brilliant N. Marak, Lalhruaizela, Balkaran S. Sran, Ashish K. Tewari, Journal of the Chinese chemical society, (**IF: 1.967**), (DOI:10.1002/jccs.202000215).
7. A step towards repurposing drug discovery for Covid-19 therapeutics through In Silico approach, Marak, Brilliant N., **Dowarah, Jayanta**, Khiangte Dinga, Ved P. Singh\*, Drug Development Research, (**IF: 4.360**) (. <https://doi.org/10.1002/ddr.21757>) (2020).
8. Study of supramolecular self-assembly of pyridone and dihydropyridone co-crystal: Synthesis, crystal structure, Hirshfeld surface, DFT and molecular docking studies, Lalhruaizela, Brilliant N Marak, Dipanta Gogoi, **Jayanta Dowarah**, Balkaran S Sran, Zodinpuia Pachuau, Ved Prakash Singh\*, Journal of Molecular Structure, (**IF: 3.196**) (DOI: 10.1016/j.molstruc.2021.130214).

9. Study of the structure-bioactivity of fleximers: synthesis, crystal structure, Hirshfeld surface analysis, and anti-inflammatory assays, Ved Prakash Singh, **Jayanta Dowarah**, Brilliant N Marak, Balkaran Singh Sran, Ashish Kumar Tewari, Journal of Molecular Structure, (**IF: 3.196**) (DOI: 10.1016/j.molstruc.2021.130513).

10. Potential drug development and therapeutic approaches for clinical intervention in COVID-19, **Jayanta Dowarah**, Brilliant N Marak, Umesh Chand Singh Yadav, Ved Prakash Singh, Bioorganic Chemistry, (**IF: 5.2**) (DOI: 10.1016/j.bioorg.2021.105016).

### **CONFERENCES AND SYMPOSIUM**

1. Poster presented in international conference on chemistry and environmental sustainability, entitled: “**Drug design & synthesis of anti-inflammatory compounds and study their biological activity**”, organised by department of chemistry, Mizoram University.

2. Paper presented in international conference on Emerging trends in chemical sciences, entitled: “**Synthesis, Structural Studies And Anti-Inflammatory Activities Of Pyridone-Based Fleximers**”, organized by department of chemistry, Gauhati University.

3. Paper presented on national conferences on functional materials and applications - 2019, entitled: “**Molecular Recognition: Synthesis and Study of Non-Covalent Interactions in Organic Fleximers**”, organized by department of BS and HSS (Physics), N.I.T Mizoram.

4. Paper presented on international seminar on recent advances in science and technology, entitled: “**Design, synthesis and in silico analysis of rosiglitazone based compounds against PPAR- $\gamma$  receptor as anti-diabetics drugs**”, organized by NEAST, Mizoram University.

## BIO-DATA

- 1. NAME** : Jayanta Dowarah
- 2. DATE OF BIRTH** : 31 December 1992
- 3. FATHER'S NAME** : Pradip Dowarah
- 4. PERMANENT ADDRESS** : Sivasagar, Assam, 785685
- 5. EMAIL ADDRESS** : jayantadowarah20@gmail.com

## 5. EDUCATIONAL QUALIFICATIONS

Examination passed	Year of Passing	Board/ University	Registration No.	Class/ Division	% of Marks	Subjects
High School Leaving Certificate Examination	2008	Board of Secondary Education, Assam	23R/0045/002866/06	I	60	Maths, Eng, Sci, S. sci, Ass, Hin
Higher Secondary School Leaving Certificate Examination	2010	Assam Higher Secondary Education Council	21B076300-0809	I	62.4	Chem, Phy, Maths, Biolg, Maths, Eng, Ass
B. Sc.	2013	Dibrugarh University (Assam)	11025469	First class with distinction	67.7	Chem(M), Phy, Maths, Eng, Env Sci
M.Sc	2015	Mizoram university	87 of 2014	Distinction (Gold Medalist)	84.55	Org Chem(spl), Ing chem, Phy chem, Anal chem

## PARTICULARS OF THE CANDIDATE

NAME OF CANDIDATE : Jayanta Dowarah  
DEGREE : Doctor of Philosophy (Ph.D)  
DEPARTMENT : Chemistry  
TITLE OF THESIS : Molecular Recognition: Synthesis and Study of  
Non-covalent Interactions in Organic Fleximers.  
DATE OF ADMISSION : 18<sup>th</sup> August, 2015

### APPROVAL OF RESEARCH PROPOSAL:

1. BOS : 13<sup>th</sup> April, 2016  
2. SCHOOL BOARD : 21<sup>st</sup> April, 2016  
MZU REGN. NO. : 87 of 2014  
Ph.D REGN. NO. & DATE : MZU/Ph.D/845 of 21.04.2016  
EXTENTION : NIL

Head

Department of Chemistry

**ABSTRACT**

**MOLECULAR RECOGNITION: SYNTHESIS AND STUDY OF  
NON-COVALENT INTERACTIONS IN ORGANIC FLEXIMERS**

**A THESIS SUBMITTED IN PARTIAL FULFILLMENT OF THE  
REQUIREMENTS FOR THE DEGREE OF DOCTOR OF  
PHILOSOPHY**

**JAYANTA DOWARAH**

**MZU REGISTRATION NO. : 87 of 2014**

**Ph.D REGISTRATION NO. : MZU/Ph.D/845 of 21.04.2016**



**DEPARTMENT OF CHEMISTRY  
SCHOOL OF PHYSICAL SCIENCES  
FEBRUARY, 2021**

**MOLECULAR RECOGNITION: SYNTHESIS AND STUDY OF NON-  
COVALENT INTERACTIONS IN ORGANIC FLEXIMERS**

**BY**

**JAYANTA DOWARAH**

**Department of Chemistry**

Under the supervision of

**Dr. VED PRAKASH SINGH**

Submitted

In partial fulfillment of the requirement of the Degree of Doctor of Philosophy in  
Chemistry of Mizoram University, Aizawl.



Non-covalent interactions are of pivotal importance in many areas of chemistry, biology, and materials science. The intermolecular interactions involving aromatic rings, in particular, are fundamental to molecular organization and recognition processes.

In summary, we have successfully synthesized five types of new molecular balances for studying arene-arene interactions.

Due to their efficient syntheses, balances with arene arms of varying size could be readily prepared and studied.

The geometrical and orientational preferences are the simplest prototype of aromatic  $\pi$ - $\pi$  interactions. Benzene dimer, unsymmetrically substituted benzene- hetero-aromatic flexible dimers unsymmetrical hetero-aromatic dimers are explored.

The role of substituents in tuning  $\pi$ - $\pi$  interaction is investigated in this study. By studying dimers of benzene with various pyridine/pyridone-containing systems (in the sandwich and T-shaped configurations), it was found that *all* of the substituted sandwich dimers considered have not shown a similar pattern as in benzene dimer.

This stability facilitated the accurate measurement of the strength of the arene-arene interactions by introducing hetero-aromatic systems. It also facilitates the conformational analysis of the arene-arene interaction in the solid-state.

The results suggested that arene-arene interaction is much affected by the size, geometry, and surroundings of molecules.

1<sup>st</sup> Chapter deals with the literature review of the whole study. This chapter also deals with the importance of all designed schemes discussed in the 1<sup>st</sup> Chapter one by one.

The hetero atom with simple methylene linked arms with different ring types plays an important role in aromatic interactions studied in Chapter 2 with unsymmetrical dimers and methylene linked monomers.

We have synthesized three series of fleximers based on 2-pyridones, 2-dihydropyridones, and dihydropyrimidinones derivatives with methylene linkers in chapter 2.

We have used *Citrus macroptera* juice for the first time to synthesize dihydropyrimidinones derivatives, which is an eco-friendly procedure. The other advantages of this procedure are better yield and shorter reaction time.

The compounds of Chapter 2 have been found to exhibit the better feature of aromatic interactions and anti-carcinogenic activity. Some of the compounds were synthesized with bio-catalyst. These studies clearly show that heterocyclic ring systems show more polarisations over simple aromatic functions and show much more stacking effects than substituted aromatic hydrocarbons.

Size also plays an important role in aromatic interactions that have been studied in flexible unsymmetrical dimers of pyridine, pyridone and dihydropyrimidinones systems. Few methylene-linked pyridone and dihydropyrimidinones are having good biological activity and less toxicity. A computational study is also done and found compatible binding mode with target receptors. Docking results are supporting to *in vitro* analysis. The anticancer activity was carried out in Human adenocarcinoma A549 cells. This study found some compounds having better activity than standard drugs.

Chapter 3 deals with the synthesis and structural studies of poly-aromatic fleximers. The structural studies of these fleximers have given clear experimental evidence of the intermolecular and intermolecular aromatic interactions in the models containing poly-aromatic moiety.

The increased area's effect was studied in Chapter 3, where two fused ring systems and three fused ring systems viz phthalimide have been selected. It was concluded that the introduction of phthalimide moiety usually enhances the aromatic interactions.

The 3<sup>rd</sup> Chapter's compounds are highly influenced by size using phthalimide and polarisation by using heteroatom nitrogen in aromatic rings.

Some PPAR $\gamma$  agonists have been synthesized based on rosiglitazone's structural features and screened for their biological activities in 4<sup>th</sup> Chapters, and computational *in silico* studies were performed for these molecules.

Few compounds are very prompt for diabetes compared to the standard drug in docking and *in vivo* activity.

Docking studies support our *in vivo* activity result that helps in screening these compounds for further studies.

A further detailed study is required for these compounds to develop more potent anti-diabetic active drugs.

In summary, the present treatise deals with the synthesis of few models and the study to understand the effects of the different structural environmental conditions by changing the substituent size and nature on aromatic interactions. However, a lot of studies are still required on different types of models to understand the mechanism of aromatic interactions. The biological study is also in an earlier stage for developing a good drug, so it requires further studies in this direction.

This study demonstrates that even in simple model systems, the study of weak, non-covalent interactions is still very challenging.